NASA
Technical
Paper
2432
C.2
June 1985

Static Investigation of Several Yaw Vectoring Concepts on Nonaxisymmetric Nozzles

Mary L. Mason and
Bobby L. Berrier

NASA

NASA
Technical
Paper
2432

1985

Static Investigation of Several Yaw Vectoring Concepts on Nonaxisymmetric Nozzles

Mary L. Mason and
Bobby L. Berrier

Langley Research Center
Hampton, Virginia

NASA
National Aeronautics
and Space Administration

Scientific and Technical
Information Branch

Summary

A test has been conducted in the static test facility of the Langley 16-Foot Transonic Tunnel to determine the flow-turning capability and the effects on nozzle internal performance of several yaw vectoring concepts.

Nonaxisymmetric convergent-divergent nozzles with throat areas simulating dry and afterburning power settings and single expansion ramp nozzles with a throat area simulating a dry power setting were modified for yaw thrust vectoring. Forward-thrust and pitch-vectored nozzle configurations were tested with each yaw vectoring concept. Four basic yaw vectoring concepts were investigated on the nonaxisymmetric convergent-divergent nozzles: translating sidewall, downstream (of throat) flaps, upstream (of throat) port/flap, and powered rudder. Selected combinations of the rudder with downstream flaps or upstream port/flap concepts were also tested. A single yaw vectoring concept, post-exit flaps, was investigated on the single expansion ramp nozzles. All testing was conducted at static (no external flow) conditions and nozzle pressure ratio varied from 2.0 up to 10.0.

Results from this investigation indicate that yaw thrust vectoring, either alone or simultaneously with pitch thrust vectoring, is feasible for both nonaxisymmetric convergent-divergent nozzles and single expansion ramp nozzles. The largest resultant yaw vector angles were produced by flaps downstream of the throat in each sidewall (downstream flap concept). At a low nozzle expansion ratio, the resultant yaw vector angle approached the geometric yaw vector angle. This yaw vectoring concept is similar to current pitch thrust vectoring concepts except the thrust deflection plane has been rotated 90°.

Introduction

Current fighter aircraft are designed for good maneuverability over a wide range of flight Mach numbers and engine power settings. A propulsion system with variable exhaust-nozzle geometry enhances aircraft performance at different engine throttle settings. Recent investigations of the effects of different nozzle designs on advanced jet aircraft performance have shown that nonaxisymmetric (or two-dimensional) nozzles not only meet performance objectives but also allow several valuable propulsion-system design options (refs. 1 through 4). The nonaxisymmetric nozzle geometry integrates well into multiengine airframe designs and can result in low installed drag (refs. 5 through 8). The utilization of nonaxisymmetric nozzles also facilitates thrust vectoring and thrust reversing capabilities which improve the overall aircraft maneuverability and agility and reduce takeoff and landing distances (refs. 3, 4, and 8).

Pitch thrust vectoring concepts which direct the exhaust flow away from the axial direction have been successfully applied to several nonaxisymmetric nozzle designs (refs. 5 through 12). The cross-sectional shape of nonaxisymmetric nozzles (rectangular instead of circular) could also be easily modified for thrust vectoring in the lateral direction, that is, yaw vectoring. Yaw vectoring controls at high angles of attack may increase jet aircraft agility and effectiveness (ref. 13). Yaw vectoring capability at low speeds could also enhance aircraft control during short takeoff and landing operation. A one-on-one flight simulation study reported in reference 13 showed a beneficial effect of increased lateral controls on the overall performance of a conventional fighter aircraft. In this case, reaction jets were used to provide additional roll and yaw control to a baseline fighter aircraft. The effect of the reaction-control jets was indicated by the percentage of advantages attained by one pilot over another in a series of simulated one-on-one encounters. The aircraft with reaction-control jets achieved advantage in about 32 percent of the encounters, whereas the baseline aircraft achieved advantage in only 8 percent of the encounters. Reference 13 indicates that much of the advantage of the reaction-control jets results from additional yaw control.

The two-dimensional convergent-divergent (2-D C-D) nozzle and the single expansion ramp nozzle (SERN) are two different generic types of nonaxisymmetric nozzles. Both nozzle concepts have been successfully adapted for pitch vectoring and thrust reversing (refs. 9 through 12). Both concepts could also be easily modified for yaw vectoring. The rectangular cross section of the SERN and 2-D C-D nozzles, with relatively flat sides, is more adaptable to yaw vectoring hardware modifications than conventional axisymmetric (circular cross section) nozzle geometries. Careful integration of yaw vectoring concepts with nonaxisymmetric nozzles which already possess a pitch thrust vectoring capability may provide a simultaneous pitch and yaw vectoring capability.

To evaluate the effectiveness of several yaw vectoring concepts on isolated nonaxisymmetric nozzle performance at static (wind off) conditions, an investigation has been conducted in the static test facility of the Langley 16-Foot Transonic Tunnel. Four basic yaw vectoring concepts and combinations of these concepts were investigated on several 2-D C-D nozzles and a single yaw vectoring concept was investigated on several SERN's. The effects of yaw vectoring were considered for several different

expansion ratios (both nozzle concepts) and throat areas simulating dry and afterburning power settings (2-D C-D nozzles only). Configurations with simultaneous pitch and yaw vectoring capabilities were also tested. The nozzle internal performance and the flow-turning capability of the various yaw vectoring nozzle configurations will be presented in this report. Selected results from this investigation were also presented in reference 14.

Symbols

All forces (with the exception of resultant gross thrust) and resultant vector angles are referred to the model centerline (body axis). A detailed discussion of the data-reduction and calibration procedures as well as definitions of forces, angles, and propulsion relationships used in this report can be found in reference 15.

AR	nozzle throat aspect ratio, w_t/h_t
A_e	nozzle exit area, in^2
A_e/A_t	nozzle expansion ratio
$(A_e/A_t)_e$	external expansion ratio for SERN (A_e measured at end of nozzle expansion ramp)
$(A_e/A_t)_i$	internal expansion ratio for SERN (A_e measured at end of nozzle lower flap)
A_p	geometric port throat (minimum) area of upstream port/flap yaw vectoring concepts, in^2
A_t	nozzle geometric throat area (includes throat area variation due to yaw vectoring concepts), in^2
c	rudder or flap chord, in.
F	measured thrust along body axis, lb
F_i	ideal isentropic gross thrust, $w_p\sqrt{\frac{RT_{t,j}}{g}\left(\frac{2\gamma}{\gamma-1}\right)\left(1-\frac{p_\infty}{p_{t,j}}\right)^{\frac{(\gamma-1)}{\gamma}}}$, lb
F_N	measured normal force, lb
F_r	resultant gross thrust, $\sqrt{F^2+F_N^2+F_S^2}$, lb
F_S	measured side force, lb
g	acceleration due to gravity, 32.174 ft/sec^2
h_e	nozzle exit height, in.
h_t	nozzle throat height, in.
l_s	axial length from nozzle throat to nozzle exit, in.
NPR	nozzle pressure ratio, $p_{t,j}/p_\infty$
$(\mathrm{NPR})_{\mathrm{des}}$	design nozzle pressure ratio (NPR for fully expanded flow at nozzle exit)
$p_{t,j}$	jet total pressure, psi
p_∞	ambient pressure, psi
R	gas constant, 53.36 ft/°R
$T_{t,j}$	jet total temperature, °R
w_i	ideal weight-flow rate, lb/sec
w_p	measured weight-flow rate, lb/sec
w_t	nozzle throat width, 4.00 in.
x_e	axial distance from nozzle connect station to nozzle exit station, in.
x_h	axial distance from nozzle connect station to flap hinge, in.
x_s	axial distance from nozzle connect station to end of left sidewall, in.
x_t	axial distance from nozzle connect station to nozzle throat station, in.
γ	ratio of specific heats, 1.3997 for air
δ	vector angle, deg
δ_p	resultant pitch vector angle, $\tan^{-1}\frac{F_N}{F}$, deg
$\delta_{v,p}$	geometric pitch vector angle measured from model centerline (positive for downward deflection angles), deg
$\delta_{v,y}$	geometric yaw vector angle; flap or rudder deflection about hinge line (positive to left looking upstream), deg
δ_y	resultant yaw vector angle, $\tan^{-1}\frac{F_S}{F}$, deg
$\delta_{y,i}$	ideal resultant yaw vector angle for upstream port/flap yaw vector concepts, deg

Abbreviations:

A/B	afterburning
conf., confs.	configuration, configurations
SERN	single expansion ramp nozzle
Sta.	model station, in.
2-D C-D	two-dimensional convergent-divergent

Configuration designations:

S1, S2, ..., S17	2-D C-D nozzle configurations with translating sidewall yaw vectoring concept
F1, F2, ..., F23	2-D C-D nozzle configurations with downstream flap yaw vectoring concept
P1, P2, ..., P19	2-D C-D nozzle configurations with upstream port/flap yaw vectoring concept
R1, R2, ..., R16	2-D C-D nozzle configurations with powered rudder yaw vectoring concept
SR1, SR2, ..., SR18	SERN configurations with post-exit flaps yaw vectoring concept

Apparatus and Methods

Static Test Facility

This investigation was conducted in the static test facility of the Langley 16-Foot Transonic Tunnel. Testing is conducted in a large room where the jet from a simulated single-engine propulsion system exhausts to atmosphere through a large open doorway. A control room is remotely located from the test area, and a closed-circuit television is used to observe the model when the jet is operating. The static test facility has an air control system which is similar to that of the 16-Foot Transonic Tunnel and includes valving, filters, and a heat exchanger to maintain the jet flow at constant stagnation temperature. The air system utilizes the same clean, dry air supply as that used by the 16-Foot Transonic Tunnel.

Single-Engine Propulsion Simulation System

A sketch of the single-engine air-powered nacelle model on which various nozzles with yaw vectoring concepts were tested is presented in figure 1. The propulsion simulation system is shown with a typical single expansion ramp nozzle (SERN) configuration installed. The body shell forward of station 20.50 was removed during this investigation.

An external high-pressure air system provided a continuous flow of clean, dry air at a controlled temperature of about 300 K. This high-pressure air was varied during jet simulation up to about 10 atm. The pressurized air was brought by six air lines through a dolly-mounted support strut and into a high-pressure plenum chamber. The air was then discharged perpendicularly into the model low-pressure plenum through eight multiholed sonic nozzles equally spaced around the high-pressure plenum. (See fig. 1.) This airflow system was designed to minimize any forces imposed by the transfer of axial momentum as the air is passed from the nonmetric high-pressure plenum to the metric (attached to the balance) low-pressure plenum. Two flexible metal bellows seal the air system (between metric and nonmetric model parts) and compensate for axial forces caused by pressurization. The low-pressure air then passed from the circular low-pressure plenum through a circular-to-rectangular transition section, a rectangular choke plate, and a rectangular instrumentation section, which were common for all nozzles tested. The instrumentation section had a ratio of flow path width to height of 1.437 and was identical in geometry to the nozzle airflow entrance (nozzle connect station). All nozzle configurations attached to the instrumentation section at model station 41.13.

Nozzle Design and Yaw Vectoring Concepts

Static yaw vectoring concepts were investigated on five previously tested 2-D C-D nozzle configurations and four previously tested SERN configurations.

2-D C-D nozzles. The 2-D C-D nozzle is a nonaxisymmetric exhaust system with symmetric pairs (upper and lower) of convergent and divergent flaps. Flat (internally) sidewalls contain the exhaust flow in the lateral direction. When this exhaust system is operated at the design nozzle pressure ratio $(\mathrm{NPR})_{\mathrm{des}}$, the entire exhaust flow expansion process occurs internally. On full-scale hardware, actuators are used to vary nozzle internal geometry to provide desired engine power setting (A_t) and/or nozzle expansion ratio A_e/A_t. Separate convergent flap and divergent flap actuators allow independent variation of engine power setting and nozzle expansion ratio to provide maximum nozzle performance over a wide range of flight conditions. The same actuators can

also provide pitch thrust vectoring capability at all engine power settings by allowing independent rotation of the divergent flaps either up or down. Development of a 2-D C-D nozzle having these multiple capabilities is described in reference 16.

All five baseline (no yaw thrust vectoring, $\delta_{v,y} = 0°$) 2-D C-D nozzles had been previously tested in the static test facility. Sketches and basic geometric parameters for each nozzle are given in figure 2. Two of the baseline configurations, S1 and S6, represent the dry power operating mode (nominal $A_t = 4.36$ in^2) with nozzle expansion ratios A_e/A_t of 1.08 and 1.78, respectively. Static internal performance of these configurations has been reported in references 9 (confs. C1 and C4) and 10 (confs. D2 and D6). It should be noted that geometric parameters given for identical nozzles in references 9 and 10 and figure 2 of this study vary slightly since measurements of throat height and width vary slightly with each nozzle assembly. The other three baseline 2-D C-D nozzles (confs. S9, S14, and S15) represented A/B power operating mode (nominal $A_t = 8.0$ in^2). Configuration S9 is representative of a subsonic combat/acceleration configuration and had an expansion ratio of 1.29. Configurations S14 and S15 were based on configuration S9 but included pitch vectoring capability. Configuration S14 had a geometric pitch vector angle $\delta_{v,p}$ of 9.79° and configuration S15 had $\delta_{v,p} = 20.28°$. Static internal performance of afterburning baseline configurations S9, S14, and S15 has been reported in reference 10 (confs. A2, A2V10, and A2V20, respectively).

All five baseline (no yaw vectoring) 2-D C-D nozzles used the same set of sidewalls. These sidewalls were sized to completely contain the exhaust flow for the dry power, $A_e/A_t = 1.78$ nozzle (conf. S6) which had an exit area $A_e = 7.78$ in^2. Consequently, the A/B power nozzle configurations, which have exit areas greater than 7.78 in^2, have gaps between the flaps and the sidewalls near the nozzle exit. (See fig. 2, confs. S9, S14, and S15.)

2-D C-D yaw vectoring concepts. Four different yaw thrust vectoring concepts were investigated on the 2-D C-D baseline nozzles. Selected combinations of these concepts were also tested. The concepts were a translating left sidewall, sidewall flaps located downstream of the nozzle throat (downstream flap yaw vectoring concept), sidewall ports or flaps located upstream of the nozzle throat (upstream port/flap yaw vectoring concept), and a powered rudder. Note that adaption of these yaw thrust vectoring concepts (with exception of powered rudder) to full-scale flight hardware would require similar modifications (e.g., flaps or ports) in each nozzle sidewall for a single-engine installation or in each "outside" sidewall for a twin-engine installation in order to provide both positive and negative side-force vectors. Because of symmetry, model yaw vectoring hardware was fabricated to provide only positive side-force vectors (positive resultant yaw vector angle). Thus, several yaw vector concepts of this investigation required modification to left sidewall hardware only. All yaw vectoring concepts were not applied to all baseline 2-D C-D nozzles. Sketches and photographs of the yaw vectoring concepts applied to the 2-D C-D nozzles are given in figures 2 through 11. Note that the total measured nozzle throat area A_t given in these figures includes area variation due to the geometry of the yaw vectoring concepts. For some configurations, it was necessary to calculate a throat area based on an assumed throat location (for example, for conf. S5).

Sketches of the translating sidewall yaw vectoring concept configurations are shown in figure 2. Photographs of selected configurations with this yaw vectoring concept are given in figure 3. The translating sidewall yaw vector concept is completely compatible with nozzle power setting, expansion ratio and pitch thrust vectoring requirements because a translating sidewall would not interfere with upper or lower flap geometry changes. To simulate a translating sidewall yaw vector concept, the left sidewall of the nozzle was truncated at different locations upstream of the nozzle exit. The nozzle was then tested with the modified left sidewall and the full-length (unmodified) right sidewall. The length of the truncated sidewall is represented by the ratio $(x_s - x_t)/l_s$, which is the distance from the nozzle throat to the downstream end of the left sidewall $x_s - x_t$ normalized by the length of the unmodified sidewall from the nozzle throat to the nozzle exit l_s. Each baseline nozzle was tested with truncated left sidewalls except the A/B power nozzle with 9.79° pitch vectoring capability, configuration S14. However, a sketch of configuration S14 is included in figure 2 to define the baseline nozzle geometry for other yaw vectoring concepts. Up to five values of $(x_s - x_t)/l_s$ were tested for the 2-D C-D nozzles. For the dry power configurations, the ratios $(x_s - x_t)/l_s$ tested were 1.00 (full-length sidewall), 0.63, 0.25, 0 (truncated at nozzle throat), and −0.25 (truncated upstream of the throat). The ratios $(x_s - x_t)/l_s$ for the A/B power nozzles differed from the ratios for the dry power nozzles because of a slight shift in baseline nozzle throat location x_t. For the A/B power configuration, the ratios $(x_s - x_t)/l_s$ tested were 1.00, 0.61, 0.23, −0.03, and −0.30. Expansion ratio A_e/A_t probably tends to increase as the sidewall is translated (truncated) in the upstream direction. However, a "true" exit area can-

not be determined because the exhaust flow now has a free boundary, and expansion ratio is not given in figure 2 for these configurations.

Sketches of the downstream flap yaw vectoring concept integrated with the 2-D C-D nozzles are shown in figure 4. Photographs of selected yaw vectoring configurations with the downstream flap concept are shown in figure 5. This yaw vectoring concept was investigated with each 2-D C-D nozzle except the A/B power nozzle with 9.79° pitch vectoring capability. The downstream flap yaw vectoring concept consists of flaps installed in the nozzle sidewalls downstream of the nozzle throat. When both sidewall flaps are deployed, one flap deflects into the nozzle internal flow whereas the other flap deflects away from the exhaust stream. This concept is similar to current pitch vectoring concepts (refs. 10 and 15) except that the reaction plane has been rotated 90° to provide side force rather than normal force. The sidewall flaps were sized to accommodate the minimum internal divergent flap contour of the unvectored ($\delta_{v,p} = 0°$) baseline nozzles, that is, for the $A_e/A_t = 1.08$, dry power nozzle (conf. S1). Since one of the downstream flaps deflects into the nozzle interior during yaw vectoring with both sidewall flaps, this flap sizing restraint allows normal nozzle operation over the complete range of nozzle power settings and expansion ratios tested. Unfortunately, the sizing restraint will probably reduce flap effectiveness, since this sizing results in flaps which cover only part of internal sidewall area for $A_e/A_t > 1.08$ and/or for A/B power settings (see confs. F10 and F13 in fig. 4, for example). When both sidewall flaps are deflected, the downstream flap yaw vector concept is not compatible with simultaneous dry power pitch vectoring operation because of physical interference between the nozzle upper divergent flap (used for pitch vectoring) and the yaw vectoring flap which deflects into the exhaust stream. However, by utilizing only the sidewall flap that deflects away from the exhaust stream (either left or right side depending on desired side-force vector), this concept could be compatible with simultaneous pitch thrust vectoring. Both sidewall flaps could still be utilized for yaw vectoring at $\delta_{v,p} = 0°$ or, for simplicity, a single flap deflection could be utilized at all flight conditions. Thus, as indicated in figures 4 and 5, two-flap (both sidewalls) and single-flap (left or right sidewall) yaw vector configurations were tested on all $\delta_{v,p} = 0°$ baseline 2-D C-D nozzles. A single sidewall flap, which deflected away from the exhaust stream (fig. 4(c)) was investigated on the $\delta_{v,p} = 20.28°$ nozzle. Deflecting a single sidewall flap results in substantial changes in nozzle expansion ratio A_e/A_t. When the sidewall flap is deflected into the exhaust stream, the throat of the dry power, $A_e/A_t = 1.08$ nozzle actually transfers to the exit, and the nozzle becomes a two-dimensional convergent nozzle with expansion ratio equal to 1.0. Similar changes probably occur when a single flap is deflected away from the exhaust stream (increasing A_e/A_t) or when either flap is deflected on nozzle configurations at other power settings and/or expansion ratios. However, since exhaust flow escapes through sidewall gaps or around the sidewall flap for these configurations, it is impossible to determine true exit area, and expansion ratio is not given in figure 4.

Two different hinge-line locations for the downstream flaps were tested. The forward-hinge flap ($x_h = 2.28$ in.) hinged at the upstream edge of the vectoring flap. (See fig. 4.) For the dry power nozzles, this results in a flap hinge line at the nozzle throat. Since the same yaw vectoring flaps and sidewalls were used for all 2-D C-D nozzles, this flap hinge line fell slightly upstream of the axial nozzle throat location ($x_t = 2.35$ in.) of the baseline A/B power nozzles. For positive side force and thus positive resultant yaw vector angle δ_y, the forward-hinge flap installed in the left sidewall (left forward-hinge flap) extended out from the nozzle internal exhaust flow; this caused an expansion turn of the flow. The forward-hinge flap installed in the right sidewall (right forward-hinge flap) extended into the nozzle exhaust flow; this caused a compression turn. The mid-hinge, downstream flap ($x_h = 3.42$ in.) yaw vectoring concept was hinged along the vertical centerline of the sidewall flap. This flap concept pivoted both into and out of the nozzles exhaust flow (similar to a butterfly valve) and opened up a rectangular-shaped port in the sidewall downstream of the throat. The hinge point of this concept always fell downstream of the nozzle throat for both dry power and A/B power nozzles. For positive geometric yaw vector angle $\delta_{v,y}$ (which produces positive side-force thrust vector), the upstream end of the left mid-hinge flap extended into the nozzle flow and "scooped" internal flow through the rectangular port in the sidewall. For positive geometric yaw vector angle, the downstream end of the right mid-hinge flap pivoted into the nozzle flow while a rectangular port opened simultaneously at the flap upstream end. (See figs. 4 and 5.) Any exhaust flow exiting from this right sidewall port would produce a negative side-force component and tend to reduce the turning effectiveness of a positive yaw flap deflection.

The third yaw vectoring concept integrated with the 2-D C-D nozzles was the upstream port/flap concept. Sketches of the upstream port/flap yaw vectoring concepts are shown in figure 6; a photograph of each type of upstream concept is shown in figure 7. The upstream port/flap concept was implemented on

the model by modifying only the left sidewall such that a positive side-force thrust component (positive geometric yaw vector angle) was obtained. The full-length unmodified right sidewall was used with each upstream port/flap concept. For actual application to full-scale hardware, the right sidewall would also be modified so that both positive and negative geometric yaw vector angles could be obtained as desired. The left sidewall was modified for yaw thrust vectoring by opening up a circular port or a rectangular port with hinged flap upstream of the nozzle throat. (See fig. 6.) Four types of upstream port/flap concepts were tested: a circular port ($\delta_{v,y} = 90°$); a $\delta_{v,y} = 40°$ forward-hinge flap ($x_h = 0.70$ in.) which hinged along the upstream edge of the flap such that, when deflected, the flap would extend away from the nozzle internal flow; a $\delta_{v,y} = 20°$ and $\delta_{v,y} = 40°$ mid-hinge flap ($x_h = 1.38$ in.) which hinged along the flap vertical centerline to pivot both into and out of the nozzle flow (similar to a butterfly valve) when deflected; and a $\delta_{v,y} = 40°$ aft-hinge flap ($x_h = 1.98$ in.) which hinged along the downstream edge of the flap such that, when deflected, it would extend completely into the nozzle internal flow. For a flight hardware application of this yaw thrust vectoring concept, the magnitude of the resultant yaw vector angle would be controlled by varying the circular port area or the rectangular port flap angle. For the current investigation, model port areas in the plane of the sidewall (with flaps removed for rectangular concepts) were sized to be no larger than 10 percent of the unvectored dry power nozzle throat area, $A_t = 4.36$ in^2. The geometric port throat (minimum) area A_p, listed in the tables of figure 6, does not occur in the plane of the sidewall for the rectangular port/flap concepts and varied with flap hinge location x_h and geometric yaw vector angle $\delta_{v,y}$. The maximum size of the port area was restricted because it was assumed that current engine control systems can adequately compensate for up to an additional 10-percent variation in nozzle throat area without extensive modification.

The last basic yaw thrust vectoring concept integrated with the 2-D C-D nozzles was the powered rudder. This concept was investigated on the dry power nozzles and the pitch-vectored A/B power nozzles. Sketches of the installed powered rudder are shown in figure 8. Photographs of the powered rudder assembled with the $A_e/A_t = 1.08$ dry power nozzle (conf. R4) are shown in figure 9. The powered rudder concept consisted of the baseline 2-D C-D nozzles, with unmodified full-length sidewalls, plus a rudder. The rudder was mounted on top of the nozzle and extended into the exhaust flow. Two different rudder chord lengths c were tested, 0.75 and 1.50 in. Geometric yaw vector angles (rudder deflection angles) of 0° and 20° were tested. The photographs in figure 9 show the rudder with the 1.50-in. chord deflected to a geometric yaw vector angle of 20°.

In addition to the four individual yaw thrust vectoring concepts, several combinations of concepts were also tested. Selected downstream flap yaw vectoring concepts were combined with the 1.50-in. chord, $\delta_{v,y} = 20°$ powered rudder concept and tested on the dry power, $A_e/A_t = 1.08$ nozzle (baseline conf. S1) and on the A/B power, $\delta_{v,p} = 20.28°$ pitch-vectored nozzle (baseline conf. S15). The upstream circular port and $\delta_{v,y} = 40°$ forward-hinge flap ($x_h = 0.70$ in.) yaw vectoring concepts were combined with the 1.50-in. chord, $\delta_{v,y} = 20°$ powered rudder concept and tested on the same two nozzles. A sketch of one of these combination yaw vectoring configurations is shown in figure 10, and photographs of two configurations are shown in figure 11. Figure 10 also contains a table listing all combined yaw vectoring concept configurations tested along with their important geometric parameters. Additional geometric details for these configurations are contained in the sketches of the individual concepts. (See figs. 4, 6, and 8.)

Single expansion ramp nozzles. Four previously tested baseline SERN configurations were utilized for static yaw vectoring tests. Sketches and basic geometric parameters for these $\delta_{v,y} = 0°$ baseline nozzles (confs. SR1, SR6, SR11, and SR16) are given in figure 12. All four nozzles represented dry power settings. Configurations SR1 and SR6 represented unvectored-thrust ($\delta_{v,p} = 0°$) cruise nozzles. SR1 had an internal expansion ratio $(A_e/A_t)_i$ of 1.24 and an external expansion ratio $(A_e/A_t)_e$ of 1.50. The other two SERN configurations used for yaw vectoring tests, SR11 and SR16, represented two different pitch vectoring concepts for configuration SR6 at $\delta_{v,p} = 20°$. Configuration SR11 represented a pitch thrust vectoring concept which utilized a short, variable flap in the trailing edge of the upper external expansion surface to vary geometric pitch vector angle. Configuration SR16 represented a pitch thrust vectoring concept which utilizes a variable full-length upper expansion surface in conjunction with a variable lower flap to vary geometric pitch vector angle. Configurations SR6, SR11, and SR16 had been previously tested and are reported in reference 11 as configurations F6, VF1(20), and V1(20), respectively.

SERN yaw vectoring. A single yaw vectoring concept was integrated with the baseline SERN configurations. The four baseline nozzles were modified for static yaw vectoring by attaching post-exit flaps to

the nozzle sidewalls. Sketches of the four baseline SERN configurations with post-exit flaps installed are shown in figure 12; photographs of selected configurations with and without yaw vectoring post-exit flaps are shown in figure 13. The yaw vectoring post-exit flaps attached to the external surface of both sidewalls such that a flush fit was obtained with the nozzle sidewall internal contour. As shown in figure 12(a), the post-exit flap hinge line was inclined at 46.7° from vertical. For configurations SR1, SR6, and SR11, the post-exit flaps were tested with two different chord lengths c of 0.75 and 1.50 in. Each set of post-exit flaps was tested at geometric yaw vector angles of 0° and 20°. Because of the inclined hinge line of the post-exit flaps, a geometric yaw vector angle (flap deflection) of 20° results in only a 14° angle in the axial or streamwise direction. Configuration SR16, which had both upper and lower nozzle flaps deflected for pitch thrust vectoring, was tested only with the yaw vectoring post-exit flaps of 0.75-in. chord length. As indicated in figure 12(b), the yaw vector post-exit flap had to be custom fit for configuration SR16 because of physical interference between the nozzle upper and lower flaps and the yaw vectoring flap.

Instrumentation

A six-component strain-gauge balance was used to measure the forces and moments on the model downstream of model station 20.50. Jet total pressure was measured at a fixed station in the instrumentation section by means of a four-probe rake through the upper surface, a three-probe rake through the side, and a three-probe rake through the corner. (See fig. 1.) A thermocouple was also positioned in the instrumentation section to measure the jet total temperature. Mass flow of the high-pressure air supplied to the nozzle was determined from pressure and temperature measurements in the high-pressure plenum calibrated with standard axisymmetric nozzles.

Data Reduction

All data were recorded simultaneously on magnetic tape. Approximately 50 frames of data, taken at a rate of 10 frames per second, were used for each data point; average values were used in computations. Data were taken in ascending order of $p_{t,j}$. With the exception of resultant gross thrust F_r, all force data in this report are referenced to the model centerline.

One of the basic performance parameters used in the presentation of results is the internal thrust ratio F/F_i, which is the ratio of the actual measured nozzle thrust along the body axis to the ideal nozzle thrust. Ideal thrust F_i is based on measured weight flow w_p, jet total pressure $p_{t,j}$, and jet total temperature $T_{t,j}$. (See section "Symbols.") The balance axial-force measurement, from which the actual nozzle thrust F is subsequently obtained, is initially corrected for model weight tares and balance interactions. Although the bellows arrangement in the air pressurization system was designed to eliminate pressure and momentum interactions with the balance, small bellows tares on the six balance components still exist. These tares result from a small pressure difference between the ends of the bellows when air system internal velocities are high and from small differences in the forward and aft bellows spring constants when the bellows are pressurized. These bellows tares were determined by running standard axisymmetric calibration nozzles with known performance over a range of expected longitudinal and lateral forces and moments. The resulting tares were then applied to the balance data to obtain thrust along the body axis F. The procedure for computing the bellows tares is discussed in detail in reference 15.

Several other parameters are used in the presentation of results. The ratio F_r/F_i is the resultant gross thrust divided by the ideal thrust. Resultant gross thrust is obtained from the measured axial (thrust along body axis), normal, and side components of the jet resultant force. From the definitions of F and F_r, it is obvious that the thrust along the body axis F includes losses which result from turning the exhaust vector away from the axial direction, whereas resultant gross thrust F_r does not. Losses included in both thrust terms are friction and pressure drags associated with the thrust vectoring hardware and, for some concepts, reductions in weight flow available for producing thrust. Resultant thrust vector angles in the longitudinal (pitch) plane δ_p and the lateral (yaw) plane δ_y are presented for evaluating the exhaust flow-turning capability of various thrust vectoring concepts. Nozzle discharge coefficient w_p/w_i is the ratio of measured weight flow to ideal weight flow where ideal weight flow is based on jet total pressure $p_{t,j}$, jet total temperature $T_{t,j}$, and measured nozzle throat area. The nozzle discharge coefficient reflects the ability of a nozzle to pass weight flow and is reduced by any momentum and vena contracta losses (ref. 17).

For the upstream port/flap concepts, the ratio of measured resultant yaw vector angle to an ideal yaw vector angle $\delta_y/\delta_{y,i}$ is presented on summary figures as an aid in determining yaw vector concept flow-turning efficiency. By assuming that the nozzle primary flow has no side-force component and that the discharge coefficients of the primary nozzle flow

and port flow are equal to unity, it can be shown that an ideal yaw vector angle can be defined as

$$\delta_{y,i} = \tan^{-1} \frac{A_p \sin \delta_{v,y}}{(A_t - A_p)\cos \delta_{v,p} + A_p \cos \delta_{v,y}} \quad (1)$$

where A_t, A_p, $\delta_{v,y}$, and $\delta_{v,p}$ are given in figure 6 for each configuration.

Presentation of Results

Comparison and summary plots of the results from this investigation are presented in figures 14 to 40, which are organized as follows:

The basic nozzle internal performance data obtained during this investigation are presented in the appendix as figures 41 through 67. An index to these figures is given in tables I and II for the 2-D C-D nozzle and SERN configurations, respectively.

Results and Discussion

2-D C-D Nozzles

Translating sidewall concept. Summary results for the translating sidewall concept integrated with the 2-D C-D nozzles are presented in figures 14 to 16. Figure 14 presents the effect of varying $(x_s - x_t)/l_s$ (translating a single sidewall) on the performance of each baseline nozzle tested with this yaw vector concept. Results are presented as internal thrust ratio F/F_i, resultant thrust ratio F_r/F_i, and resultant yaw vector angle δ_y as functions of nozzle pressure ratio. The value of design nozzle pressure ratio $(\text{NPR})_{\text{des}}$ for each nozzle is indicated in the resultant yaw vector angle plots. Each of the four baseline configurations tested with a truncated sidewall achieved some yaw vectoring capability ($\delta_y > 0°$) depending on NPR and amount of sidewall truncation (translation). The dry power nozzle with $A_e/A_t = 1.08$ produced positive yaw vector angles at all values of $(x_s - x_t)/l_s < 1.0$ for NPR greater than 2.7; the dry power nozzle with $A_e/A_t = 1.78$ had positive yaw vector angles above NPR = 7.0. Both the forward-thrust A/B nozzle and the 20° pitch-vectored A/B nozzle had positive yaw vector angles above NPR = 4.5. In general, the resultant yaw vector angles are positive when the nozzle is underexpanded (operating above design NPR) and negative when the nozzle is overexpanded (operating below design NPR), particularly for values of $(x_s - x_t)/l_s > 0$. The ineffective yaw turning capability of this concept for overexpanded nozzles was expected, since NPR $< (\text{NPR})_{\text{des}}$; consequently, at this condition, there

would be no tendency for the exhaust flow to expand (turn) out the open sidewall. Thus, the translating sidewall concept is effective (generates positive values of δ_y) only when the nozzle is underexpanded. For an underexpanded nozzle, yaw vector angle increases as the ratio $(x_s - x_t)/l_s$ decreases, with the largest values of δ_y occurring when the sidewall is truncated upstream of the nozzle throat so that $(x_s - x_t)/l_s$ is negative. (See figs. 14(a) and 14(c).) These results are also clearly indicated by the data of summary figure 15. Resultant yaw vector angles up to 12° can be achieved with only small losses in internal (body axis) and resultant thrust ratios. Thrust losses are negligible for values of $(x_s - x_t)/l_s > 0$. Similar results for symmetric sidewall truncation (both sidewalls) were reported in references 9 and 10. Although yaw vectoring by sidewall truncation upstream of the nozzle throat ($(x_s - x_t)/l_s < 0$) has only a small effect on thrust, there is a 4- to 8-percent decrease in discharge coefficient from the baseline nozzle. (Compare appendix figs. 42(a) with 42(e) and 44(a) with 44(e).) The low value of w_p/w_i for $(x_s - x_t)/l_s < 0$ may be due in part to error in estimating the location of the nozzle throat and, subsequently, in computing A_t for the configuration with the upstream truncated sidewall. As expected, truncating the sidewall to values of $(x_s - x_t)/l_s > 0$ had little effect on discharge coefficient.

Since $(\text{NPR})_{\text{des}}$ is unique for each nozzle expansion ratio A_e/A_t, the relationship of δ_y to $(\text{NPR})_{\text{des}}$ is related to expansion ratio. The magnitude of δ_y may also be affected by the nozzle throat area A_t. The effects of nozzle expansion ratio on resultant yaw vector angle are summarized in figure 15. Resultant yaw vector angle is presented as a function of $(x_s - x_t)/l_s$ for the three forward-thrust ($\delta_{v,p} = 0°$) nozzles at different nozzle pressure ratios. At each NPR above 2.0, δ_y increases as A_e/A_t decreases and is positive when nozzle pressure ratio is above design. If the translating sidewall yaw vector concept is to be a viable candidate for full-scale flight hardware application, the interdependence of δ_y and A_e/A_t must be considered. The translating sidewall geometry (which controls yaw vectoring) and the nozzle upper and lower flaps (which control nozzle expansion ratio) must be coordinated so that adjustments in A_e/A_t can be used to maximize δ_y while maintaining underexpanded flow for effective yaw vectoring ($\delta_y > 0.0$). Such precise coordination would probably require the addition of integrated flight and propulsion controls to the in-flight computer capabilities. With computer-controlled nozzle geometry, the nozzle A_e/A_t could be automatically reduced, at least to an underexpanded nozzle condition and preferably to $A_e/A_t = 1.0$ (to obtain maximum resultant yaw vector angle). Decreasing A_e/A_t to insure effective yaw vector control could result in some thrust losses, but the losses could be minimized by limiting yaw vectoring to short periods of application (for example, during high-speed maneuvers or during takeoff and landing).

The feasibility of simultaneous pitch and yaw thrust vectoring was also considered during this investigation. Although all the yaw vector concepts were not compatible with pitch-vectored nozzle configurations, the translating sidewall concept was. The translating sidewall concept was investigated on the 2-D C-D pitch-vectored nozzle with a 20.28° pitch vector angle (baseline nozzle conf. S15). The results of simultaneous pitch and yaw vectoring are presented in figure 16. Resultant pitch vector angles and resultant yaw vector angles are presented as functions of the ratio $(x_s - x_t)/l_s$ at three different nozzle pressure ratios. Although the 20.28° pitch-vectored nozzle was overexpanded ($\text{NPR} < (\text{NPR})_{\text{des}}$) for the NPR range of the current test, which would tend to limit yaw vectoring capability, these results indicate that effective simultaneous pitch and yaw vectoring is feasible for the translating sidewall yaw vectoring concept. At NPR = 6.0 which is near $(\text{NPR})_{\text{des}}$, up to 6° of resultant yaw vector angle was obtained concurrent with 17° of resultant pitch vector angle at $(x_s - x_t)/l_s = -0.03$. Pitch thrust vectoring generally had a small favorable influence on resultant yaw vector angle (compare circles with squares in figure 16(b)). However, yaw thrust vectoring (decreasing values of $(x_s - x_t)/l_s$) had an adverse effect on resultant pitch vector angle as shown in figure 16(a). The detrimental effect of yaw vectoring on resultant pitch vector angle probably results because some of the nozzle internal flow expands through the truncated sidewall before it can be turned in the pitch plane by the nozzle upper and lower flaps.

Downstream flap yaw vectoring concepts. Results of the downstream flap yaw vectoring concepts are presented in figures 17 through 23. As discussed previously, downstream yaw vectoring flaps were sized for the minimum nozzle internal divergent flap contour of the 2-D C-D nozzles, that is, for the dry power, $A_e/A_t = 1.08$ nozzle. The same downstream flaps were then used for each 2-D C-D nozzle tested, regardless of expansion ratio, throat area, or geometric pitch vector angle. Effects of the sizing of the downstream flaps are included in this discussion.

The results of deflecting left and right downstream sidewall flaps on the static performance of the three forward-thrust ($\delta_{v,p} = 0°$) nozzles are presented in figure 17. The concept of using two sidewall flaps to direct the nozzle internal flow for yaw thrust

vectoring is very similar to typical 2-D C-D pitch vectoring concepts, except for the vectoring direction. Above NPR = 3.3, the dry power, $A_e/A_t = 1.08$ nozzle with left and right downstream flaps has resultant yaw vector angles which are approximately equal to the geometric yaw vector angles (fig. 17(a)); this result is a common characteristic of resultant pitch vector angles of 2-D C-D pitch-vectored nozzles. Of the two different downstream flap hinge concepts tested on the dry, $A_e/A_t = 1.08$ nozzle, the mid-hinge flaps produce slightly larger values of δ_y than the forward-hinge concept (for NPR > 3.3) but also have up to a 6-percent loss in F_r/F_i throughout the test nozzle pressure ratio range. For NPR < 3.3, which is typical of low-speed operation (Mach number less than 0.6), the forward-hinge downstream flaps are clearly superior to the mid-hinge flaps based on both resultant yaw vector angle and resultant thrust ratio results. Since F_r is the resultant gross thrust (including normal and side components) and does not include any loss that results when the actual thrust vector does not coincide with the body axis (δ_p and/or δ_y not equal to zero), a decrease in F_r/F_i (from the baseline) indicates a friction or pressure loss in the nozzle that is associated with turning the exhaust flow (turning losses) and, for some concepts, is due to installation of the yaw thrust vectoring hardware (installation losses). For the downstream flap yaw vector concepts, the geometry of the $\delta_{v,y} = 0°$ configurations is identical to the baseline (no yaw vector hardware) configuration and, thus, there are no installation losses for these concepts. All the decrease in F_r/F_i for the mid-hinge downstream flaps results from turning losses. These turning losses are probably associated with exhaust flow separation on the left sidewall flap and a reverse thrust component through the right sidewall flap port. (See fig. 4.)

The other two forward-thrust nozzles (dry power, $A_e/A_t = 1.78$ and A/B power, $A_e/A_t = 1.29$) show the same trends in thrust ratios and in δ_y (figs. 17(b) and 17(c)) as the dry power, $A_e/A_t = 1.08$ nozzle but produce lower values of resultant yaw vector angle. This loss in yaw vector effectiveness as power setting and/or A_e/A_t increases is associated with the size of the sidewall flap relative to total internal sidewall area. These effects are discussed in detail later in the text.

A potential disadvantage of the combined left and right downstream flaps yaw vectoring concept is that it may not be compatible with simultaneous pitch and yaw vectoring. The yaw vectoring flap which hinges into the nozzle internal flow (for positive $\delta_{v,y}$, the right downstream flap) would interfere with the upper (for positive $\delta_{v,p}$) and lower (for negative $\delta_{v,p}$) pitch vectoring with flaps without a redesign of the flap shapes. Consequently, a single downstream yaw vectoring flap in the left sidewall was also tested in addition to the combined downstream flaps already discussed. For positive $\delta_{v,y}$, the left sidewall flap deflects away from the upper and lower nozzle flaps, and thus simultaneous pitch thrust vectoring could be accomplished. Note that when simultaneous pitch and yaw vectoring are not required, both sidewall flaps could still be utilized for yaw thrust vectoring if desired. For data completeness and also to aid data analysis, right sidewall flap deflections were also tested on two $\delta_{v,p} = 0°$ baseline nozzles at a positive geometric yaw vector angle; simultaneous pitch thrust vectoring is not compatible with positive right sidewall deflections without redesigning flap shape.

The results of deflecting the left downstream flap alone on the performance of three baseline forward-thrust nozzles are presented in figure 18. The results of deflecting the right downstream flap alone on the performance of two of the same nozzles are presented in figure 19. Figure 20 presents results on the effects of simultaneous pitch and yaw thrust vectoring using only the left sidewall flap (fig. 4(c)) for positive values of $\delta_{v,y}$. Although the single-flap yaw vectoring configurations do not provide as much yaw vectoring capability as the combined left and right sidewall flaps yaw vectoring configurations (compare fig. 17 with figs. 18 and 19), resultant yaw vectoring angles up to 11° were obtained. Similar to the result observed when both sidewall flaps were deflected, the largest values of resultant yaw vector angle δ_y for all single-flap yaw vectoring configurations were obtained with the dry power, $A_e/A_t = 1.08$ baseline nozzle. For the left downstream flap configurations (expansion turn), the mid hinge location (fig. 4) produced larger resultant yaw vector angles (for NPR > 2.5) than the forward hinge location; this result is similar to the one observed for the left and right downstream flaps configurations at the higher NPR tested. "Scooping" or forcing the internal flow through a sidewall port opened by the mid-hinge flap is a better flow-turning mechanism than an expansion turn around a corner formed by the forward-hinge flap. An opposite result is shown for the right downstream flap configurations. For these configurations (fig. 19), the forward hinge location produced larger resultant yaw vector angles than the mid hinge location. For the mid-hinge flap, part of the positive yaw vector thrust component produced by the flap internal surface is probably offset by a negative yaw vector thrust component resulting from exhaust flow through the right sidewall port opened upstream of the hinge by the downstream mid-hinge yaw vector flap.

Resultant thrust ratio F_r/F_i and internal thrust

ratio F/F_i of all single-flap yaw vectoring configurations tested vary significantly from baseline ($\delta_{v,y} = 0°$) values. (See figs. 18 and 19.) This trend differs considerably from the result shown previously for yaw vectoring with both left and right downstream forward-hinge flaps (fig. 17) which indicated little effect of yaw vector angle on thrust ratio. It is hypothesized that all the variation in F_r/F_i and F/F_i shown in figures 18 and 19 for the forward-hinge, single-flap configurations is caused by a variation in nozzle expansion ratio A_e/A_t as geometric yaw vector angle varies. When both left and right forward-hinge sidewall flaps are utilized for yaw thrust vectoring, nozzle expansion ratio does not vary if gaps caused by flap deflection are ignored. For the forward-hinge flap in the left sidewall only, nozzle exit area and thus expansion ratio increase as geometric yaw vector angle increases. Increasing nozzle expansion ratio would increase design nozzle pressure ratio ($(\mathrm{NPR})_{\mathrm{des}} = 2.89$ for $A_e/A_t = 1.08$ baseline nozzle). Thus increasing nozzle expansion ratio (from the baseline value) would move maximum nozzle performance to higher values of NPR, increase nozzle overexpansion losses at low NPR, and decrease nozzle underexpansion losses at high NPR; these are the exact trends with increasing $\delta_{v,y}$ shown in figure 18 for the left forward-hinge flap. For the forward-hinge flap in the right sidewall only, nozzle exit area, expansion ratio, and design nozzle pressure ratio decrease as geometric yaw vector angle increases. In fact, for the dry power, $A_e/A_t = 1.08$ nozzle, the nozzle exit area for both yaw vector angles tested ($\delta_{v,y} = 10°$ and $20°$) with the right forward-hinge flap is smaller than the baseline nozzle throat area. Thus, for these configurations (F2 and F5), the nozzle throat transfers to the exit and the nozzle becomes a nonaxisymmetric convergent nozzle with $(\mathrm{NPR})_{\mathrm{des}} = 1.89$. Relative to the baseline nozzle performance, decreasing nozzle expansion ratio (by increasing $\delta_{v,y}$ with right forward-hinge flap) would move maximum nozzle performance to a lower value of NPR, decrease nozzle overexpansion losses at low NPR, and increase nozzle underexpansion losses at high NPR; these are the exact trends with increasing $\delta_{v,y}$ shown in figure 19 for the forward-hinge (right sidewall only) flap. In fact, the thrust ratios of the $\delta_{v,y} = 10°$ (conf. F2) and $\delta_{v,y} = 20°$ (conf. F5) configurations, which were known to have identical expansion ratios of 1.0, are essentially the same.

The decreases in resultant thrust ratio F_r/F_i and internal thrust ratio F/F_i from the baseline nozzles ($\delta_{v,y} = 0°$) for the mid-hinge, single-flap configurations are substantially larger than for the forward-hinge, single-flap configurations. The magnitude of the resultant thrust losses, up to 4 percent of ideal thrust for the left sidewall flap (fig. 18) and up to 6 percent of ideal thrust for the right sidewall flap (fig. 19), is too large to be completely attributed to a variation in nozzle expansion ratio as was the case for the forward-hinge flap. As discussed previously for the left and right downstream flap configurations (fig. 17), it is believed that additional thrust losses on the mid-hinge flaps are associated with exhaust flow separation on the left sidewall flap and a reverse thrust component, which could be quite large, through the right sidewall flap port. The thrust losses shown in figures 18 and 19 for the mid-hinge, single-flap configurations do not add up to equal the thrust loss shown in figure 17 for both sidewall flaps deflected, probably because of indeterminate variations in nozzle expansion ratio for the single-flap configurations.

A comparison of resultant yaw vector angles for individual and combined downstream yaw vector flap deployments is shown in figure 21. Deflection of the left sidewall flap outward (expansion turn), which is compatible with simultaneous pitch thrust vectoring, generally produced larger resultant yaw vector angles than deflection of the right sidewall flap inward (compression turn). Also shown in figure 21 is a comparison of the algebraic sum of δ_y from the left and right single-flap configurations (dashed line) with δ_y obtained with both flaps deflected. This comparison indicates that the individual flap deployment results are not additive (algebraic sum of individual δ_y less than δ_y for both flaps deflected), particularly for the dry power nozzle. Obviously, for a single-flap deflection, only the exhaust flow near the sidewall is turned through an angle near the flap geometric vector angle $\delta_{v,y}$; successively less exhaust flow turning would occur as the opposite nozzle sidewall is approached. Measured resultant yaw vector angle δ_y shown in figure 21 is essentially the exhaust flow turning angle (which probably ranges from $20°$ at one sidewall to $0°$ at the other) integrated across the nozzle exit. When both left and right flaps are deflected, a favorable or synergistic interaction occurs. For these configurations, particularly the dry power, $A_e/A_t = 1.08$ nozzle, the exhaust flow turning angles near the nozzle centerline are probably much closer to the geometric yaw vector angle than results for a single-flap deflection.

Summary figure 22 presents the effects of power setting (A_t), nozzle expansion ratio, and geometric yaw vector angle on resultant yaw vector angle for the three types of downstream flap deflections. The nozzle expansion ratios given at the top of figure 22 are for the baseline ($\delta_{v,y} = 0°$) nozzles only. Above NPR = 2.0, resultant yaw vector angle increases almost linearly with geometric yaw vector angle for all

configurations tested. This result indicates that larger resultant yaw vector angles could be obtained by larger downstream flap deflections. The nonlinear variation of δ_y with $\delta_{v,y}$ at low NPR when the left downstream flap or both downstream flaps are deflected is probably caused by exhaust flow separation on the yaw vector flap. Separation on the flap would tend to increase with increasing $\delta_{v,y}$. Another possible reason for nonlinear effects is the variation in A_e/A_t with $\delta_{v,y}$ discussed previously for single-flap yaw vector configurations.

It is obvious from figure 22 that resultant yaw vector angle is a strong function of A_e/A_t and that power setting (A_t) has at least a secondary effect on δ_y. Both of these parameters affect the size of the sidewall flap relative to total sidewall area. Comparing configurations with the same throat area (the two dry power nozzles) shows that, similar to the translating sidewall concept, decreasing nozzle expansion ratio significantly improves yaw vectoring capability; the largest values of δ_y were always obtained with the $A_e/A_t = 1.08$ nozzle. There are two reasons for this trend. The first reason is the relationship between design NPR and operating NPR discussed previously for the translating sidewall concepts. Nozzles with low expansion ratios would operate underexpanded over most of the NPR range (NPR > 2.89 for $A_e/A_t = 1.08$) and nozzle internal flow would tend to expand out the sidewall and along the downstream yaw vector flap. Nozzles with high expansion ratios would operate overexpanded over much of the NPR range (NPR < 8.62 for $A_e/A_t = 1.78$), and nozzle internal flow would not tend to expand out the sidewall. This decrease in yaw vectoring capability at NPR < $(\text{NPR})_{\text{des}}$ probably explains the large decreases in δ_y at low NPR shown in figures 17, 18, and 21. As discussed previously for the translating sidewall yaw vectoring concept, yaw vectoring capability could be optimized by coordinating yaw vector demands with expansion ratio adjustments in an integrated flight and propulsion control system. The second reason for improved yaw vector capability with reduced A_e/A_t is the variation in downstream yaw vector flap size relative to total sidewall area. As noted previously, the downstream yaw vector flaps were sized for the dry power, $A_e/A_t = 1.08$ baseline nozzle. Thus, for this configuration, the yaw vector flaps cover the entire available sidewall area. However, when A_e/A_t is increased by increasing A_e (compare confs. F1 and F10 on fig. 4(a)), the downstream yaw vector flaps do not cover the entire available sidewall area; thus, some of the internal exhaust flow can bypass the yaw vector flaps without being turned.

The secondary effect of power setting (A_t) on resultant yaw vector angle is difficult to interpret in figure 22 because nozzle expansion ratio changed when power setting was increased to afterburning. However, examination of figure 22(b) indicates that the trend of increasing δ_y with decreasing A_e/A_t is dependent to a degree on A_t since the dry power, $A_e/A_t = 1.78$ nozzle produces larger values of δ_y at NPR > 3.0 than the A/B power, $A_e/A_t = 1.29$ nozzle. The explanation for this trend reversal is the variation with A_t in downstream yaw vector flap size relative to total sidewall area. Comparing configuration F10 (fig. 4(a)) with configuration F13 (fig. 4(b)) illustrates that the A/B power yaw vector flaps (although the same physical size as the dry power yaw vector flaps) would allow a large percentage of the exhaust flow to bypass the yaw vector flaps without being turned. Based on these observations, it can be safely assumed that increasing nozzle power setting (A_t) decreases the yaw capability of the downstream flap yaw vectoring concept.

Summary figure 23 shows the relationship between resultant pitch and yaw thrust vector angles during simultaneous pitch and yaw thrust vectoring operation. As discussed previously, only single downstream yaw vector flap deployments are compatible with simultaneous pitch thrust vectoring (see fig. 4(c)). Above NPR = 2, there is no effect of pitch thrust vectoring on resultant yaw vector angle (compare circles and squares in fig. 23(b) at NPR = 4.0 and NPR = 6.0). However, as shown in figure 23(a), there is a detrimental effect of yaw thrust vectoring on resultant pitch vector angle. Increasing δ_y (by increasing $\delta_{v,y}$) decreases δ_p. As nozzle internal flow is deflected laterally during yaw thrust vectoring, less internal flow is available for pitch thrust vectoring, and δ_p decreases from levels generated without yaw vectoring ($\delta_{v,y} = 0°$).

Even though yaw vectoring has an adverse effect on pitch vectoring, δ_p values are still much larger than δ_y values. The difference in magnitude is due to the difference in the size of the pitch and yaw thrust vectoring flaps. The downstream yaw vectoring sidewall flaps are much smaller than the pitch vectoring flaps (nozzle upper and lower divergent flaps). Nozzle throat aspect ratio (ratio of throat width to throat height) gives a good indication of relative flap sizes. The downstream yaw vector flaps were sized for baseline configuration S1 (fig. 2(a)) which has a throat aspect ratio of 3.67. Thus, the nozzle upper and lower flaps (used for pitch thrust vectoring) are more than three times as wide as the downstream yaw vector flaps at the throat. Redesigning the nozzle to a lower throat aspect ratio would decrease the pitch vectoring flap size and increase the yaw vectoring flap size. Thus, if desired, a better balance between pitch and yaw vectoring capabilities ($\delta_y \approx \delta_p$)

could be achieved during simultaneous pitch and yaw thrust vectoring operation.

Upstream port/flap yaw vectoring concept. The results of the upstream port/flap yaw vectoring concepts (figs. 6 and 7) are presented in figures 24 to 26. The data of figures 24 and 25 include the additional port/flap turning efficiency parameter $\delta_y/\delta_{y,i}$. (See section "Data Reduction.") This parameter is a measure of the relative yaw flow-turning capability of various upstream port/flap yaw vector configurations with different port areas and geometric yaw vector angles. In general, the magnitude of resultant yaw vector angles generated by the upstream yaw vectoring concepts is small, less than 5°, regardless of port/flap type, nozzle geometry, or nozzle pressure ratio. The small resultant yaw vector angles are due to the sizing of the upstream port. The maximum (flap removed) port throat area A_p of each port (circular or rectangular) was sized to be no larger than 10 percent of the throat area of the dry power baseline nozzles. This limit on port size was chosen for compatibility with current engine control systems. To obtain larger resultant yaw vector angles δ_y for the current upstream port/flap yaw vector concepts, the maximum size of the upstream port would have to be increased. This would, of course, increase the percentage change in total nozzle throat area to above the 10-percent level of the current port/flap concepts and would probably require modifications of the engine control system.

The variation of $\delta_y/\delta_{y,i}$ with upstream port/flap concept gives an indication of how efficient each concept is in turning the exhaust flow in the lateral direction. Although the circular port concept generally produced the largest values of δ_y (see fig. 24(a), for example), it also had low values of $\delta_y/\delta_{y,i}$ and thus was one of the least efficient upstream yaw vectoring concepts. Turning efficiency of the circular port concept could probably be improved by rounding the inside lip of the port and/or by reducing geometric yaw vector angle (canting the sidewall port passage aft). Although the port passage centerline was perpendicular to the internal flow ($\delta_{v,y} = 90°$), it is hypothesized that the flow exits through the port at an angle substantially less than 90°; thus, resultant vector angles of 40 to 70 percent of the ideal yaw vector angle are produced. The 40° aft-hinge flap always had the highest values of $\delta_y/\delta_{y,i}$, regardless of nozzle configuration. The aft-hinge flap hinges into the nozzle (see fig. 6) to "scoop" or capture part of the internal flow upstream of the nozzle throat. This hinge location was the most efficient of the three hinge locations tested and produced values of δ_y only slightly lower than the circular port concept. The 40° mid-hinge flap, which operates similar to a butterfly valve, positions the upstream flap both into and out of the nozzle internal flow. (See fig. 6.) This hinge location generally produced values of $\delta_y/\delta_{y,i}$ between the circular port and 40° aft-hinge flap concepts. At low nozzle pressure ratios (less than NPR = 3.0), the forward-hinge flap produces values of δ_y and δ_y/δ_i which are comparable to results of the other port/flap configurations. However, as NPR increases, both δ_y and $\delta_y/\delta_{y,i}$ rapidly decrease. At NPR greater than 4.0, the forward hinge location produced the lowest values of resultant yaw vector angle and turning efficiency of all upstream port/flap concepts tested. The decrease in δ_y and $\delta_y/\delta_{y,i}$ with NPR is probably caused by flow separation on the internal surface of the upstream forward-hinge flap.

Each upstream yaw vectoring concept had an adverse effect on both F/F_i and F_r/F_i. The upstream port/flap concepts decreased thrust ratios as much as 6 percent. (See figs. 24(a) and 24(b).) Since both F/F_i and F_r/F_i show the same losses, these decreases in thrust ratio reflect gross thrust losses and not simply F/F_i losses due to turning the gross thrust vector away from the body axis. The upstream port/flap concepts deflect part of the nozzle internal flow before it reaches the throat. The deflected portion of model weight flow w_p is not accelerated through the nozzle throat and thus is not available for producing axial thrust. Since ideal thrust is based on total throat area (total weight flow), both thrust ratios generally decrease with increasing geometric port throat area A_p. (See fig. 6.) However, the percentage changes in F/F_i and F_r/F_i are not as large as the percentage changes in total nozzle A_t due to the port/flap geometries. For example, the circular port concept changes A_t by about 10 percent but decreases the thrust ratios by about 6 percent when applied to the dry power nozzle, baseline $A_e/A_t = 1.08$. (See fig. 24(a).) The internal flow deflected by the upstream concepts to produce a side-force thrust component also produces an axial-force thrust component (if flow does not exit the port perpendicular to body axis) so that the nozzle recovers some thrust from the flow accelerating through the yaw vectoring port throat. Examination of the basic data figures contained in the appendix indicates that the nozzle discharge coefficient w_p/w_i was decreased up to 2.5 percent by addition of the upstream port/flap yaw vector concepts. (For example, compare fig. 51 with fig. 42(a).) This decrease is probably caused by upstream port discharge coefficients which are significantly lower than the baseline nozzle discharge coefficient.

The effects of expansion ratio and power setting on the performance of three upstream port/flap

concepts are summarized in figure 25. Results are presented for the circular port, the 40° forward-hinge flap, and the 40° aft-hinge flap. Increasing power setting (A_t) generally has a detrimental effect on δ_y (recall that both baseline dry power nozzles have the same A_t). As A_t increases, so does the weight flow w_p and thrust F for a given nozzle pressure ratio. Since the geometric port area A_p of the upstream port/flap concepts does not vary with nozzle primary throat area, the amount of nozzle weight flow deflected during yaw thrust vectoring and thus the side force component of deflected thrust F_S should not appreciably vary with power setting changes. Thus, a smaller percentage of the total nozzle weight flow is deflected during yaw thrust vectoring and δ_y decreases with increasing A_t. For reasons not currently understood, increasing nozzle expansion ratio (by increasing nozzle exit area A_e) had a favorable effect on resultant yaw vector angle for all upstream port/flap yaw vector concepts tested.

Thrust ratios F/F_i and F_r/F_i shown in figure 25 exhibit trends with varying NPR and A_e/A_t typical of 2-D C-D nozzles. (See refs. 9 and 10 and baseline nozzle data (figs. 42(a), 43(a), and 44(a)) of the current test). Of course, the absolute levels reflect the thrust losses noted previously for the upstream port/flap yaw vector concepts.

One advantage of the upstream port/flap yaw vector concepts is that they are all compatible with simultaneous pitch vector operation. The upstream port/flap concepts were tested on pitch-vectored 2-D C-D nozzles with $\delta_{v,p} = 9.79°$ and $\delta_{v,p} = 20.28°$. The effects of geometric pitch vector angle on resultant yaw vector angle and of geometric yaw vector angle on resultant pitch vector angle are summarized in figure 26. As discussed previously, the values of δ_y are low (generally less than 2°) because both pitch-vectored nozzles are A/B power configurations. For the upstream port/flap yaw vector concepts, geometric yaw vector angle had little or no effect on resultant pitch vector angle (compare flagged symbols with dashed lines). Similarly, geometric pitch vector angle had little or no effect on resultant yaw vector angle (compare different plain symbols).

Powered rudder yaw vectoring concept. Results of the powered rudder yaw vectoring concepts are presented in figures 27 through 30. The effects of this yaw vector concept on nozzle performance are presented in figure 27 for several different nozzles. Each nozzle was tested with two rudders, one with $c = 0.75$ in. and the other with $c = 1.50$ in. Each rudder was tested at two geometric yaw vector angles, $\delta_{v,y} = 0°$ and $\delta_{v,y} = 20°$. For a geometric yaw vector angle of 20°, the values of δ_y only approached about 40 percent of the geometric yaw vector angle, regardless of nozzle geometry. The magnitude of δ_y depended on the rudder chord length c. For $c = 0.75$ in., the maximum δ_y reached approximately 4.5°; for $c = 1.50$ in., the maximum δ_y was about 8.5°. The effect of rudder chord on resultant yaw vector angle (for $\delta_{v,p} = 0°$ configurations) is more clearly shown by the cross plot of figure 29. As indicated in figure 29, increasing rudder chord produces a linear increase in resultant yaw vector angles. Thus, increasing c above 1.50 in. would increase δ_y. Also shown in figure 29 is the effect of nozzle expansion ratio on resultant yaw vector angle. This effect is not as well-defined as the effect of c on δ_y. At low nozzle pressure ratios (NPR = 2.0 and 4.0), the nozzle with the higher expansion ratio produces the larger values of δ_y. For the low-expansion-ratio nozzle, δ_y increases as NPR increases; this indicates that δ_y increases with the size of the exhaust plume (larger portion of rudder affected by exhaust). However, for the high-expansion-ratio nozzle, δ_y decreases (up to NPR = 6.0) as NPR increases. The reason for this behavior of the high-expansion-ratio nozzle is not understood.

Both F/F_i and F_r/F_i (fig. 27) show substantial losses with the powered rudder concepts. There is an initial installation loss in both thrust ratios which results from installing the rudder at $\delta_{v,y} = 0°$. Chord length does not affect this rudder installation penalty. The powered rudder is the only yaw vectoring concept which incurred a performance penalty even when yaw vectoring was not deployed ($\delta_{v,y} = 0°$). An additional thrust loss, which increases with increasing rudder chord, occurs when the rudder is deflected to $\delta_{v,y} = 20°$.

The thrust losses which result from the powered rudder concept are presented in more detail in figure 28. This figure breaks down the total F_r/F_i loss into individual losses due to rudder geometry and to yaw vectoring. The results are summarized for the dry power nozzle, baseline $A_e/A_t = 1.08$, with the 1.50-in. chord rudder. The powered rudder installation penalty mentioned previously is the initial thrust loss shown in figure 28 (compare the circles and the squares). This thrust loss (3 to 4 percent of resultant thrust ratio) is caused by pressure and friction drag on the rudder at $\delta_{v,y} = 0°$. An estimate of rudder pressure drag was computed by assuming a differential pressure (equal to jet total pressure minus atmospheric pressure) acting on the rudder frontal cross-sectional area which was exposed to the nozzle exhaust flow. The estimated pressure drag was then added to F_r/F_i for configuration R3 (indicated by the squares). The resulting sum is shown in figure 28 as a dashed line. The agreement between the

dashed line and the rudder-off baseline F_r/F_i data (circles) indicates that most of the powered rudder installation penalty is pressure drag rather than friction drag. This is why the rudder installation penalty does not vary with rudder chord. (See fig. 27.) The rudder utilized for the current test was designed as a flat plate with thickness of 0.20 in.; it had a blunt leading edge and a flat trailing edge (fig. 8). The pressure drag loss could be reduced by redesigning the rudder with aerodynamic contours and a thinner profile.

A second resultant thrust loss of 2 to 3 percent (compare the squares and the open diamonds in fig. 28) results from turning losses associated with deflecting the rudder ($\delta_{v,y} = 20°$). The exhaust flow probably separates from the expansion (leeward) side of the rudder, and shock losses may occur on the compression (windward) side of the rudder. This thrust loss increases with rudder chord length. (See fig. 27.) The third loss (compare the open diamonds and the solid diamonds) is caused by turning the thrust vector away from the body axis an amount equal to δ_y. Note that this loss is the difference between F_r/F_i and F/F_i. This loss increases with δ_y and also occurs for all other yaw vectoring concepts.

The effect of simultaneous pitch and yaw vectoring on resultant thrust vector angles is presented in figure 30. Results are presented for both pitch-vectored nozzle configurations tested. The effect of pitch thrust vectoring on δ_y is shown for $\delta_{v,y} = 20°$ (left side of figure). The effect of yaw thrust vectoring on δ_p is shown for the 1.50-in. chord rudder only (right side of figure).

Increasing geometric pitch vector angle from 9.79° to 20.28° decreases the value of δ_y. Both rudder chord lengths show the same adverse effect of $\delta_{v,p}$ on δ_y, but the effect is more pronounced for the longer chord ($c = 1.50$). This negative effect of pitch thrust vectoring on resultant yaw vector angle is probably due to the geometry of the $\delta_{v,p} = 20.28°$ pitch vectored configuration. (See fig. 8(b).) The flow at the nozzle exit of this configuration is already vectored in pitch before it reaches the rudder, and part of the pitch vectored flow apparently bypasses the bottom of the rudder. It is believed that a similar decrease in δ_y may not exist when the geometric pitch vector angle is increased from 0° to 9.79°. Unfortunately, the $\delta_{v,p} = 0°$ A/B nozzle (conf. S9) was not tested with the powered rudder concept and this hypothesis cannot be confirmed. In contrast to the negative effect of pitch thrust vectoring on δ_y, geometric yaw vector angle has a positive effect on δ_p. This favorable effect suggests that the presence of the yaw-deflected rudder ($\delta_{v,y} = 20°$) in the exhaust jet reduces any losses in δ_p due to flow separation from the lower pitch vectoring flap. Installing the undeflected rudder ($\delta_{v,y} = 0°$) had little or no effect on δ_p (compare dashed lines with circles).

Combination yaw vectoring concepts. The powered rudder yaw vectoring concept is installed on the 2-D C-D nozzle downstream of the nozzle exit and thus would not physically interfere with the operation of any of the other yaw vectoring concepts tested. To investigate the effects on performance of combined yaw vector concepts, the powered rudder concept was tested on selected downstream flap and upstream port/flap yaw vector configurations. The combination yaw vectoring geometries were tested on the dry power forward-thrust nozzle with baseline $A_e/A_t = 1.08$ and on the A/B power nozzle with $\delta_{v,p} = 20.28°$. Effects of yaw thrust vectoring on the performance of the combination yaw vectoring configurations are presented in figures 31 through 34. In general, the results are as expected from discussion of the individual yaw vector concepts. For example, all the combination yaw vector configurations suffer the large thrust penalty discussed earlier for installation of the powered rudder at $\delta_{v,y} = 0°$ and, in general, δ_y tends to increase with increasing $\delta_{v,y}$.

Comparison plots of the effects of individual and combined rudder/downstream flap yaw vector concepts on F_r/F_i and δ_y are presented in figure 35 for the dry power (baseline $A_e/A_t = 1.08$) nozzle. Similar results for the combined rudder/upstream circular port concepts on the dry power (baseline $A_e/A_t = 1.08$) nozzle are presented in figure 36. Although results summarized in these figures are for the dry power nozzle, the A/B power pitch thrust vectored nozzle has similar trends in F_r/F_i and δ_y. The algebraic sums of δ_y resulting from the individual concepts are presented as dashed lines in the plots of δ_y as a function of NPR.

Values of resultant thrust ratio for the combined powered rudder and downstream flap concepts fall between the resultant thrust ratio results of the individual concepts. (See fig. 35.) Similar to the powered rudder results discussed previously for pitch thrust vectored configurations, the deflected rudder apparently reduces internal flow separation, in this case on the left (expansion turn) downstream sidewall flap. Although nozzle expansion ratio A_e/A_t varies when a single sidewall flap (left side of fig. 35) is deflected and causes some of the variation in F_r/F_i, the favorable effect of the combined power rudder/downstream flap concept on resultant thrust ratio is obvious for both the single and two sidewall downstream flaps. The combined rudder/downstream flap concepts produced larger resultant yaw vector angles than either individual concept (powered rudder or downstream

flaps) produced alone. However, by comparing the dashed line with the triangles, it can be seen that δ_y values for individual yaw vector angles are not additive. In fact, for the left and right downstream flaps concept (right side of fig. 35(b)), addition of the powered rudder at $\delta_{v,y} = 20°$ increased δ_y by only 10 to 20 percent. It is obvious that the left and right downstream flaps have already turned most of the exhaust flow and installation of the powered rudder provides little additional turning. This result also helps explain why the F_r/F_i loss for the combined concept configuration is less than the loss for the powered rudder alone. Since the exhaust flow at the nozzle exit and the powered rudder are nearly at the same angle for this configuration, any thrust loss due to separation on the rudder leeward side would be eliminated. Addition of the powered rudder to the single-flap configuration (left side of fig. 35(b)) provides a larger percentage increase in δ_y since, as discussed previously, the turning effectiveness of the single flap probably decreases as the undeflected opposite sidewall is approached and thus the rudder becomes more effective. However, the individual resultant yaw vector angles are still not additive even for this case.

Combining the powered rudder concept with the upstream circular port concept resulted in large resultant thrust ratio losses of up to 12 percent. (See fig. 36.) The thrust losses of each individual concept were essentially additive (within 1 percent) for this combined configuration. As indicated by comparing the dashed line with the triangles, the sum of the individual resultant yaw vector angles of the powered rudder and the upstream circular port is approximately equal to δ_y for the combined concept. The upstream circular port concept provides flow turning by bleeding away a portion of the internal flow upstream of the primary nozzle throat. The remainder of the internal flow, which accelerates through the primary nozzle throat, remains unturned ($\delta_y \approx 0°$). Thus, addition of the rudder at $\delta_{v,y} = 20°$ operates as designed and provides additional flow turning at the nozzle exit. The F_r/F_i and δ_y results discussed previously indicate that the powered rudder concept and upstream port/flap concept operate independently of each other even when combined into a single configuration.

The effect of simultaneous pitch and yaw thrust vectoring on δ_p and δ_y is shown in figure 37. The value of the resultant pitch vector angle δ_p for the combination yaw vector concept depends on the effects of the individual concepts on δ_p. For the rudder/downstream flap configuration (fig. 37(a)), values of δ_p fall below the results of the baseline nozzle ($\delta_{v,y} = 0°$, $\delta_{v,p} = 20.28°$). This combined yaw vector concept has values of δ_p which are close to the values of δ_p for only the left downstream flap deflected. This result probably occurs because both configurations lose the same amount of pitch vectoring capability when internal flow is turned laterally out the sidewall and bypasses the upper and lower pitch vector flaps. The rudder contributes a slight improvement in δ_p, probably by eliminating separation on the sidewall flap. The rudder/upstream port configuration produces larger δ_p than the baseline nozzle (fig. 37(b)). For this combined yaw vector concept, the values of δ_p are the same as the values of δ_p for the powered-rudder-alone configuration. This relationship was expected since the upstream port/flap concepts had very small effects on δ_p during simultaneous pitch thrust vectoring. As indicated on the right side of figure 37, the combined yaw vector concepts produced resultant yaw vector angles during simultaneous pitch thrust vectoring ($\delta_{v,p} = 20.28°$), which were nearly equal to the sum of δ_y for the individual yaw vector concepts. Thus, simultaneous pitch and yaw vectoring is feasible for combined yaw vector concepts but pitch thrust vectoring effectiveness depends on which individual concepts are utilized.

Single Expansion Ramp Nozzles With Post-Exit Flaps Yaw Vectoring Concept

The results for four SERN configurations (two forward thrust and two pitch vectored) with a post-exit flaps yaw vectoring concept installed are shown in figures 38 through 40. The results for the two forward-thrust SERN configurations are discussed first. (See figs. 38(a), 38(b), and 39.) The post-exit flaps were not very effective and the maximum value of δ_y for the post-exit flaps concept was only about 5° for the SERN with 1.50-in-chord flap at $\delta_{v,y} = 20°$. As discussed in the section "Nozzle Design and Yaw Vectoring Concepts," flap deflection $\delta_{v,y}$ of 20° results in only a 14° axial or streamwise flap angle. Yaw thrust vectoring by deflection of the post-exit flaps decreased F/F_i and F_r/F_i, but only by about 1 percent for the 0.75-in. chord and by 1.5 to 2 percent for the 1.50-in. chord. The thrust loss when the flaps are deflected is probably caused by exhaust flow separation from the left-hand (expansion turn) flap. There was no measurable SERN thrust loss when the exit flaps were not deployed ($\delta_{v,y} = 0°$).

The rather low values of δ_y shown in figure 38 may be near the maximum which can be obtained by the post-exit flaps concept without increasing $\delta_{v,y}$. The value of δ_y for $c = 1.50$ in. is larger than values of δ_y for $c = 0.75$ in., but as shown in figure 39, this increase is nonlinear. Resultant yaw vector angle appears to be leveling off as c increases from 0.75 to 1.50 in. (unlike the linear effect of c on δ_y of the

2-D C-D nozzle powered rudder concept). Increasing flap chord length above 1.50 in. may provide only small additional increases in resultant yaw vector angle. The magnitude of δ_y is perhaps limited by the high velocity of the SERN flow at the nozzle exit. The previously discussed 2-D C-D yaw vector concepts which produced good yaw vectoring (such as the downstream flap concepts) were implemented upstream of the nozzle exit and acted on flow with lower velocity than the flow at the nozzle exit. The supersonic flow at the SERN exit may be more difficult to turn efficiently than the internal flow of the 2-D C-D nozzles; thus, low δ_y results for the post-exit flaps concept.

The effects of the post-exit flaps on the basic performance of two pitch-vectoring SERN concepts are similar to the results discussed previously for the forward-thrust nozzles (small thrust losses, low δ_y). The data in figure 40 indicate that there are favorable interactions between the yaw vectoring post-exit flaps and the SERN pitch vectoring flaps. Increasing δ_p generally increased δ_y; the configuration with $\delta_{v,p} = 20°$, which utilizes the upper flap only for pitch thrust vectoring (fig. 12(b)), nearly doubled resultant yaw vector angle at some NPR. This favorable interaction is probably caused by an increase in pressure on the upper pitch-vectored SERN flap which would tend to cause a lateral spreading of the exhaust flow and thus improve yaw vector capability. For the upper-flap-only pitch thrust vectored SERN (left side of fig. 40(b)), simply installing the unvectored ($\delta_{v,y} = 0°$) post-exit flaps increased δ_p; deflecting the post-exit flaps did not reduce this favorable effect. The post-exit flaps act as sidewall extensions and prevent early lateral spreading of the exhaust flow during pitch thrust vector operation. For the SERN with both upper and lower flaps vectored (right side of fig. 40(b)), installing the undeflected yaw vectoring flaps had little effect on δ_p but deflecting the flaps to $\delta_{v,y} = 20°$ increased δ_p. Thus, simultaneous pitch and yaw thrust vectoring is not only feasible but mutually favorable for the SERN with a post-exit flaps yaw vector concept installed.

Summary of Results

A static investigation of several yaw vectoring concepts installed on two types of nonaxisymmetric nozzles has been conducted in the static test facility of the Langley 16-Foot Transonic Tunnel. Four different yaw thrust vectoring concepts were investigated on two-dimensional convergent-divergent nozzles at throat areas simulating dry and afterburning power settings. Pitch thrust vectored configurations were also tested with each yaw vectoring concept. The four yaw vectoring concepts were translating sidewall, downstream (of throat) yaw vectoring flaps, upstream (of throat) yaw vectoring port/flap, and powered rudder. Selected combinations of the powered rudder concept with downstream or upstream concepts were also tested. A single yaw vectoring concept, post-exit flaps, was investigated on four single expansion ramp nozzles which included two forward-thrust geometries and two pitch-vectored geometries. All configurations were tested at static conditions (no external flow). The nozzle pressure ratio was varied up to approximately 10 depending on configuration.

Results from this investigation indicate that yaw thrust vectoring, either used alone or simultaneously with pitch thrust vectoring, is feasible for both two-dimensional convergent-divergent nozzles and single expansion ramp nozzles. The largest resultant yaw vector angles were produced by flaps downstream of the throat in each sidewall (downstream yaw vector flap concept). At a low nozzle expansion ratio, resultant yaw vector angle approached the geometric yaw vector (flap) angle. This yaw vector concept is similar to current methods for obtaining a pitch thrust vectoring capability except the thrust deflection plane has been rotated 90°. The remaining results are subdivided under nozzle type and yaw thrust vectoring concept.

Two-Dimensional Convergent-Divergent Nozzles

Translating sidewall concept.

1. Resultant yaw vector angle increases with increasing sidewall translation (decreasing sidewall length).

2. Resultant yaw vector angle is significantly increased by decreasing nozzle expansion ratio. Positive turning angles were generated at underexpanded nozzle operating conditions but negative turning angles were found at overexpanded nozzle operating conditions. Integrated flight and propulsion controls could eliminate this problem by reducing nozzle expansion ratio when yaw thrust vectoring is required.

3. Thrust losses for this concept are small, particularly if sidewall translation does not go forward of the nozzle throat.

4. Although effective simultaneous pitch and yaw thrust vectoring is possible with this concept, yaw thrust vectoring (sidewall translation) has an unfavorable effect on resultant pitch vector angle.

Downstream flap concept.

1. Deflection of flaps in both nozzle sidewalls produced the largest resultant yaw vector angles of any individual yaw vectoring concept tested during this

investigation. However, simultaneous pitch thrust vectoring is not feasible when both sidewall flaps are deflected.

2. Although deflection of a single sidewall flap was not as effective as deflection of both sidewall flaps, resultant yaw vector angles up to 11° were obtained for a single sidewall deflection of 20°. Deflection of a single sidewall flap outward (expansion turn), which is compatible with simultaneous pitch thrust vectoring, generally produced larger resultant yaw vector angles than deflection of a single sidewall flap inward (compression turn).

3. When both sidewall flaps or an expansion turn single flap are utilized for yaw thrust vectoring, a flap mid-hinge location generally produced larger resultant yaw vector angles than a forward hinge located at the nozzle throat. However, resultant thrust ratio losses were substantially larger for the mid hinge location when compared with those for the forward hinge location.

4. At nozzle pressure ratios greater than 2.0, resultant yaw vector angle increased almost linearly with increasing geometric flap angle for the range of flap angles tested (up to 20°).

5. Resultant yaw vector angles of the downstream flap concepts (either one flap or two flaps) were increased significantly by decreasing nozzle expansion ratio and/or power setting. Part of the reason for this trend is that the size of the sidewall flap relative to total sidewall area increases with decreasing nozzle expansion ratio and/or power setting (throat area). Thus, similar to the translating sidewall concept, resultant yaw vector angle could be maximized by an integrated flight and propulsion control system.

6. By utilizing a single sidewall flap deployed outward (expansion turn), the downstream flap yaw vector concept is compatible with simultaneous pitch thrust vectoring. Yaw thrust vectoring with this concept had an adverse effect on resultant pitch vector angle, but even so, the resultant pitch vector angles were generally much larger than the resultant yaw vector angles.

Upstream port/flap concept.

1. Resultant yaw vector angles obtained with this concept were small, primarily because port area was restricted to 10 percent of the baseline nozzle throat area.

2. The largest resultant yaw vector angles (approximately 4°) were obtained with the upstream circular port because of its larger port area and geometric vector angle of 90°. However, the most efficient flow-turning concept was a rectangular port with an aft-hinge flap which deployed internal to the nozzle and scooped exhaust flow through the port.

3. Flow-turning efficiency tended to increase as the flap hinge location moved aft or as more exhaust flow was "scooped" from the nozzle. Results on the forward-hinge flap, which deployed external to the nozzle and did not scoop any exhaust flow, indicated exhaust flow separation on the flap at most nozzle pressure ratios tested.

4. Resultant thrust ratio losses for the upstream port/flap concept increased with port area and were quite large (up to 6 percent).

5. The upstream port/flap concepts are all compatible with simultaneous pitch thrust vectoring operation. Little interaction occurred between the pitch and yaw flow turning mechanisms. However, port area would have to exceed 10 percent of the nozzle throat area in order to obtain reasonable magnitudes of resultant yaw vector angle.

Powered rudder concept.

1. For the test range of rudder chord lengths, resultant yaw vector angle produced by the powered rudder concept increased linearly with increasing rudder chord length.

2. The powered rudder concept was the only yaw vector concept which produced a thrust loss due to installation of the yaw vector concept itself (geometric yaw vector angle equal zero). This thrust loss resulted primarily from pressure drag on the rudder and caused a 3 to 4 percent decrease in resultant thrust ratio. An additional resultant thrust ratio loss of 2 to 3 percent resulted from turning losses when the rudder was deflected.

3. The powered rudder concept is compatible with simultaneous pitch thrust vectoring. Pitch thrust vectoring had a small adverse effect on resultant yaw vector angle, and yaw thrust vectoring had a small favorable effect on resultant pitch vector angle.

Combined yaw vector concepts.

Combined yaw vector concepts produced larger resultant yaw vector angles than those produced by the individual concepts but the magnitude depends on which yaw vector concepts are combined.

Single Expansion Ramp Nozzles With Post-Exit Flaps Concept

1. The post-exit flaps installed on forward thrust nozzles (geometric pitch vector angle equals zero) were not very effective, and the resultant yaw vector angles were low for all flap chord lengths tested. Consequently, the resultant thrust ratio loss was also small (1 to 2 percent).

2. Although increasing flap chord length increased resultant yaw vector angle, the increase

was not linear, and further increases in chord length would probably produce only small increases in resultant yaw vector angle.

3. During simultaneous pitch and yaw thrust vectoring operation, pitch and yaw thrust vectoring had mutually favorable effects on each other. For some nozzle pressure ratios, the resultant yaw vector angle was nearly doubled when geometric pitch vector angle was increased from 0° to 20°.

NASA Langley Research Center
Hampton, VA 23665
February 5, 1985

References

1. Capone, Francis J.: Summary of Propulsive-Lift Research in the Langley 16-Ft. Transonic Tunnel. *J. Aircr.*, vol. 13, no. 10, Oct. 1976, pp. 803–808.
2. Hiley, P. E.; Wallace, H. W.; and Booz, D. E.: Nonaxisymmetric Nozzles Installed in Advanced Fighter Aircraft. *J. Aircr.*, vol. 13, no. 12, Dec. 1976, pp. 1000–1006.
3. Berrier, Bobby L.; Palcza, J. Lawrence; and Richey, G. Keith: Nonaxisymmetric Nozzle Technology Program—An Overview. AIAA Paper 77-1225, Aug. 1977.
4. Capone, Francis J.: The Nonaxisymmetric Nozzle—It Is For Real. AIAA Paper 79-1810, Aug. 1979.
5. Capone, Francis J.; and Maiden, Donald L.: *Performance of Twin Two-Dimensional Wedge Nozzles Including Thrust Vectoring and Reversing Effects at Speeds up to Mach 2.20.* NASA TN D-8449, 1977.
6. Capone, Francis J.; and Berrier, Bobby L.: *Investigation of Axisymmetric and Nonaxisymmetric Nozzles Installed on a 0.10-Scale F-18 Prototype Airplane Model.* NASA TP-1638, 1980.
7. Capone, Francis J.; and Reubush, David E.: *Effects of Varying Podded Nacelle-Nozzle Installations on Transonic Aeropropulsive Characteristics of a Supersonic Fighter Aircraft.* NASA TP-2120, 1983.
8. *F-15 2-D Nozzle System Integration Study. Volume I—Technical Report.* NASA CR-145295, 1978.
9. Berrier, Bobby L.; and Re, Richard J.: *Effect of Several Geometric Parameters on the Static Internal Performance of Three Nonaxisymmetric Nozzle Concepts.* NASA TP-1468, 1979.
10. Re, Richard J.; and Leavitt, Laurence D.: *Static Internal Performance Including Thrust Vectoring and Reversing of Two-Dimensional Convergent-Divergent Nozzles.* NASA TP-2253, 1984.
11. Re, Richard J.; and Berrier, Bobby L.: *Static Internal Performance of Single Expansion-Ramp Nozzles With Thrust Vectoring and Reversing.* NASA TP-1962, 1982.
12. Capone, Francis J.; Re, Richard J.; and Bare, E. Ann: Thrust Reversing Effects on Twin-Engine Aircraft Having Nonaxisymmetric Nozzles. AIAA Paper 81-2639, Dec. 1981.
13. Lacey, David W.: Air Combat Advantages From Reaction Control Systems. SAE Tech. Paper Ser. 801177, Oct. 1980.
14. Berrier, Bobby L.; and Mason, Mary L.: A Static Investigation of Yaw Vectoring Concepts on Two-Dimensional Convergent-Divergent Nozzles. AIAA Paper 83-1288, June 1983.
15. Capone, Francis J.: *Static Performance of Five Twin-Engine Nonaxisymmetric Nozzles With Vectoring and Reversing Capability.* NASA TP-1224, 1978.
16. Stevens, H. L.; Thayer, E. B.; and Fullerton, J. F.: Development of the Multi-Function 2-D/C-D Nozzle. AIAA Paper 81-1491, July 1981.
17. Shapiro, Ascher H.: *The Dynamics and Thermodynamics of Compressible Fluid Flow,* Volume 1. Ronald Press Co., c.1953.

Appendix

Basic Data

The basic nozzle internal performance data obtained during this investigation are presented in figures 41 to 67. Figure 41 is included to show the good repeatability of nozzle internal performance data (for conf. S1). Data on this configuration were obtained at periodic intervals throughout the investigation. The basic data in these figures consist of F/F_i, w_p/w_i, δ_p, and δ_y presented as functions of nozzle pressure ratio NPR. An index to the basic data figures for the 2-D C-D nozzle configurations is given in table I, and a similar index for the SERN configurations is given in table II.

TABLE I. INDEX TO BASIC DATA FIGURES FOR 2-D C-D NOZZLES WITH YAW VECTORING CONCEPTS

Yaw vectoring concepts	Dry power		A/B power		
	$\delta_{v,p} = 0°$ baseline $A_e/A_t = 1.08$	$\delta_{v,p} = 0°$ baseline $A_e/A_t = 1.78$	$\delta_{v,p} = 0°$ baseline $A_e/A_t = 1.29$	$\delta_{v,p} = 9.79°$ baseline $A_e/A_t = 1.35$	$\delta_{v,p} = 20.28°$ baseline $A_e/A_t = 1.51$
Translating sidewall:					
$(x_s - x_t)/l_s =$					
1.00	42(a)	43(a)	44(a)	45	46(a)
0.63 or 0.61	42(b)	43(b)	44(b)		46(b)
0.25 or 0.23	42(c)		44(c)		
0 or −0.03	42(d)	43(c)	44(d)		46(c)
−0.25 or −0.30	42(e)		44(e)		
Downstream flaps:					
Forward hinge					
Left $\delta_{v,y} = 10°$, right $\delta_{v,y} = 0°$	47(a)		49(a)		50(a)
Left $\delta_{v,y} = 0°$, right $\delta_{v,y} = 10°$	47(b)		49(b)		
Left $\delta_{v,y} = 10°$, right $\delta_{v,y} = 10°$	47(c)		49(c)		
Left $\delta_{v,y} = 20°$, right $\delta_{v,y} = 0°$	47(d)	48(a)	49(d)		50(b)
Left $\delta_{v,y} = 0°$, right $\delta_{v,y} = 20°$	47(e)		49(e)		
Left $\delta_{v,y} = 20°$, right $\delta_{v,y} = 20°$	47(f)	48(b)	49(f)		
Mid hinge					
Left $\delta_{v,y} = 20°$, right $\delta_{v,y} = 0°$	49(g)		49(g)		
Left $\delta_{v,y} = 0°$, right $\delta_{v,y} = 20°$	47(h)		49(h)		
Left $\delta_{v,y} = 20°$, right $\delta_{v,y} = 20°$	47(i)	48(c)	49(i)		
Upstream port/flap:					
Circular port, $\delta_{v,y} = 90°$	51(a)	52(a)	53(a)	54(a)	55(a)
Forward-hinge flap, $\delta_{v,y} = 40°$	51(b)	52(b)	53(b)		55(b)
Mid-hinge flap, $\delta_{v,y} = 20°$	51(c)		53(c)		
Mid-hinge flap, $\delta_{v,y} = 40°$	51(d)		53(d)		55(c)
Aft-hinge flap, $\delta_{v,y} = 40°$	51(e)	52(c)	53(e)	54(b)	55(d)
Powered rudder:					
$c = 0.75$ in., $\delta_{v,y} = 0°$	56(a)	57(a)		58(a)	59(a)
$c = 0.75$ in., $\delta_{v,y} = 20°$	56(b)	57(b)		58(b)	59(b)
$c = 1.50$ in., $\delta_{v,y} = 0°$	56(c)	57(c)		58(c)	59(c)
$c = 1.50$ in., $\delta_{v,y} = 20°$	56(d)	57(d)		58(d)	59(d)
Rudder and downstream flaps:					
$c = 1.50$ in., rudder $\delta_{v,y} = 20°$, forward hinge					
Left $\delta_{v,y} = 10°$, right $\delta_{v,y} = 0°$	60(a)				61(a)
Left $\delta_{v,y} = 20°$, right $\delta_{v,y} = 0°$	60(b)				61(b)
Left $\delta_{v,y} = 10°$, right $\delta_{v,y} = 10°$	60(c)				
Left $\delta_{v,y} = 20°$, right $\delta_{v,y} = 20°$	60(d)				
$c = 1.50$ in., rudder $\delta_{v,y} = 20°$, mid hinge					
Left $\delta_{v,y} = 20°$, right $\delta_{v,y} = 20°$	60(e)				
Rudder and upstream port/flap:					
$c = 1.50$ in., rudder $\delta_{v,y} = 20°$, circular port	62(a)				63(a)
$c = 1.50$ in., rudder $\delta_{v,y} = 20°$, 40°, forward hinge	62(b)				63(b)

TABLE II. INDEX TO BASIC DATA FIGURES FOR SERN WITH POST-EXIT FLAPS YAW VECTORING CONCEPT

Post-exit flaps configuration	$\delta_{v,p} = 0°$ $(A_e/A_t)_i = 1.10$ $(A_e/A_t)_e = 1.41$	$\delta_{v,p} = 0°$ $(A_e/A_t)_i = 1.24$ $(A_e/A_t)_e = 1.50$	$\delta_{v,p} = 20°$ upper flap vectored	$\delta_{v,p} = 20°$ both flaps vectored
No exit flaps	64(a)	65(a)	66(a)	67(a)
$c = 0.75$ in., $\delta_{v,y} = 0°$	64(b)	65(b)	66(b)	67(b)
$c = 0.75$ in., $\delta_{v,y} = 20°$	64(c)	65(c)	66(c)	67(c)
$c = 1.50$ in., $\delta_{v,y} = 0°$	64(d)	65(d)	66(d)	
$c = 1.50$ in., $\delta_{v,y} = 20°$	64(e)	65(e)	66(e)	

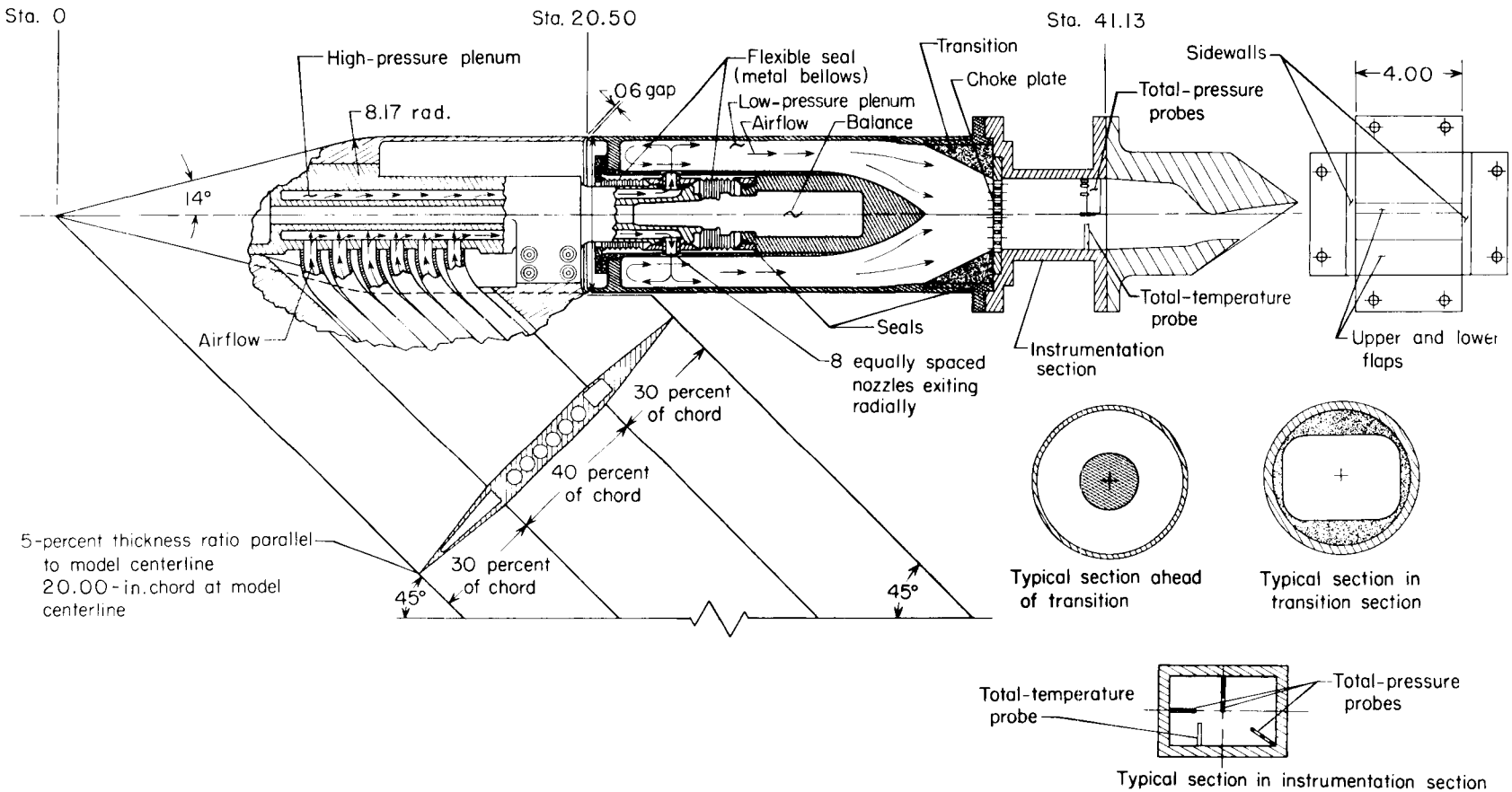

Figure 1. Sketch of air-powered nacelle model with typical SERN installed. Linear dimensions are in inches.

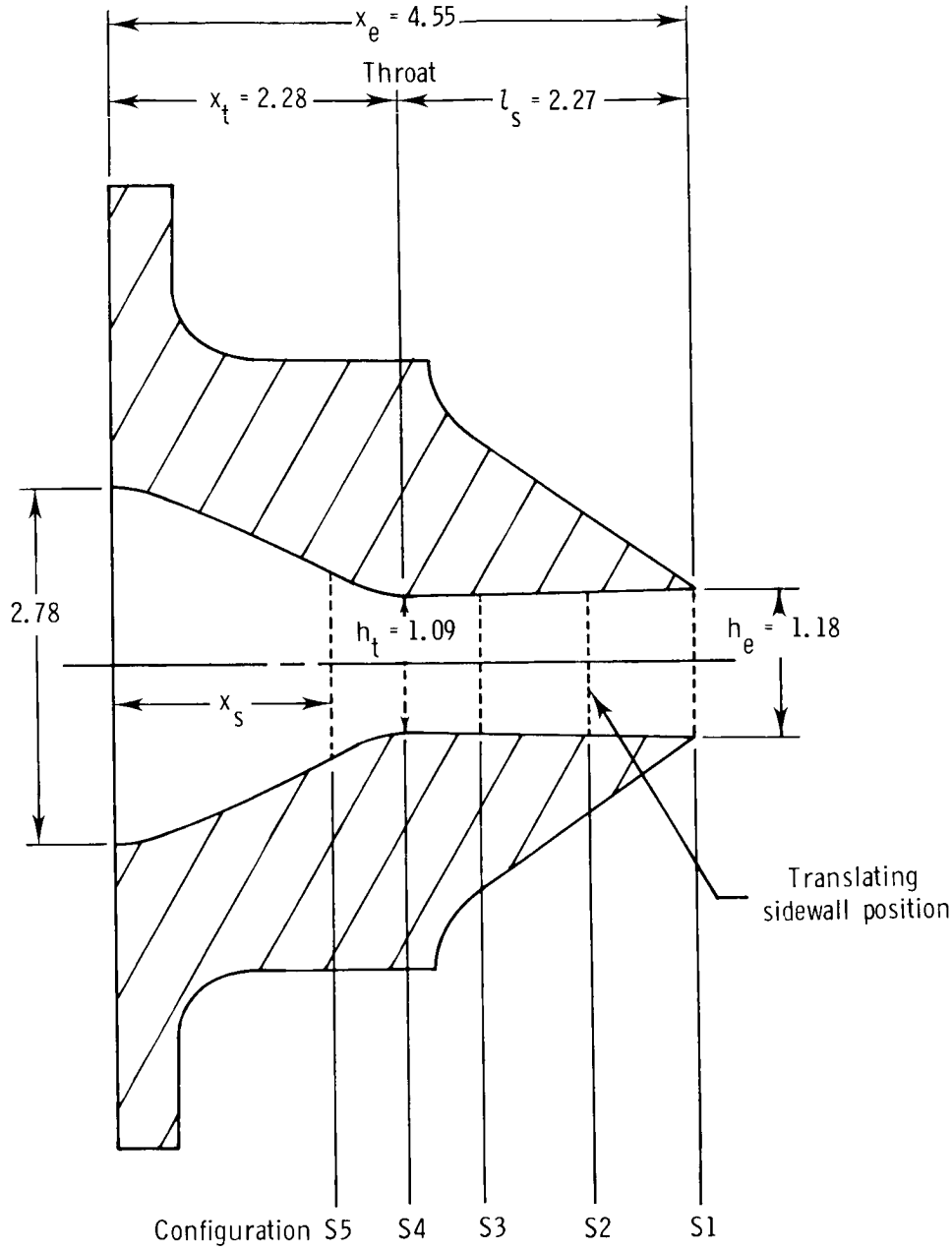

Configuration	A_t, in.^{2}	A_e, in.^{2}	A_e/A_t	AR	$\delta_{v,p}$, deg	x_s, in.	$(x_s - x_t)/l_s$
S1	4.36	4.72	1.08	3.67	0	4.55	1.00
S2	↓	-	-	↓	↓	3.70	0.63
S3	↓	-	-	↓	↓	2.85	0.25
S4	↓	-	-	↓	↓	2.28	0.00
S5	4.98	-	-	-	↓	1.70	-0.25

(a) Dry power nozzles, $A_e/A_t = 1.08$.

Figure 2. Sketches of nonaxisymmetric convergent-divergent nozzle configurations with translating sidewall yaw vectoring concept. Linear dimensions are in inches.

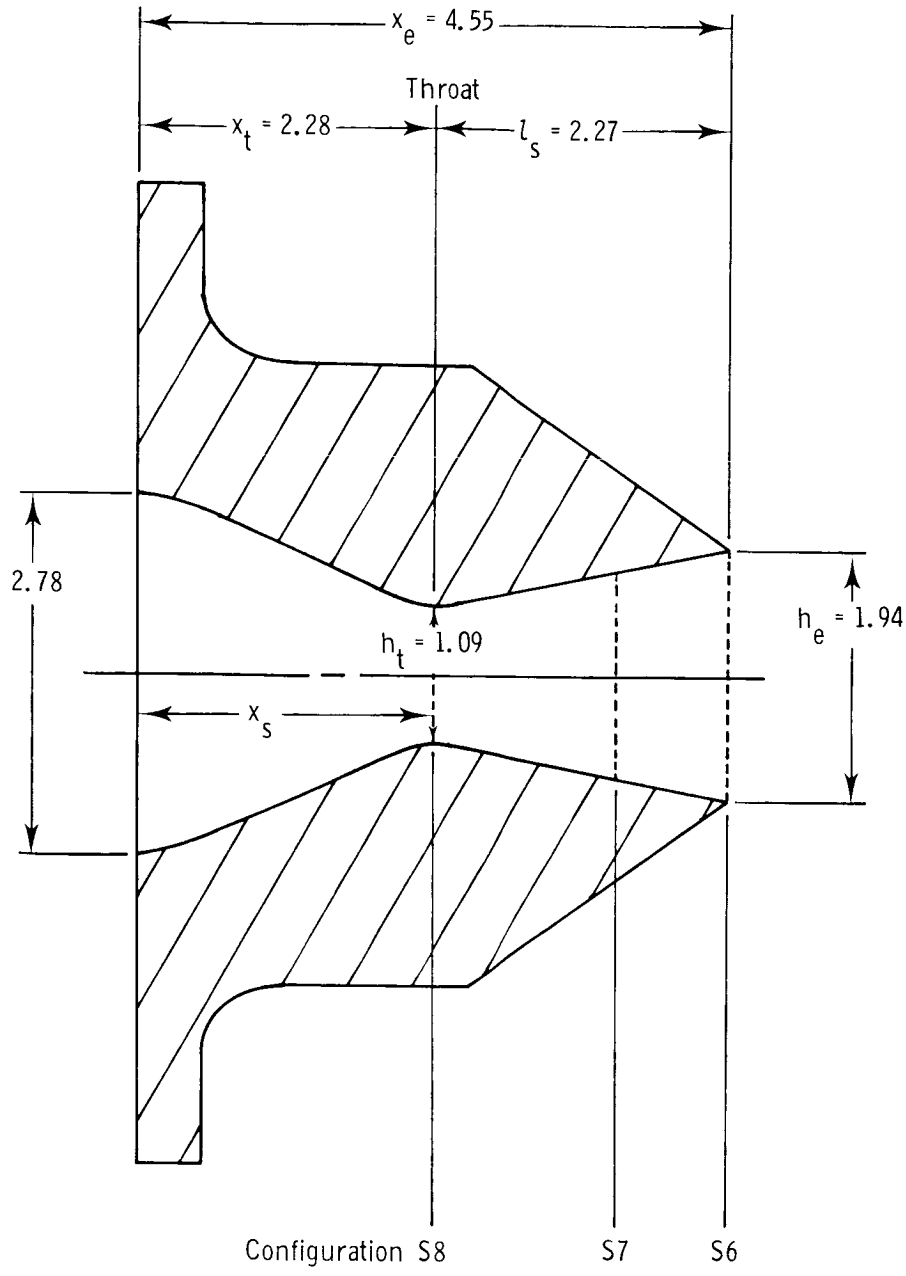

Configuration	A_t, in.^{2}	A_e, in.^{2}	A_e/A_t	AR	$\delta_{v,p}$, deg	x_s, in.	$(x_s - x_t)/l_s$
S6	4.36	7.78	1.78	3.67	0	4.55	1.00
S7	↓	-	-	↓	↓	3.70	0.63
S8	↓	-	-	↓	↓	2.28	0.00

(b) Dry power nozzles, $A_e/A_t = 1.78$.

Figure 2. Continued.

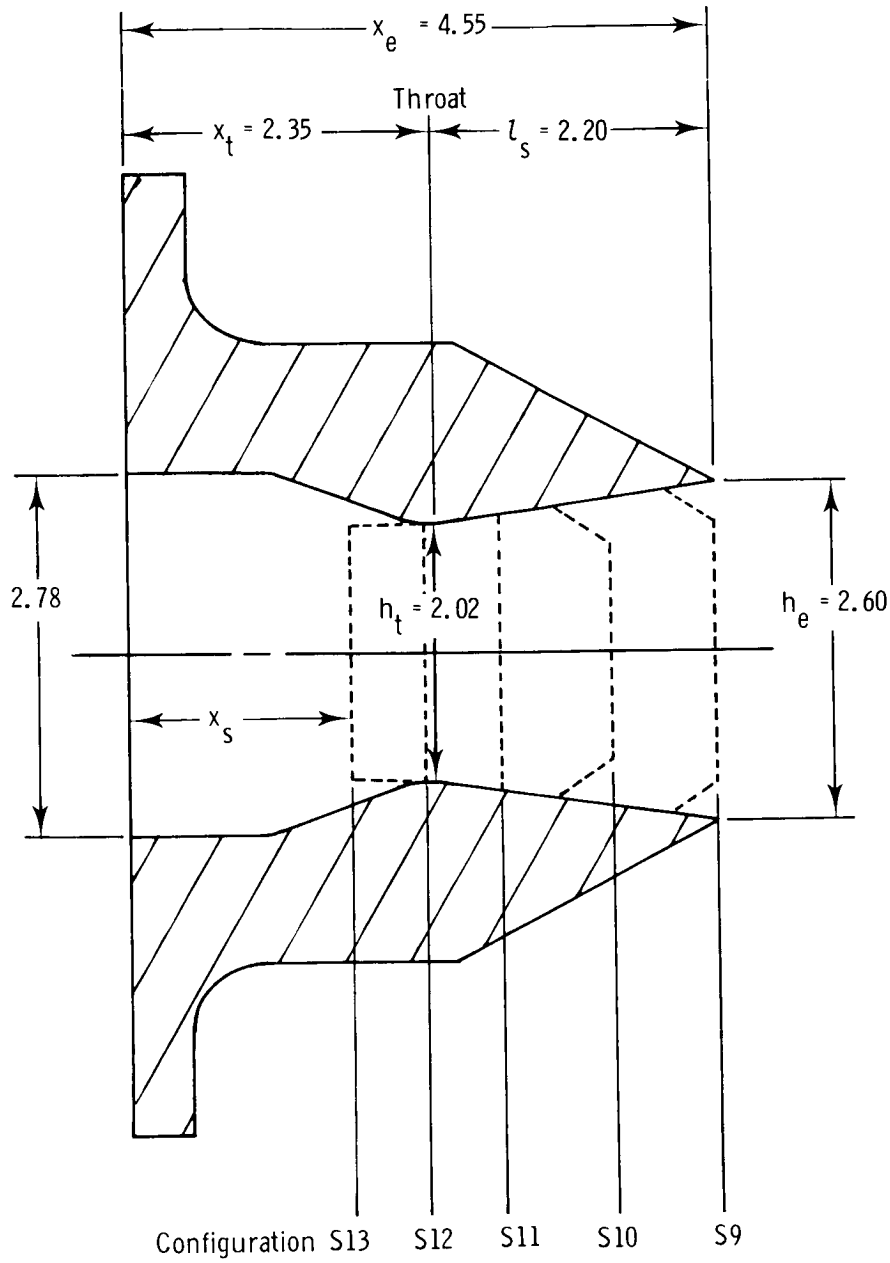

Configuration	A_t, in.^{2}	A_e, in.^{2}	A_e/A_t	AR	$\delta_{v,p}$, deg	x_s, in.	$(x_s - x_t)/l_s$
S9	8.06	10.40	1.29	1.99	0	4.55	1.00
S10	↓	-	-	↓	↓	3.70	0.61
S11	↓	-	-	↓	↓	2.85	0.23
S12	↓	-	-	↓	↓	2.28	-0.03
S13	9.30	-	-	-	↓	1.70	-0.30

(c) A/B power nozzles, $A_e/A_t = 1.29$.

Figure 2. Continued.

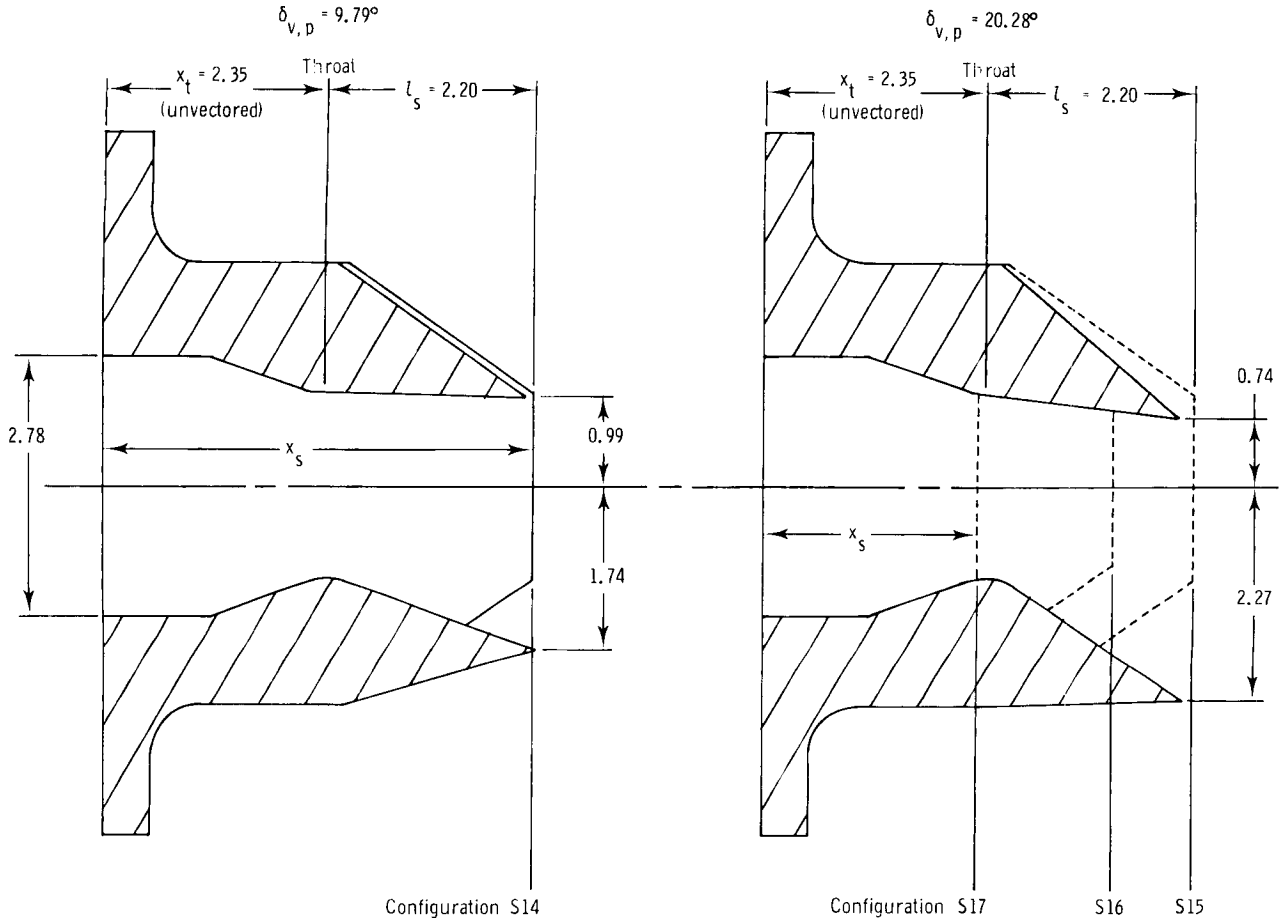

Configuration	A_t, in.^{2}	A_e, in.^{2}	A_e/A_t	AR	$\delta_{v,p}$, deg	x_s, in.	$(x_s - x_t)/l_s$
S14	8.07	10.92	1.35	1.98	9.79	4.55	1.00

Configuration	A_t, in.^{2}	A_e, in.^{2}	A_e/A_t	AR	$\delta_{v,p}$, deg	x_s, in.	$(x_s - x_t)/l_s$
S15	7.99	12.04	1.51	2.00	20.28	4.55	1.00
S16	↓	-	-	↓	↓	3.70	0.61
S17		-	-			2.28	-0.03

(d) A/B power pitch vectoring nozzles.

Figure 2. Concluded.

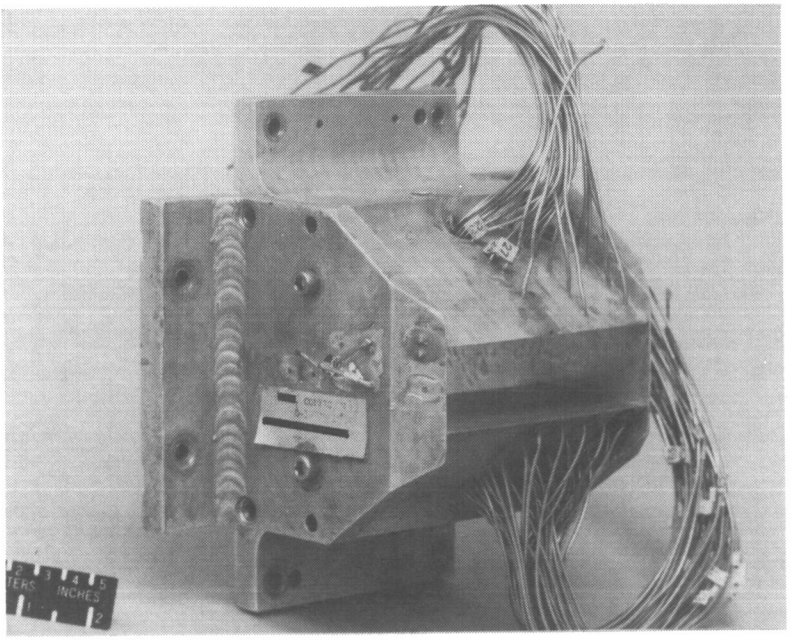

Three-quarter rear view

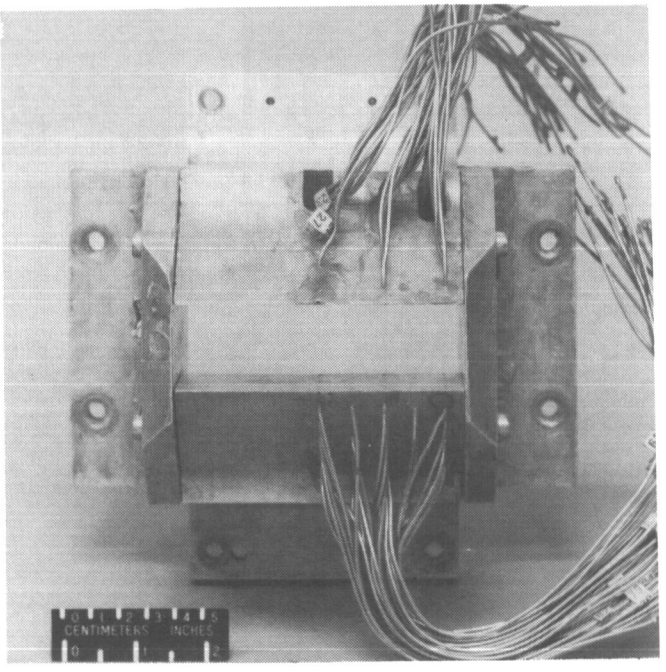

Rear view

L-85-16

(a) Configuration S1; $(x_s - x_t)/l_s = 1.00$.

Figure 3. Photographs of nonaxisymmetric convergent-divergent nozzle configurations with translating sidewall yaw vectoring concept.

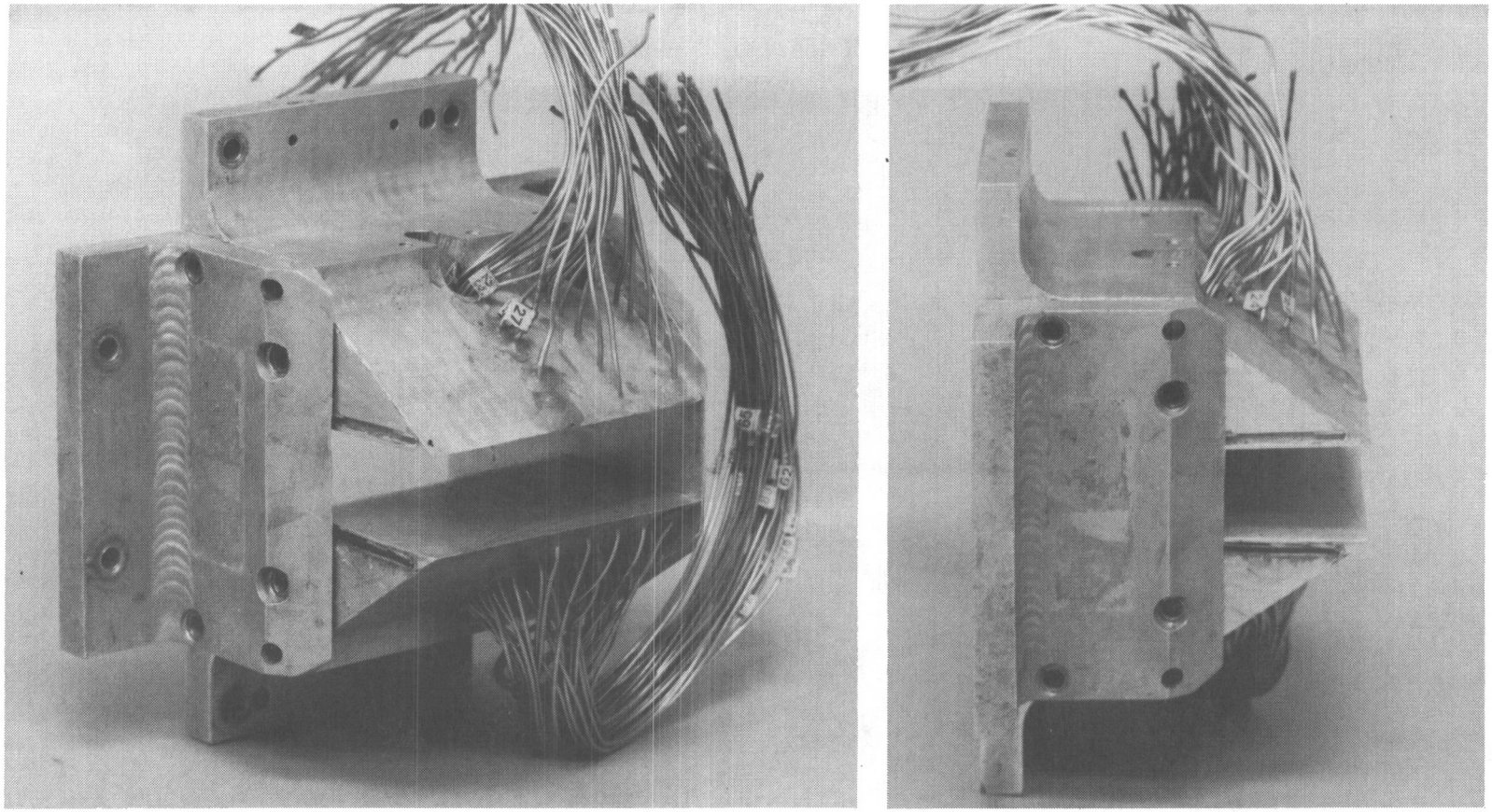

Three-quarter rear view

Side view

L-85-17

(b) Configuration S3; $(x_s - x_t)/l_s = 0.25$.

Figure 3. Continued.

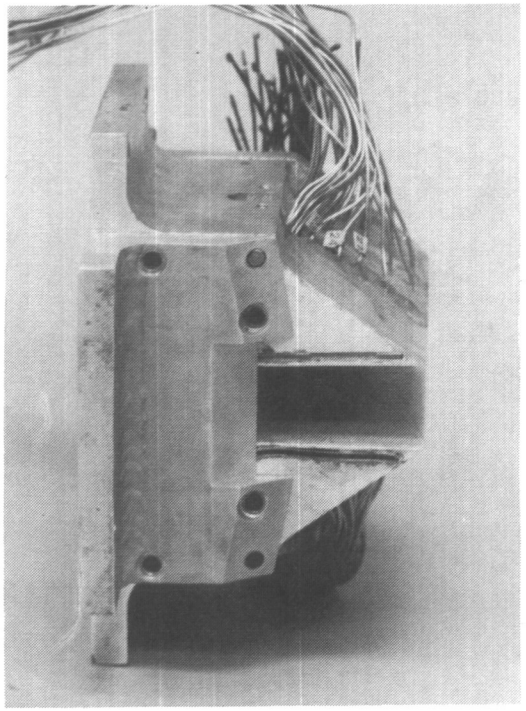

Configuration S4

Dry power nozzle; $\delta_{v,p} = 0^0$; $(x_s - x_t)/l_s = 0$

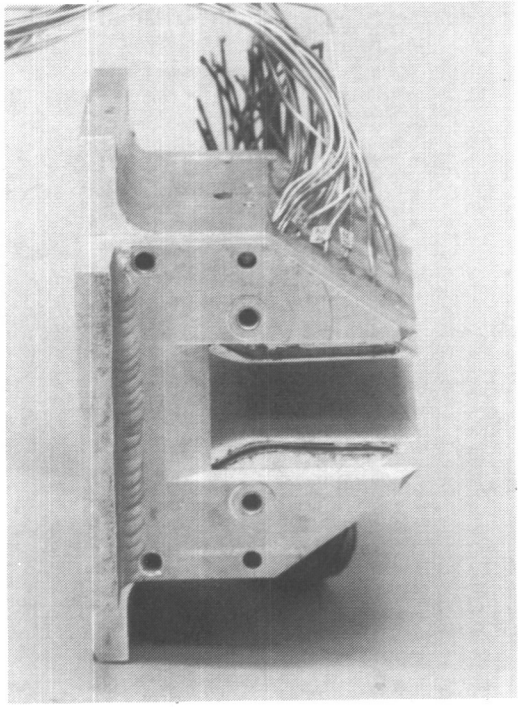

Configuration S5

Dry power nozzle; $\delta_{v,p} = 0^0$; $(x_s - x_t)/l_s = -0.25$

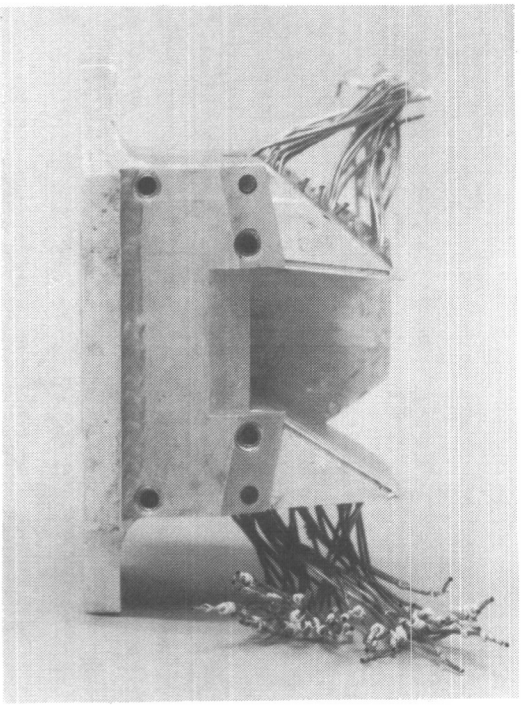

Configuration S17

A/B power nozzle; $\delta_{v,p} = 20.28^0$; $(x_s - x_t)/l_s = -0.03$

L-85-18

(c) Configurations S4, S5, and S17.

Figure 3. Concluded.

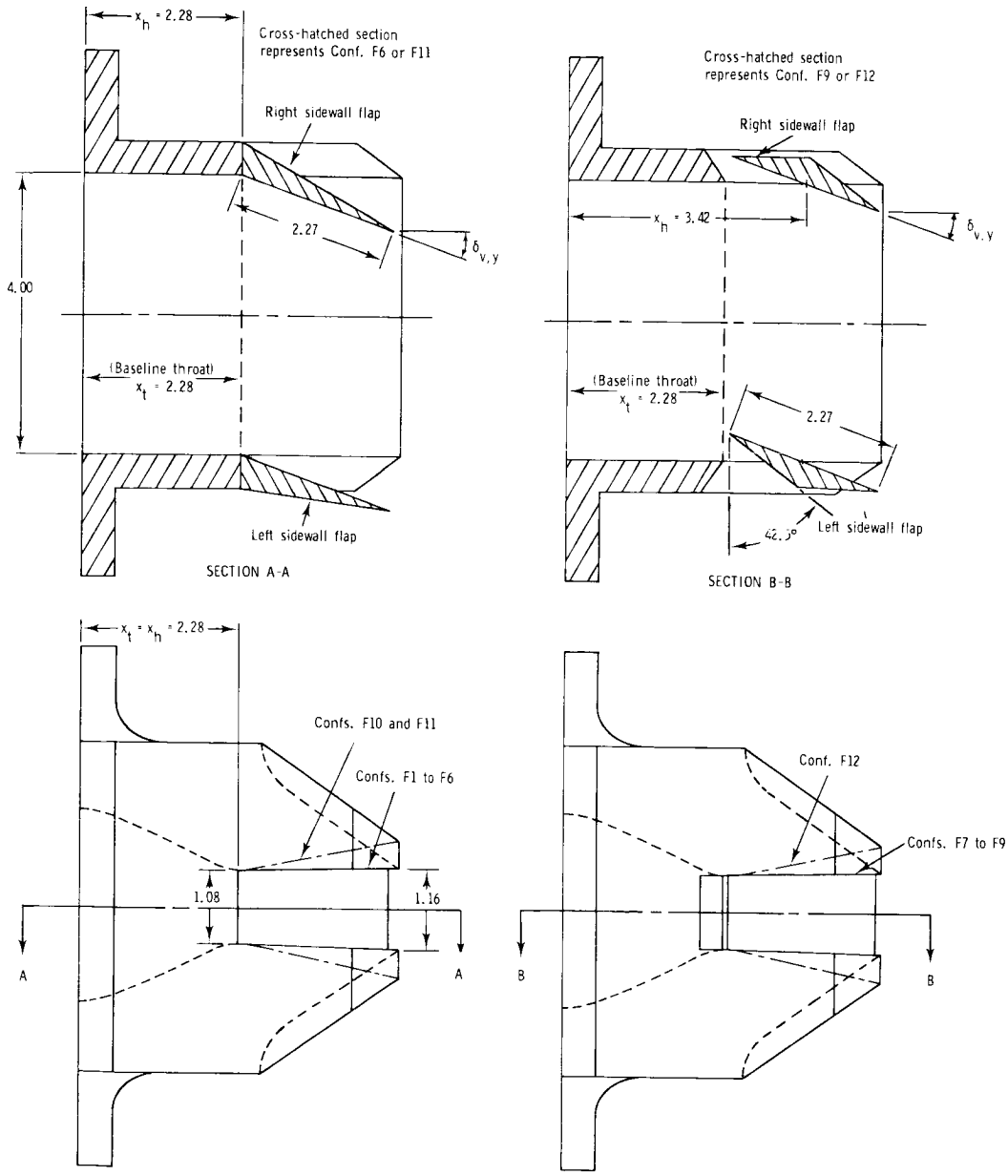

Configuration	A_t, in.^{2}	A_e/A_t	x_h, in.	$\delta_{v,y}$, deg	
				Left sidewall	Right sidewall
Baseline S1	4.36	1.08	2.28	0	0
F1	↓	-	↓	10	0
F2	4.28	1.00	↓	0	10
F3	4.33	-	↓	10	10
F4	4.36	-	↓	20	0
F5	3.81	1.00	↓	0	20
F6	4.18	-	↓	20	20
F7	4.31	-	3.42	20	0
F8	4.60	-	↓	0	20
F9	4.31	-	↓	20	20
Baseline S6	4.36	1.78	2.28	0	0
F10	↓	-	↓	20	0
F11	↓	-	↓	20	20
F12	4.30	-	3.42	20	20

(a) Dry power nozzles; A_e/A_t = 1.08 and 1.78.

Figure 4. Sketches of nonaxisymmetric convergent-divergent nozzle configurations with downstream yaw vector flap concepts. Linear dimensions are in inches.

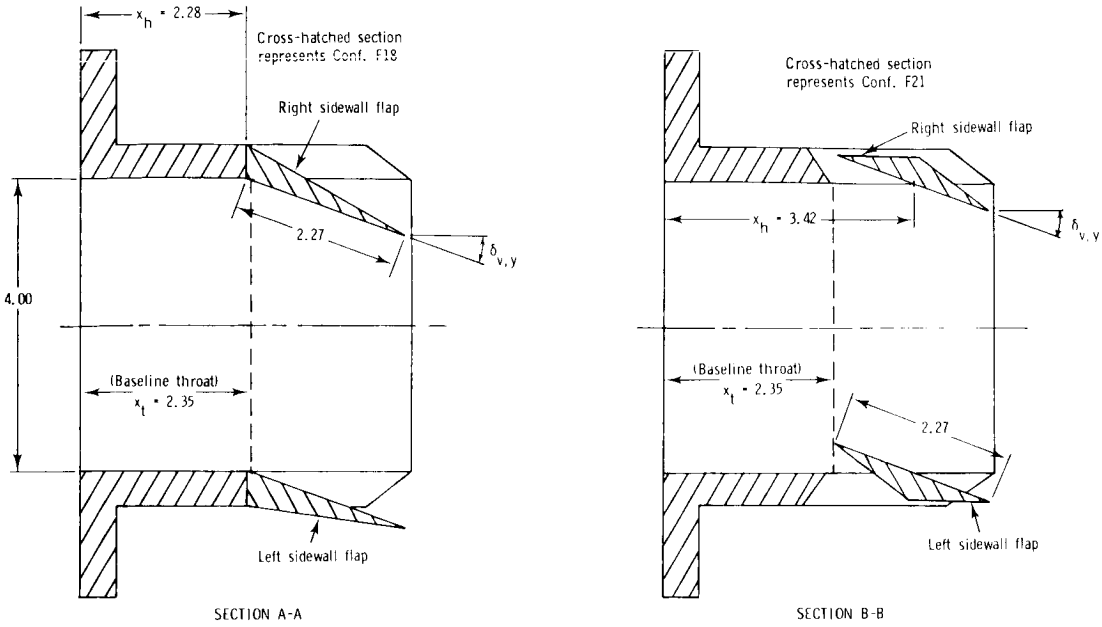

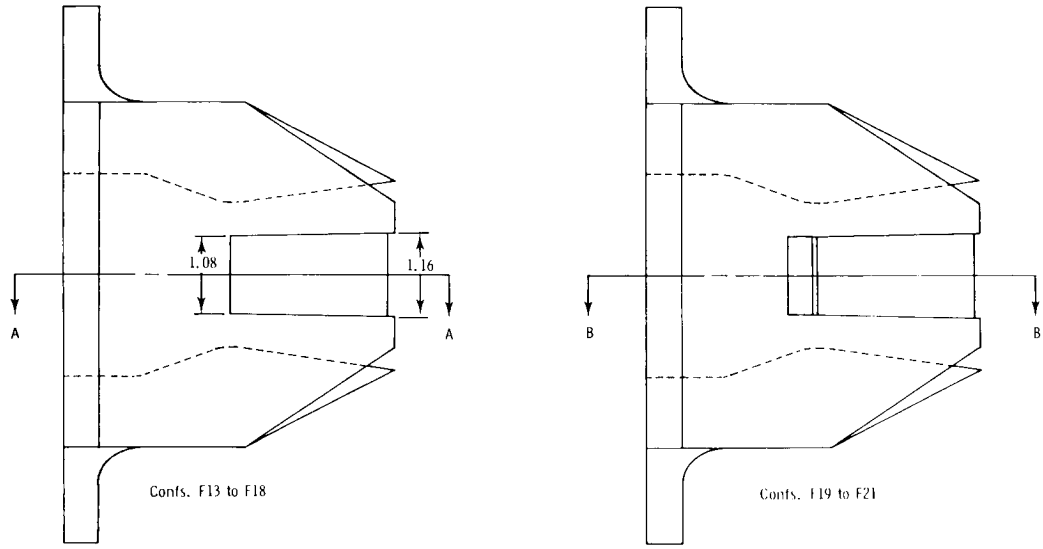

Configuration	A_t, in.^{2}	A_e/A_t	x_h, in.	$\delta_{v,y}$, deg	
				Left sidewall	Right sidewall
Baseline S9	8.06	1.29	2.28	0	0
F13	↓	-	↓	10	0
F14	8.07	-		0	10
F15	↓	-		10	10
F16	8.06	-		20	0
F17	8.07	-		0	20
F18	↓	-	↓	20	20
F19	8.02	-	3.42	20	0
F20	8.07	-	↓	0	20
F21	8.03	-	↓	20	20

(b) A/B power nozzles; $\delta_{v,p} = 0°$.

Figure 4. Continued.

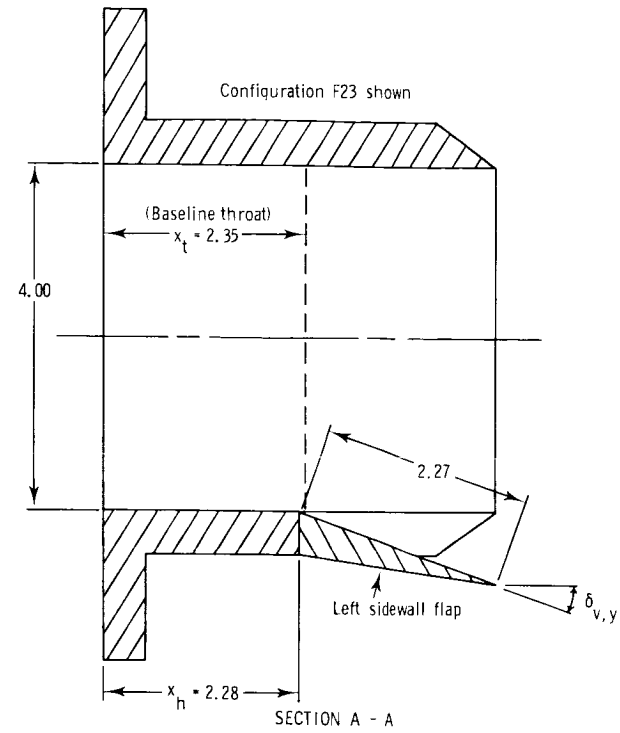

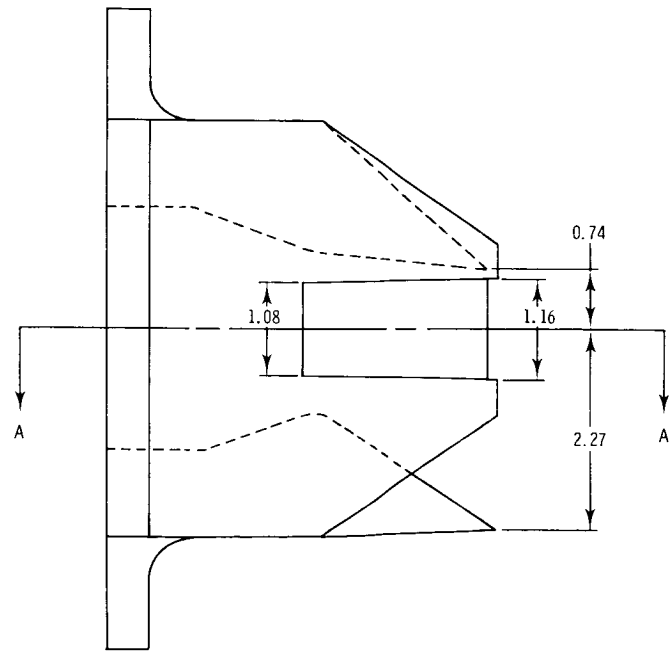

Configuration	A_t, in.^{2}	A_e/A_t	x_h, in.	$\delta_{v,y}$, deg	
				Left sidewall	Right sidewall
Baseline S15	7.99	-	2.28	0	0
F22	↓	-	↓	10	0
F23		-		20	0

(c) A/B power nozzle; $\delta_{v,p} = 20.28°$.

Figure 4. Concluded.

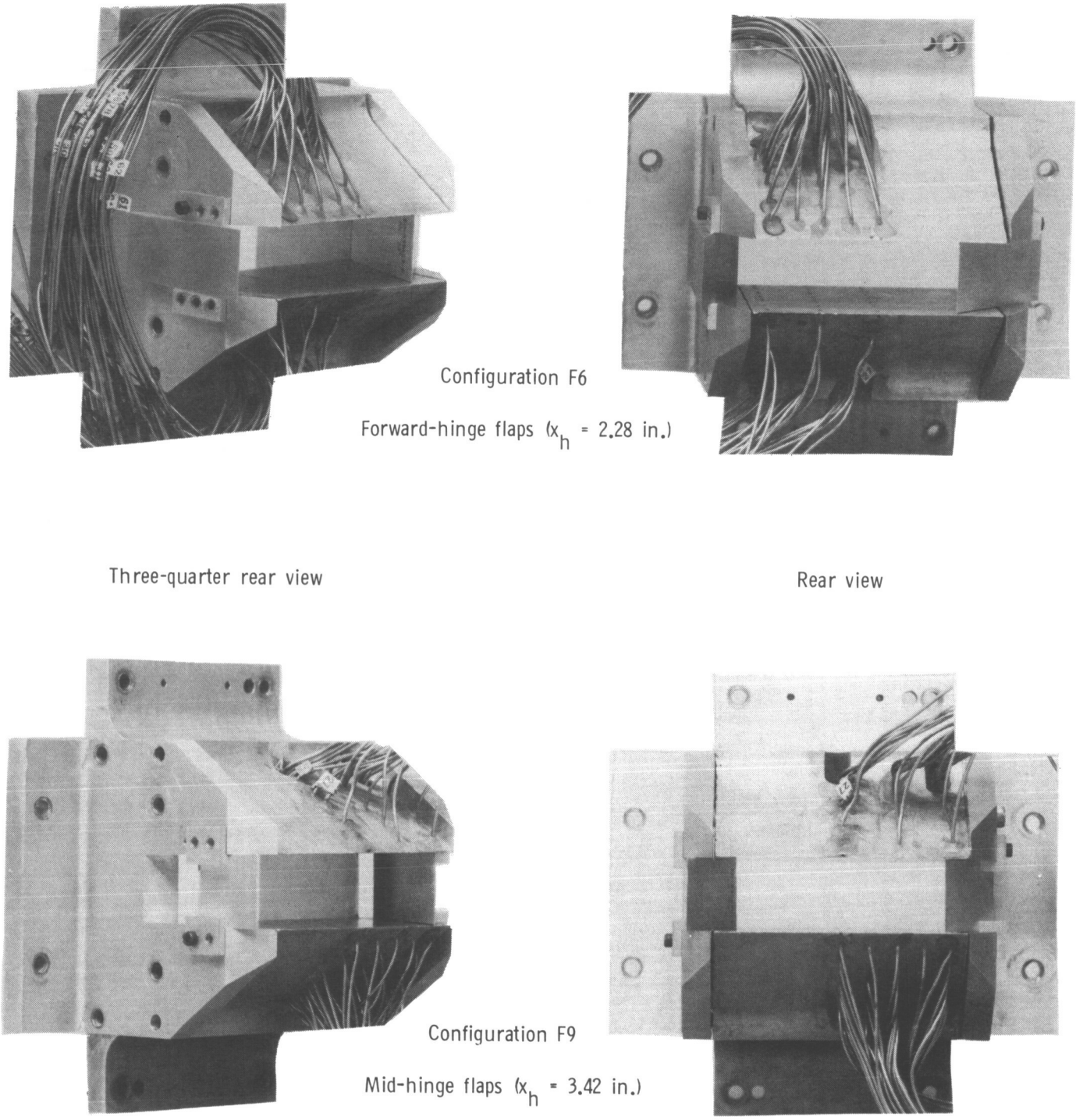

(a) Configurations F6 and F9; left- and right-hand sidewall flaps.

Figure 5. Photographs of nonaxisymmetric convergent-divergent nozzle configurations with downstream flap yaw vectoring concept.

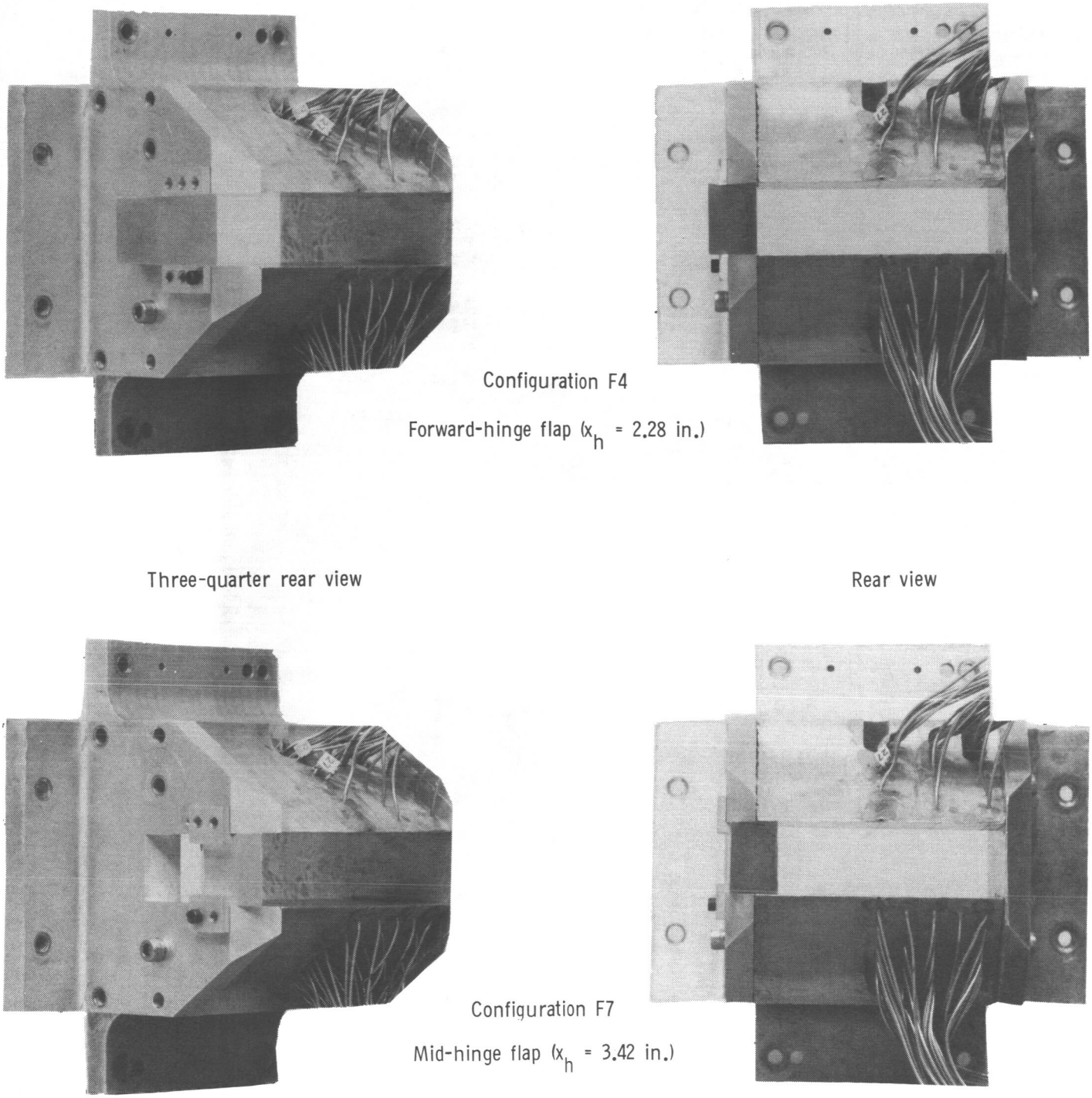

(b) Configurations F4 and F7; left-hand sidewall flap only.

Figure 5. Continued.

Forward-hinge flap (x_h = 2.28 in.)

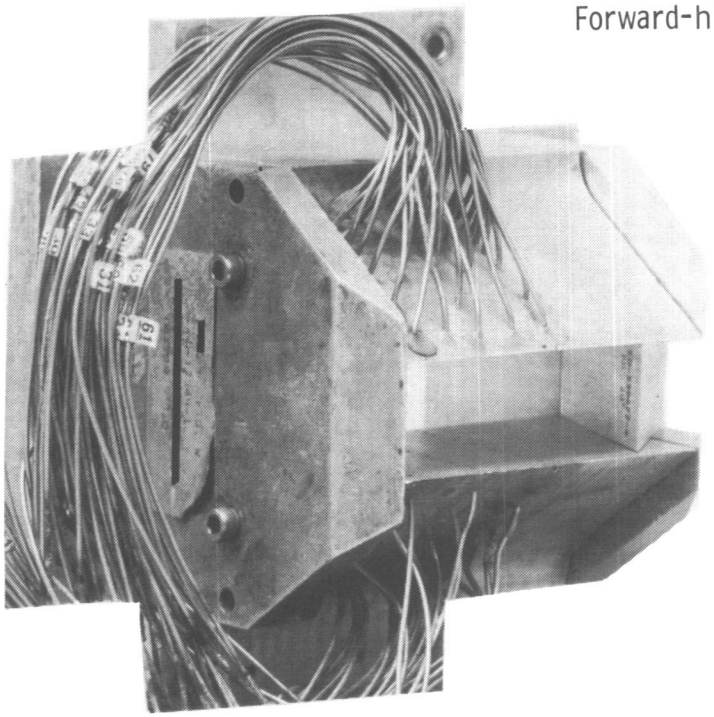

Three-quarter rear view

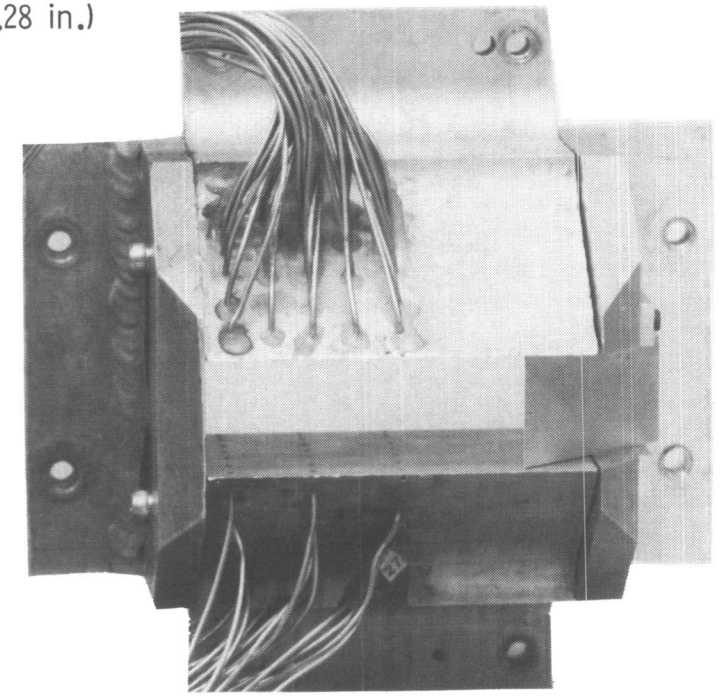

Rear view

L-85-21

(c) Configuration F5; right-hand sidewall flap only.

Figure 5. Continued.

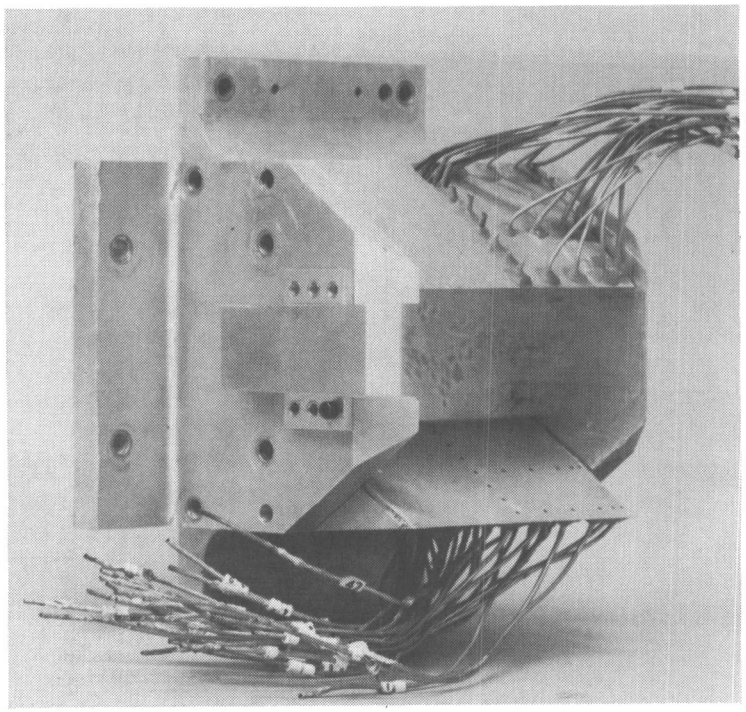

Three-quarter rear view

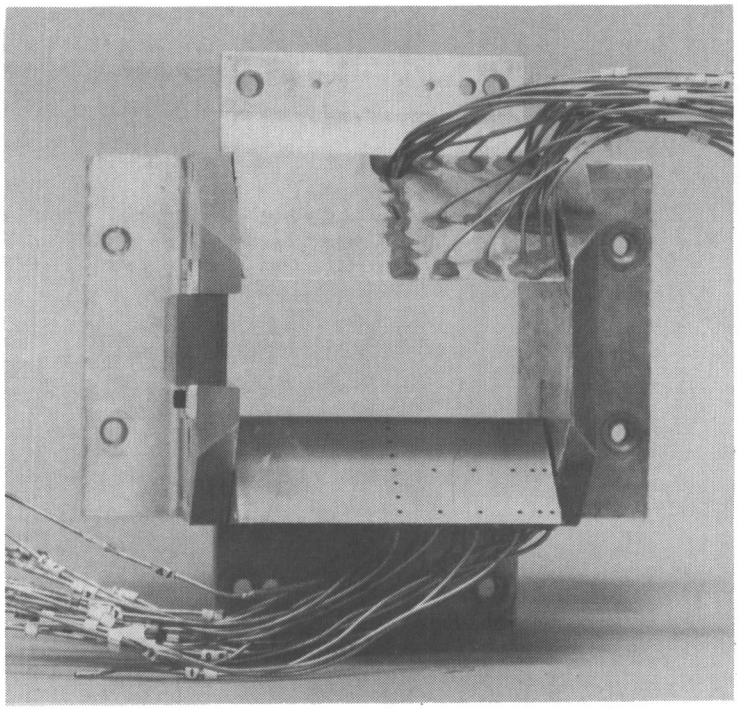

Rear view

Forward-hinge flap (x_h = 2.28 in.)

L-85-22

(d) Configuration F23; $\delta_{v,p} = 20.28°$ with left-hand sidewall flap only.

Figure 5. Concluded.

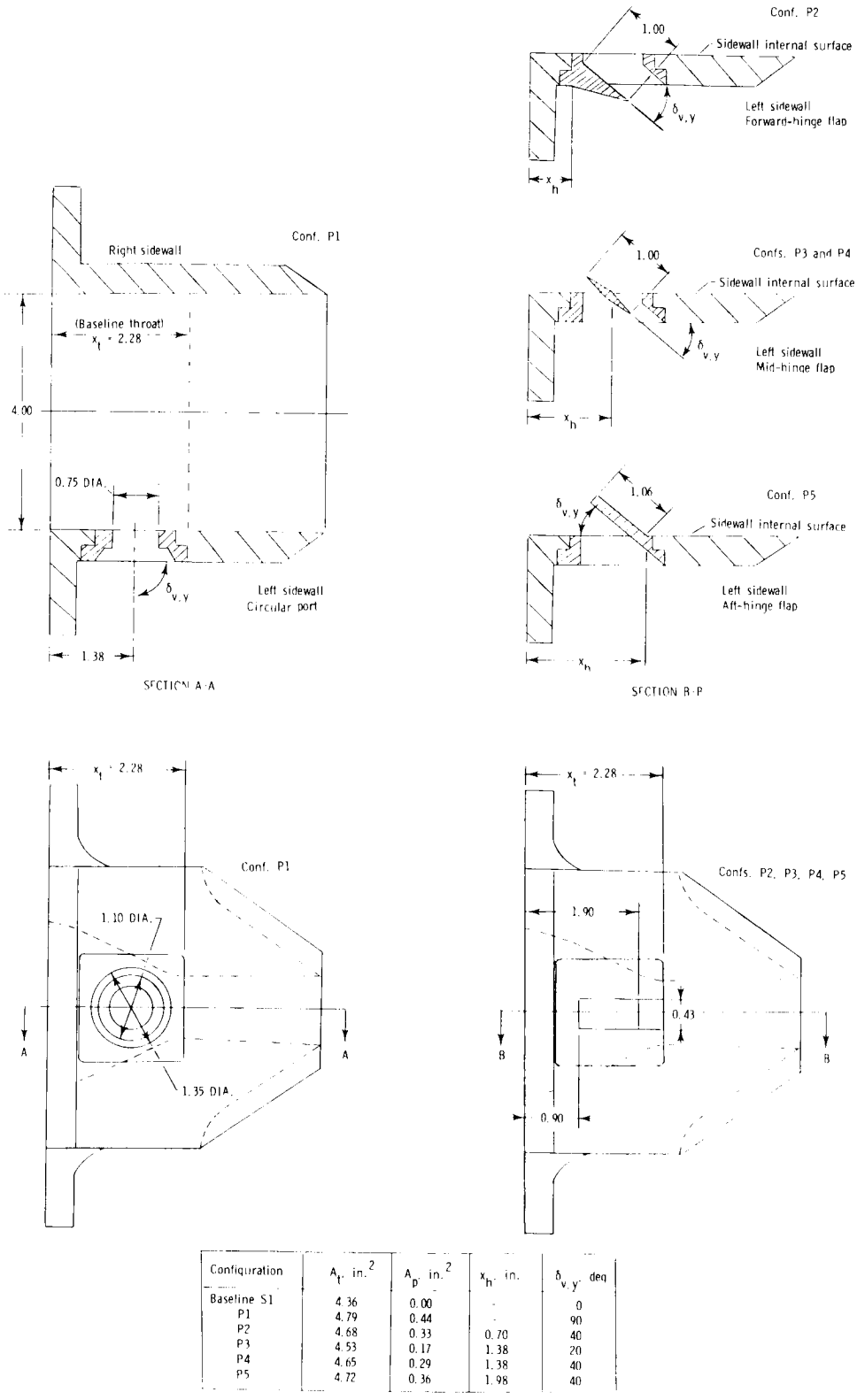

Configuration	A_t, in.^{2}	A_p, in.^{2}	x_h, in.	$\delta_{v,y}$, deg
Baseline S1	4.36	0.00	-	0
P1	4.79	0.44	-	90
P2	4.68	0.33	0.70	40
P3	4.53	0.17	1.38	20
P4	4.65	0.29	1.38	40
P5	4.72	0.36	1.98	40

(a) Dry power nozzle; $A_e/A_t = 1.08$; $\delta_{v,p} = 0°$.

Figure 6. Sketches of nonaxisymmetric convergent-divergent nozzles with yaw vector upstream port/flap concepts. Linear dimensions are in inches.

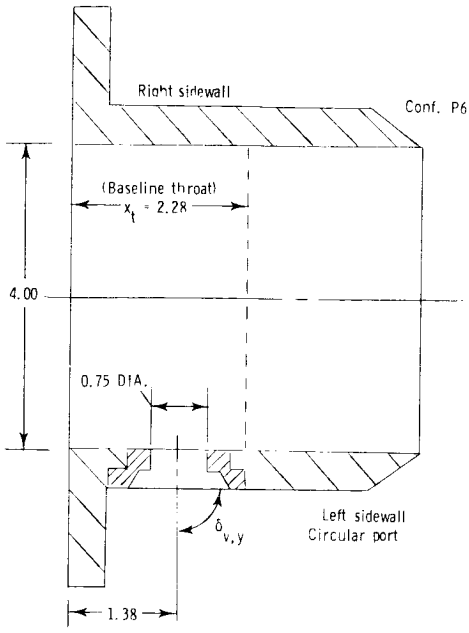

SECTION A-A

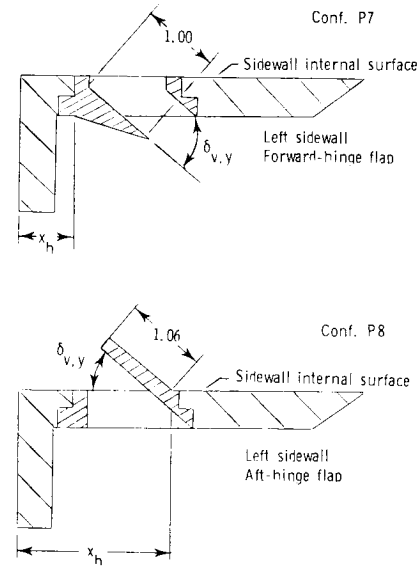

SECTION B-B

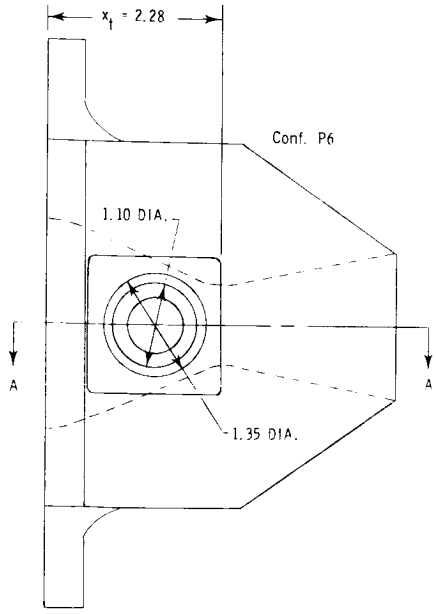

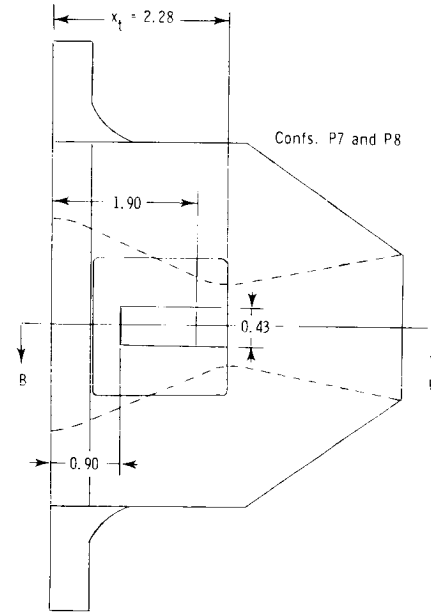

Configuration	A_t, in.^{2}	A_p, in.^{2}	x_h, in.	$\delta_{v,y}$, deg
Baseline S6	4.36	0.00	-	0
P6	4.81	0.44	-	90
P7	4.70	0.33	0.70	40
P8	4.74	0.36	1.98	40

(b) Dry power nozzle; $A_e/A_t = 1.78$; $\delta_{v,p} = 0°$.

Figure 6. Continued.

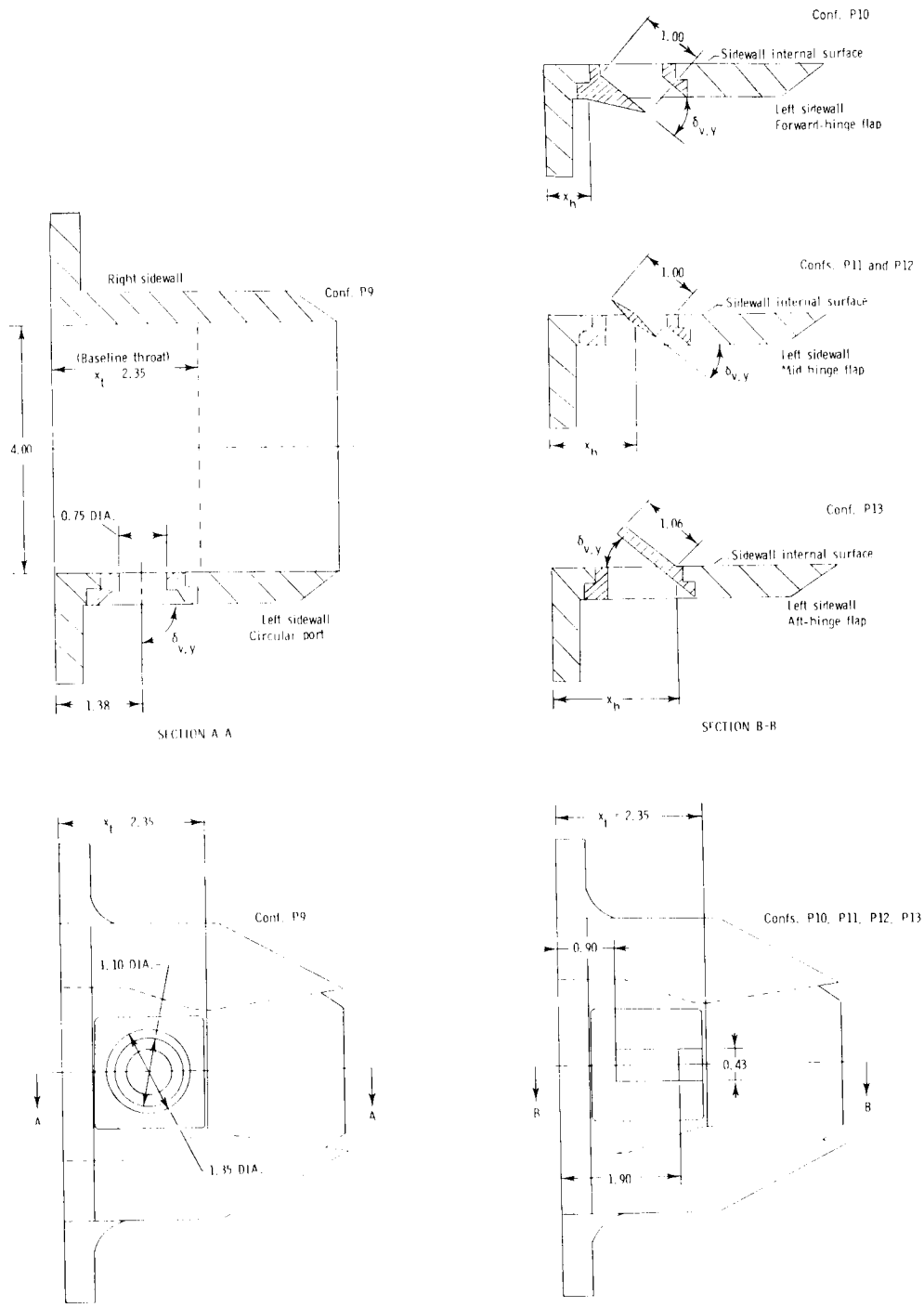

Configuration	A_t, in.^{2}	A_p, in.^{2}	x_h, in.	$\delta_{v,y}$, deg
Baseline S9	8.06	0.00		0
P9	8.49	0.44	-	90
P10	8.38	0.33	0.70	40
P11	8.22	0.17	1.38	20
P12	8.34	0.29	1.38	40
P13	8.41	0.36	1.98	40

(c) A/B power nozzles; $A_e/A_t = 1.29$; $\delta_{v,p} = 0°$.

Figure 6. Continued.

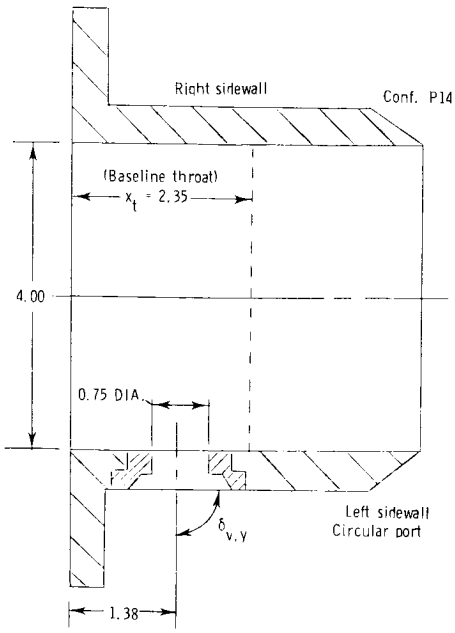

SECTION A-A

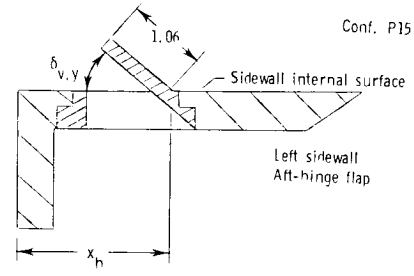

SECTION B-B

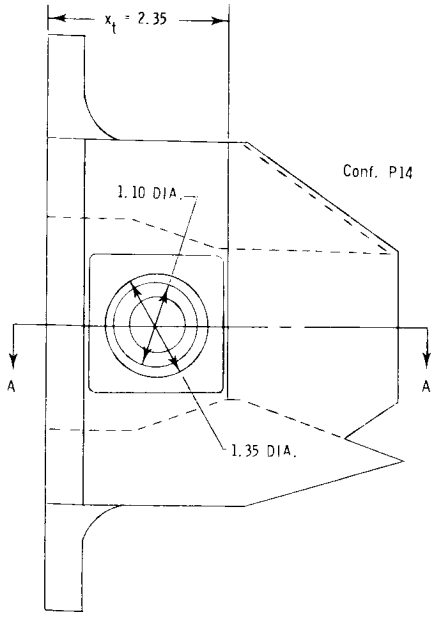

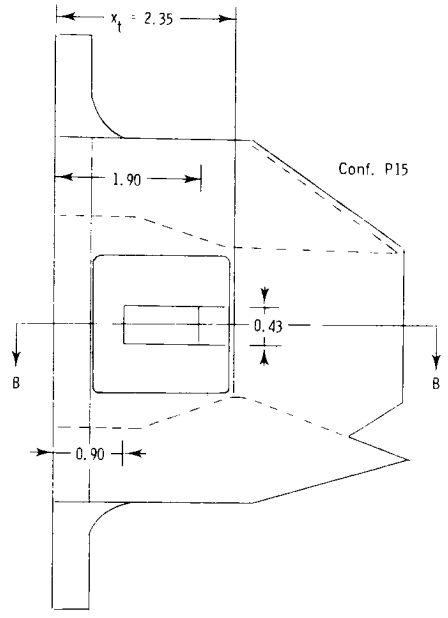

Configuration	A_t, in.^{2}	A_p, in.^{2}	x_h, in.	$\delta_{v,y}$, deg
Baseline S14	8.07	0.00	-	0
P14	8.51	0.44	-	90
P15	8.43	0.36	1.98	40

(d) A/B power nozzles; $\delta_{v,p} = 9.79°$.

Figure 6. Continued.

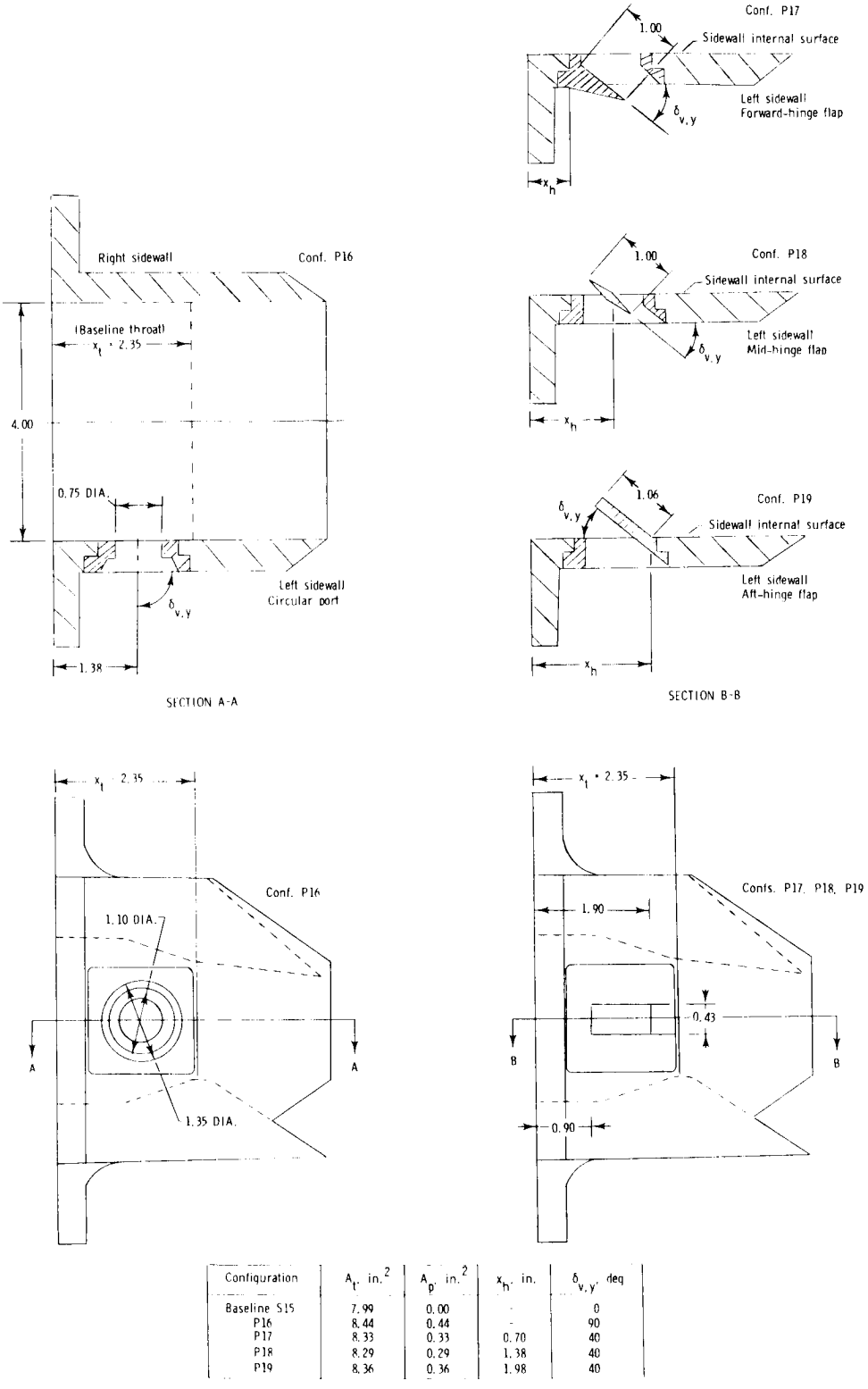

Configuration	A_t, in.^{2}	A_p, in.^{2}	x_h, in.	$\delta_{v,y}$, deg
Baseline S15	7.99	0.00	-	0
P16	8.44	0.44	-	90
P17	8.33	0.33	0.70	40
P18	8.29	0.29	1.38	40
P19	8.36	0.36	1.98	40

(e) A/B power nozzles; $\delta_{v,p} = 20.28°$.

Figure 6. Concluded.

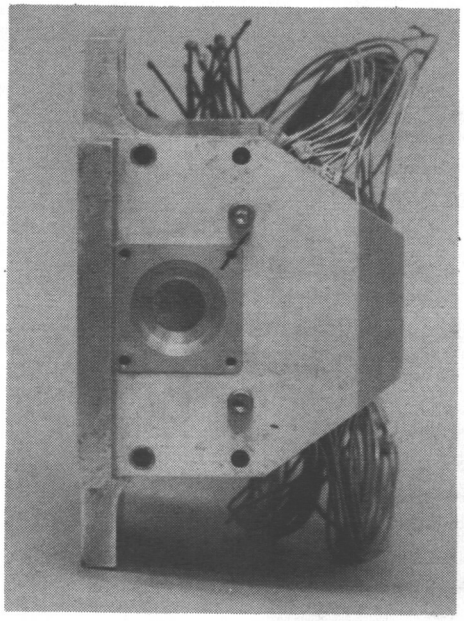

Side view

Configuration P1

Circular port

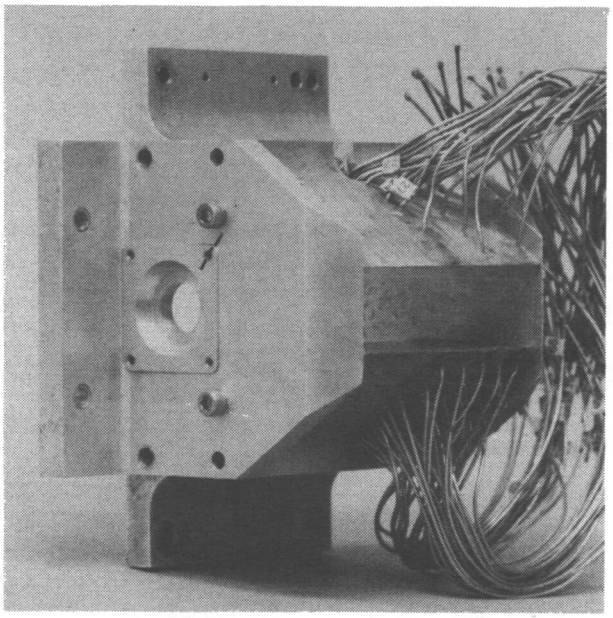

Three-quarter rear view

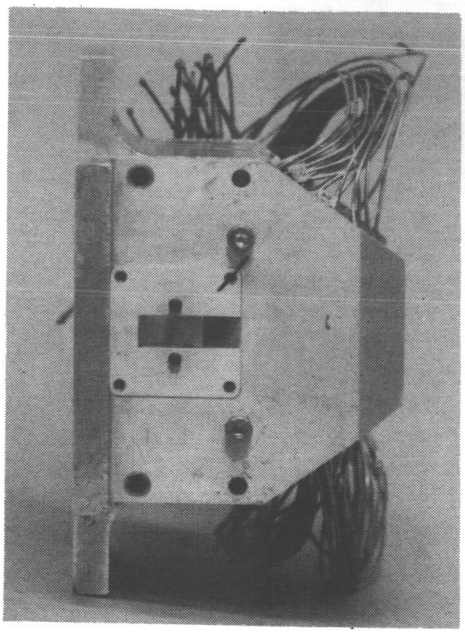

Configuration P4

Mid-hinge flap

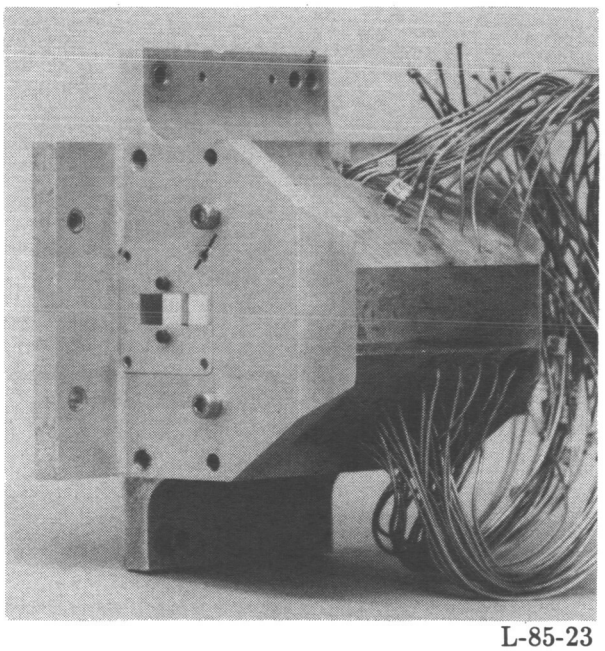

L-85-23

(a) Configurations P1 and P4.

Figure 7. Photographs of nonaxisymmetric convergent-divergent nozzle configurations with upstream port yaw vectoring concept.

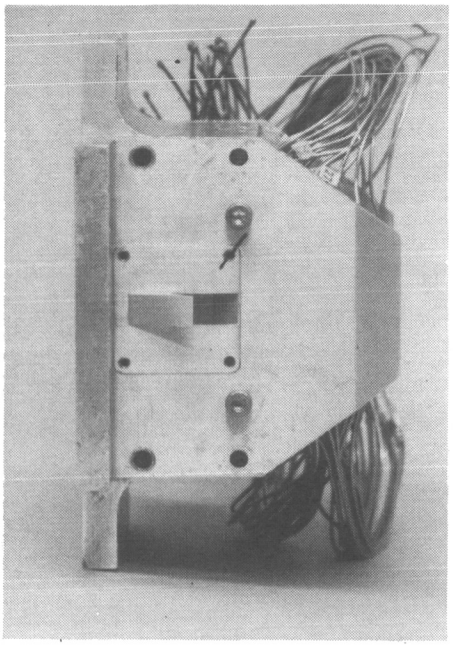

Configuration P2

Forward-hinge flap

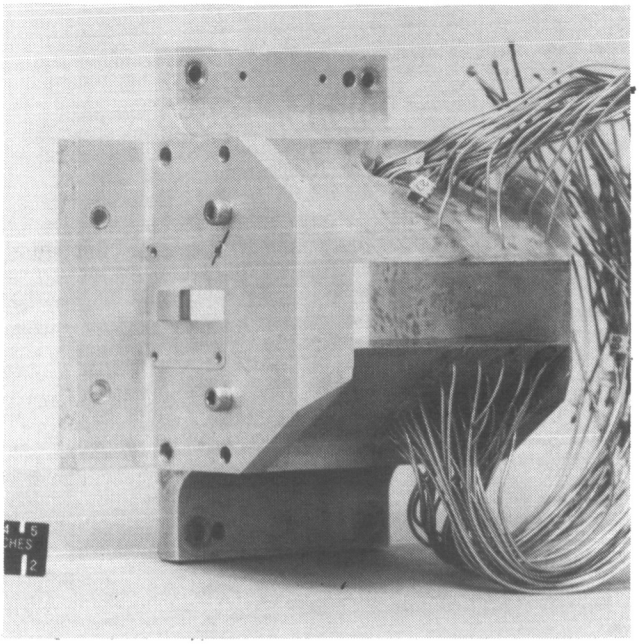

Side view

Three-quarter rear view

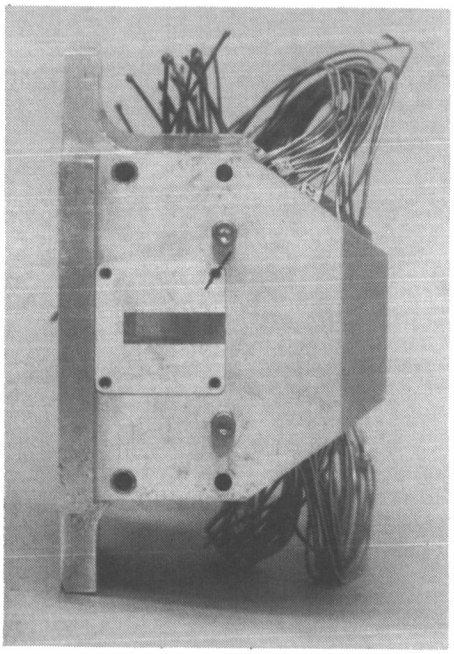

Configuration P5

Aft-hinge flap

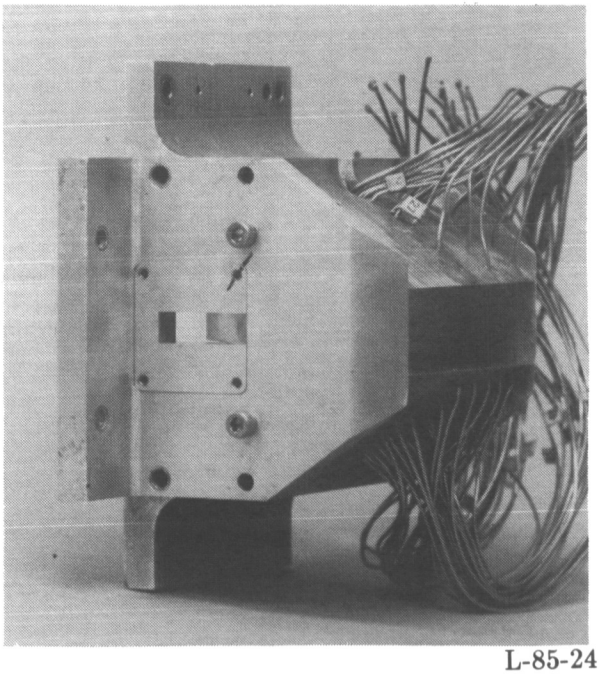

L-85-24

(b) Configurations P2 and P5.

Figure 7. Continued.

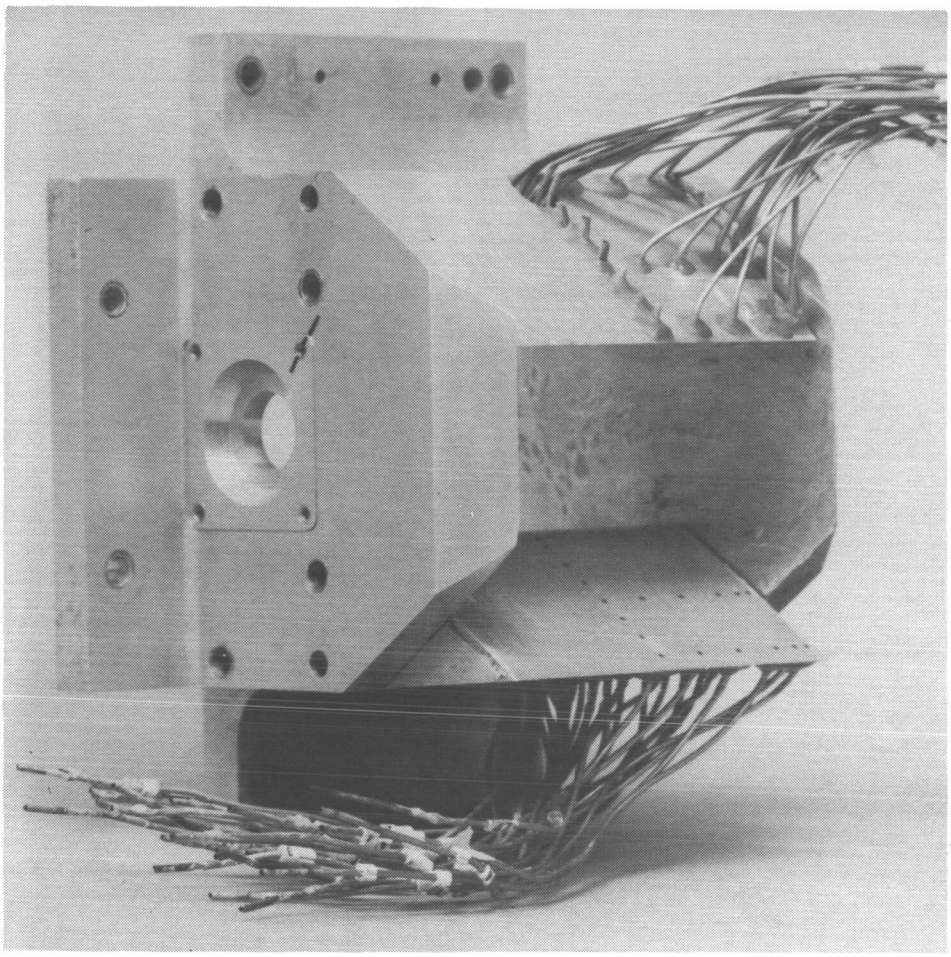

Circular port; $\delta_{v,p} = 20^{o}$

L-82-12,093

(c) Configuration P16.

Figure 7. Concluded.

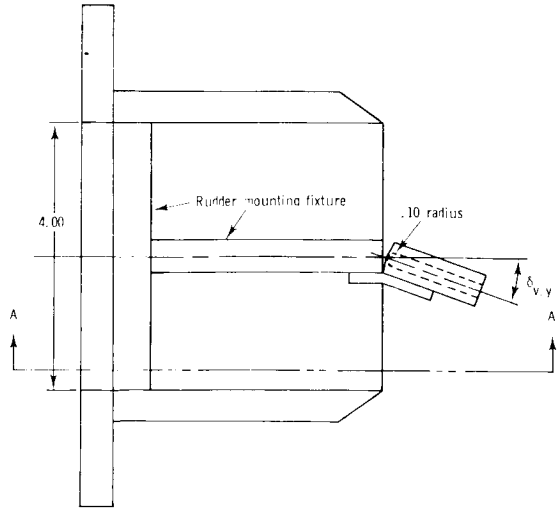

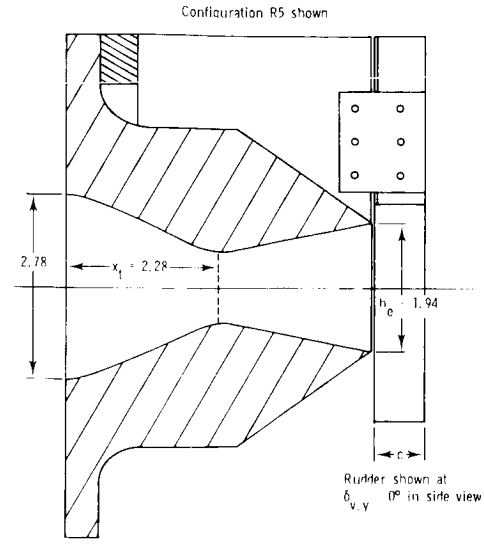

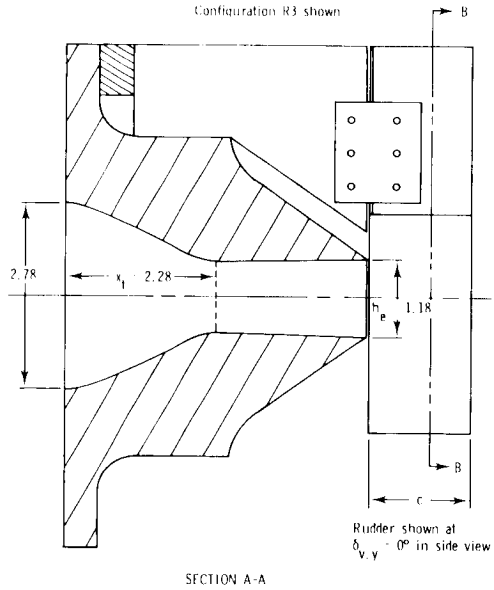

SECTION A-A

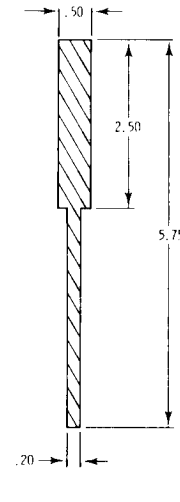

SECTION B-B

Configuration	A_t, in.^{2}	A_e, in.^{2}	A_e/A_t	c, in.	$\delta_{v,p}$, deg	$\delta_{v,y}$, deg
R1	4.35	4.72	1.09	0.75	0	0
R2	↓	↓	↓	↓	↓	20
R3	↓	↓	↓	1.50	↓	0
R4	↓	↓	↓	↓	↓	20
R5	4.37	7.76	1.78	0.75	↓	0
R6	↓	↓	↓	↓	↓	20
R7	↓	↓	↓	1.50	↓	0
R8	↓	↓	↓	↓	↓	20

(a) Dry power nozzles; $A_e/A_t = 1.09$ and 1.78; $\delta_{v,y} = 0°$.

Figure 8. Sketches of nonaxisymmetric convergent-divergent nozzle configurations with powered rudder yaw vector concept. Linear dimensions are in inches.

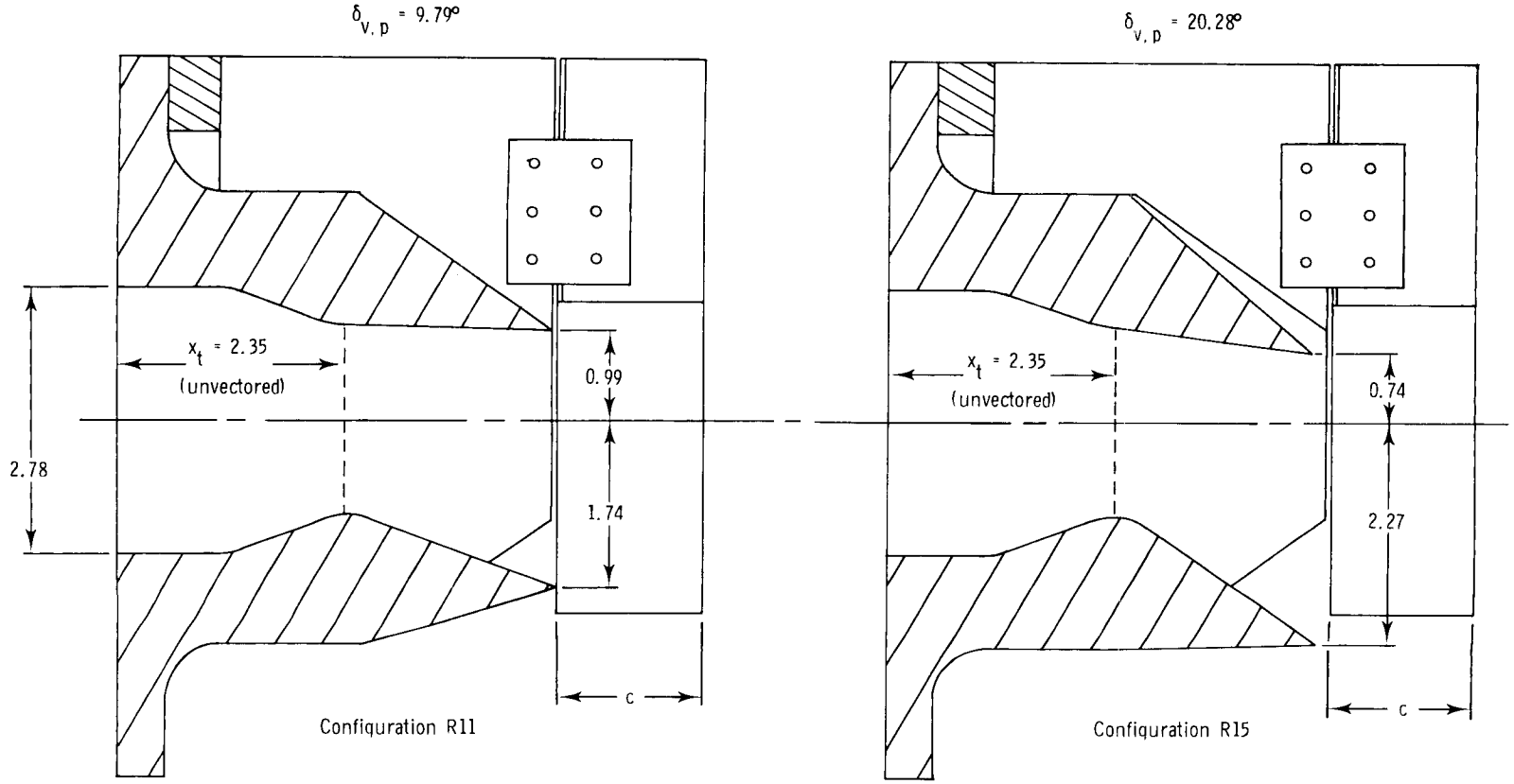

Configuration	A_t, in.^{2}	A_e, in.^{2}	A_e/A_t	c, in.	$\delta_{v,p}$, deg	$\delta_{v,y}$, deg
R9	8.07	10.92	1.35	0.75	9.79	0
R10	↓	↓	↓	↓	↓	20
R11				1.50		0
R12				↓		20
R13	7.99	12.04	1.51	0.75	20.28	0
R14	↓	↓	↓	↓	↓	20
R15				1.50		0
R16				↓		20

(b) A/B power nozzles; pitch vectoring configurations.

Figure 8. Concluded.

Configuration R4

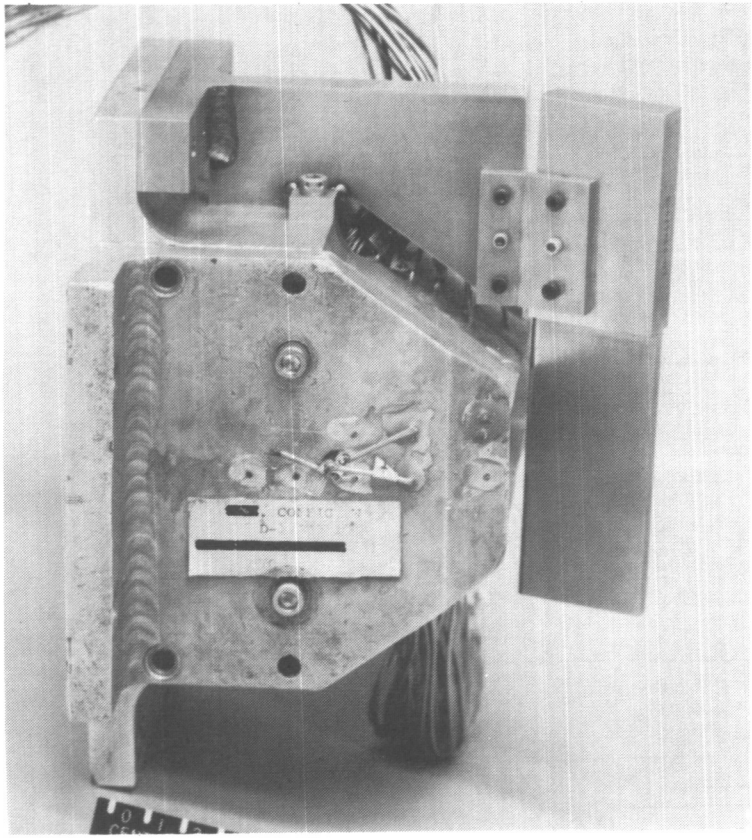

Side view

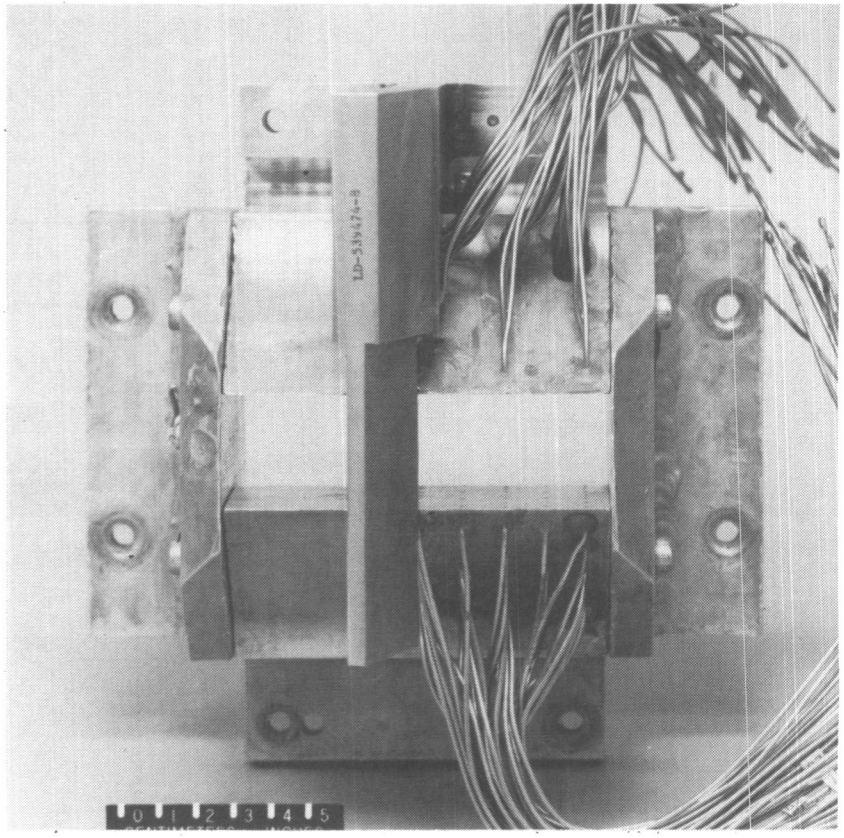

Rear view

L-85-25

Figure 9. Photographs of nonaxisymmetric convergent-divergent nozzle configuration with powered rudder yaw vectoring concept.

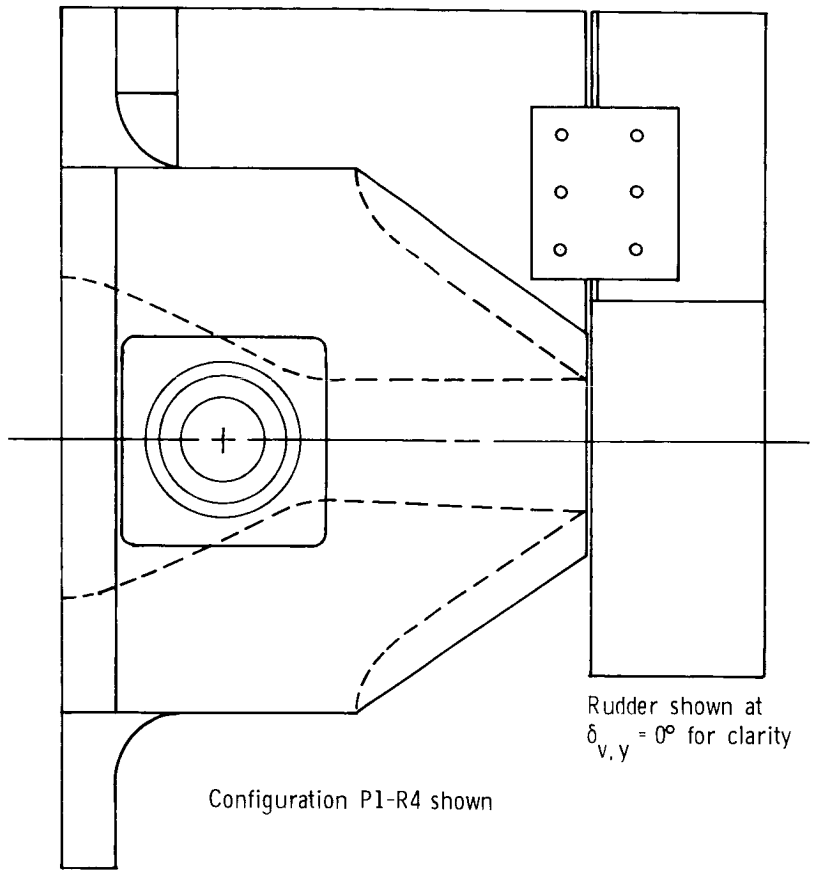

Configuration	A_t, in.^{2}	Baseline A_e/A_t	A_p, in.^{2}	x_h, in.	c, in.	$\delta_{v,y}$, deg			$\delta_{v,p}$, deg
						Left sidewall	Right sidewall	Rudder	
F1-R4	4.36	1.08	-	2.28	1.50	10	0	20	0.00
F4-R4	↓	↓	-	↓	↓	20	↓	↓	↓
F3-R4	4.33	↓	-	↓	↓	10	10	↓	↓
F6-R4	4.18	↓	-	↓	↓	20	20	↓	↓
F9-R4	4.31	↓	-	3.42	↓	↓	↓	↓	↓
F22-R16	7.99	1.51	-	2.28	↓	10	0	↓	20.28
F23-R16	↓	↓	-	↓	↓	20	↓	↓	↓
P1-R4	4.79	1.08	0.44	-	↓	90	-	↓	0.00
P2-R4	4.68	↓	0.33	0.70	↓	40	-	↓	↓
P16-R16	8.44	1.51	0.44	-	↓	90	-	↓	20.28
P17-R16	8.33	↓	0.33	0.70	↓	40	-	↓	↓

Figure 10. Sketch of nonaxisymmetric convergent-divergent nozzle configuration with a combination of yaw vector concepts installed. Linear dimensions are in inches.

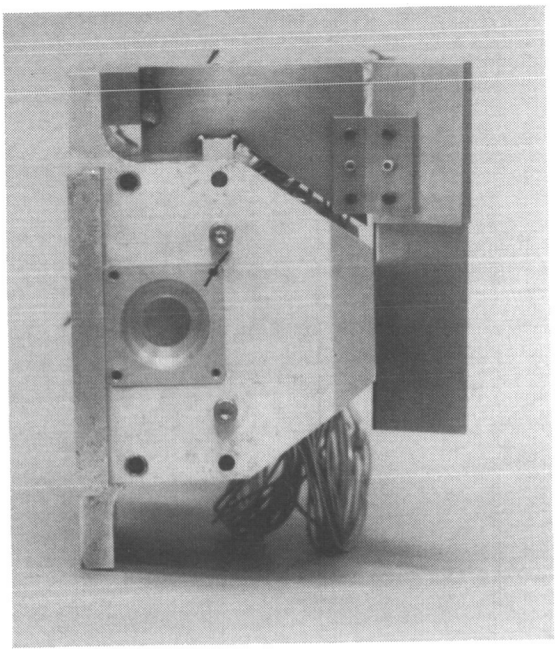

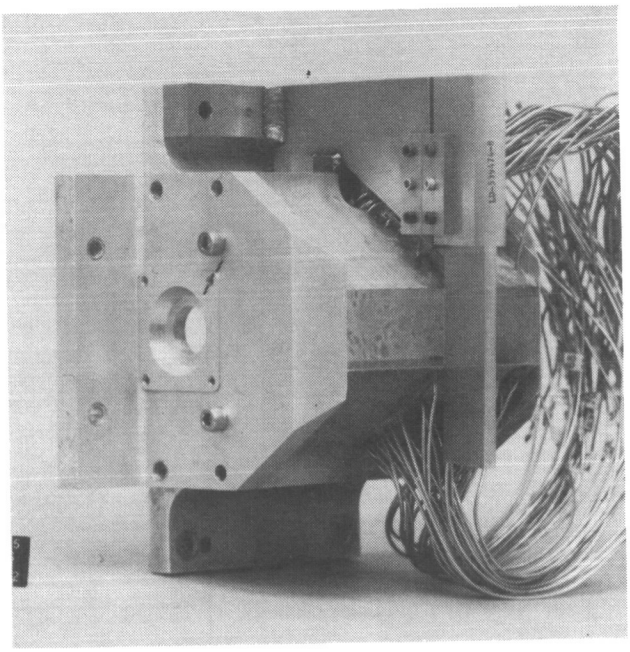

Configuration P1-R4

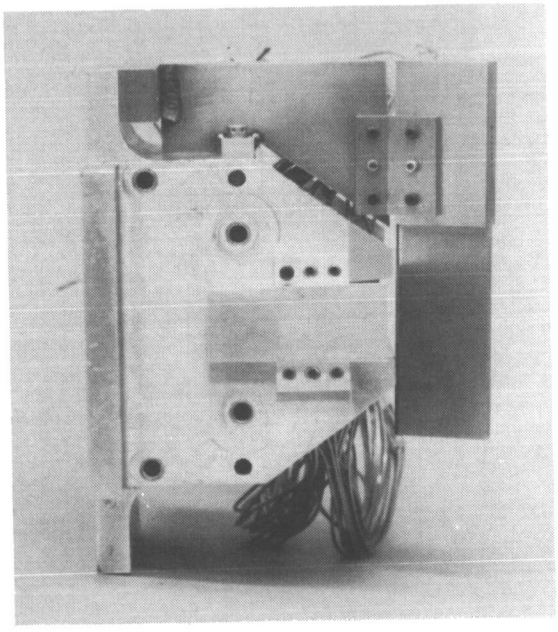

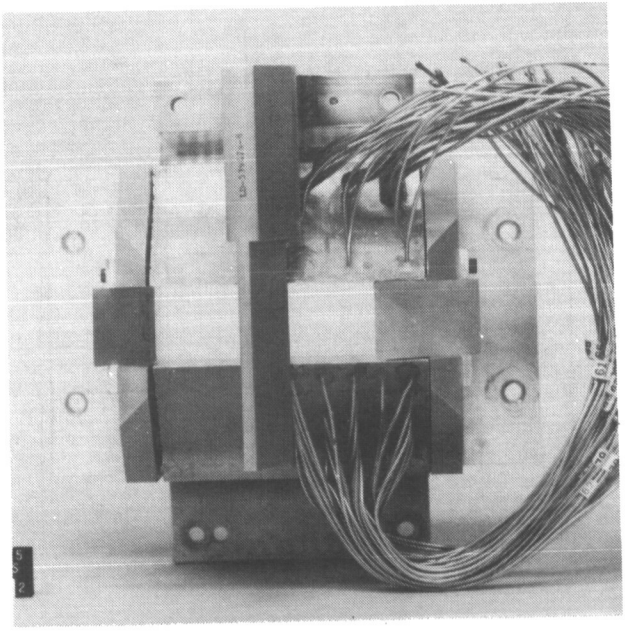

Configuration F6-R4

L-85-26

Figure 11. Photographs of nonaxisymmetric convergent-divergent nozzle configurations with combination yaw vectoring concepts.

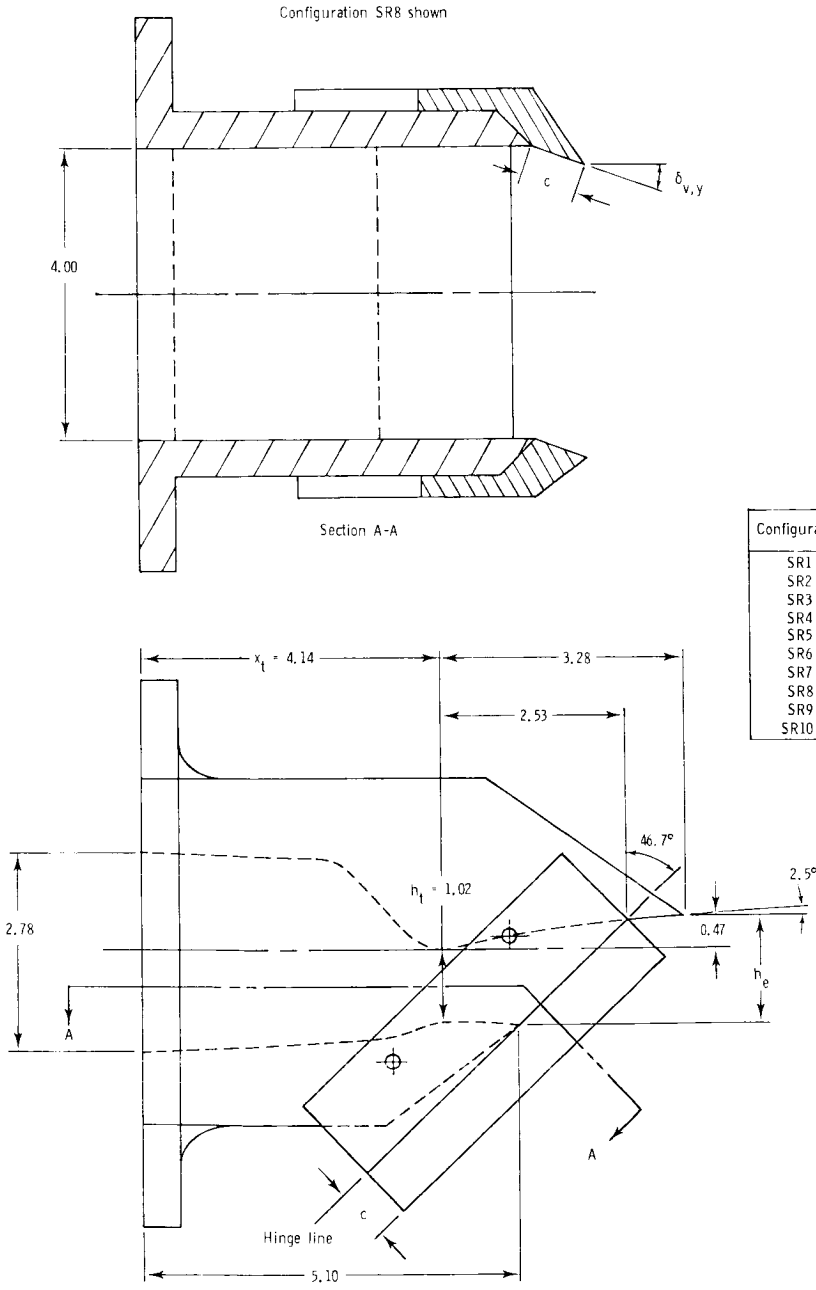

Note: Flap angle in axial or stream direction for $\delta_{v,y}$ = 20° is 14°.

Configuration	A_t, in.^{2}	h_e, in.	$(A_e/A_t)_i$	$(A_e/A_t)_e$	AR	c, in.	$\delta_{v,y}$, deg
SR1	4.07	1.43	1.10	1.41	3.92	Off	Off
SR2	↓	↓	↓	↓	↓	0.75	0
SR3	↓	↓	↓	↓	↓	↓	20
SR4	↓	↓	↓	↓	↓	1.50	0
SR5	↓	↓	↓	↓	↓	↓	20
SR6	↓	1.53	1.24	1.50	↓	Off	Off
SR7	↓	↓	↓	↓	↓	0.75	0
SR8	↓	↓	↓	↓	↓	↓	20
SR9	↓	↓	↓	↓	↓	1.50	0
SR10	↓	↓	↓	↓	↓	↓	20

(a) $\delta_{v,p} = 0°$ configurations.

Figure 12. Sketches of nonaxisymmetric single expansion ramp nozzle configurations with post-exit flaps yaw vectoring concept. Linear dimensions are in inches.

Configuration SR13 shown

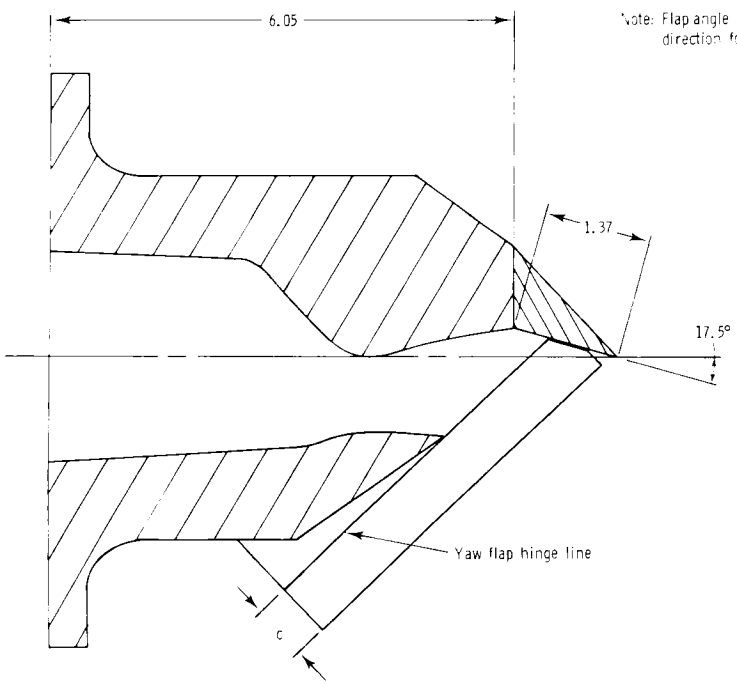

Note: Flap angle in axial or stream direction for $\delta_{v,p}$ = 20° is 14°.

Configuration SR18 shown

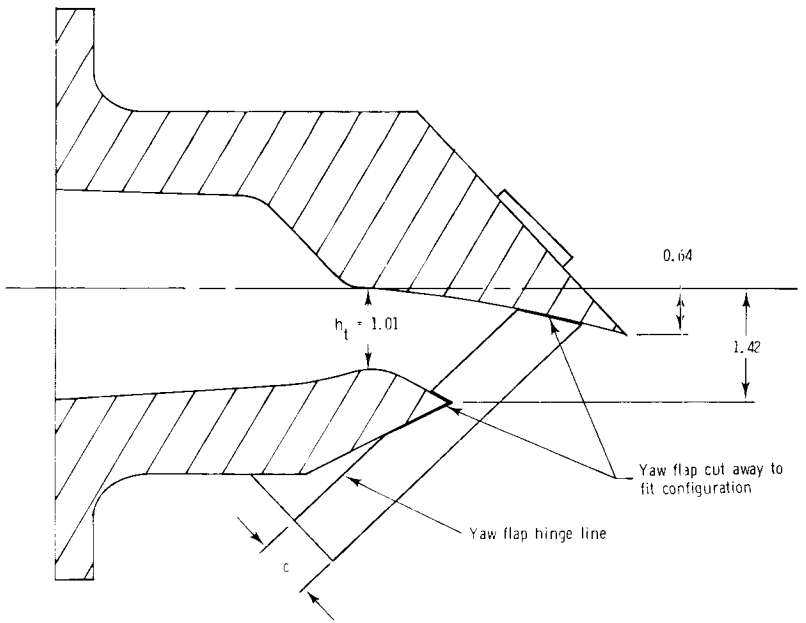

Note: Geometry of pitch-vectored configurations ($\delta_{v,p}$ = 20°) is identical to configurations SR6 to SR10 except as noted.

Configuration	A_t, in.^{2}	$\delta_{v,p}$, deg	c, in.	$\delta_{v,y}$, deg
SR11	4.08	20	Off	Off
SR12			0.75	0
SR13				20
SR14			1.50	0
SR15				20

Configuration	A_t, in.^{2}	$\delta_{v,p}$, deg	c, in.	$\delta_{v,y}$, deg
SR16	4.03	20	Off	Off
SR17			0.75	0
SR18				20

(b) $\delta_{v,p} = 20°$ configurations.

Figure 12. Concluded.

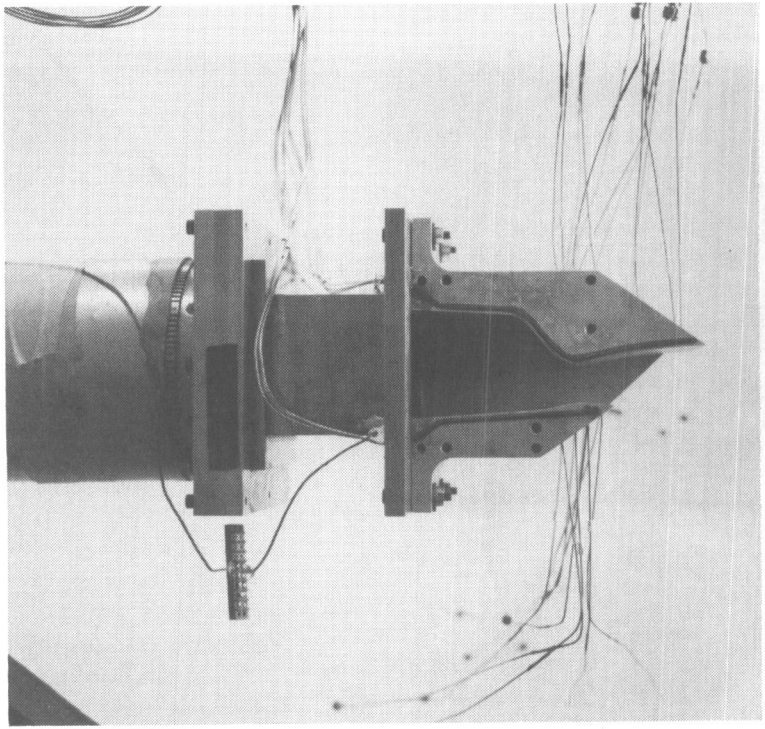

Configuration SR6

Installed on test rig with sidewall removed

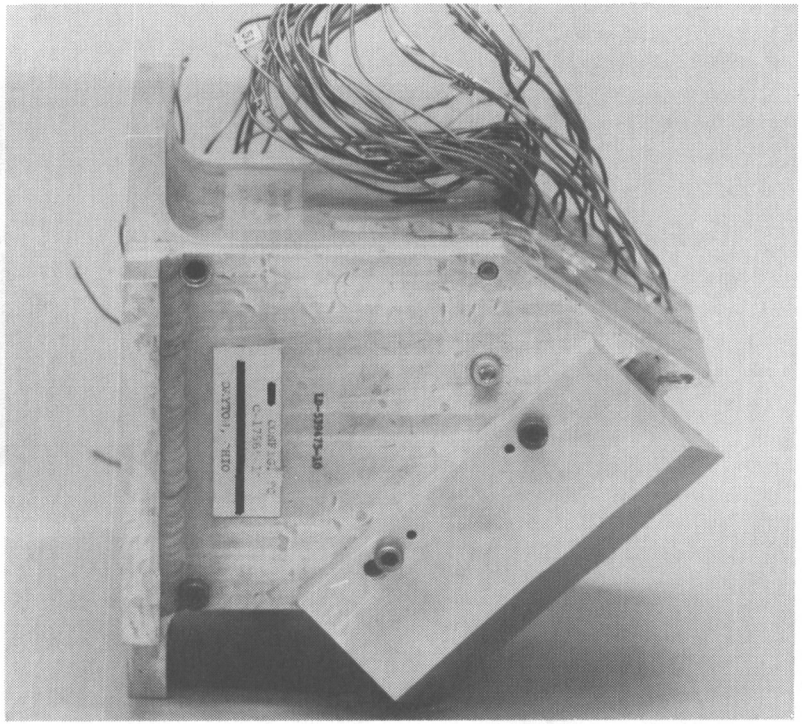

Configuration SR8

Sidewall and yaw vector flaps installed

L-85-27

(a) Configurations SR6 and SR8.

Figure 13. Photographs of nonaxisymmetric single expansion ramp nozzle configurations.

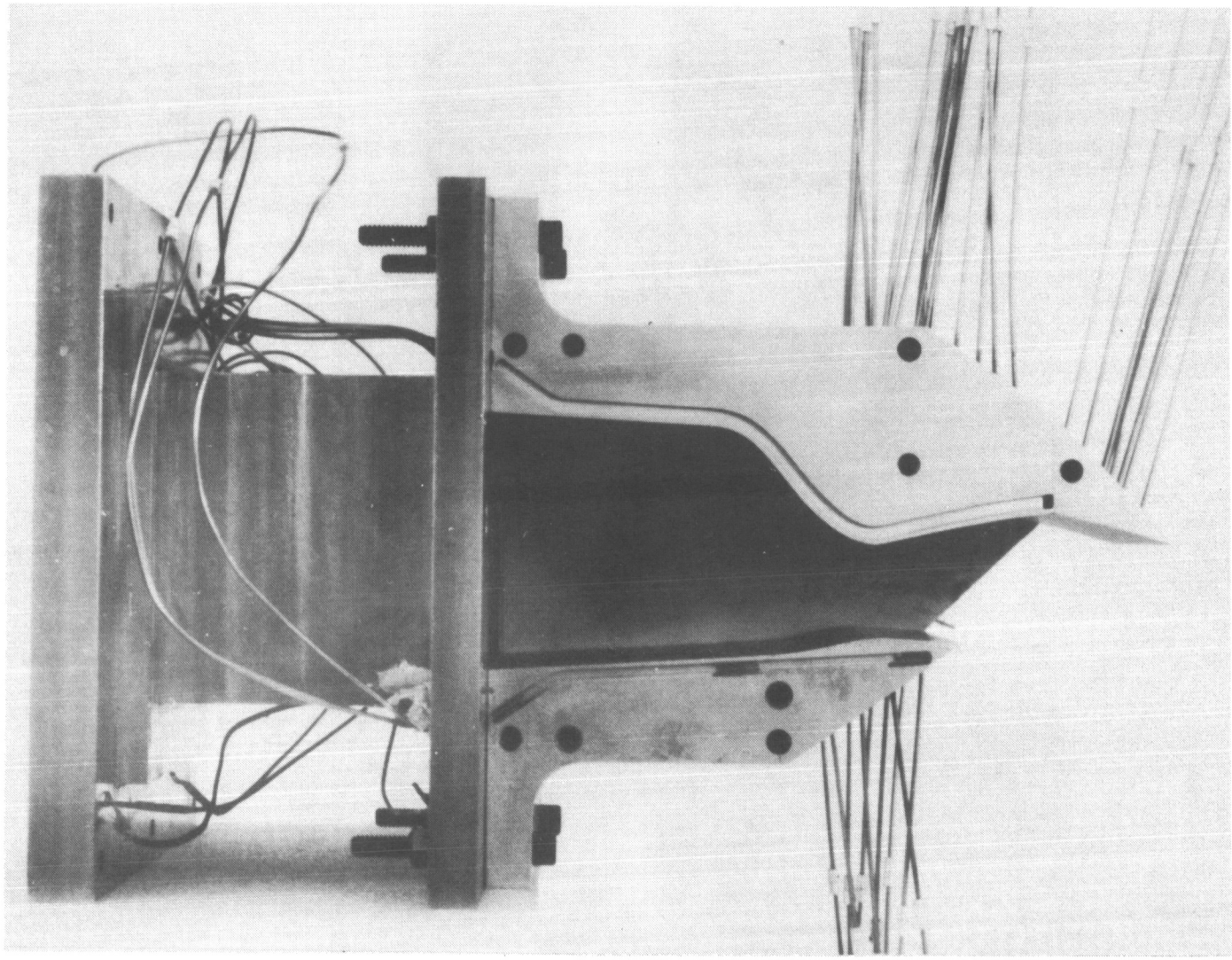

$\delta_{v,p} = 20^{0}$; post-exit flaps off

L-82-514

(b) Configuration SR11.

Figure 13. Concluded.

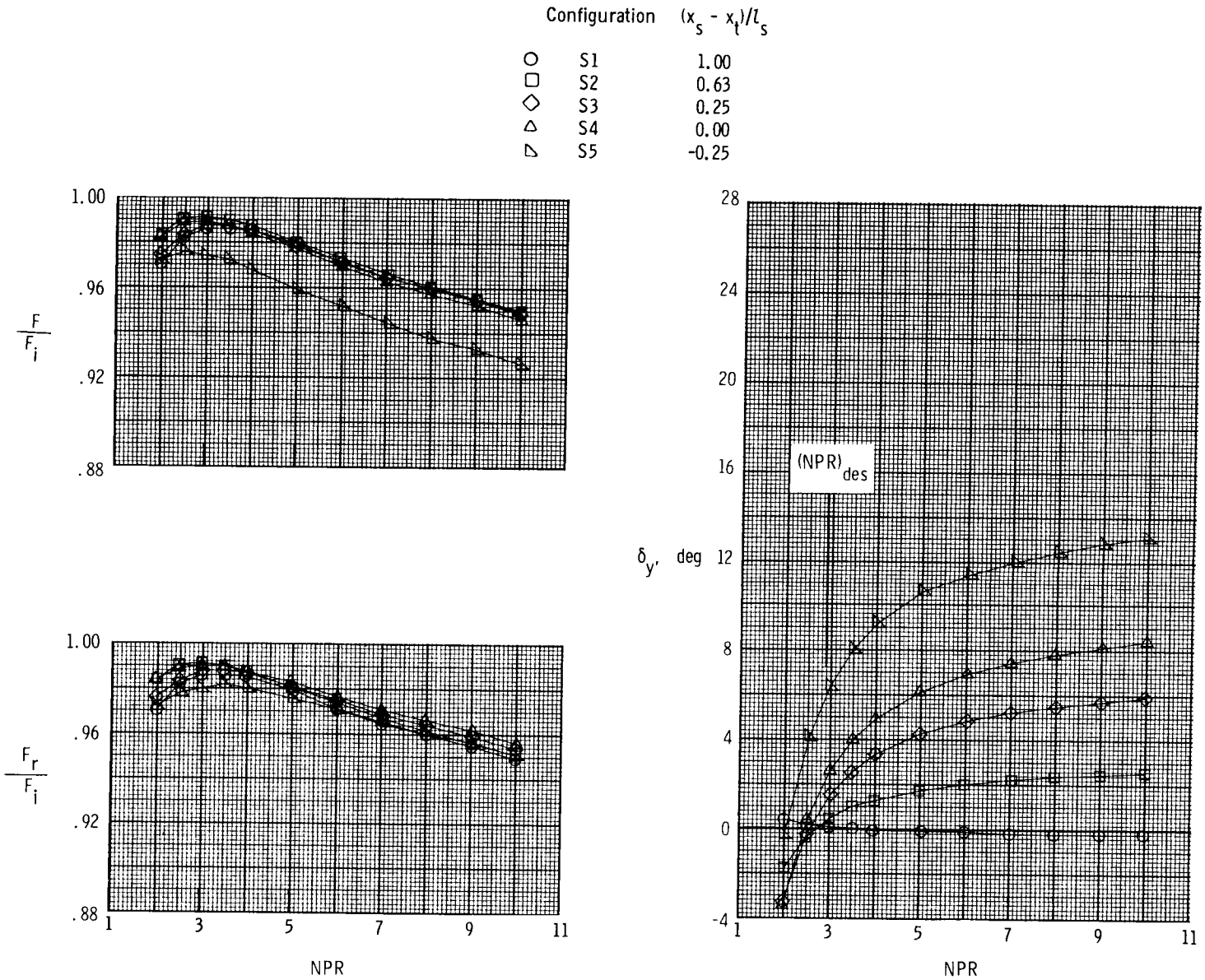

(a) Dry power nozzle, baseline $A_e/A_t = 1.08$ and $\delta_{v,p} = 0°$.

Figure 14. Effect of yaw vectoring on nozzle thrust ratio, resultant thrust ratio, and resultant yaw vector angle for 2-D C-D nozzle configurations with translating sidewall yaw vectoring concept.

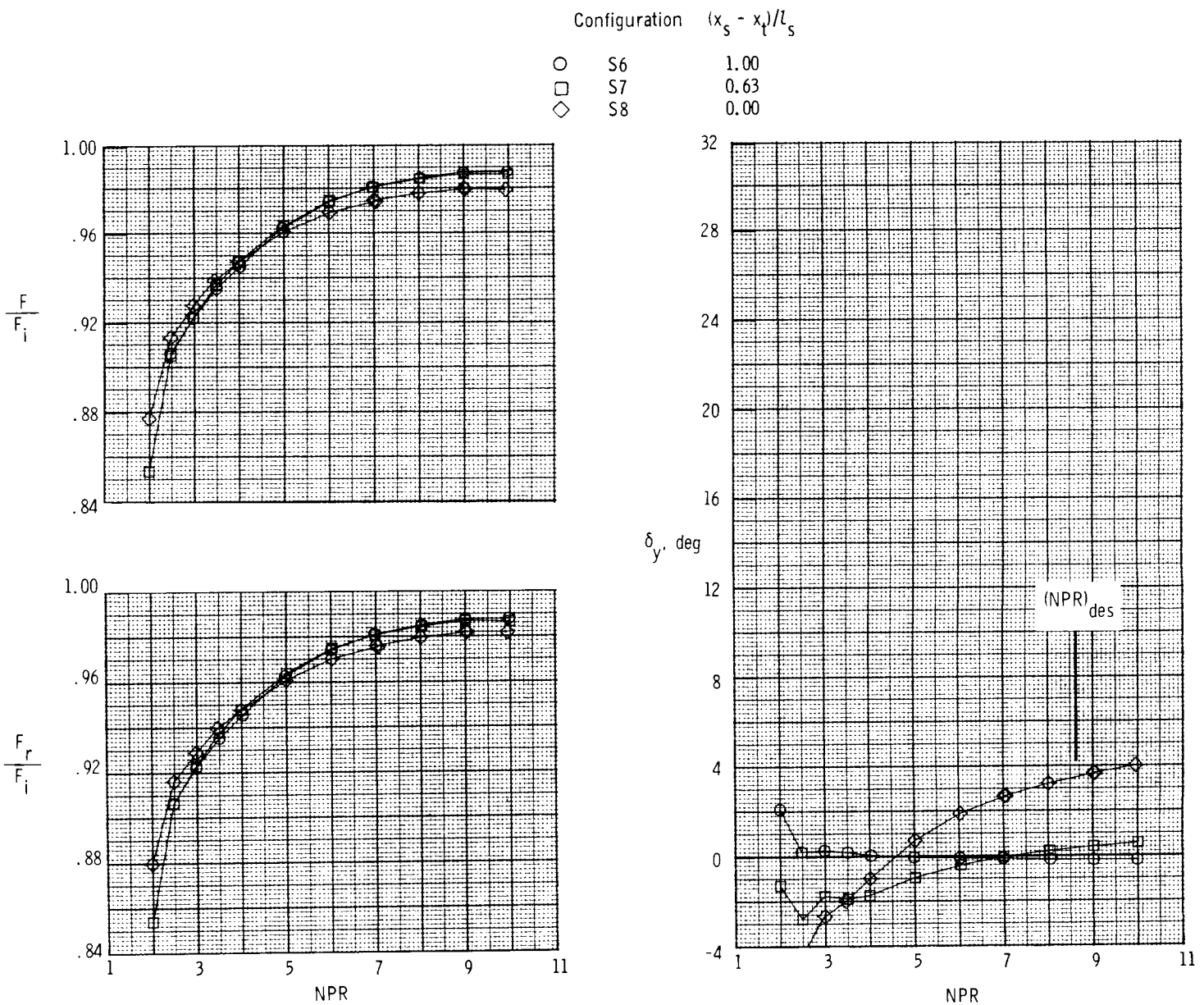

(b) Dry power nozzle, baseline $A_e/A_t = 1.78$ and $\delta_{v,p} = 0°$.

Figure 14. Continued.

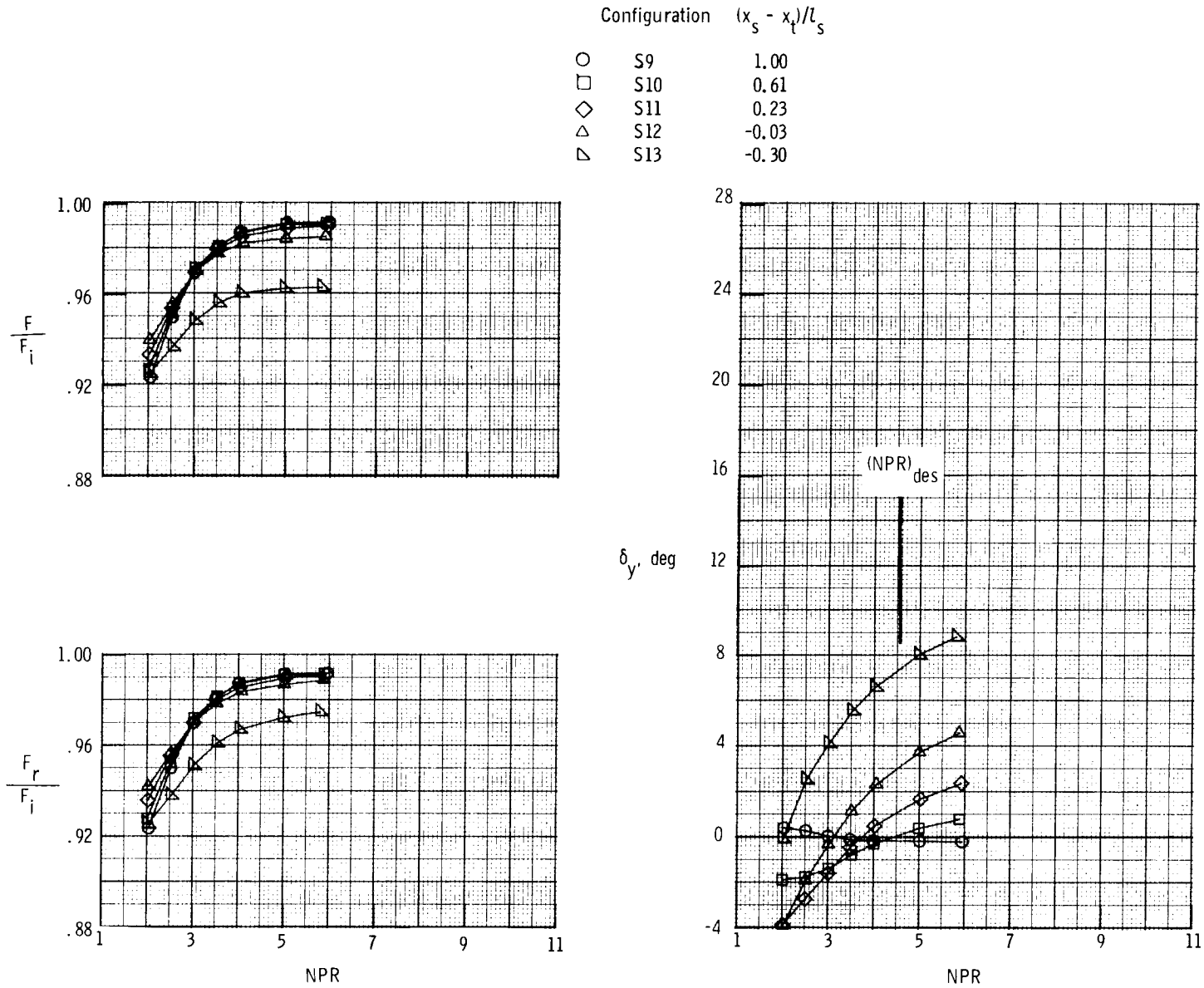

(c) A/B power nozzle, baseline $A_e/A_t = 1.29$ and $\delta_{v,p} = 0°$.

Figure 14. Continued.

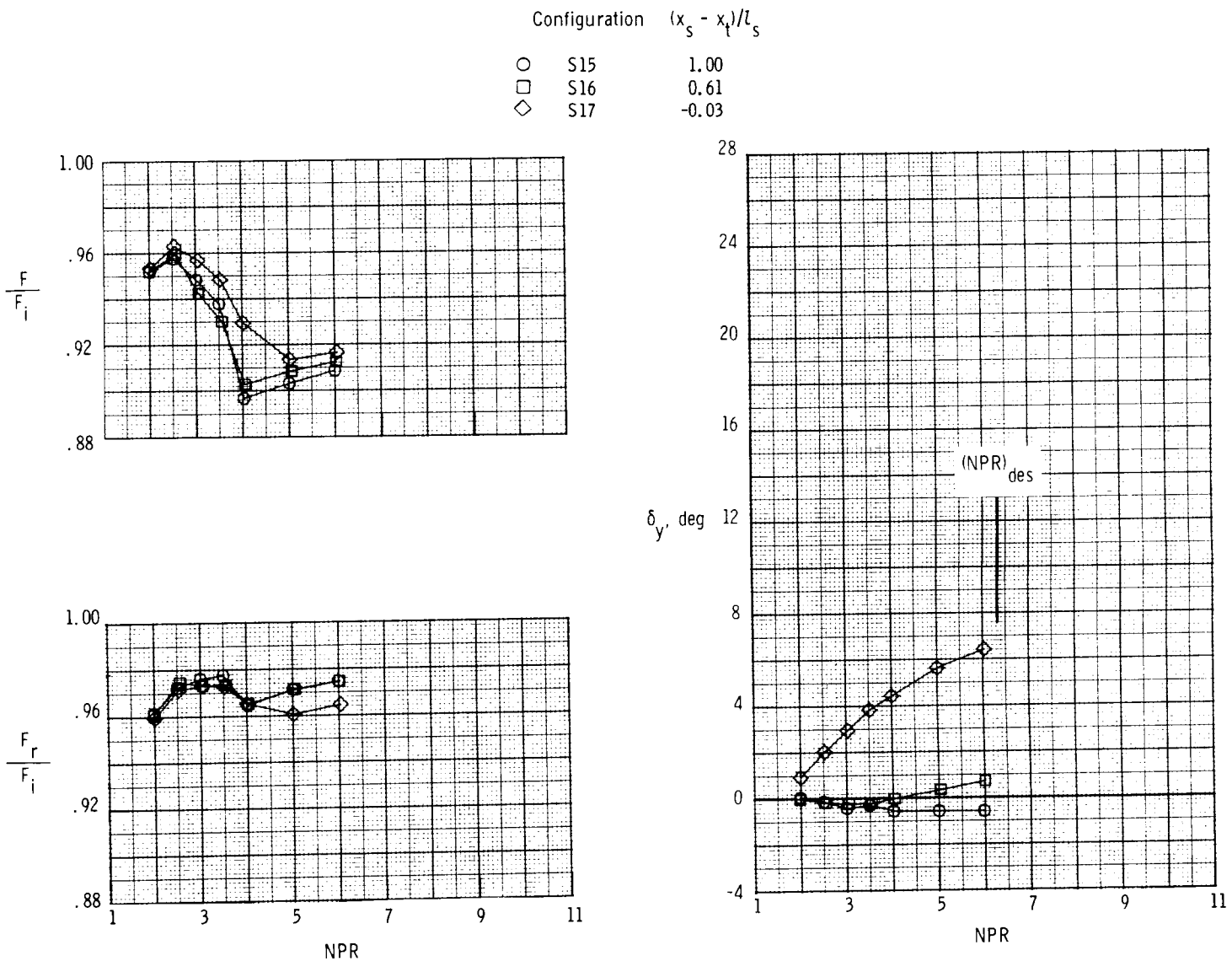

(d) A/B power nozzle, baseline $A_e/A_t = 1.51$ and $\delta_{v,p} = 20.28°$.

Figure 14. Concluded.

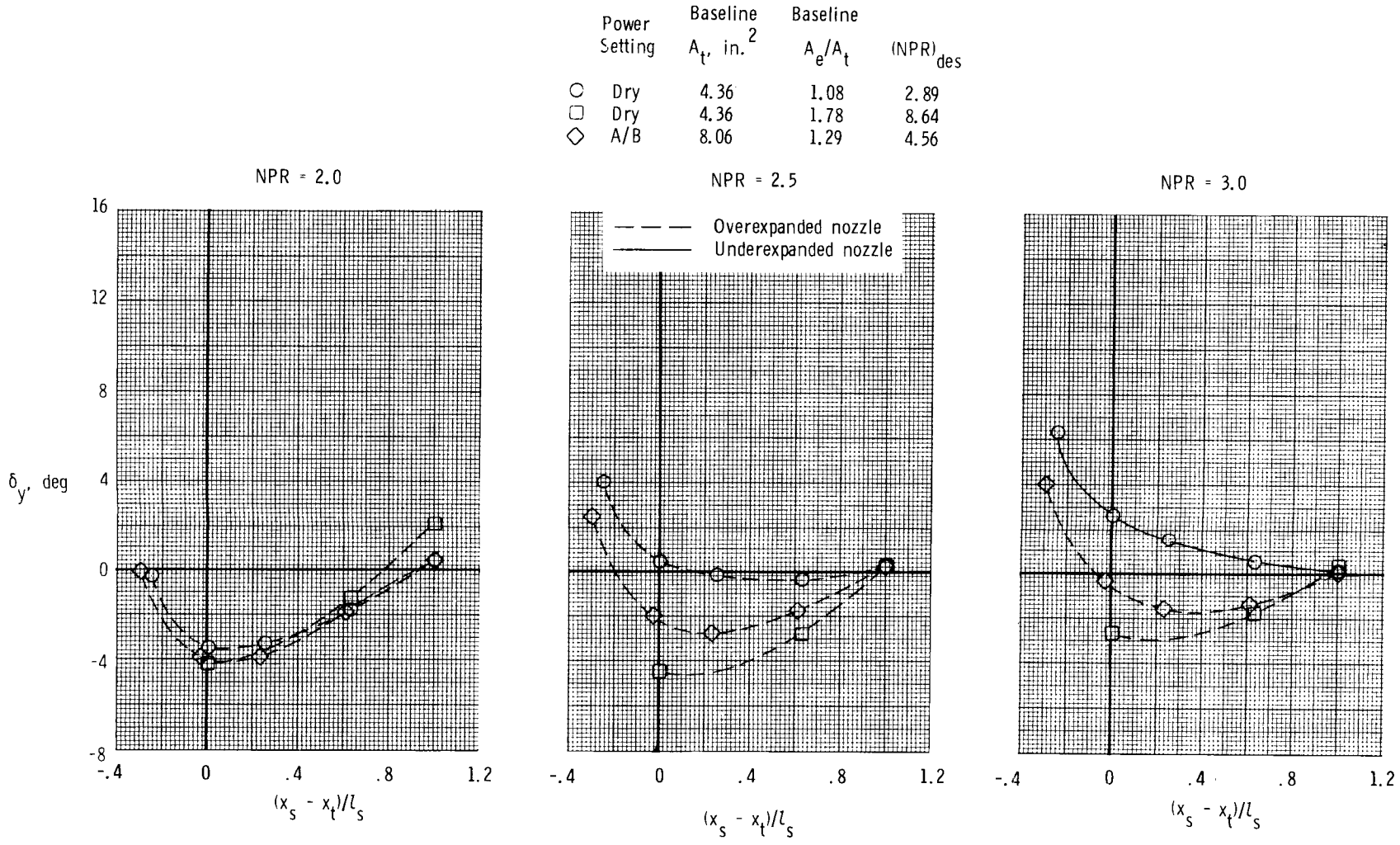

(a) NPR = 2.0, 2.5, and 3.0.

Figure 15. Summary of resultant yaw vector angle results for translating sidewall concept with $\delta_{v,p} = 0°$. Data are cross plotted; symbols are for line identification only.

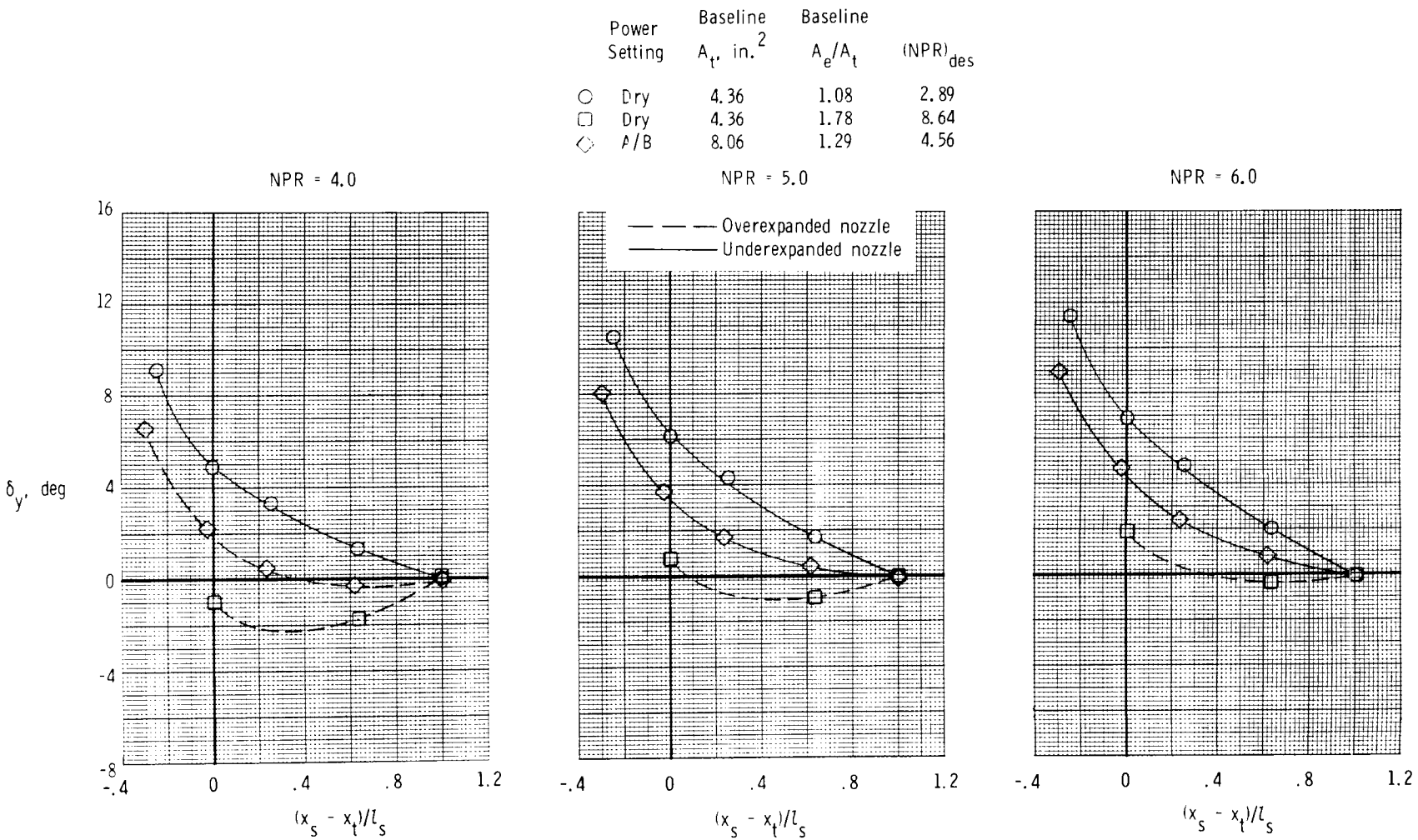

(b) NPR = 4.0, 5.0, and 6.0.

Figure 15. Continued.

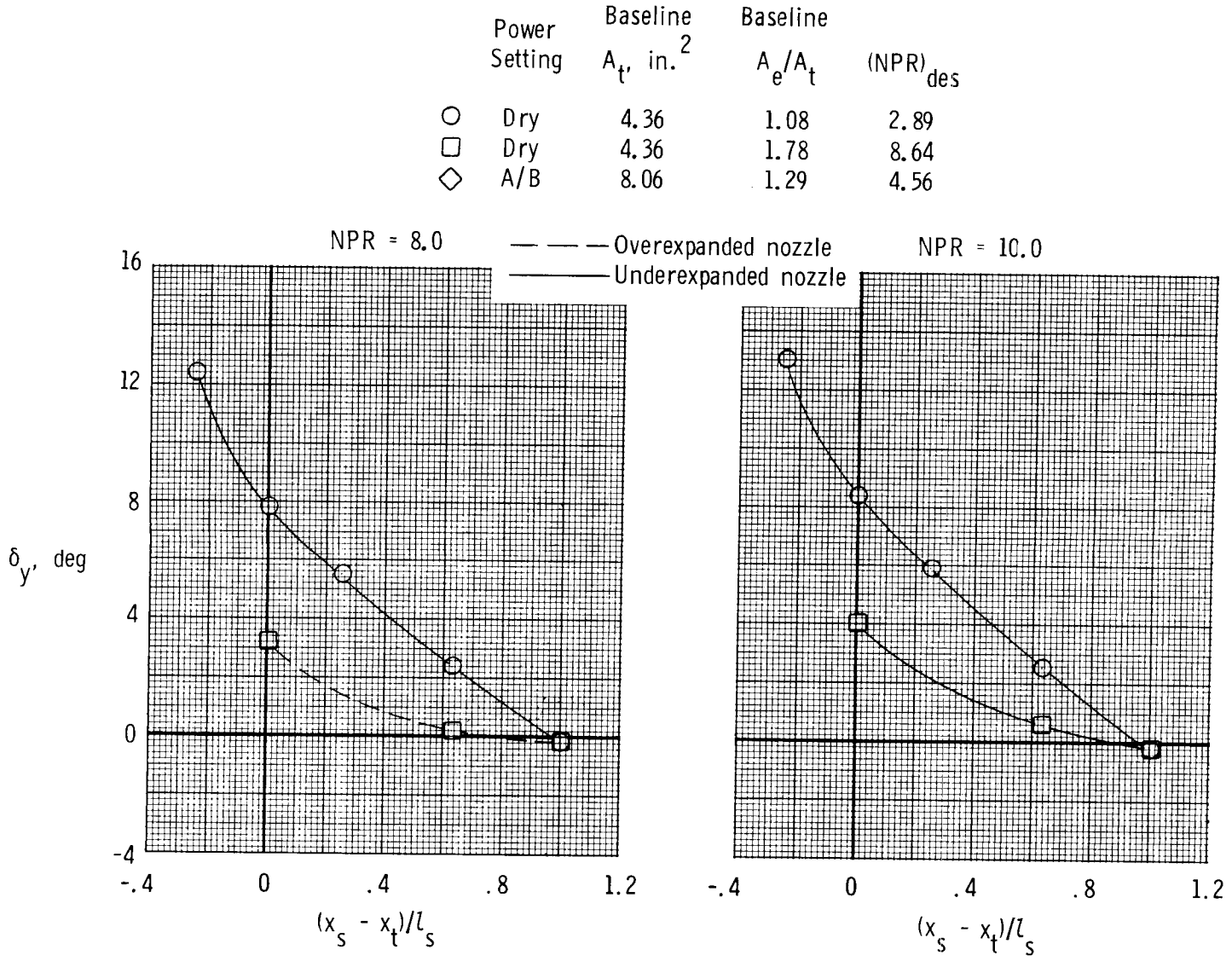

(c) NPR = 8.0 and 10.0.

Figure 15. Concluded.

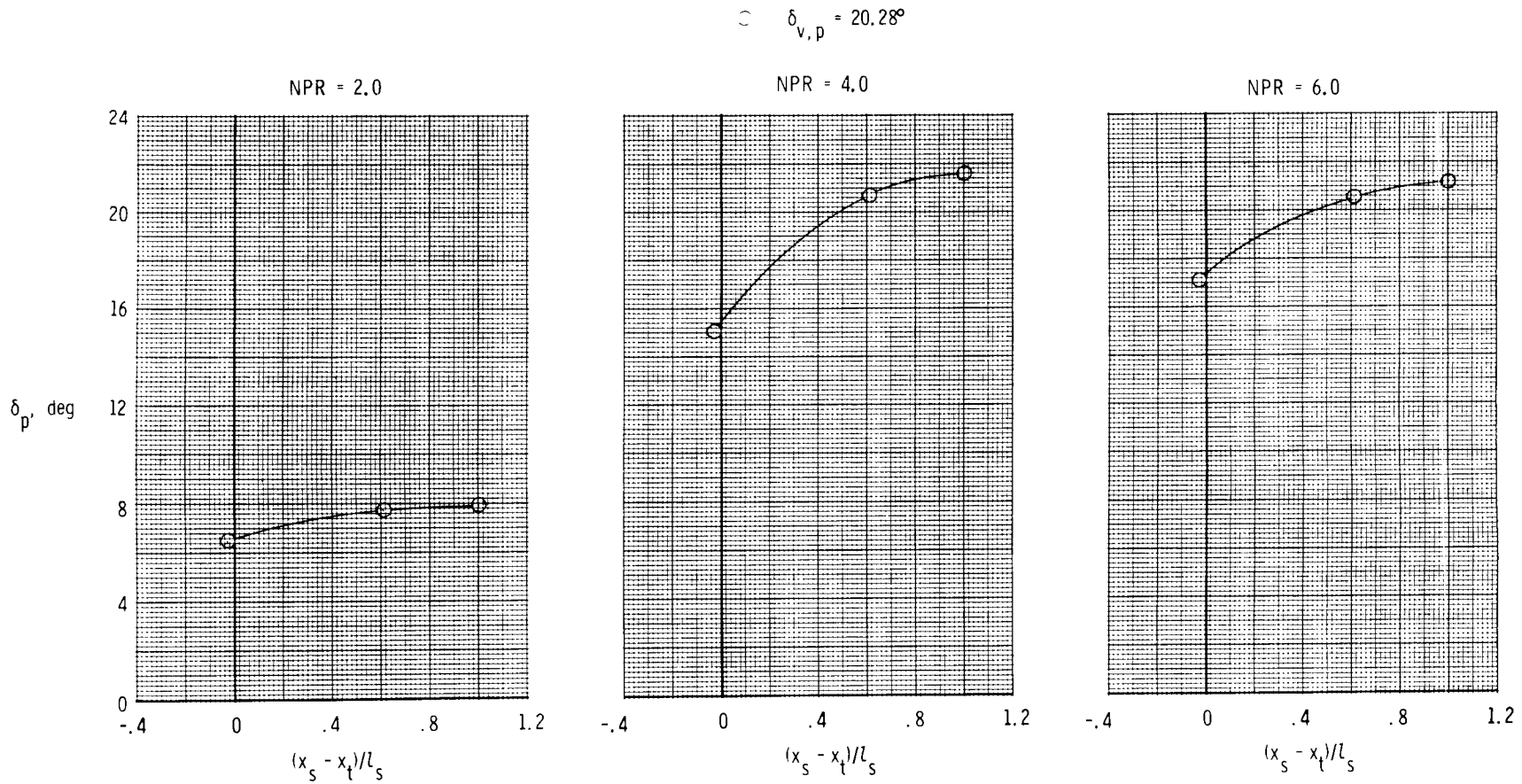

(a) Effect of yaw vectoring on resultant pitch vector angle.

Figure 16. Summary of simultaneous pitch and yaw thrust vectoring results for translating sidewall concept on A/B power 2-D C-D nozzle (baseline $A_e/A_t = 1.29$). Data are cross plotted; symbols are for line identification only.

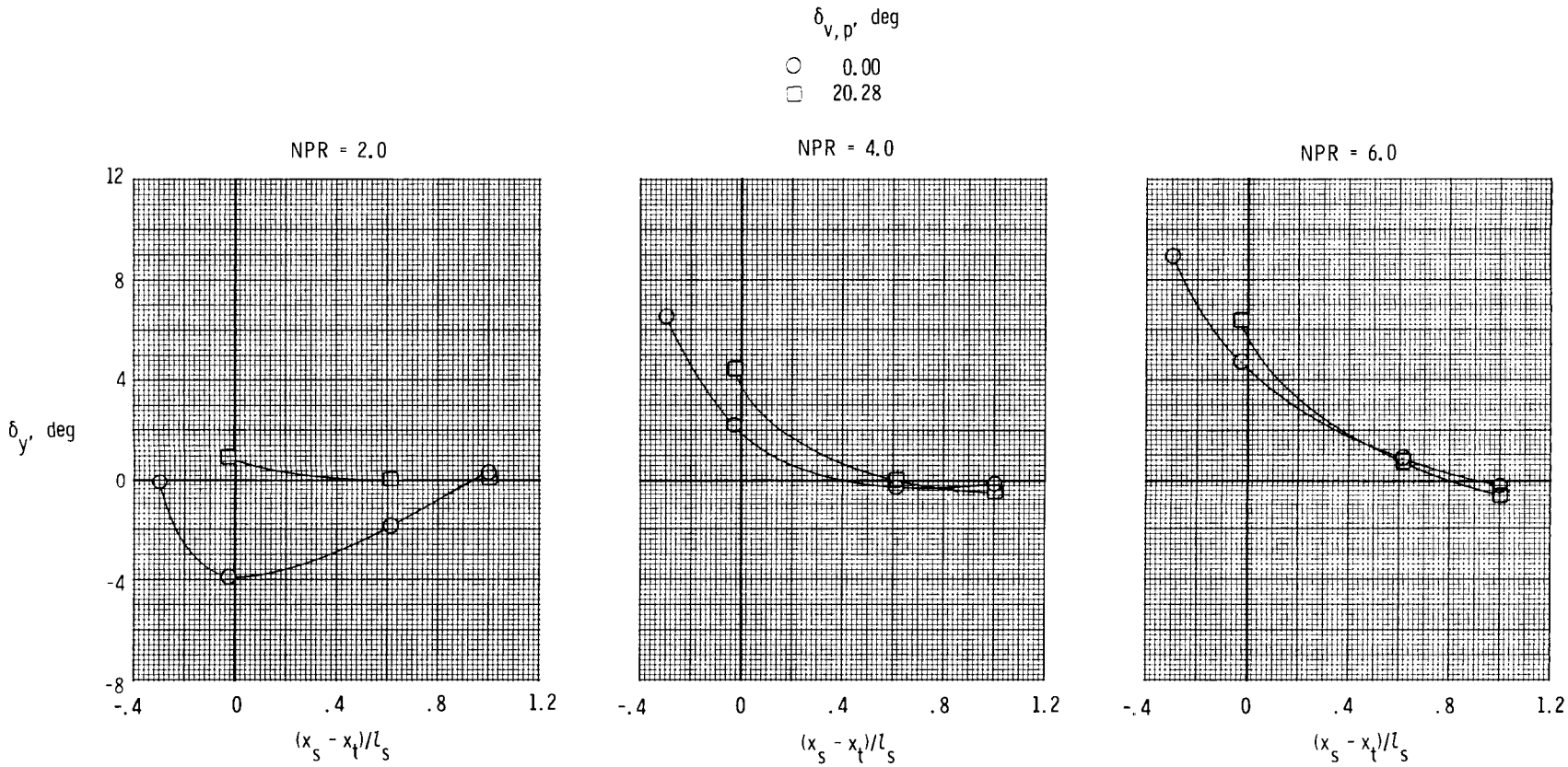

(b) Effect of pitch vectoring on resultant yaw vector angle.

Figure 16. Concluded.

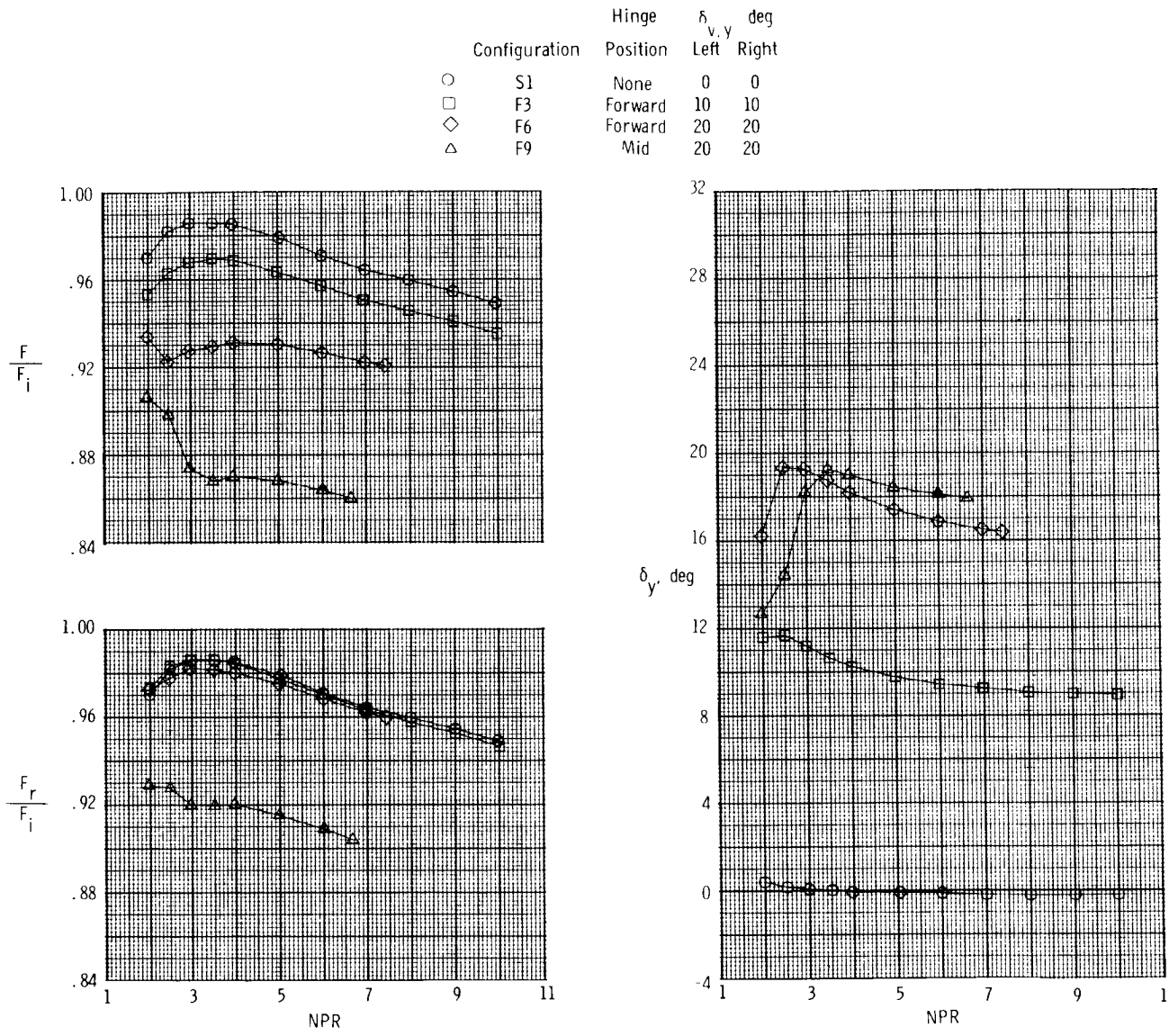

(a) Dry power nozzle; baseline $A_e/A_t = 1.08$.

Figure 17. Effect of yaw vectoring on nozzle thrust ratio, resultant thrust ratio, and resultant yaw vector angle for 2-D C-D nozzles, $\delta_{v,p} = 0°$, with left and right downstream flaps yaw vectoring concept.

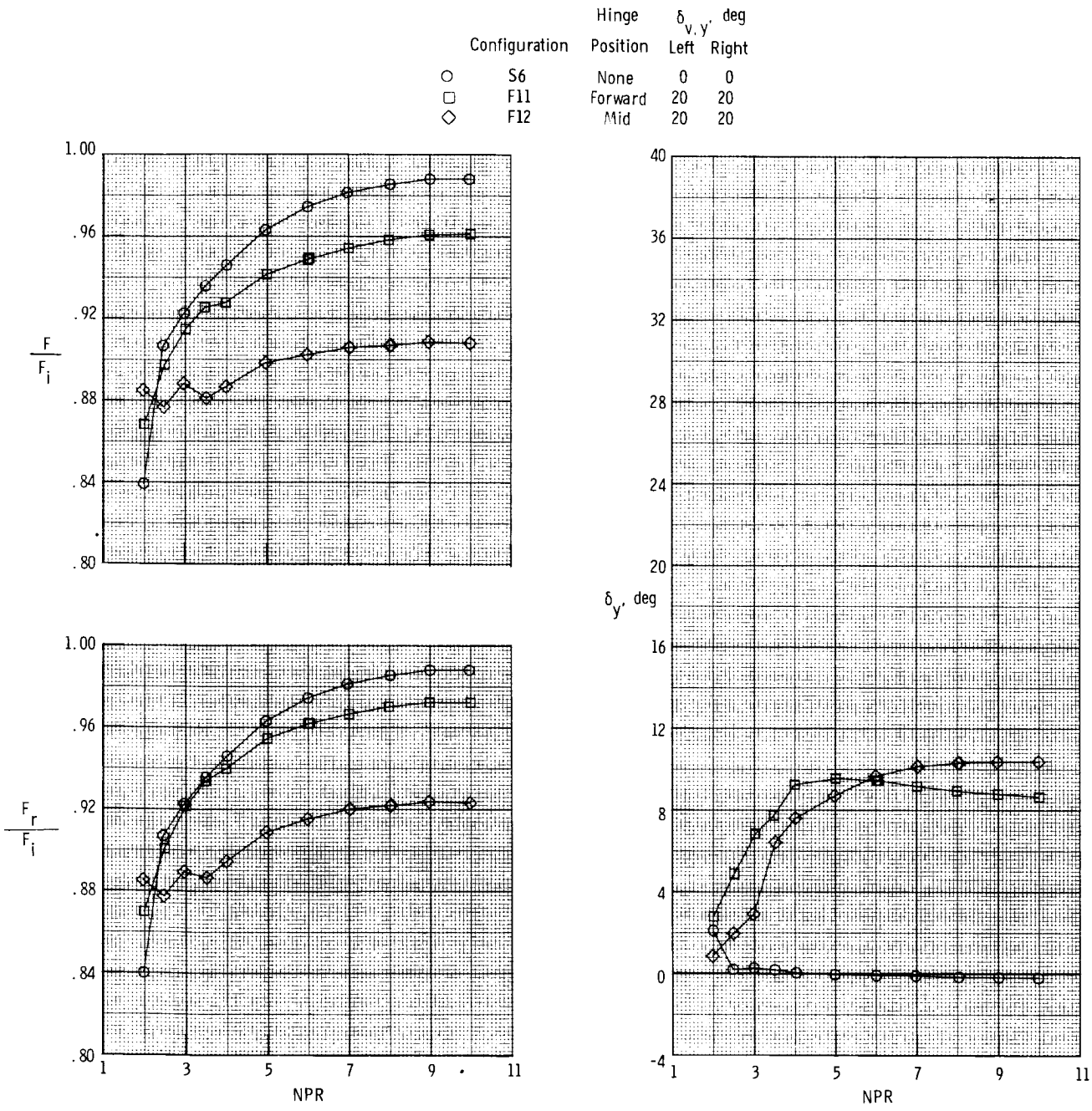

(b) Dry power nozzle, baseline $A_e/A_t = 1.78$.

Figure 17. Continued.

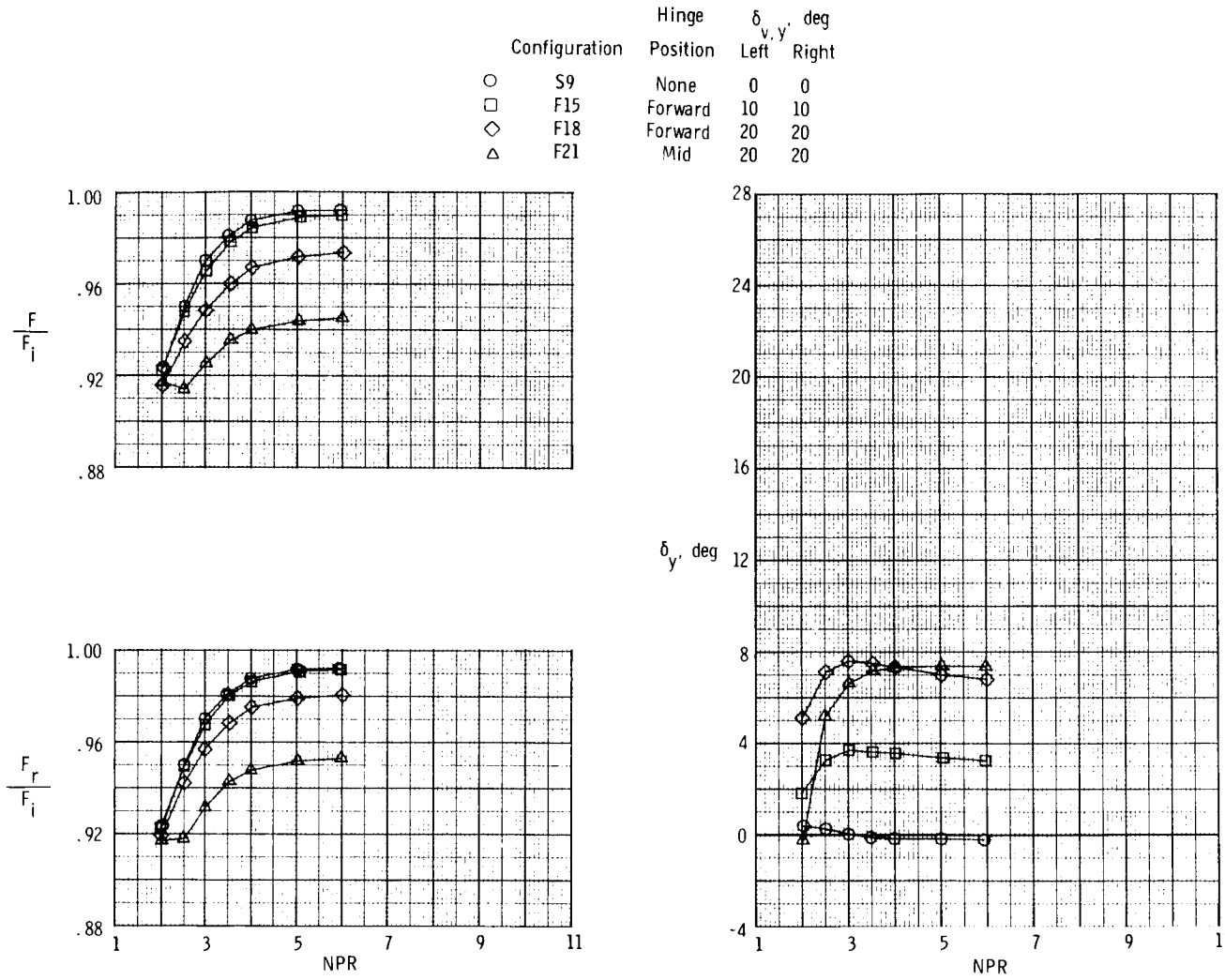

(c) A/B power nozzle, baseline $A_e/A_t = 1.29$.

Figure 17. Concluded.

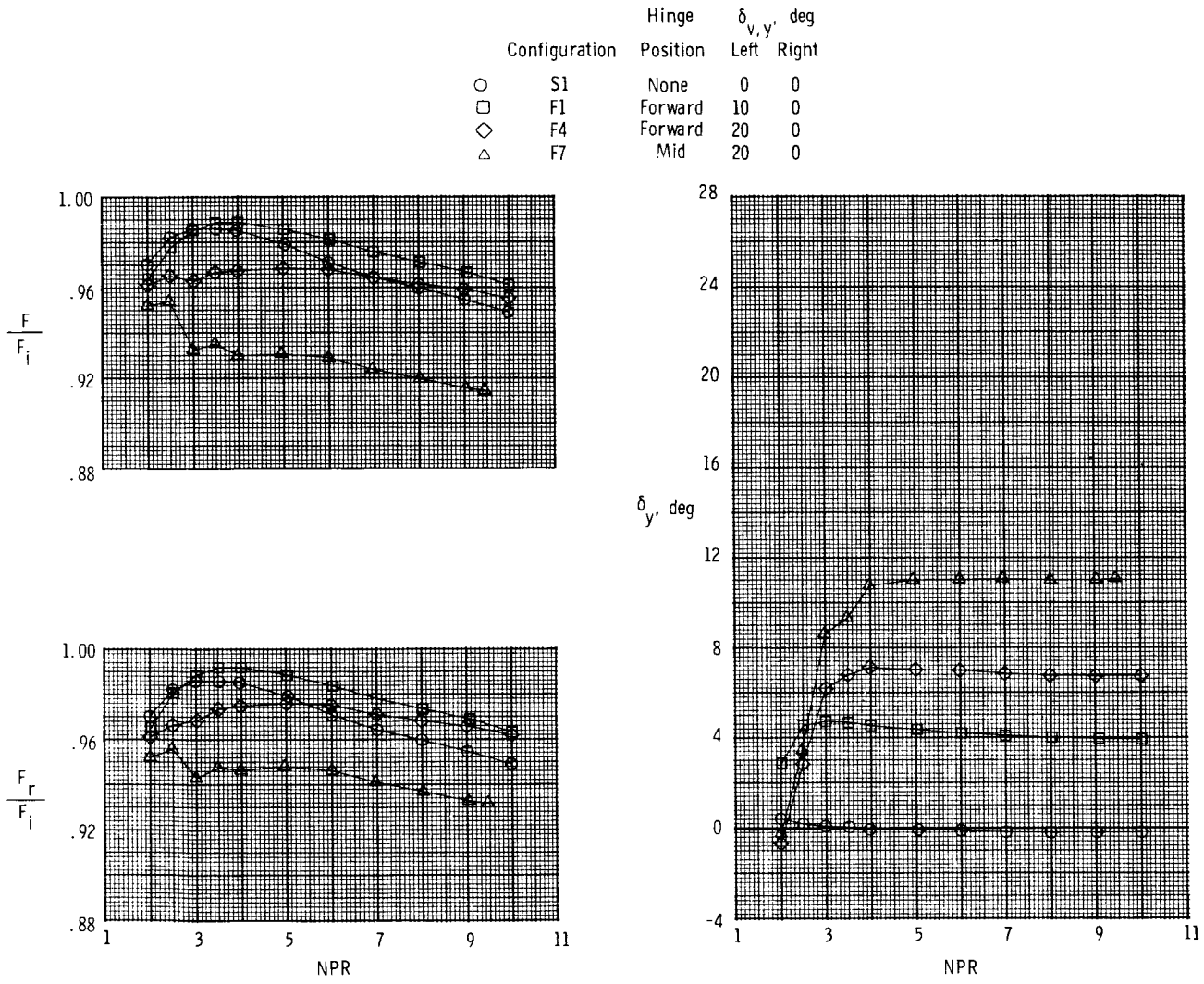

(a) Dry power nozzle, baseline $A_e/A_t = 1.08$.

Figure 18. Effect of yaw vectoring on nozzle thrust ratio, resultant thrust ratio, and resultant yaw vector angle for 2-D C-D nozzles, $\delta_{v,p} = 0°$, with left downstream flap yaw vectoring concept.

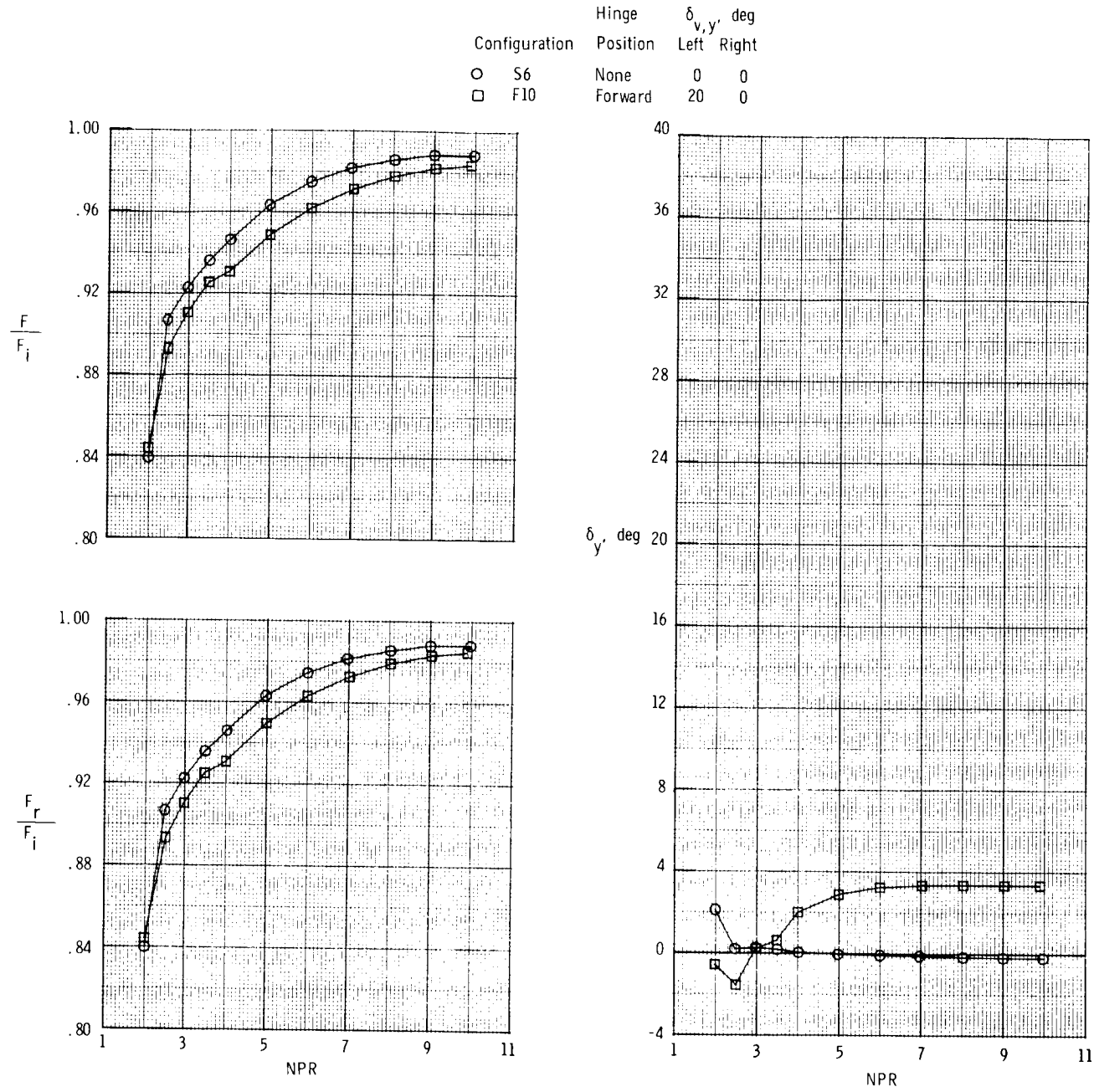

(b) Dry power nozzle, baseline $A_e/A_t = 1.78$.

Figure 18. Continued.

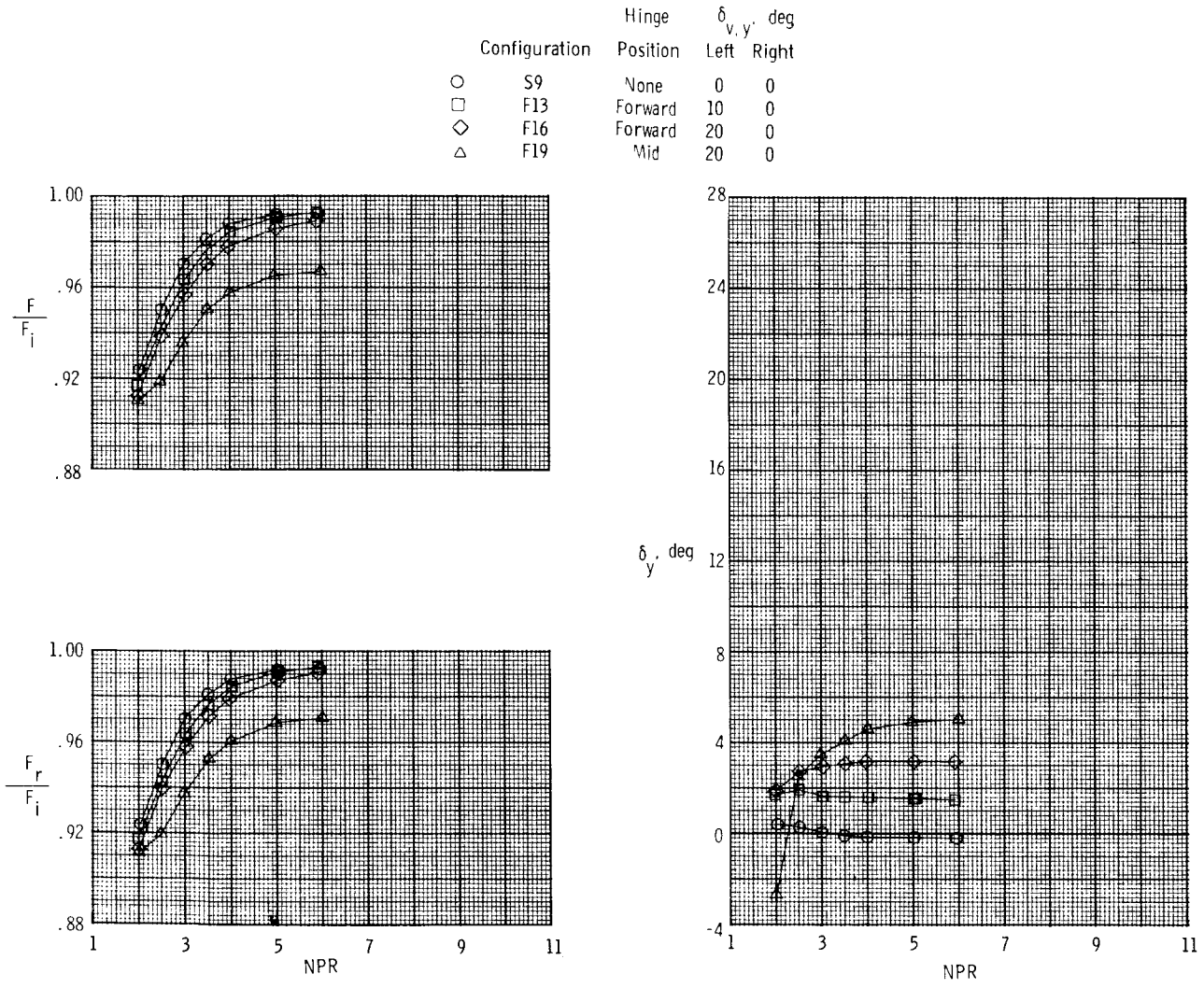

(c) A/B power nozzle, baseline $A_e/A_t = 1.29$.

Figure 18. Concluded.

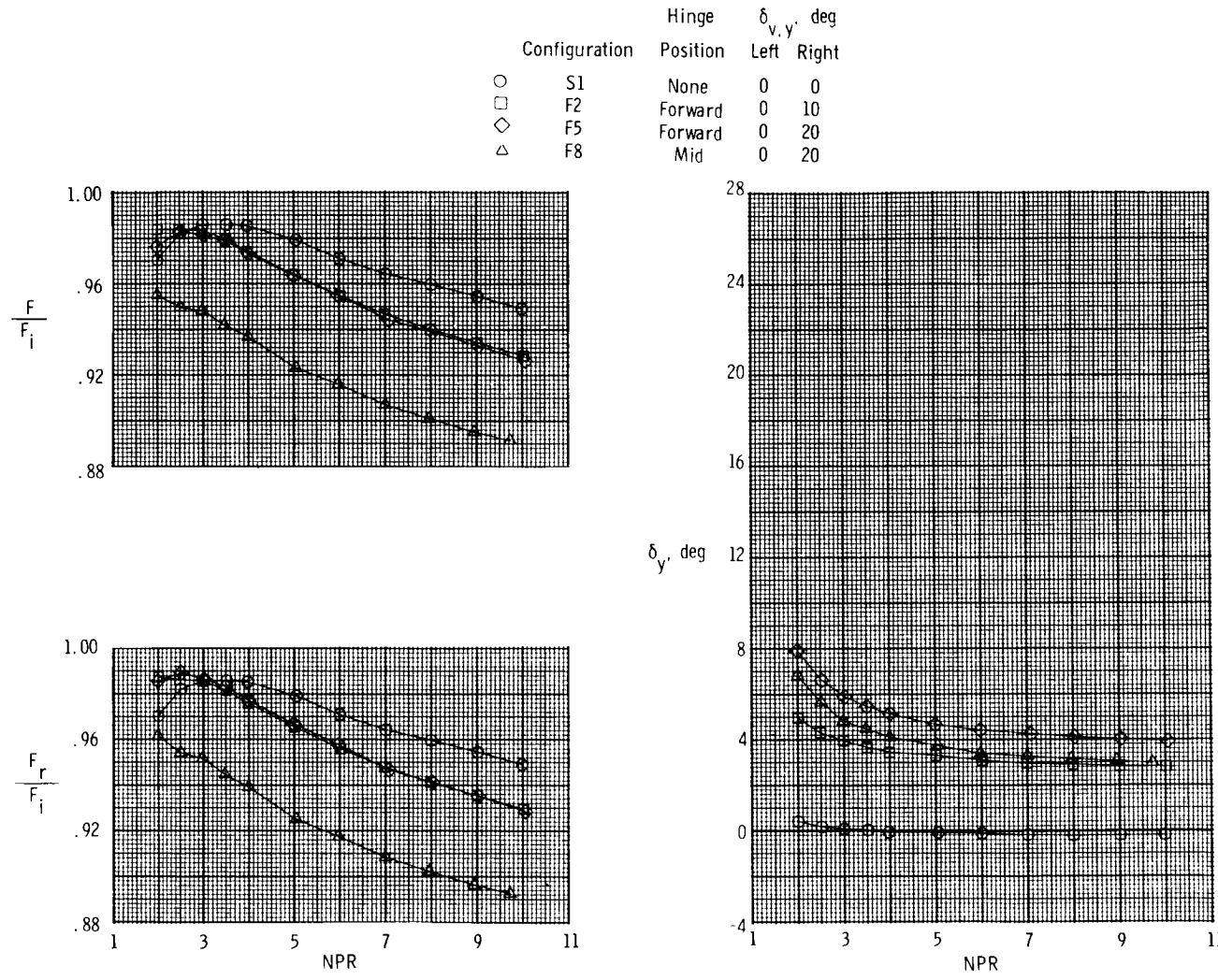

(a) Dry power nozzle, baseline $A_e/A_t = 1.08$.

Figure 19. Effect of yaw vectoring on nozzle thrust ratio, resultant thrust ratio, and resultant yaw vector angle for 2-D C-D nozzles, $\delta_{v,p} = 0°$, with right downstream flap yaw vectoring concept.

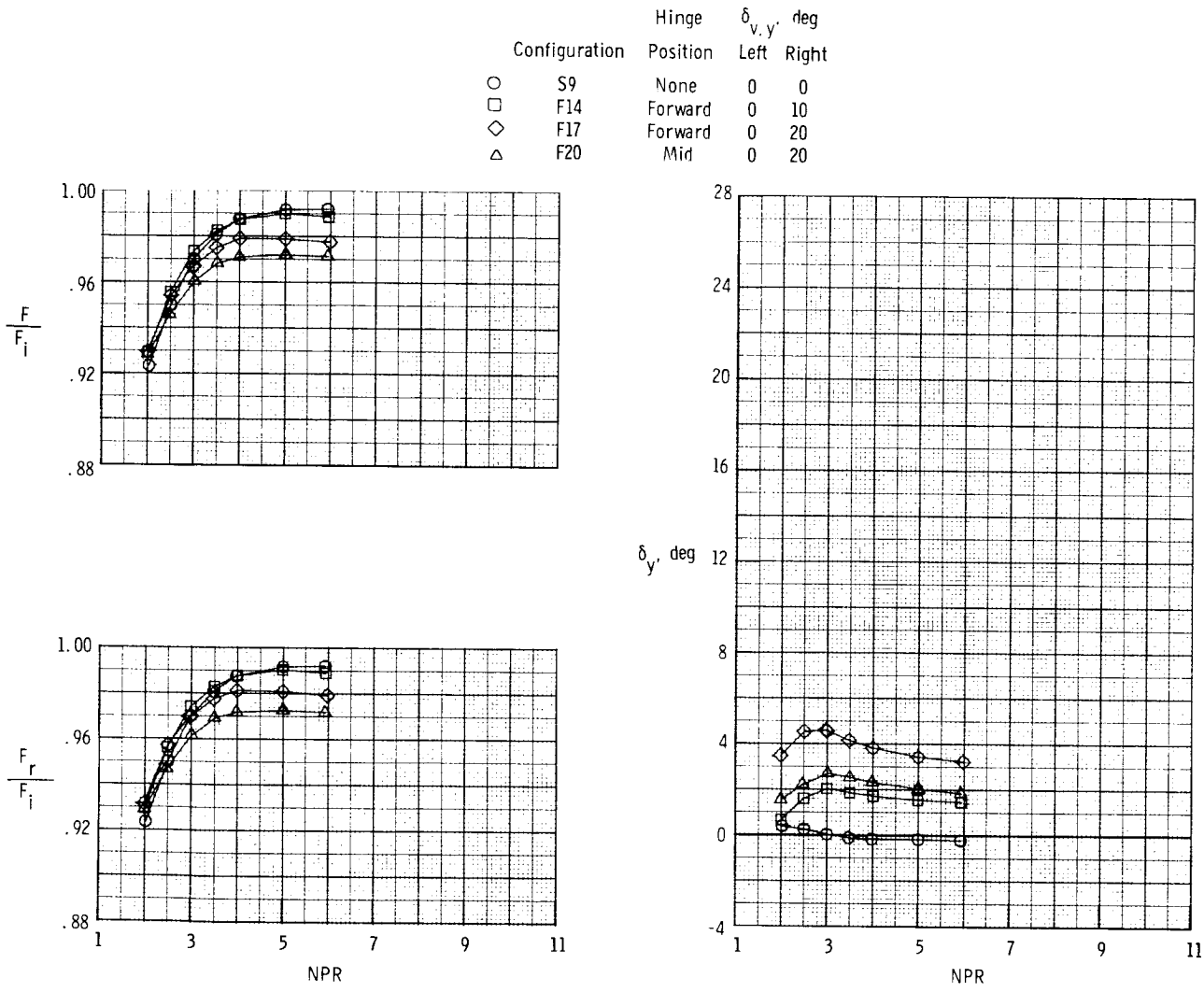

(b) A/B power nozzle, baseline $A_e/A_t = 1.29$.

Figure 19. Concluded.

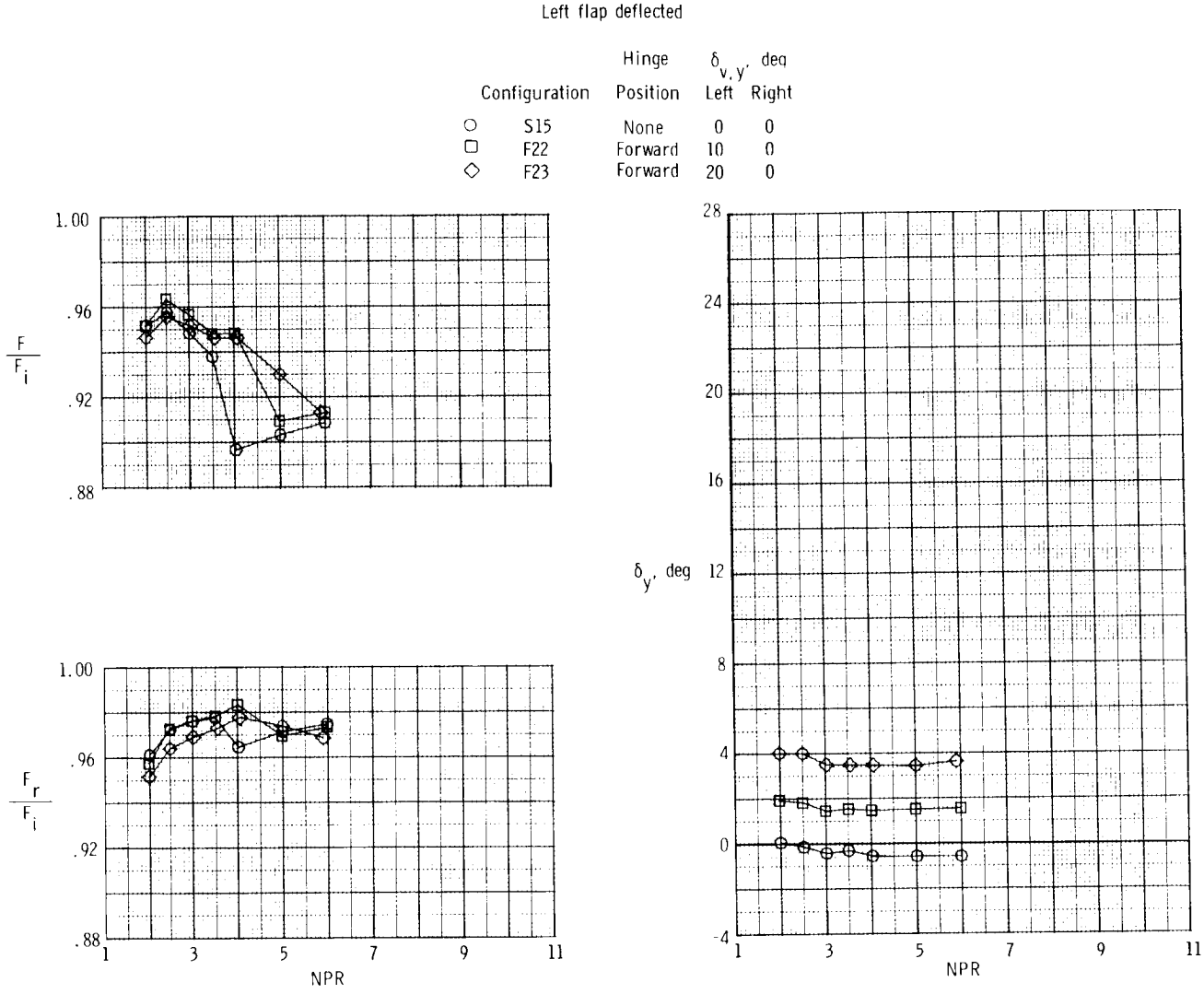

Figure 20. Effect of yaw vectoring on nozzle thrust ratio, resultant thrust ratio, and resultant yaw vector angle for 2-D C-D A/B power nozzle, $\delta_{v,p} = 20.28°$, with downstream flaps yaw vectoring concept. Left flap deflected.

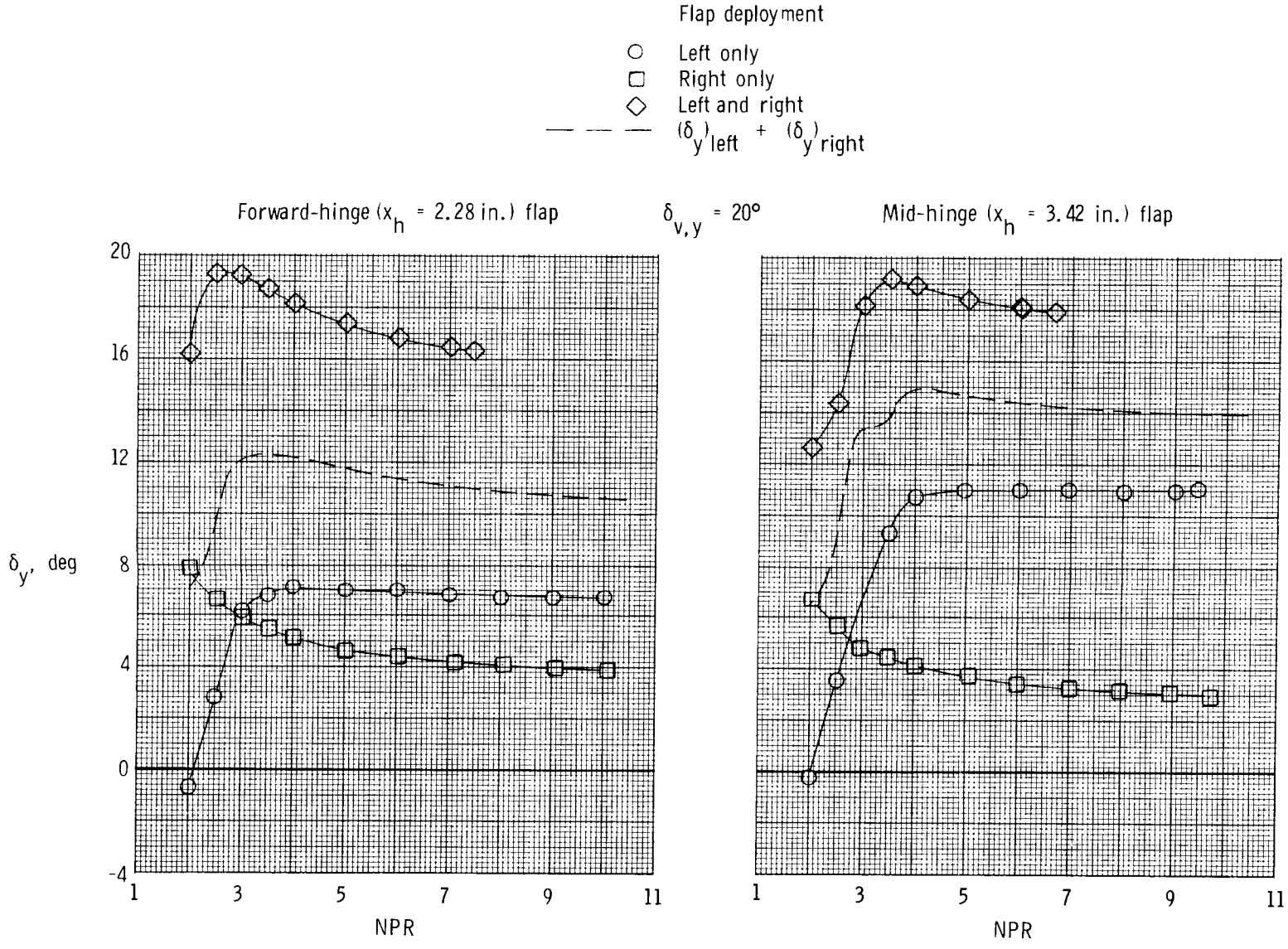

(a) Dry power nozzle, baseline $A_e/A_t = 1.08$ and $\delta_{v,p} = 0°$.

Figure 21. Comparison of resultant yaw vector angles for individual and combined downstream yaw vector flap deployments. $\delta_{v,y} = 20°$.

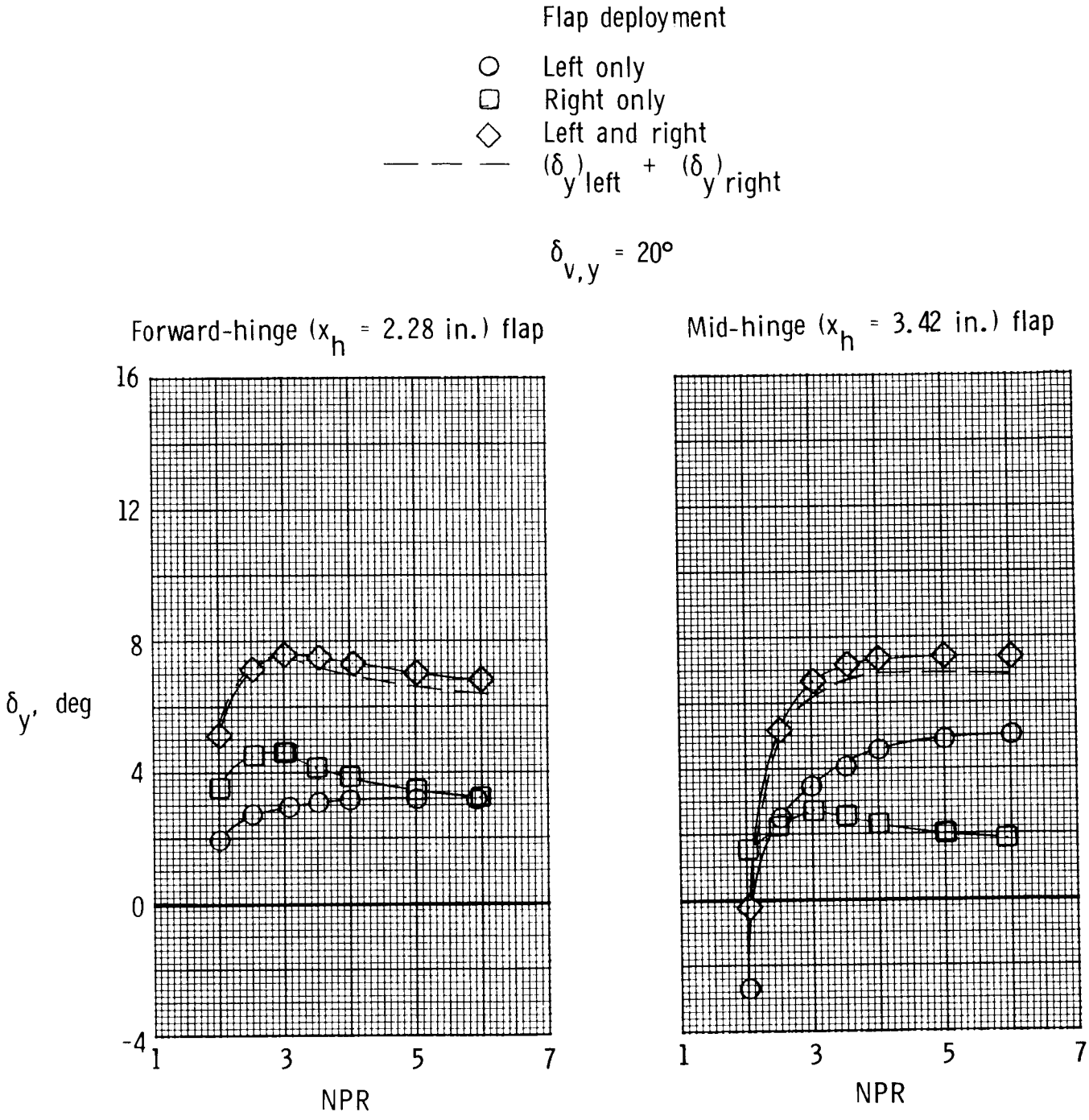

(b) A/B power nozzle, baseline $A_e/A_t = 1.29$ and $\delta_{v,p} = 0°$.

Figure 21. Concluded.

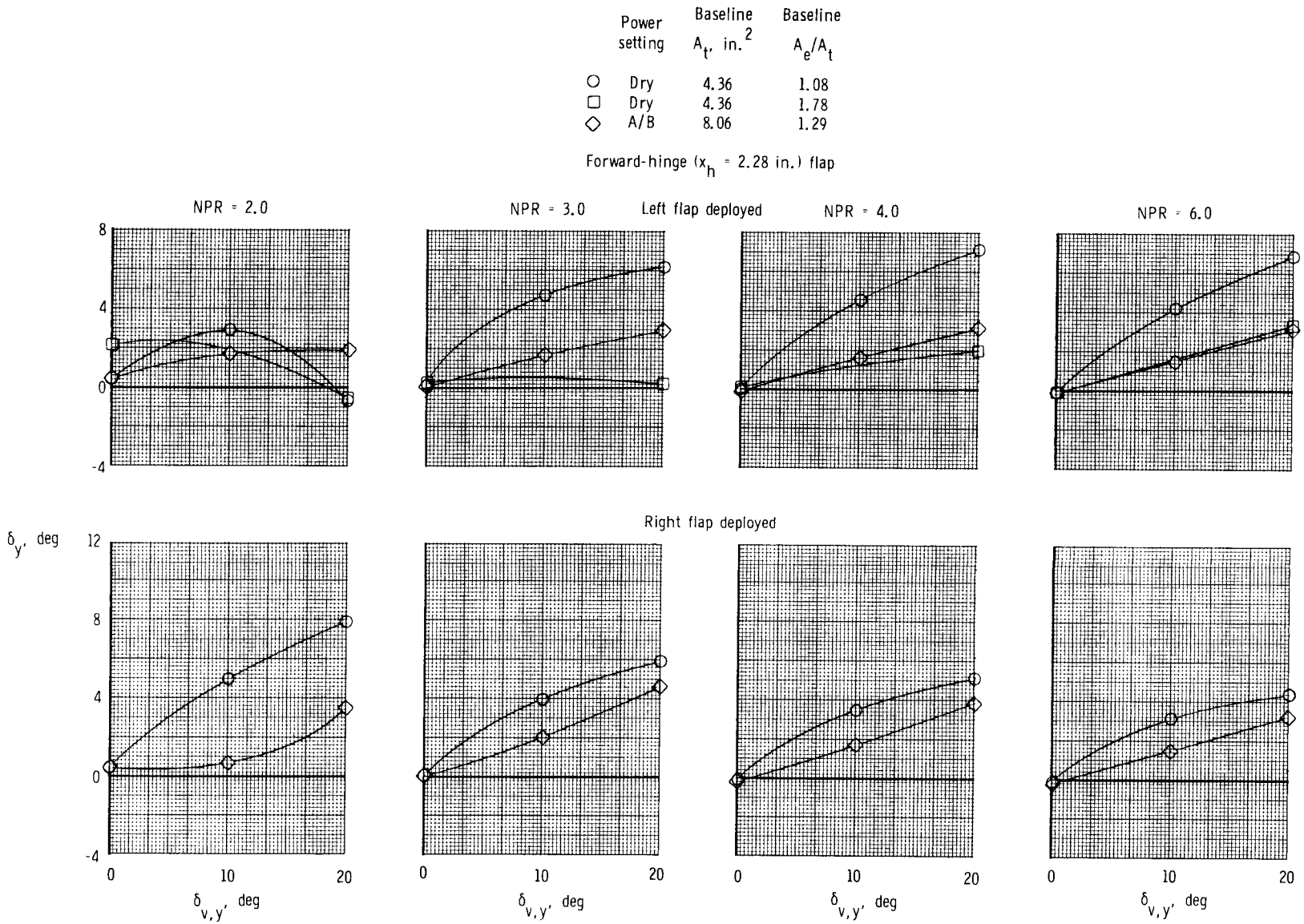

(a) Individual flap deployments.

Figure 22. Summary of resultant yaw vector angle results for downstream flaps yaw vectoring concept with forward hinge ($x_h = 2.28$ in.) and $\delta_{v,p} = 0°$. Data are cross plotted; symbols are for line identification only.

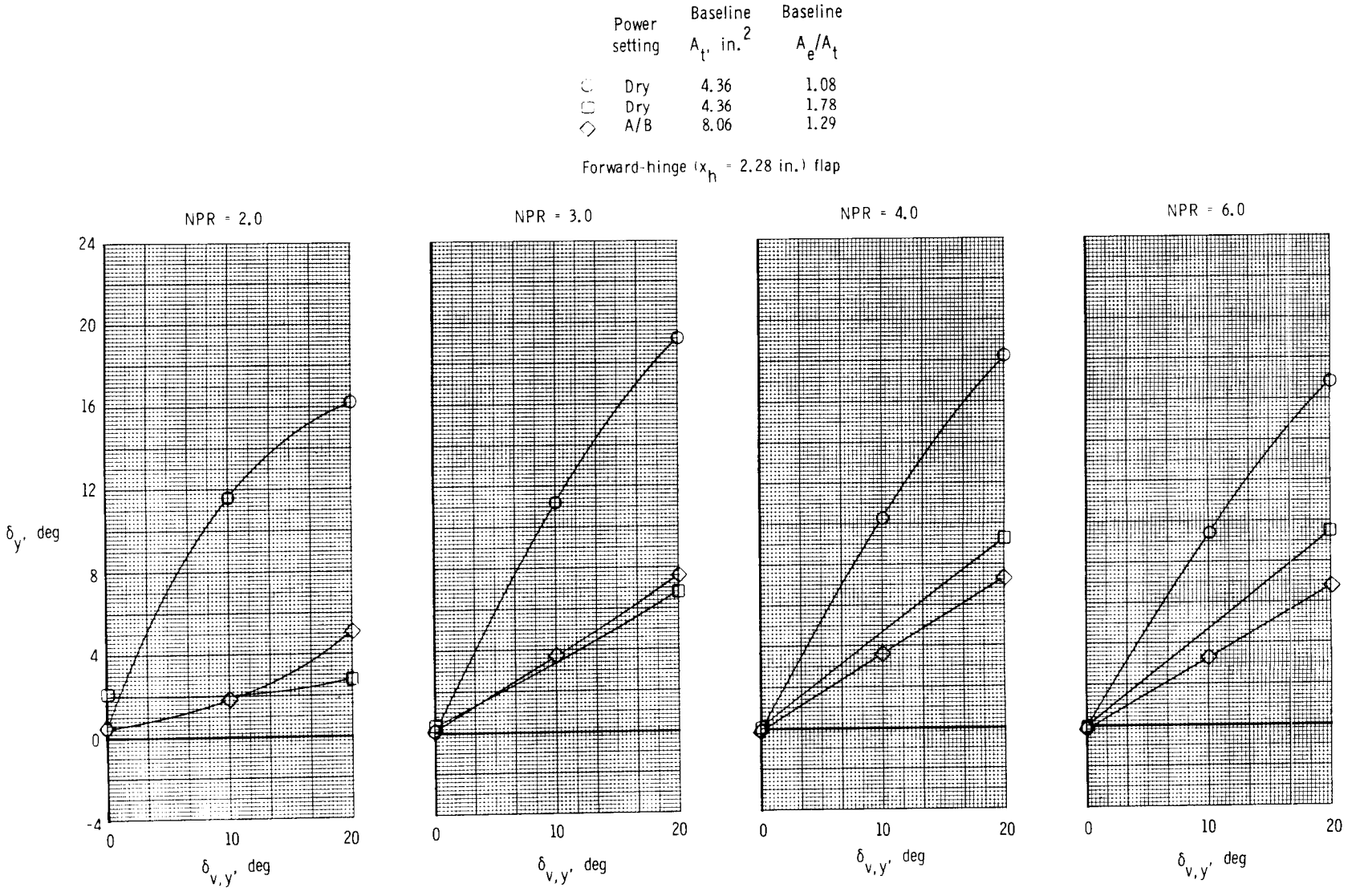

(b) Left and right flaps deployed.

Figure 22. Concluded.

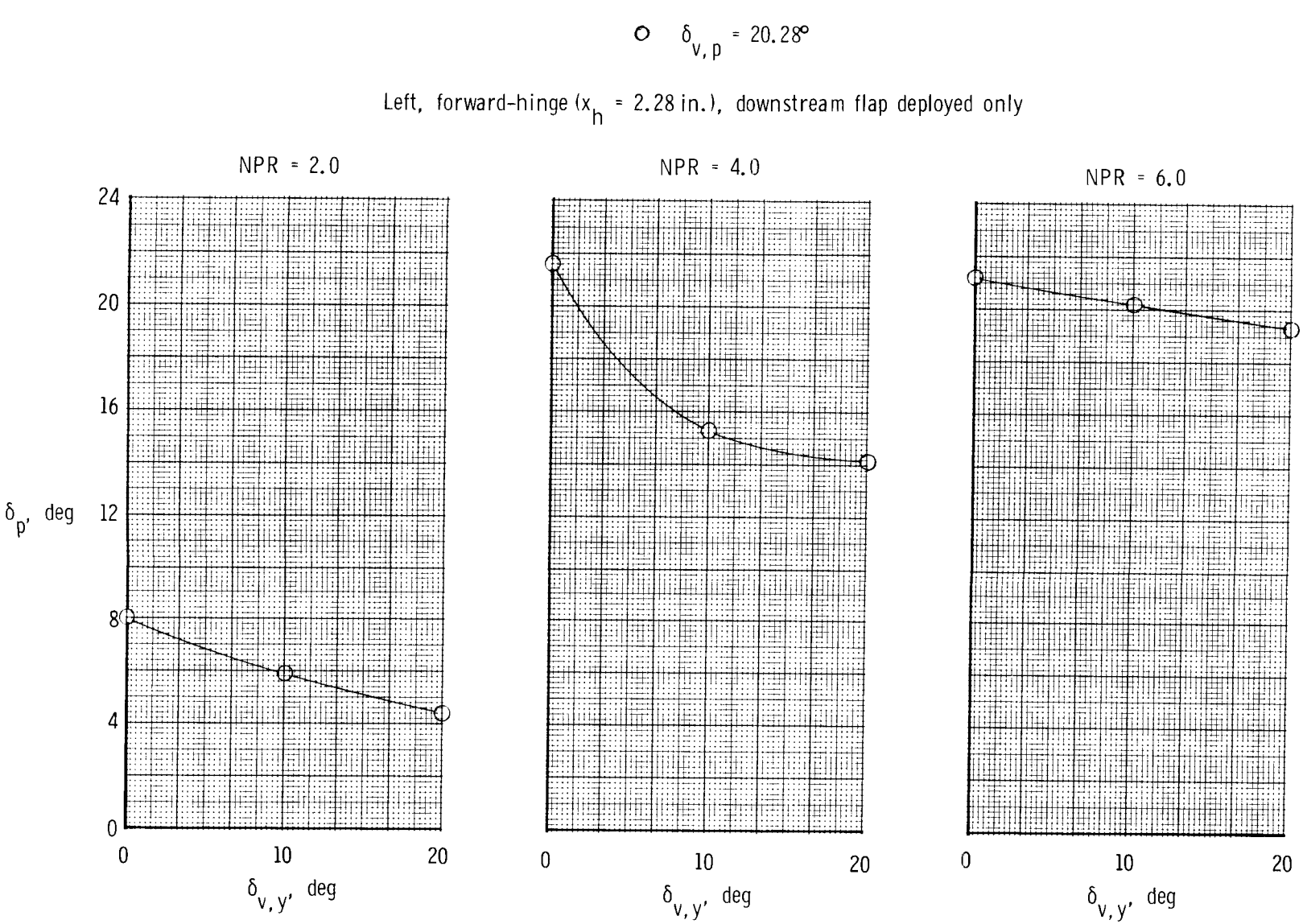

(a) Effect of yaw vectoring on resultant pitch vector angle.

Figure 23. Summary of simultaneous pitch and yaw vectoring results for a single downstream flap concept installed on A/B power 2-D C-D nozzle (baseline $A_e/A_t = 1.29$). Data are cross plotted; symbols are for line identification only.

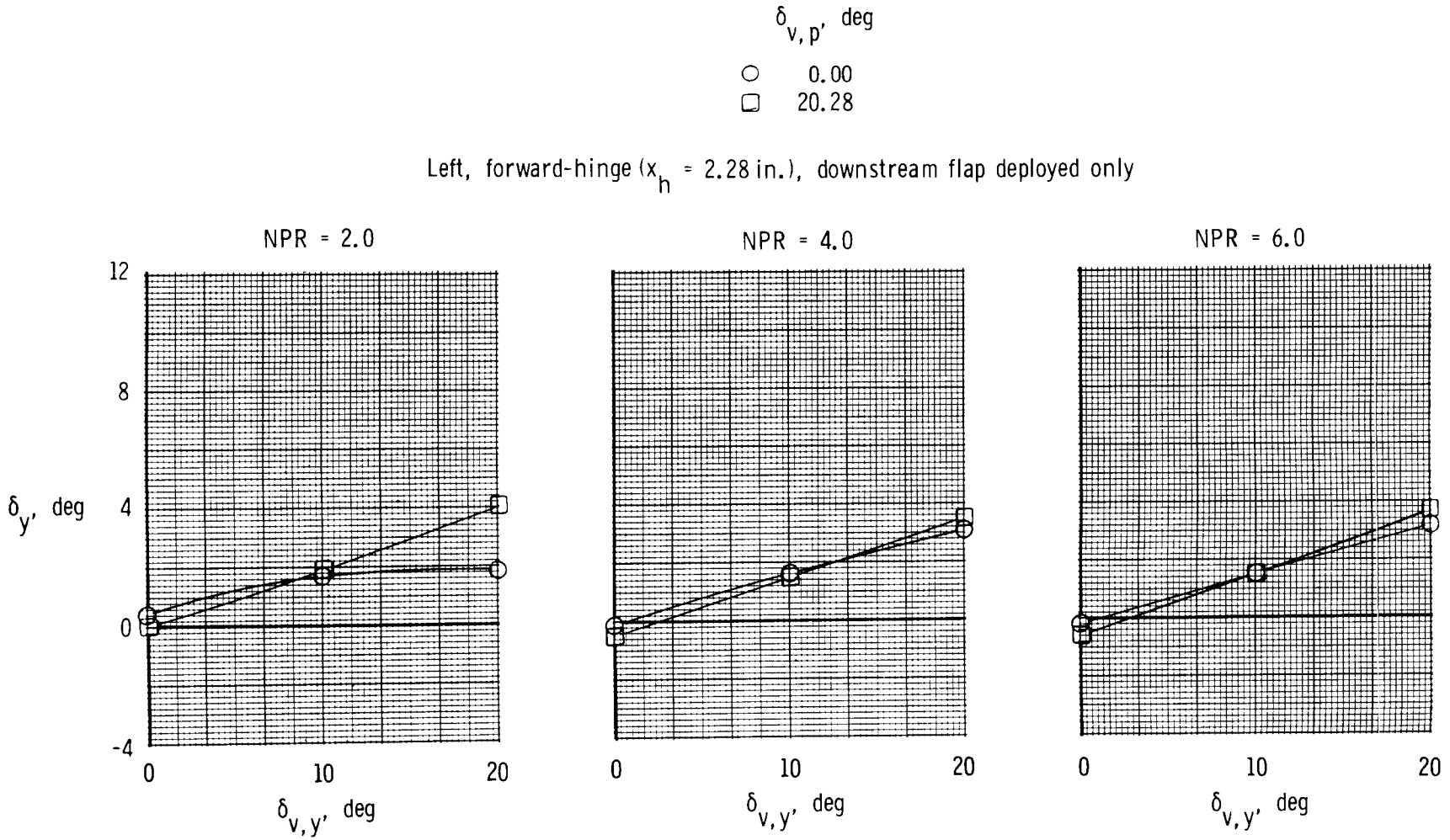

(b) Effect of pitch vectoring on resultant yaw vector angle.

Figure 23. Concluded.

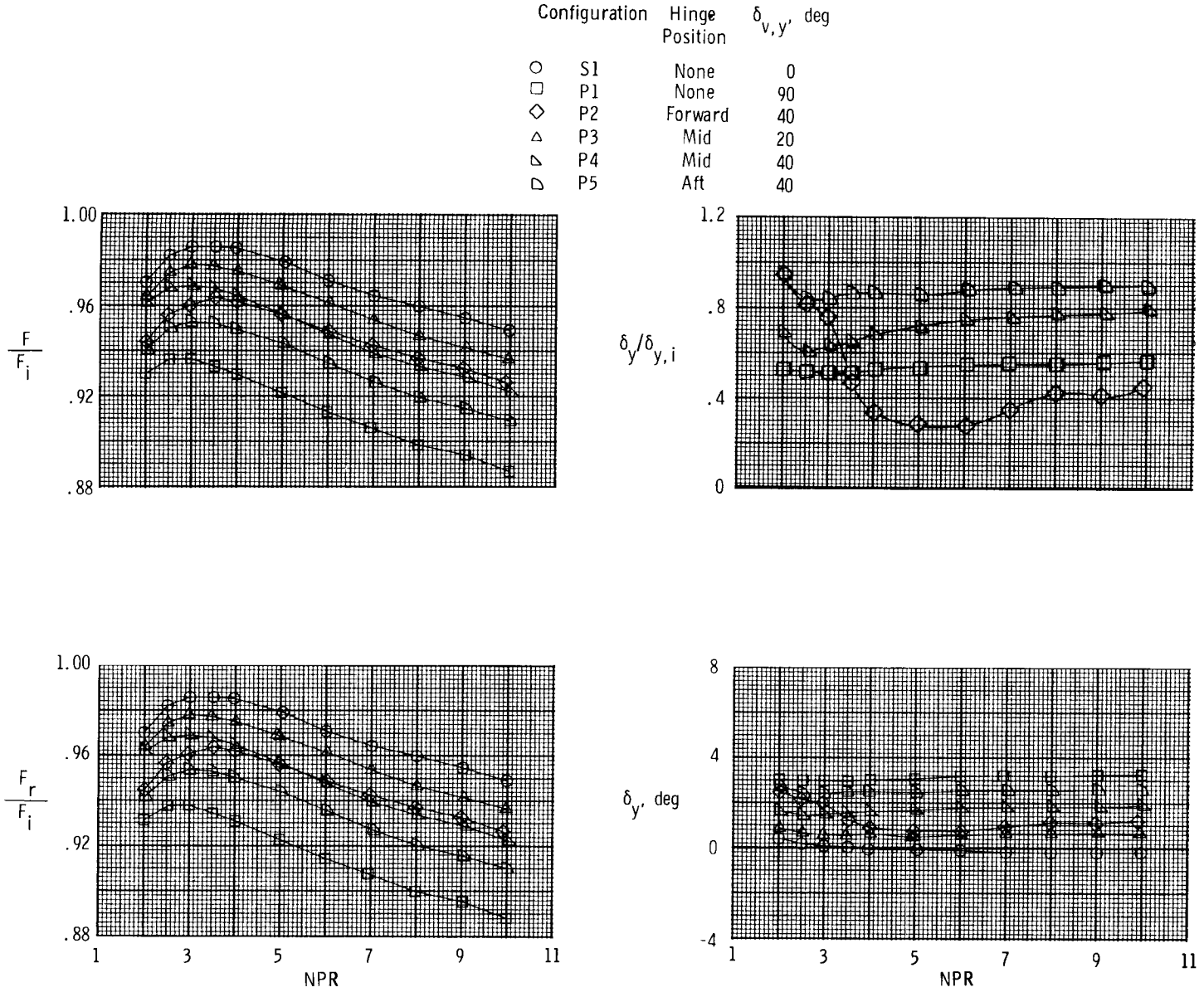

(a) Dry power nozzle, baseline $A_e/A_t = 1.08$ and $\delta_{v,p} = 0°$.

Figure 24. Effect of yaw vectoring on nozzle thrust ratio, resultant thrust ratio, and resultant yaw vector angle for 2-D C-D nozzles with upstream port/flap yaw vector concept.

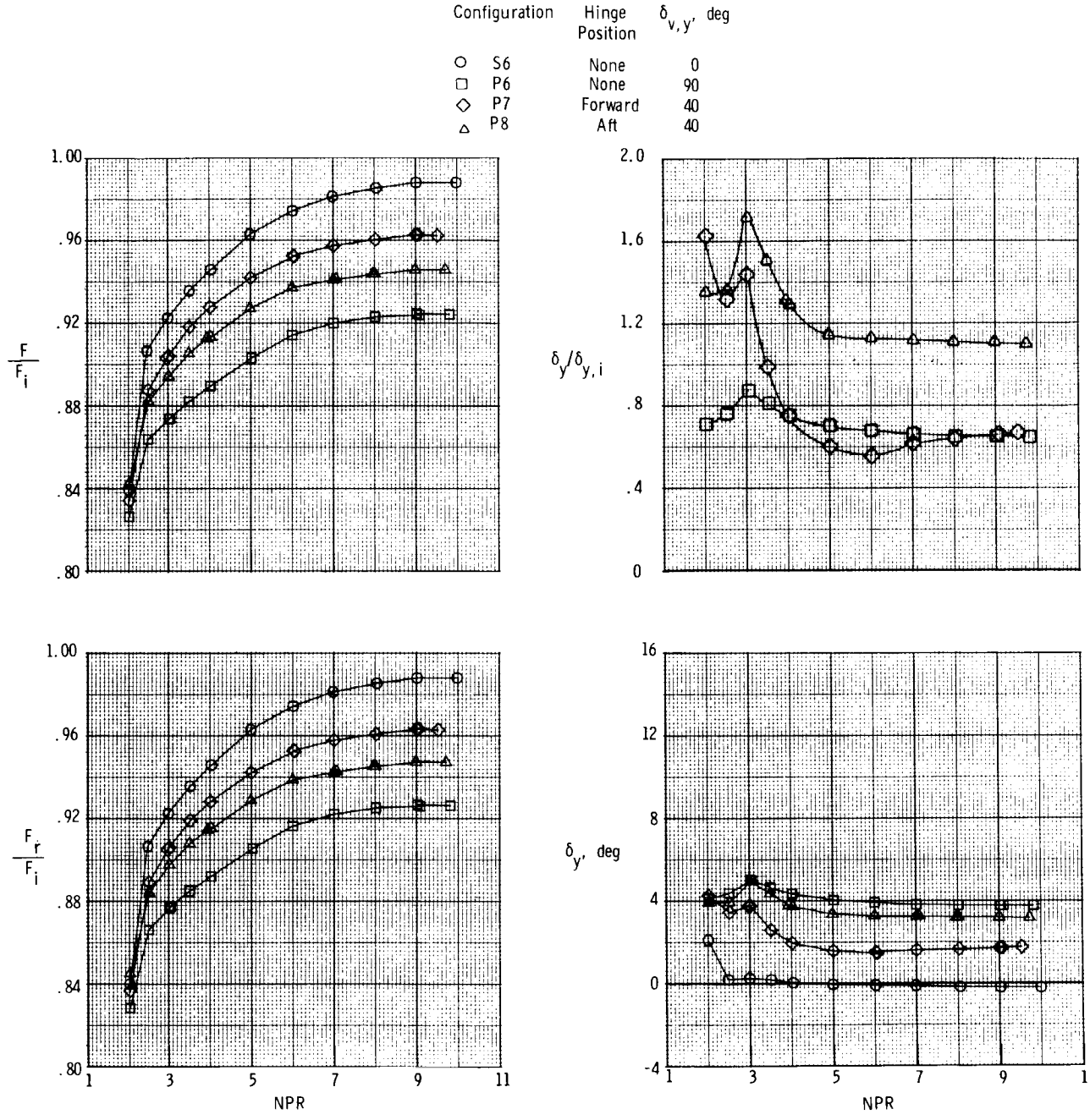

(b) Dry power nozzle, baseline $A_e/A_t = 1.78$ and $\delta_{v,p} = 0°$.

Figure 24. Continued.

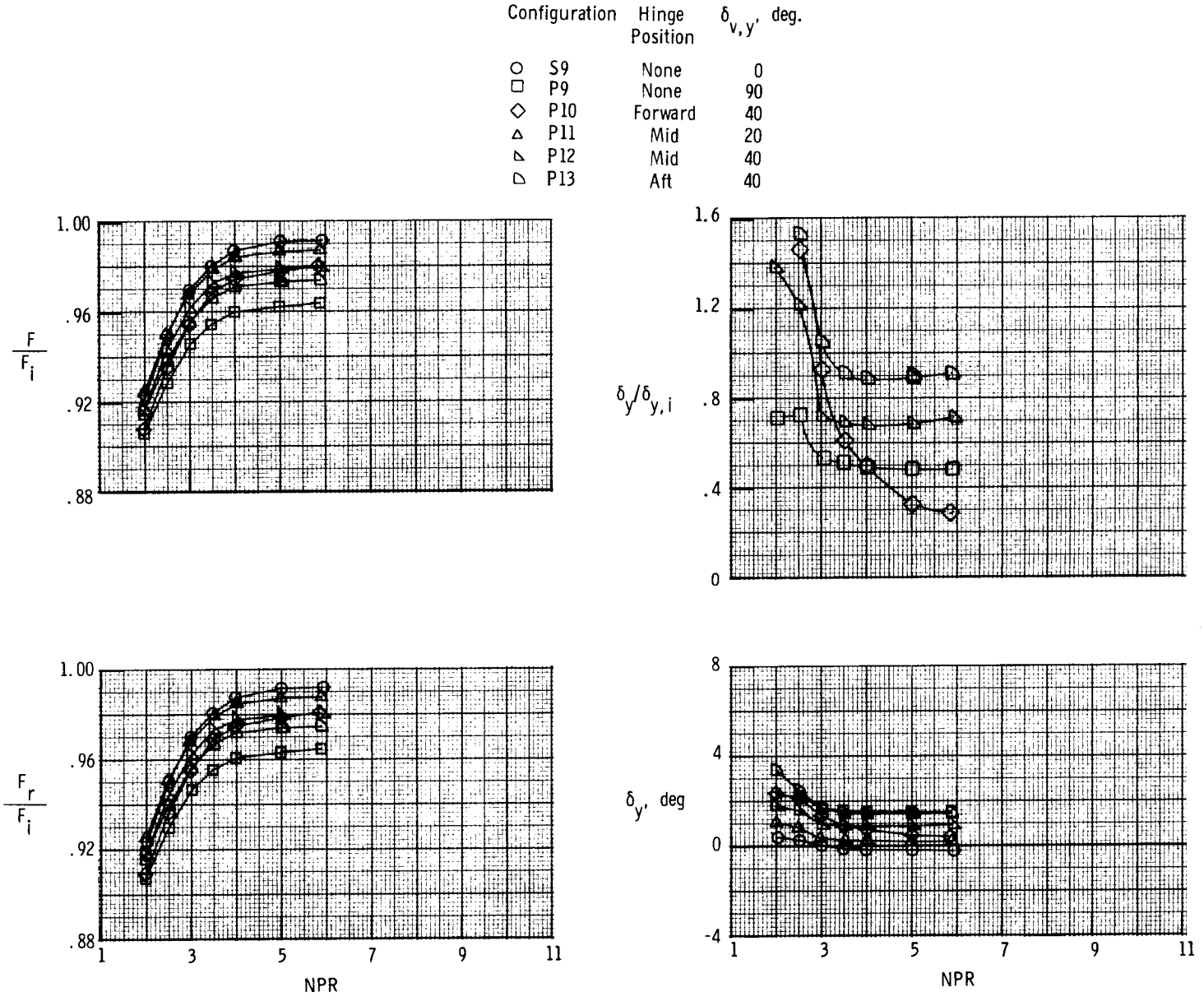

(c) A/B power nozzle, baseline $A_e/A_t = 1.29$ and $\delta_{v,p} = 0°$.

Figure 24. Continued.

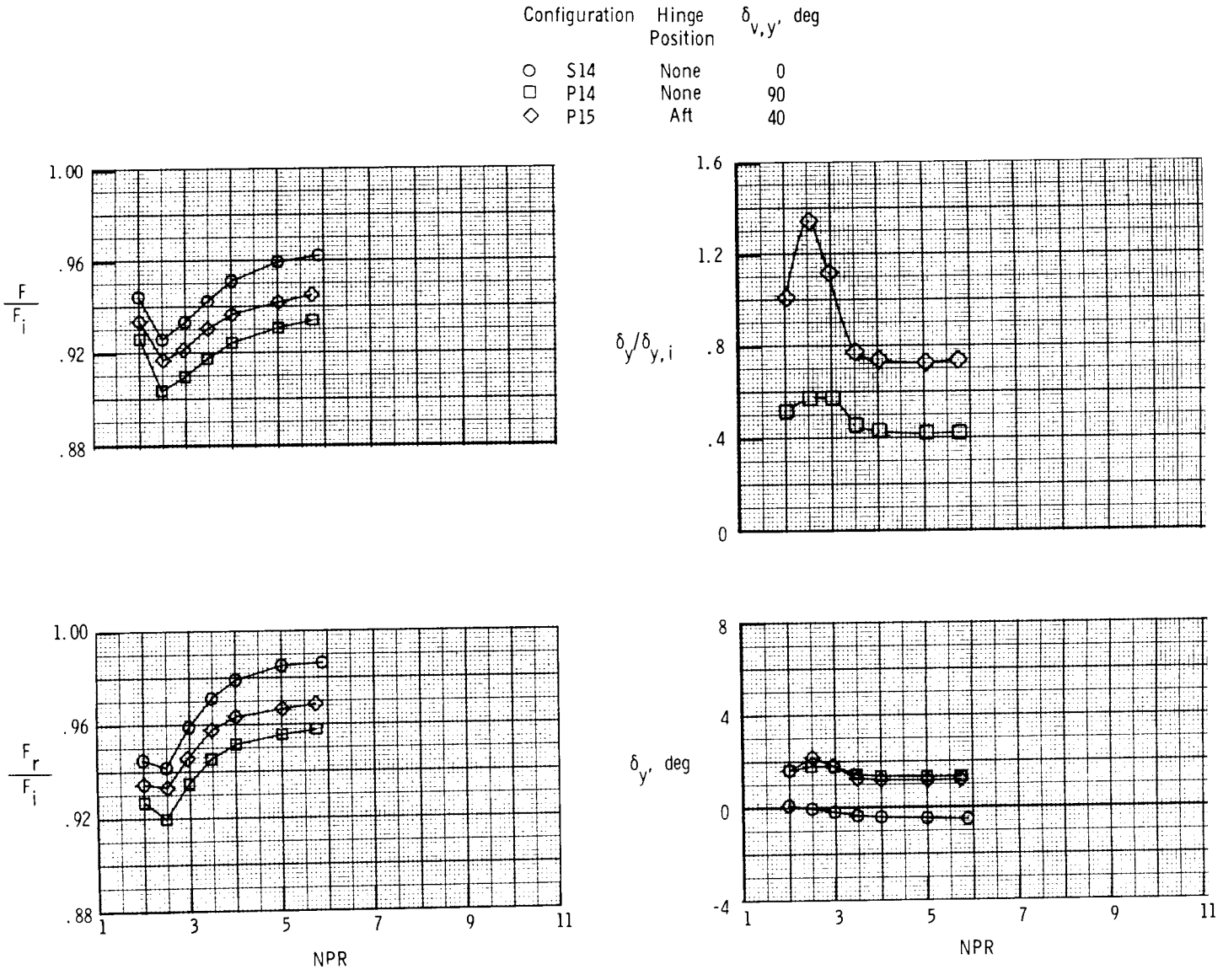

(d) A/B power nozzle; $\delta_{v,p} = 9.79°$.

Figure 24. Continued.

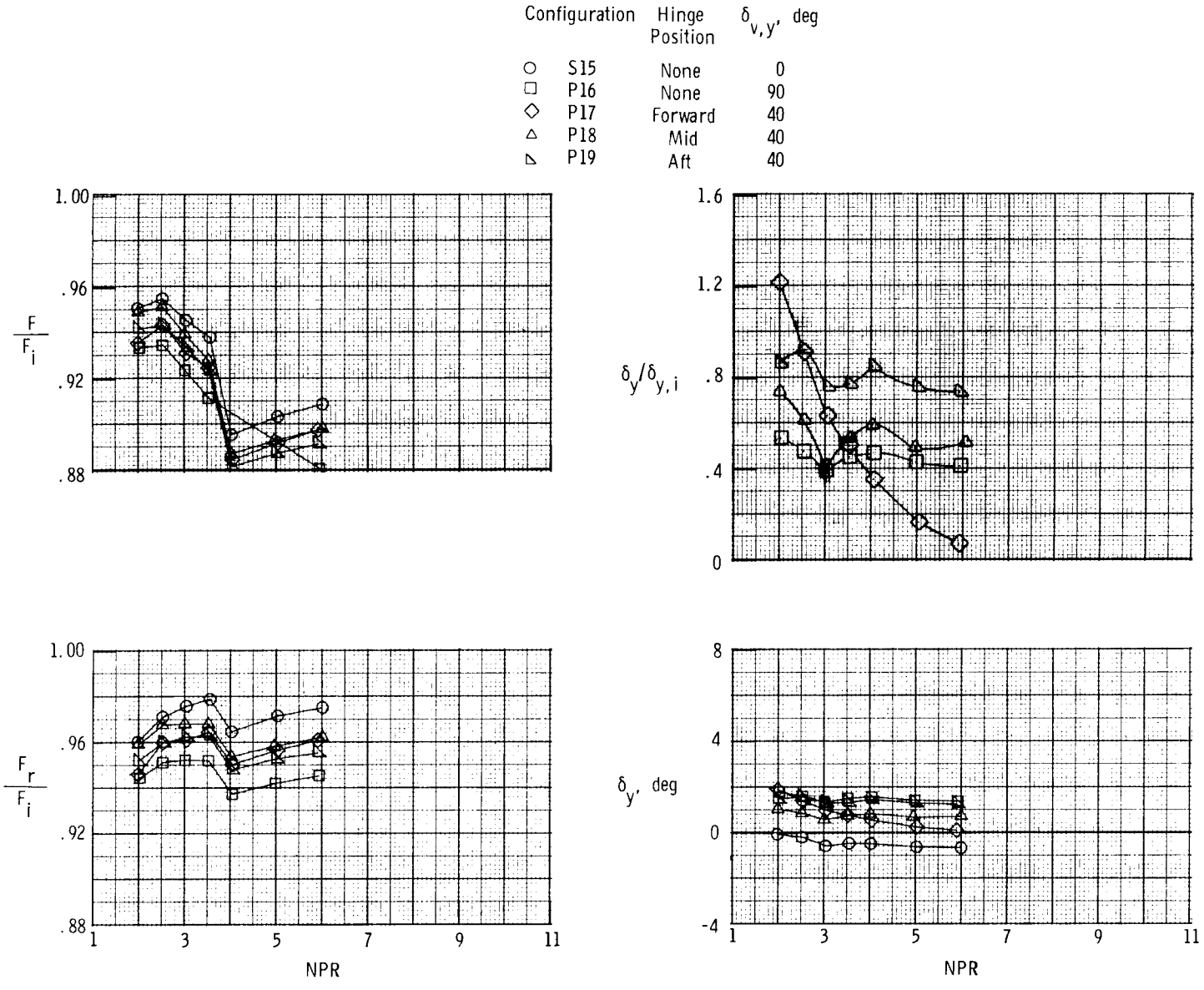

(e) A/B power nozzle; $\delta_{v,p} = 20.28°$.

Figure 24. Concluded.

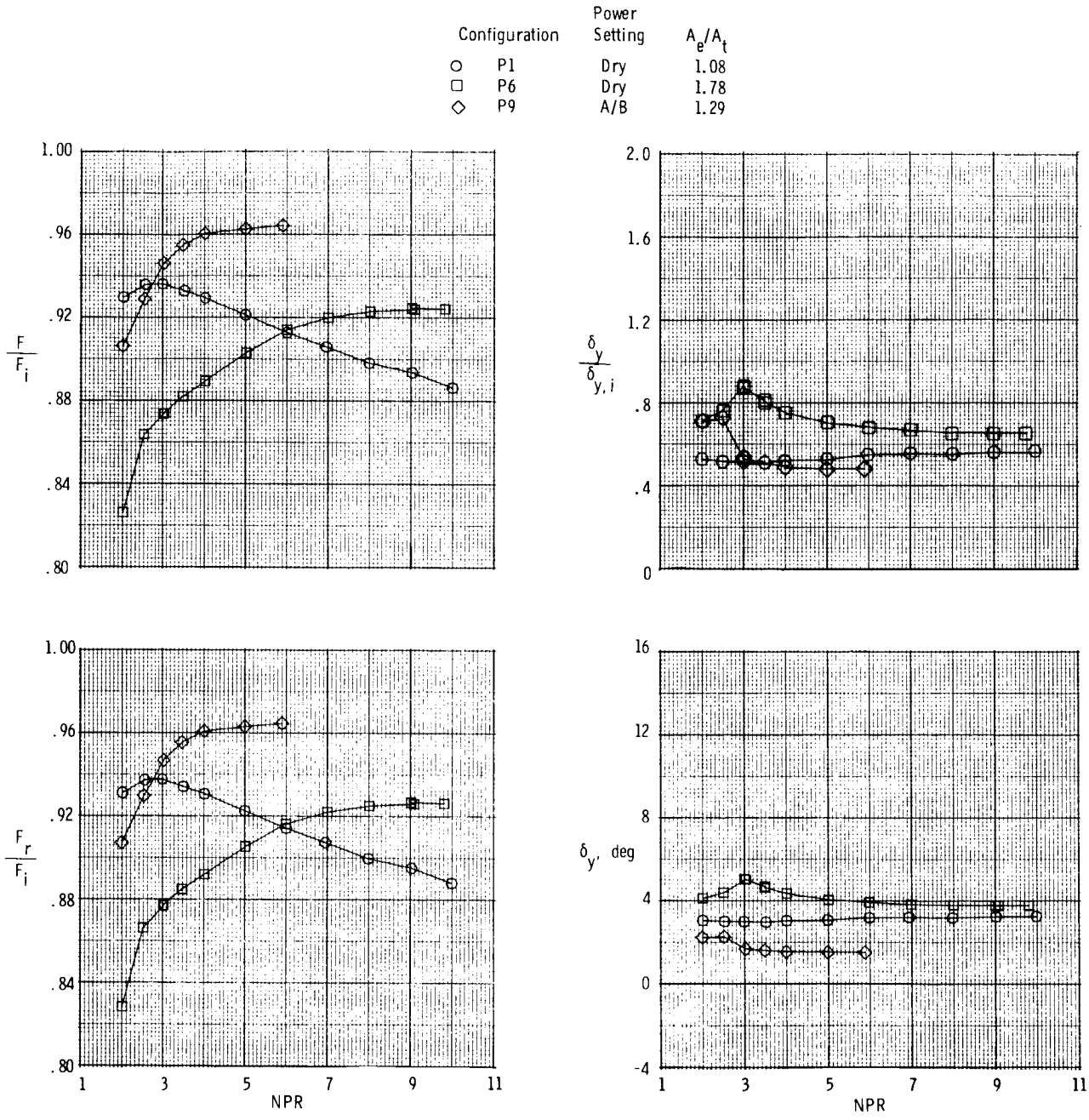

(a) Circular port; $\delta_{v,y} = 90°$.

Figure 25. Effect of expansion ratio and power setting on 2-D C-D nozzle performance with upstream port/flap yaw vector concept installed and $\delta_{v,p} = 0°$.

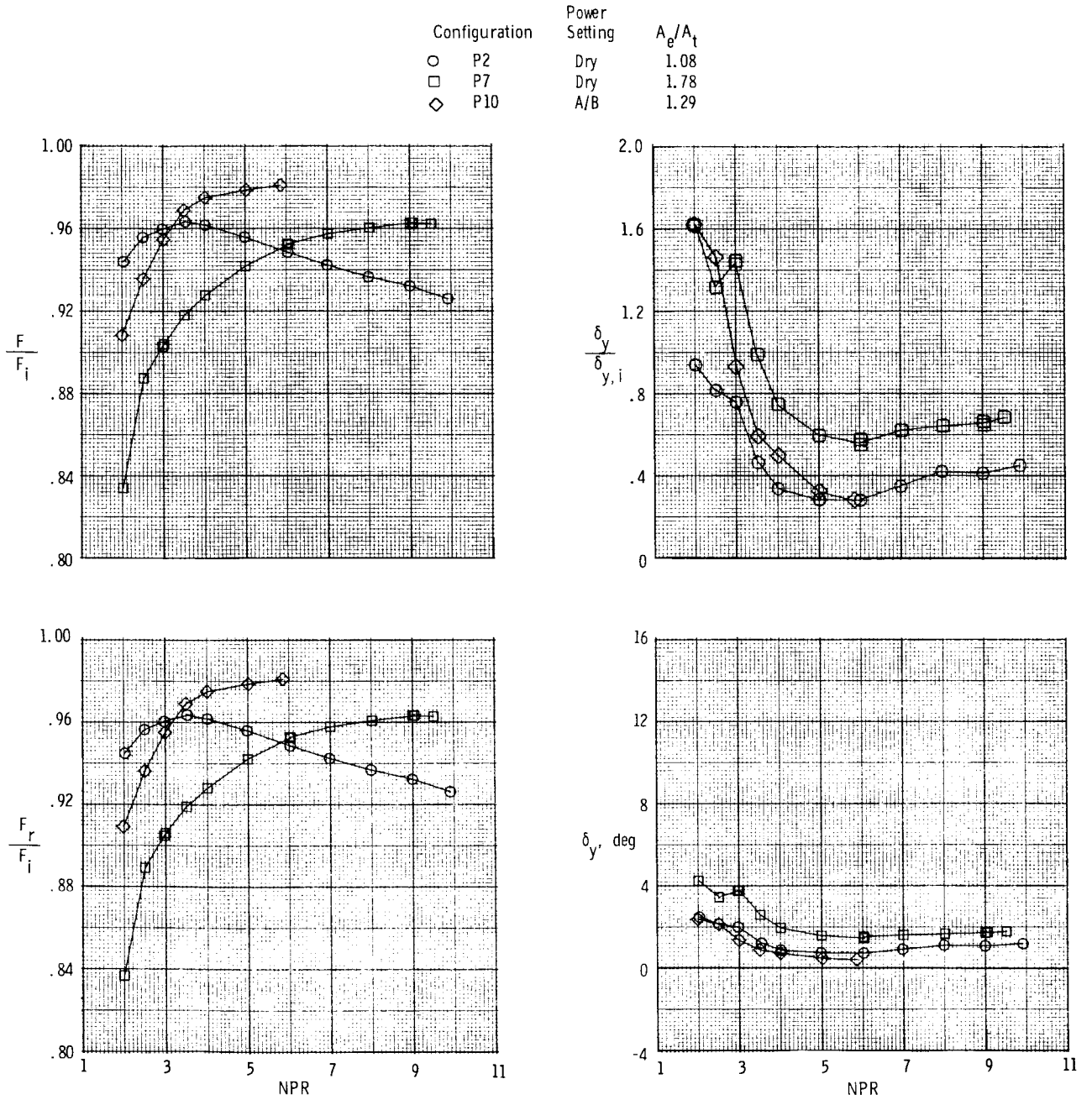

(b) Forward-hinge ($x_h = 0.70$ in.) rectangular flap; $\delta_{v,y} = 40°$.

Figure 25. Continued.

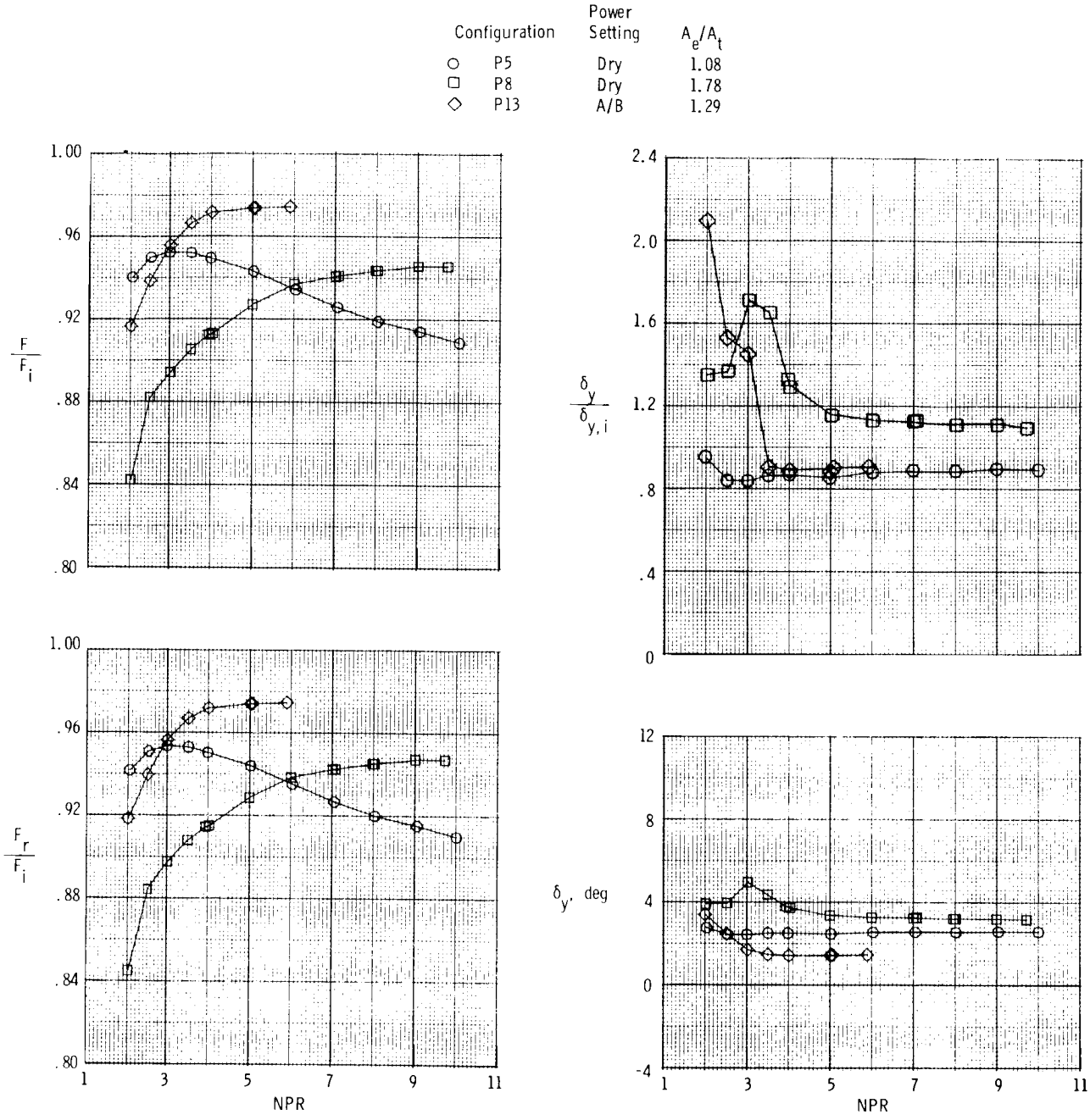

(c) Aft-hinge ($x_h = 1.98$ in.) rectangular flap; $\delta_{v,y} = 40°$.

Figure 25. Concluded.

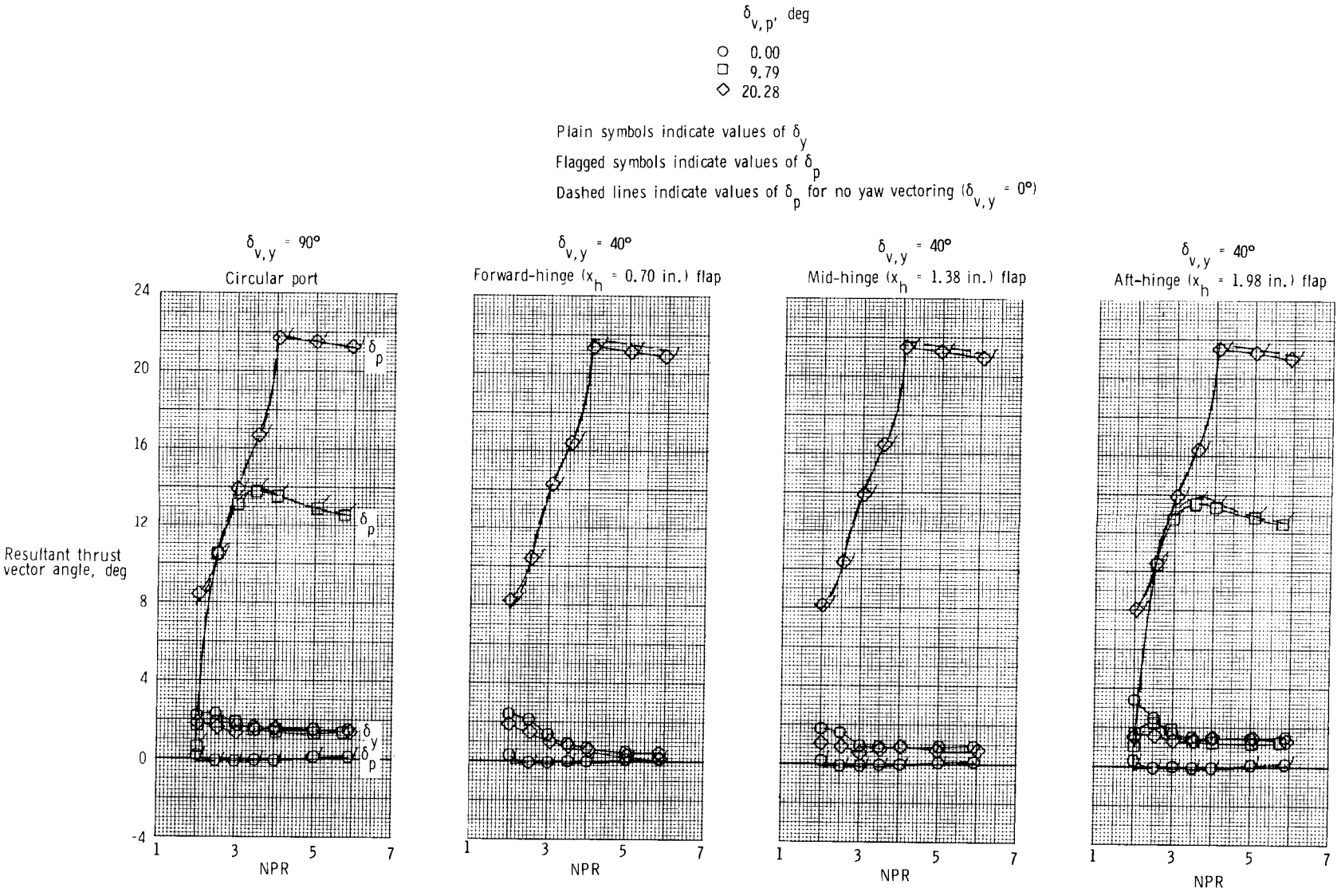

Figure 26. Effect of simultaneous pitch and yaw thrust vectoring on resultant vector angles of 2-D C-D nozzle with upstream port/flap yaw thrust vectoring concept installed. A/B power nozzle, baseline $A_e/A_t = 1.29$.

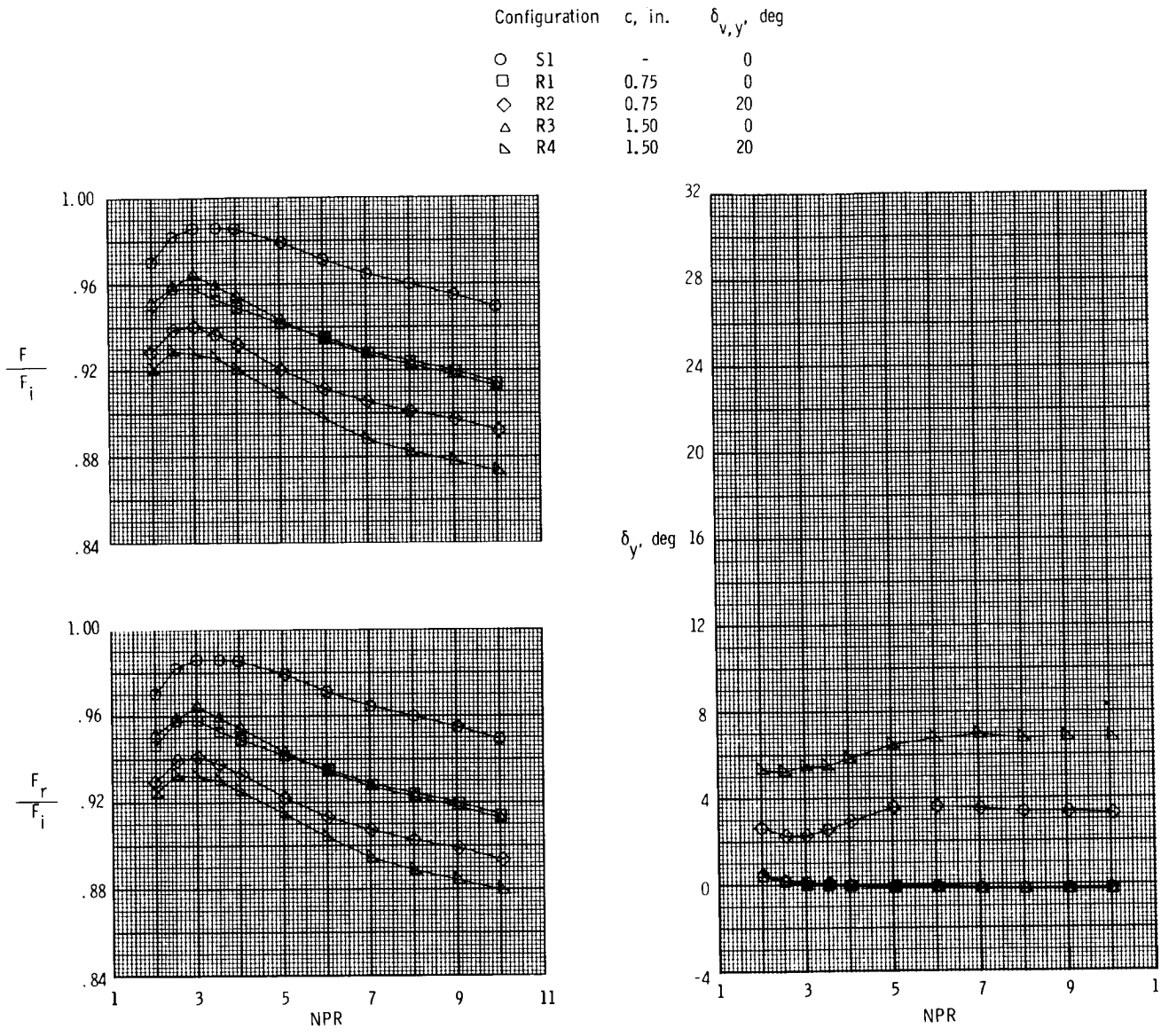

(a) Dry power nozzle, baseline $A_e/A_t = 1.08$ and $\delta_{v,p} = 0°$.

Figure 27. Effect of yaw vectoring on nozzle thrust ratio, resultant thrust ratio, and resultant yaw vector angle for 2-D C-D nozzles with powered rudder yaw vector concept.

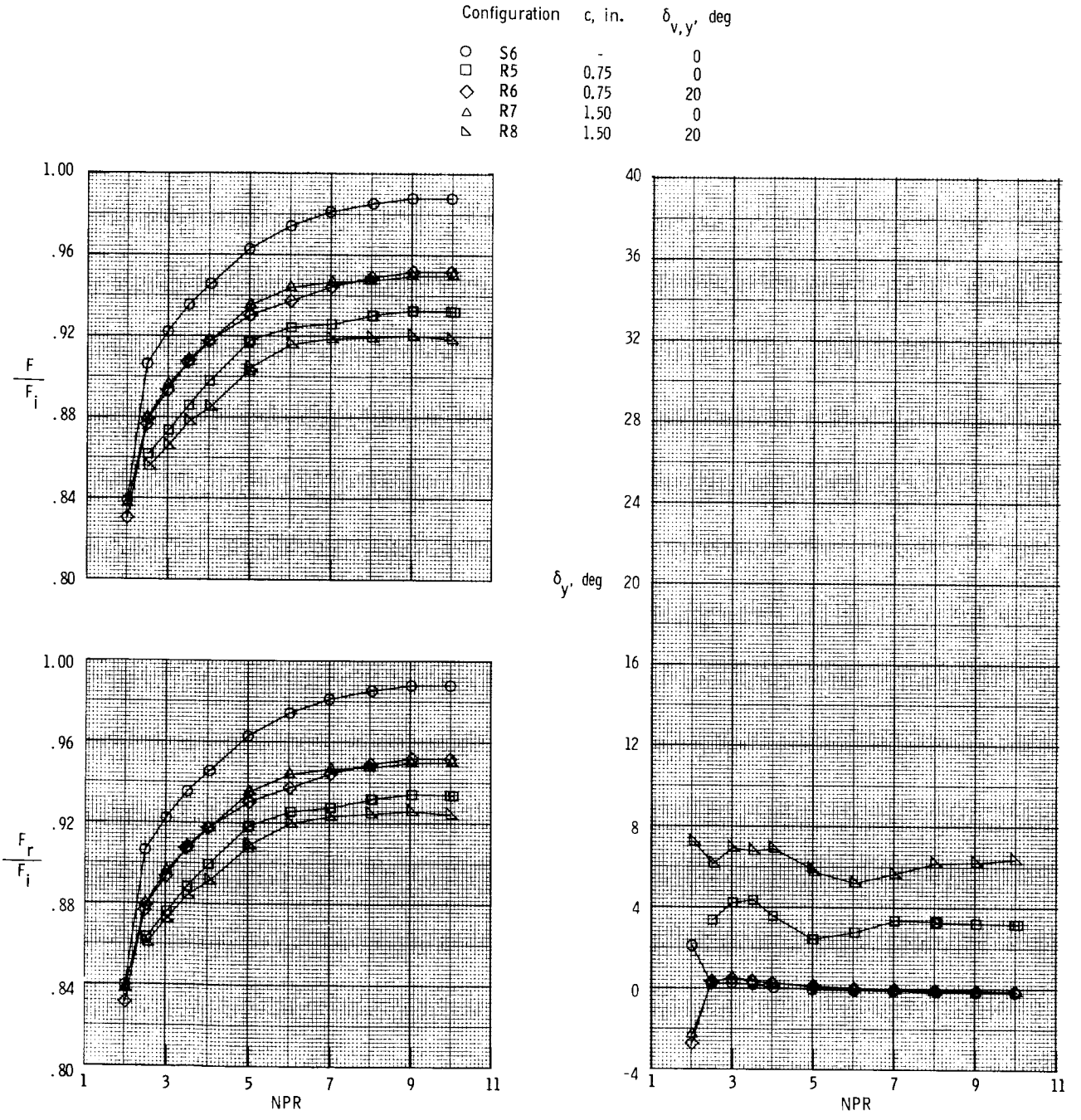

(b) Dry power nozzle, baseline $A_e/A_t = 1.78$ and $\delta_{v,p} = 0°$.

Figure 27. Continued.

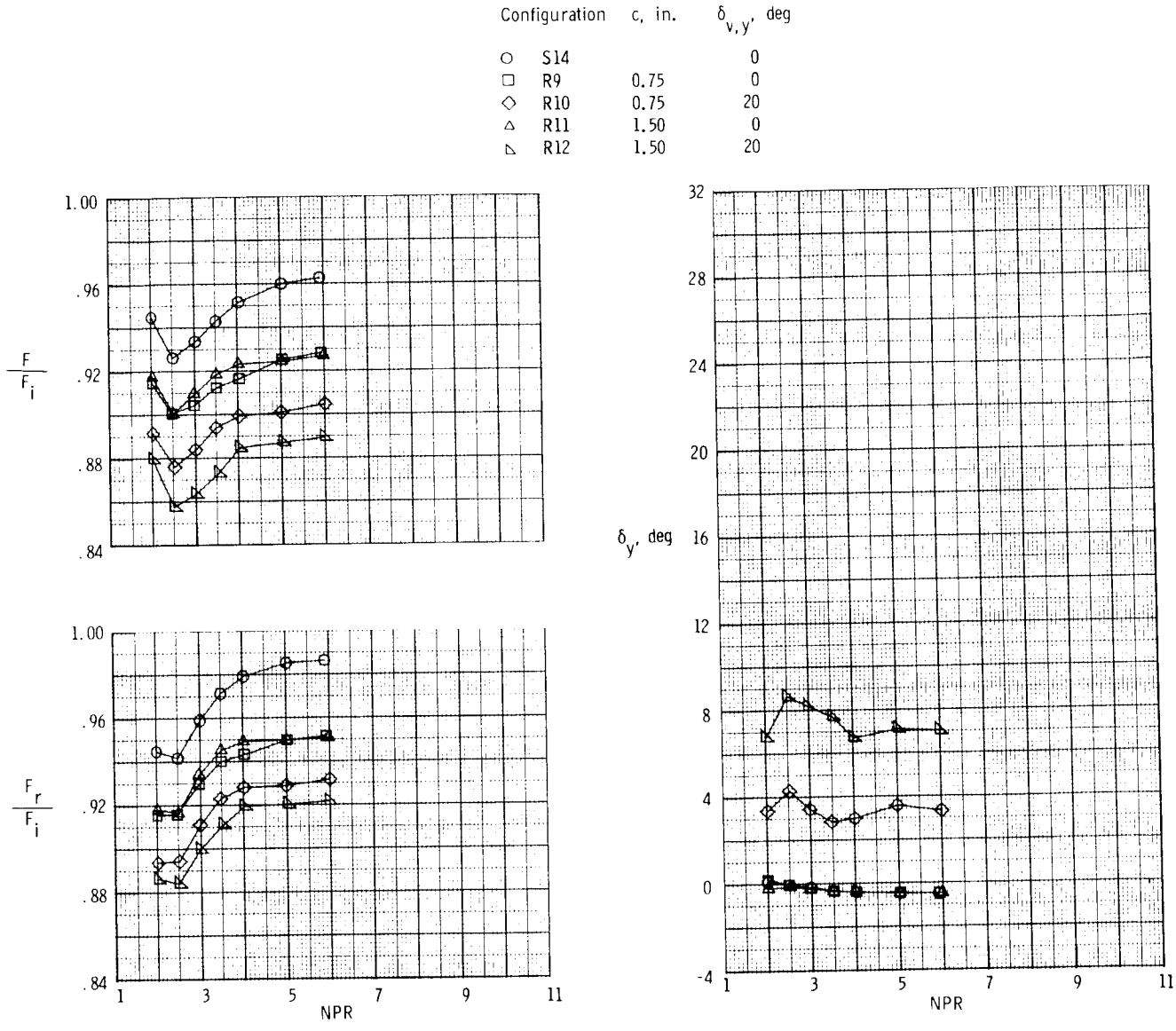

(c) A/B power nozzle, $\delta_{v,p} = 9.79°$.

Figure 27. Continued.

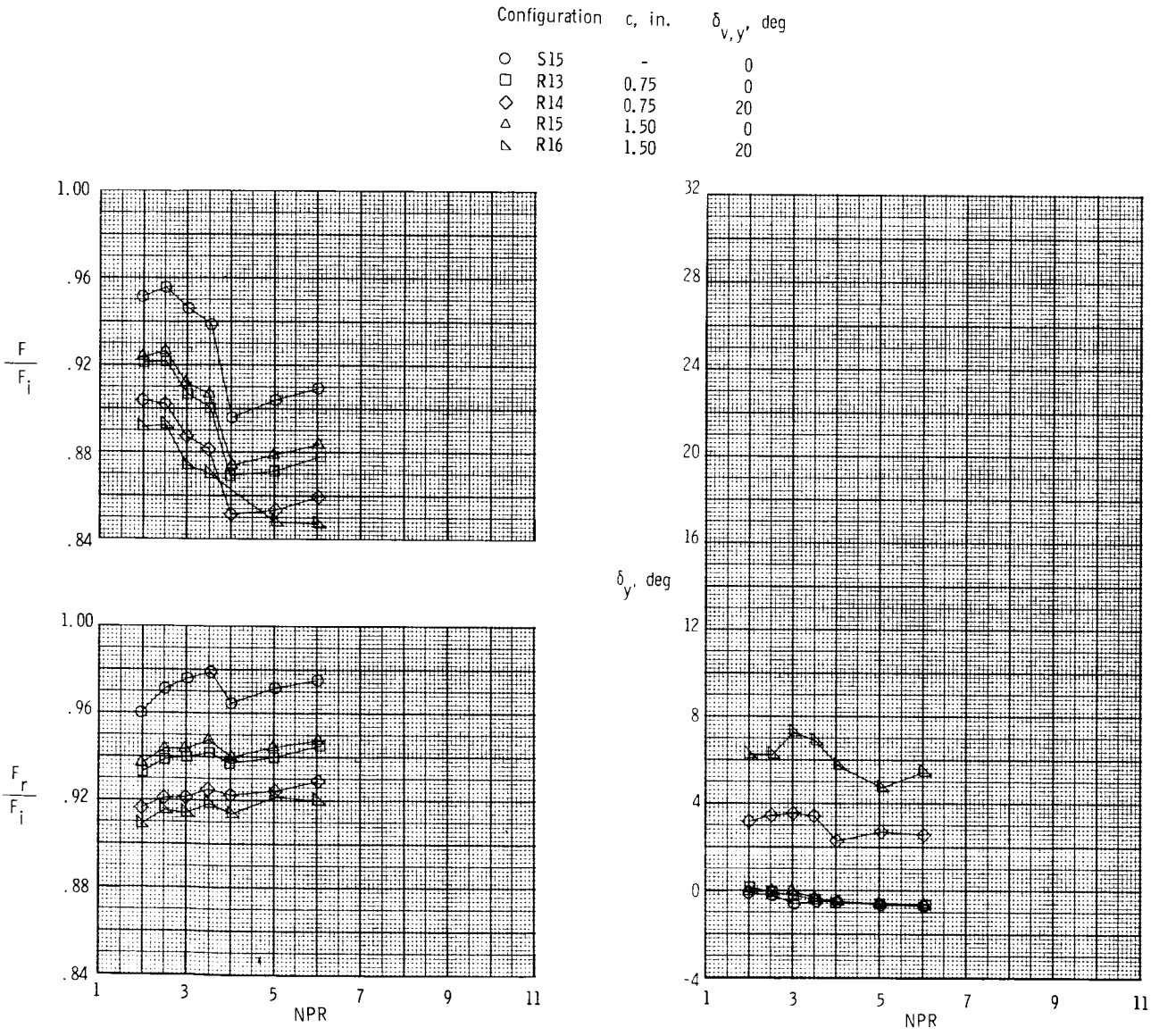

(d) A/B power nozzle, $\delta_{v,p} = 20.28°$.

Figure 27. Concluded.

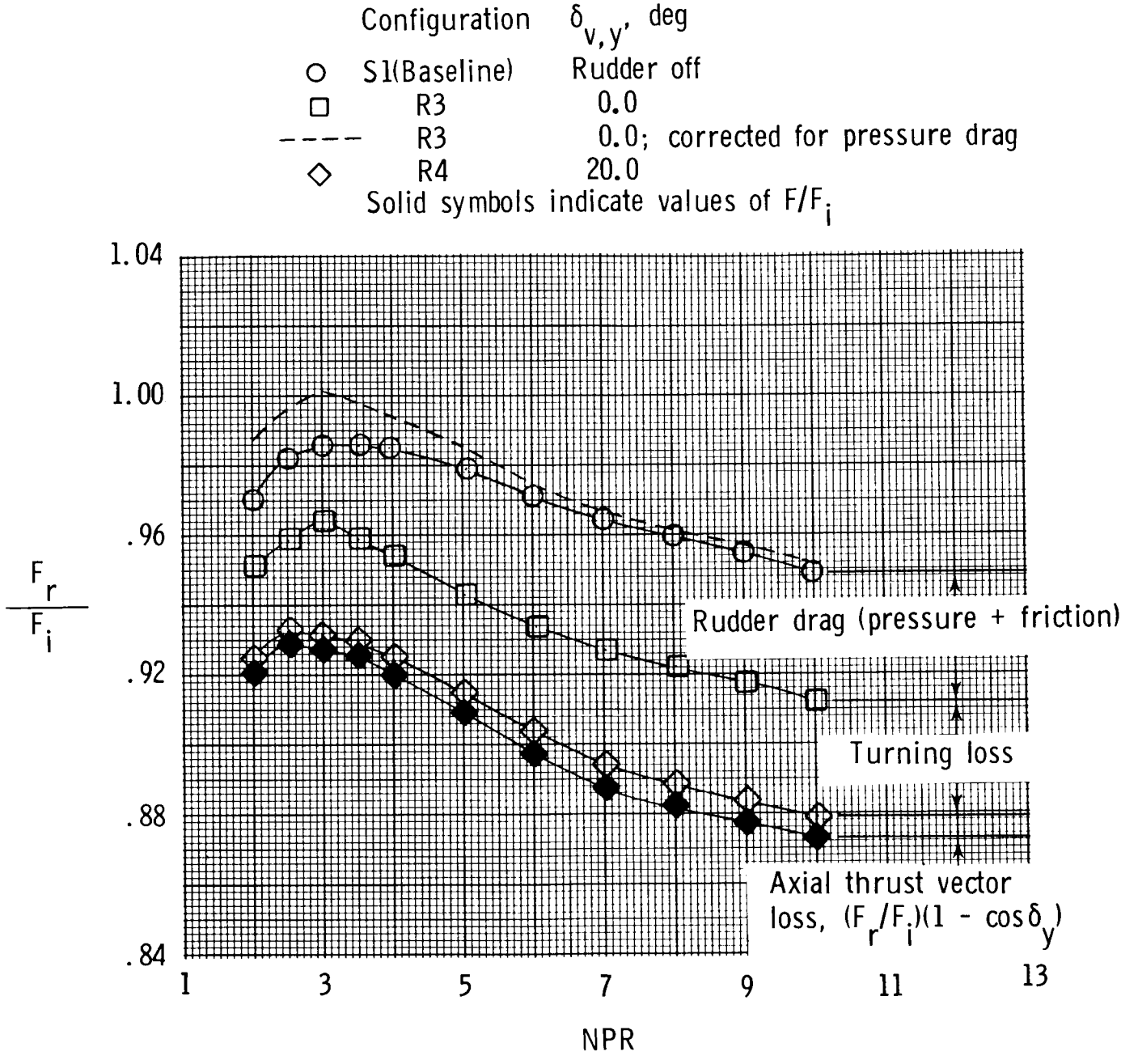

Figure 28. Summary of thrust losses for powered rudder concept installed on dry power 2-D C-D nozzle. $A_e/A_t = 1.08$; $c = 1.50$ in.

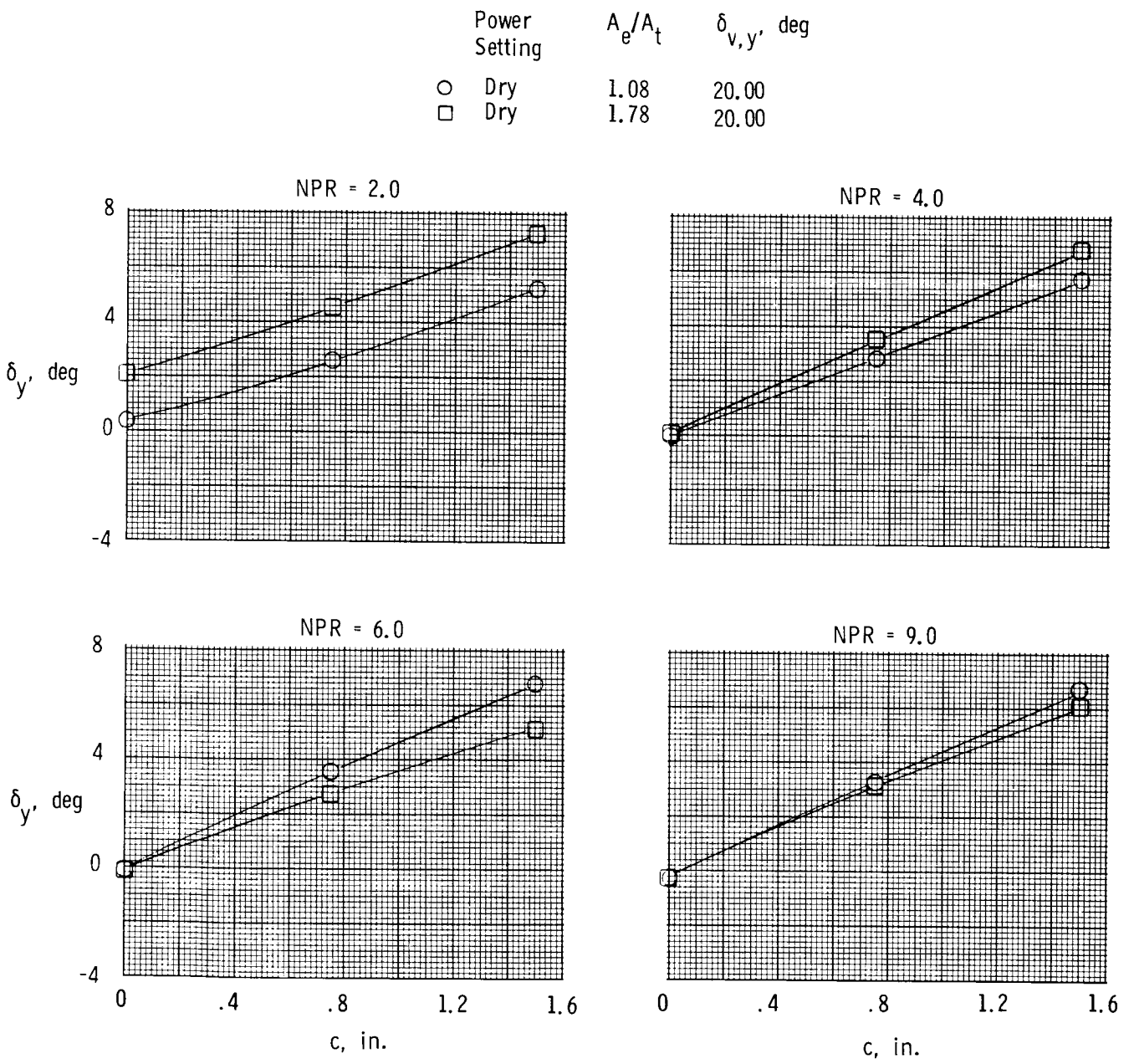

Figure 29. Effect of rudder chord length and nozzle expansion ratio on resultant yaw vector angle for dry power 2-D C-D nozzle with powered rudder yaw vectoring concept installed. $\delta_{v,p} = 0°$. Data are cross plotted and symbols are for line identification only.

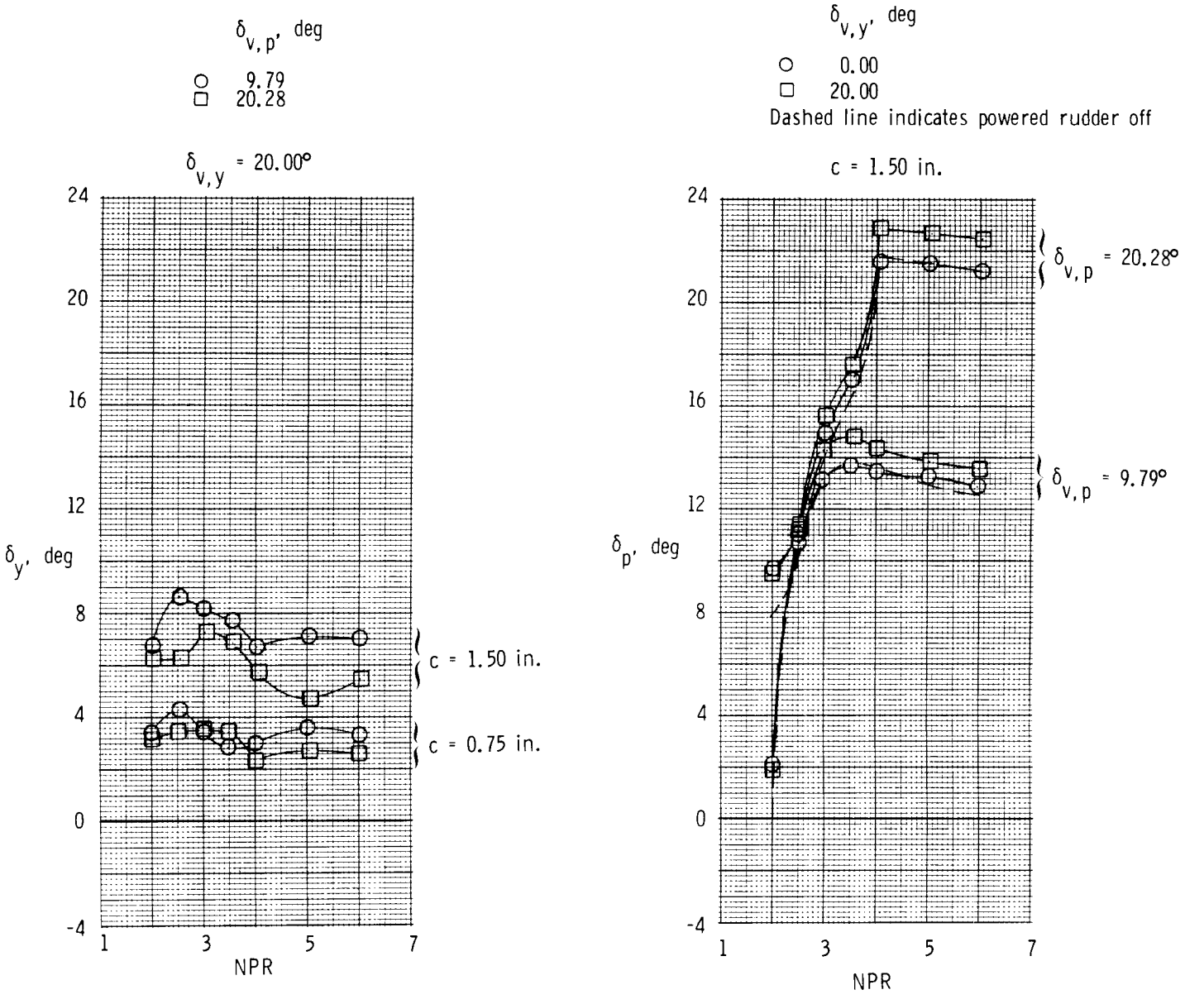

Figure 30. Effect of simultaneous pitch and yaw thrust vectoring on resultant vector angles of 2-D C-D nozzle with powered rudder yaw vectoring concept installed. A/B power nozzle, baseline $A_e/A_t = 1.29$.

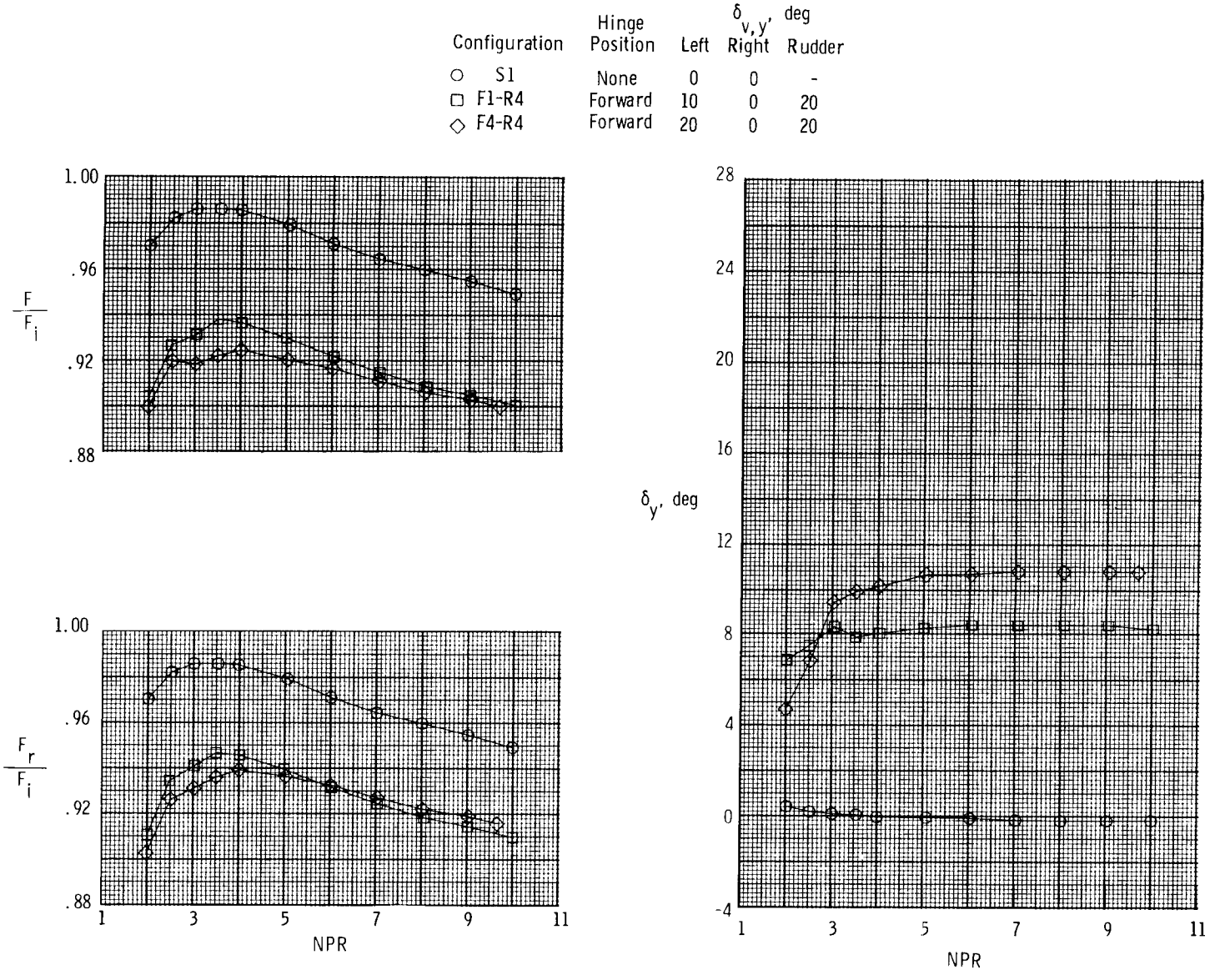

(a) Left downstream flap deflected.

Figure 31. Effect of yaw vectoring on nozzle thrust ratio, resultant thrust ratio, and resultant yaw vector angle for dry power 2-D C-D nozzle, baseline $A_e/A_t = 1.08$ and $\delta_{v,p} = 0°$, with a combination of the downstream flap and the powered rudder yaw vector concepts.

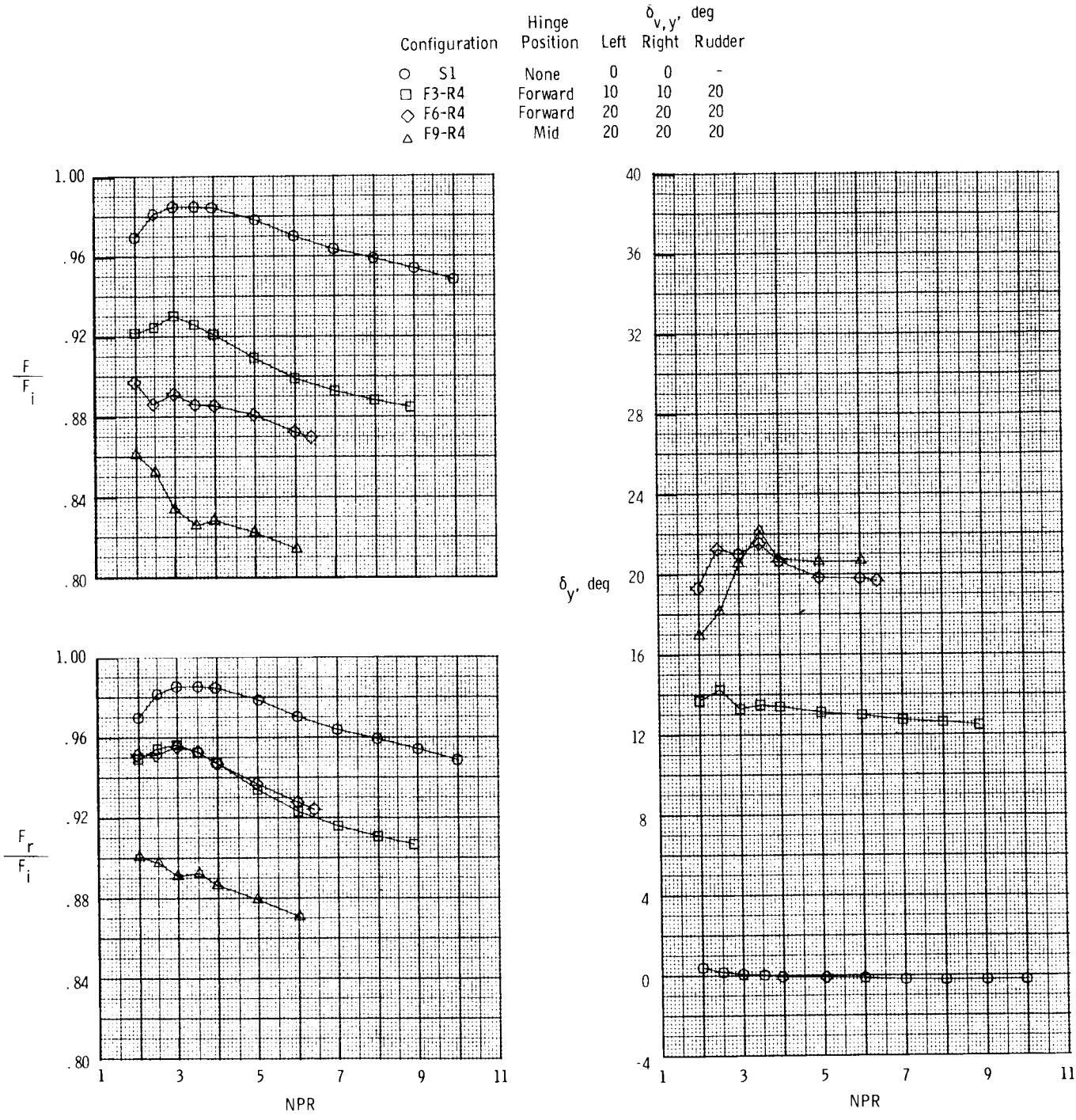

(b) Left and right downstream flaps deflected.

Figure 31. Concluded.

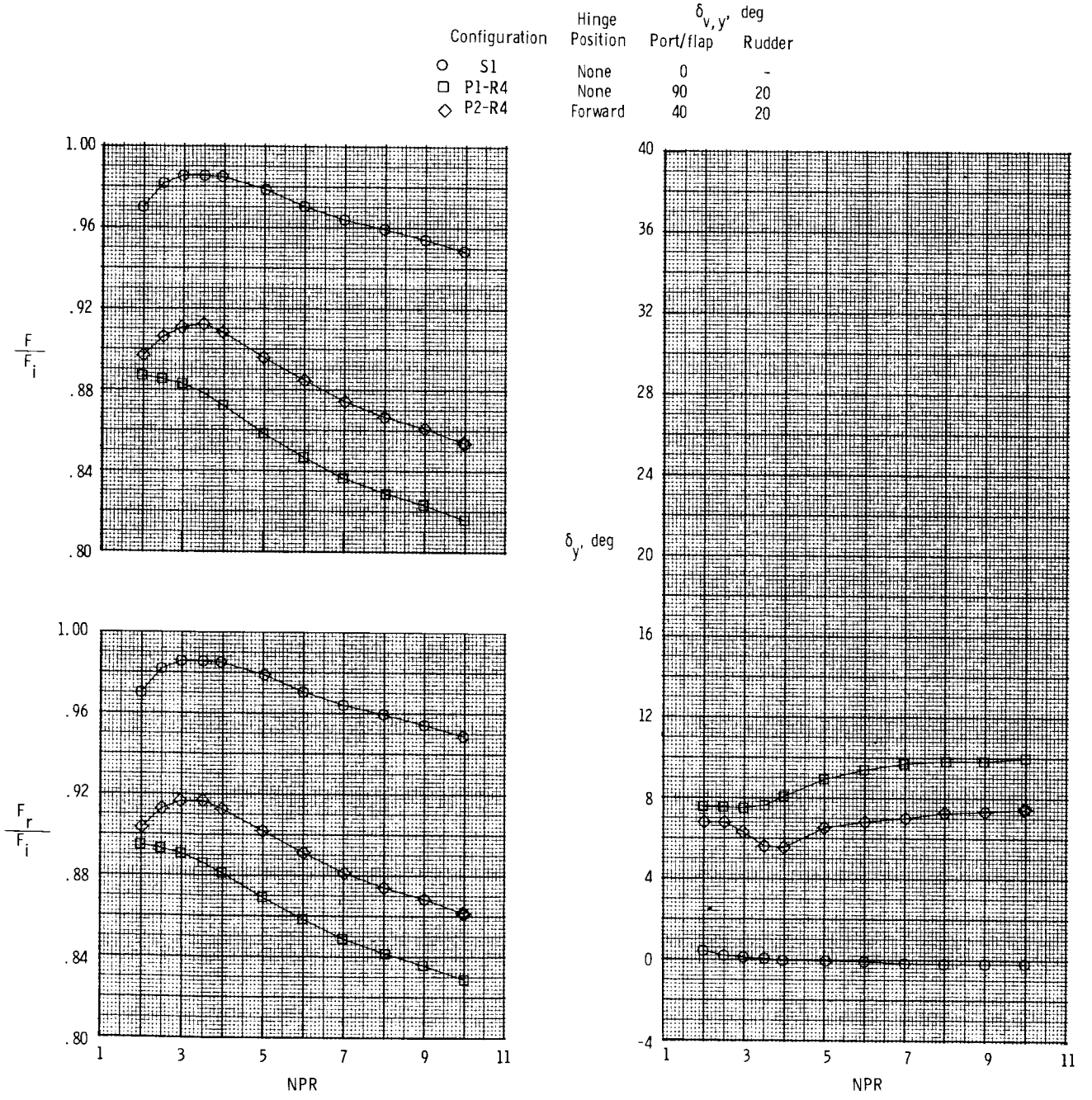

Figure 32. Effect of yaw vectoring on nozzle thrust ratio, resultant thrust ratio, and resultant yaw vector angle for dry power 2-D C-D nozzle, baseline $A_e/A_t = 1.08$ and $\delta_{v,p} = 0°$, with a combination of the upstream port/flap and the powered rudder yaw vector concepts.

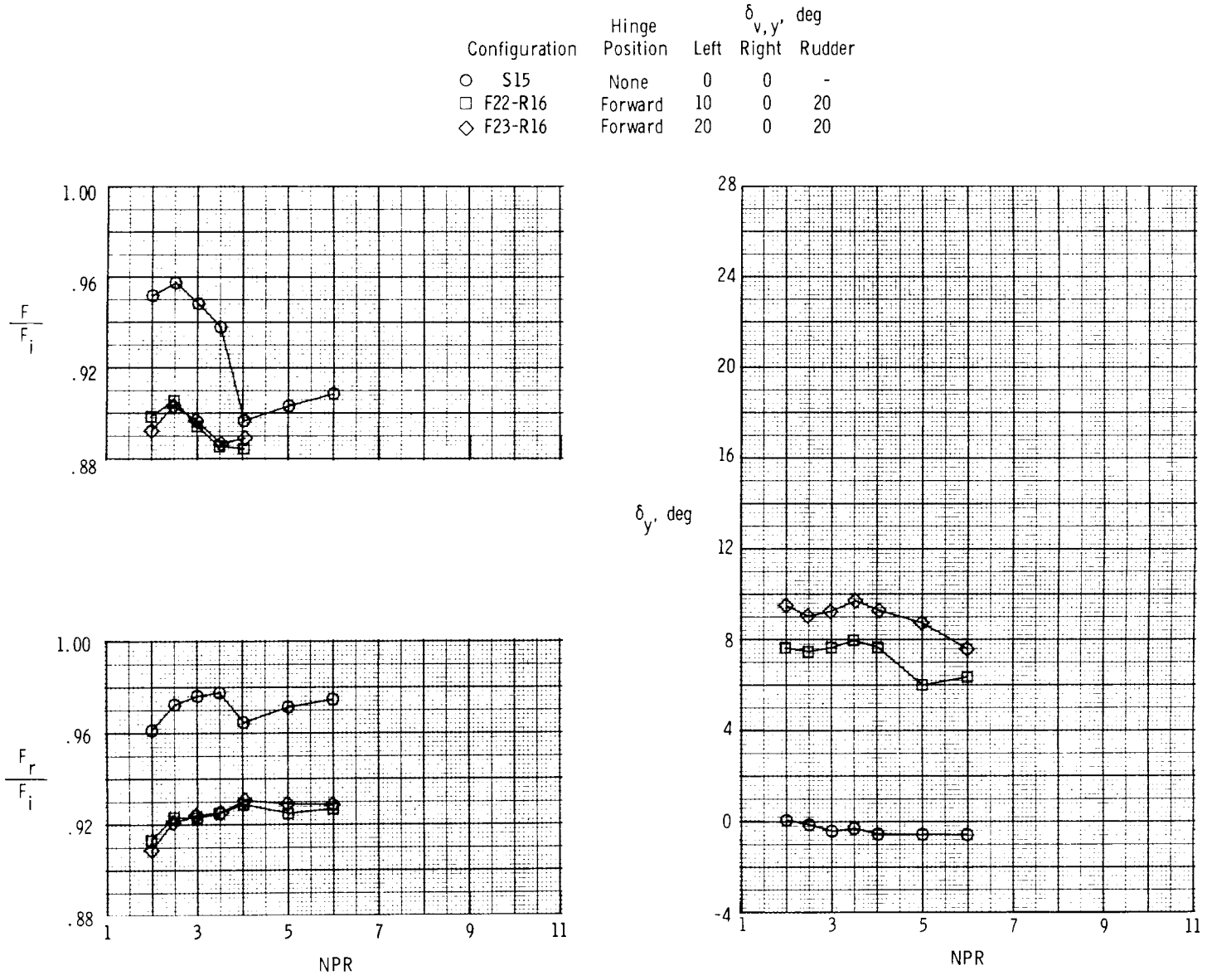

Figure 33. Effect of yaw vectoring on nozzle thrust ratio, resultant thrust ratio, and resultant yaw vector angle for A/B power 2-D C-D nozzle, $\delta_{v,p} = 20.28°$, with a combination of the downstream flap and the powered rudder yaw vector concepts. Left downstream flap deflected.

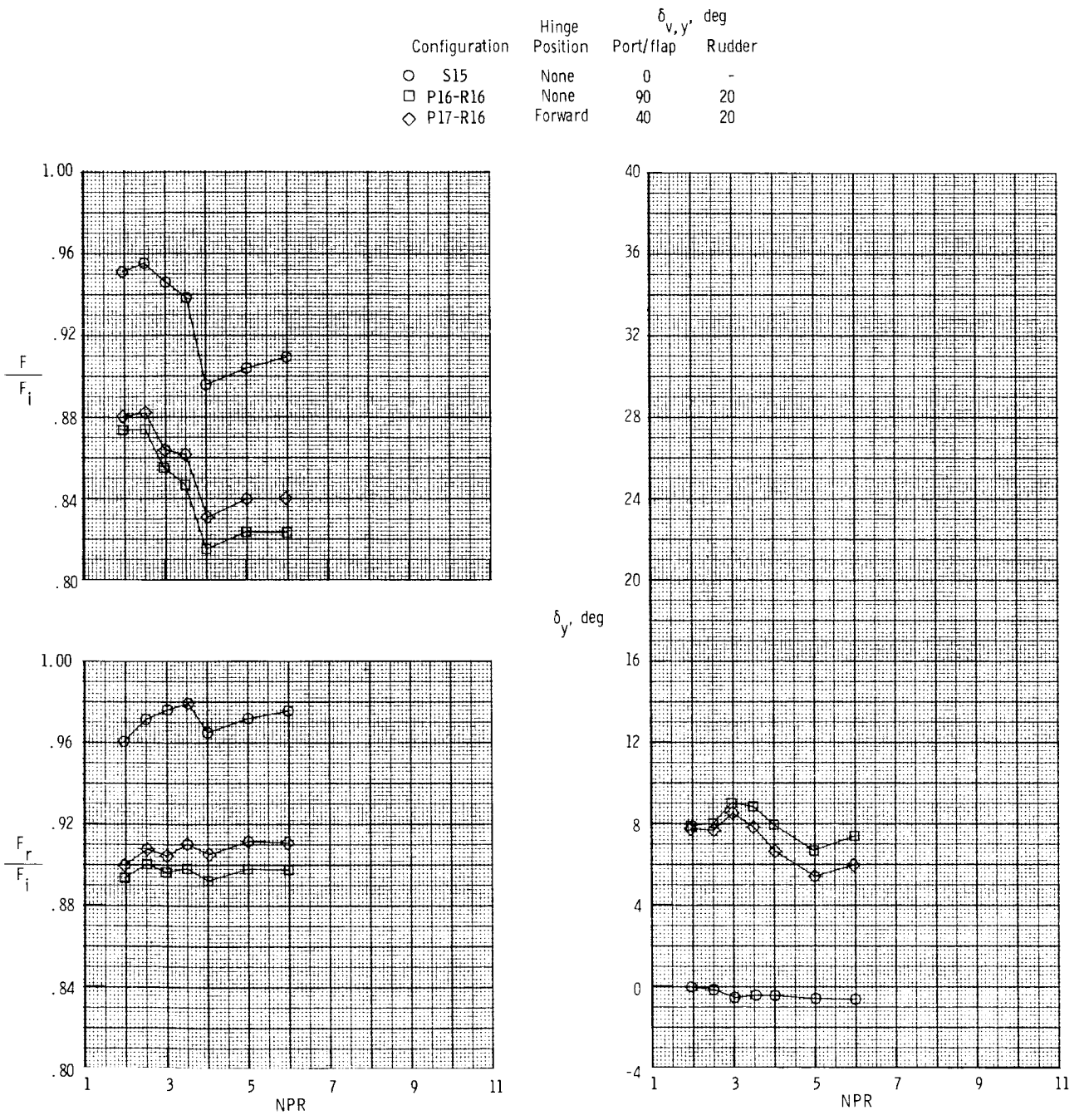

Figure 34. Effect of yaw vectoring on nozzle thrust ratio, resultant thrust ratio, and resultant yaw vector angle for A/B power 2-D C-D nozzle, $\delta_{v,p} = 20.28°$, with a combination of the upstream port/flap and the powered rudder yaw vector concepts.

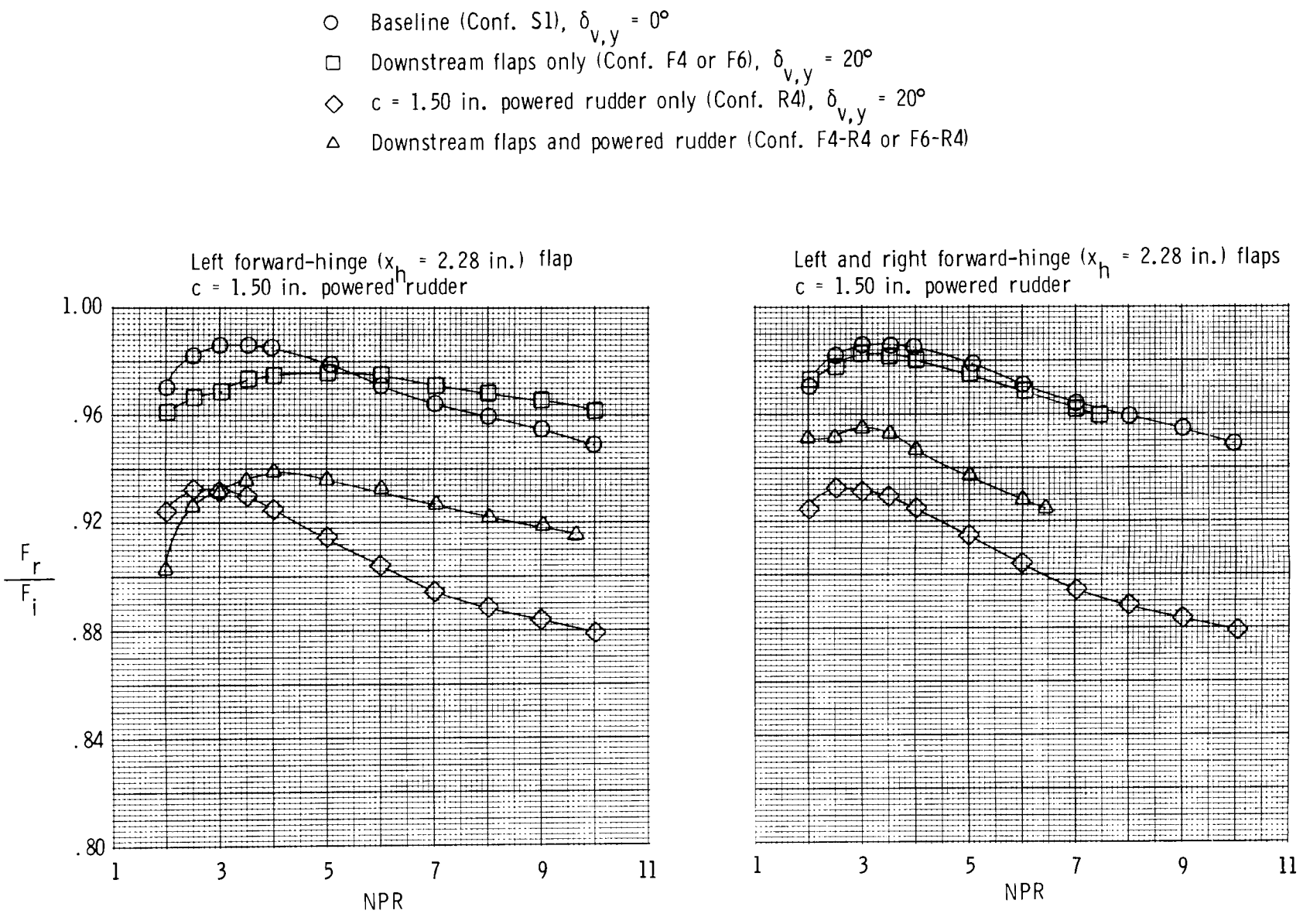

(a) Resultant thrust ratio.

Figure 35. Comparison of dry power (baseline $A_e/A_t = 1.08$) 2-D C-D nozzle performance with individual and combination yaw vectoring concepts (downstream flaps and/or powered rudder) installed. $\delta_{v,p} = 0°$.

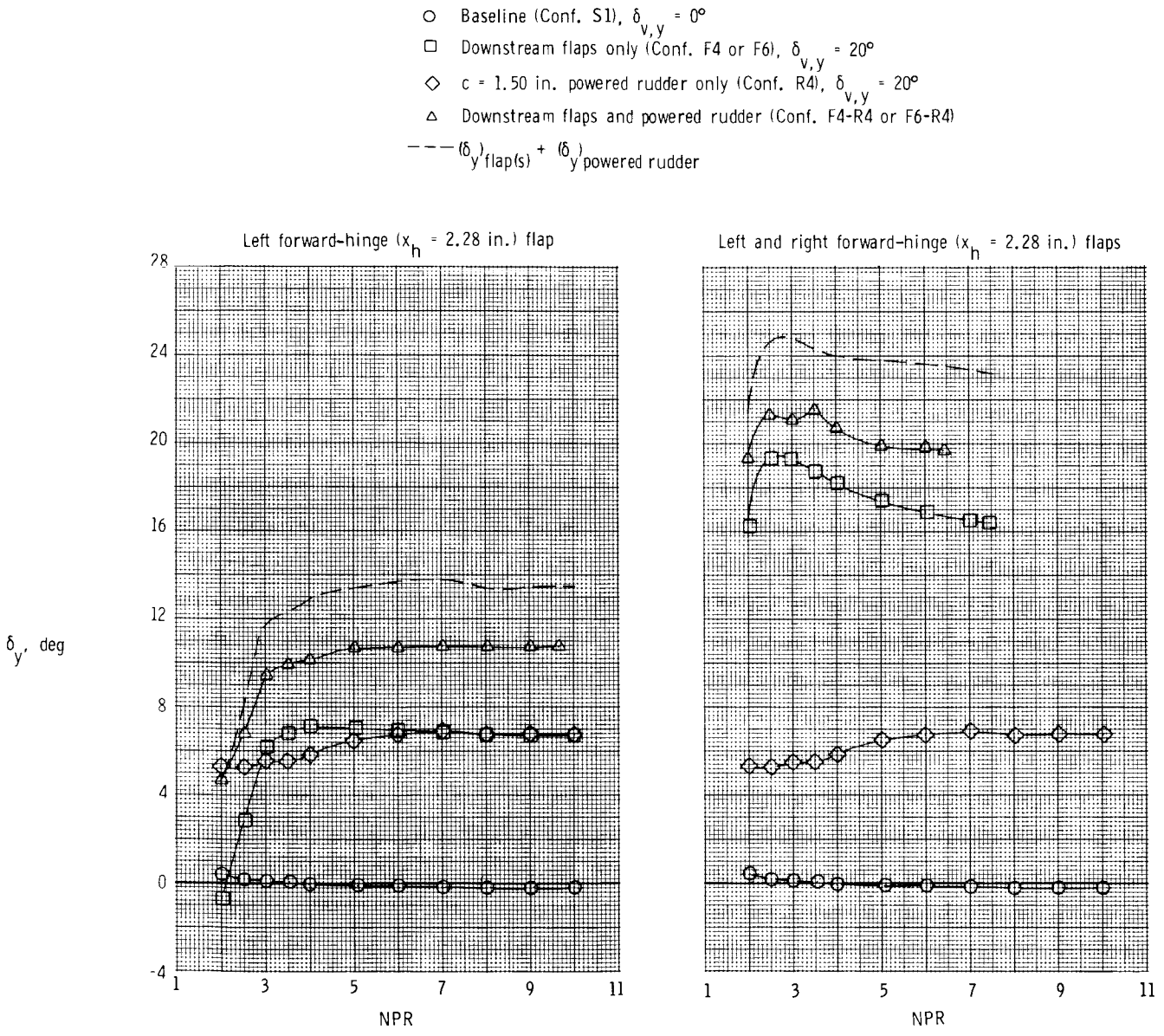

(b) Resultant yaw vector angle.

Figure 35. Concluded.

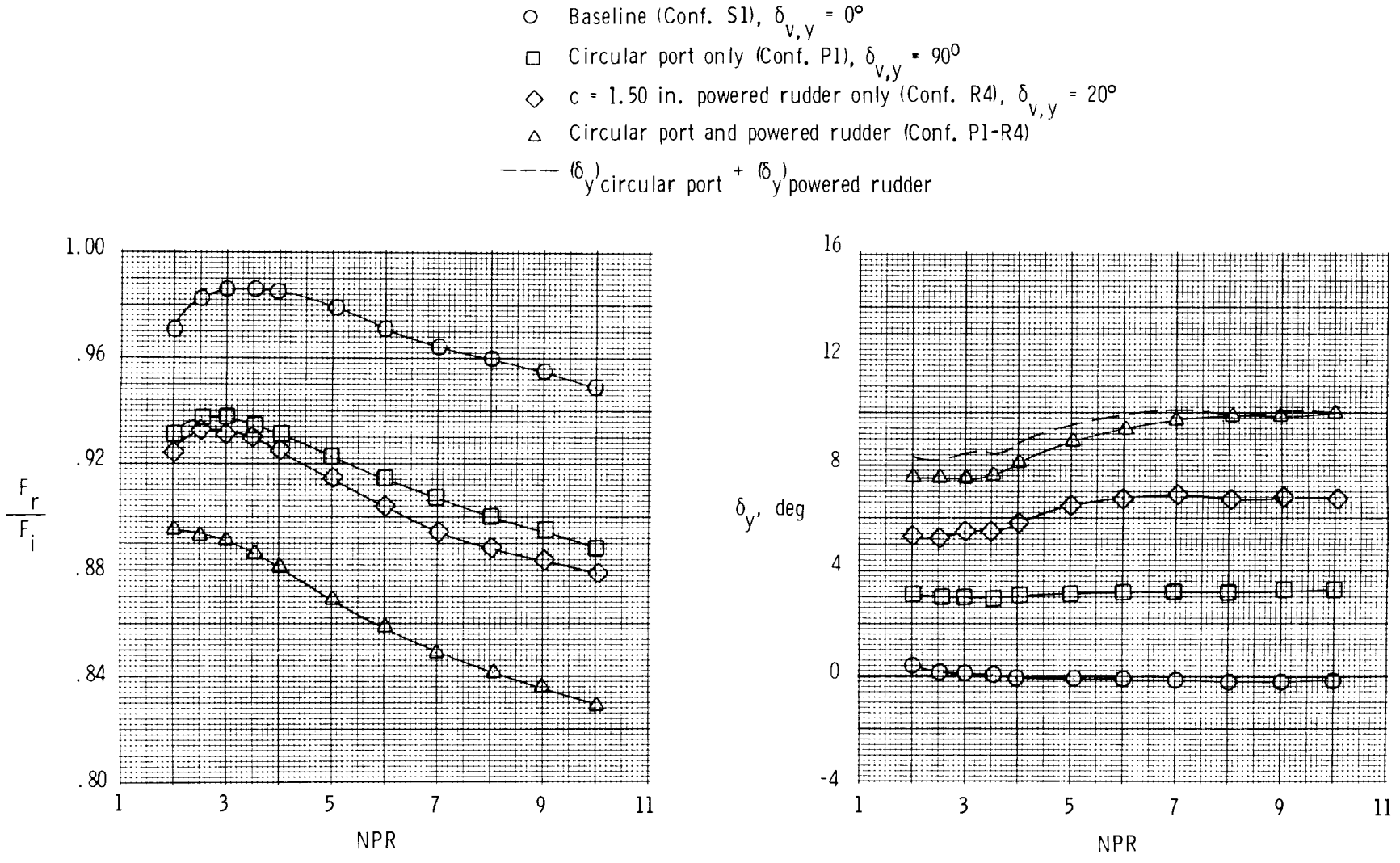

Figure 36. Comparison of dry power (baseline $A_e/A_t = 1.08$) 2-D C-D nozzle performance with individual and combined yaw vectoring concepts (circular port and/or powered rudder) installed. $\delta_{v,p} = 0°$.

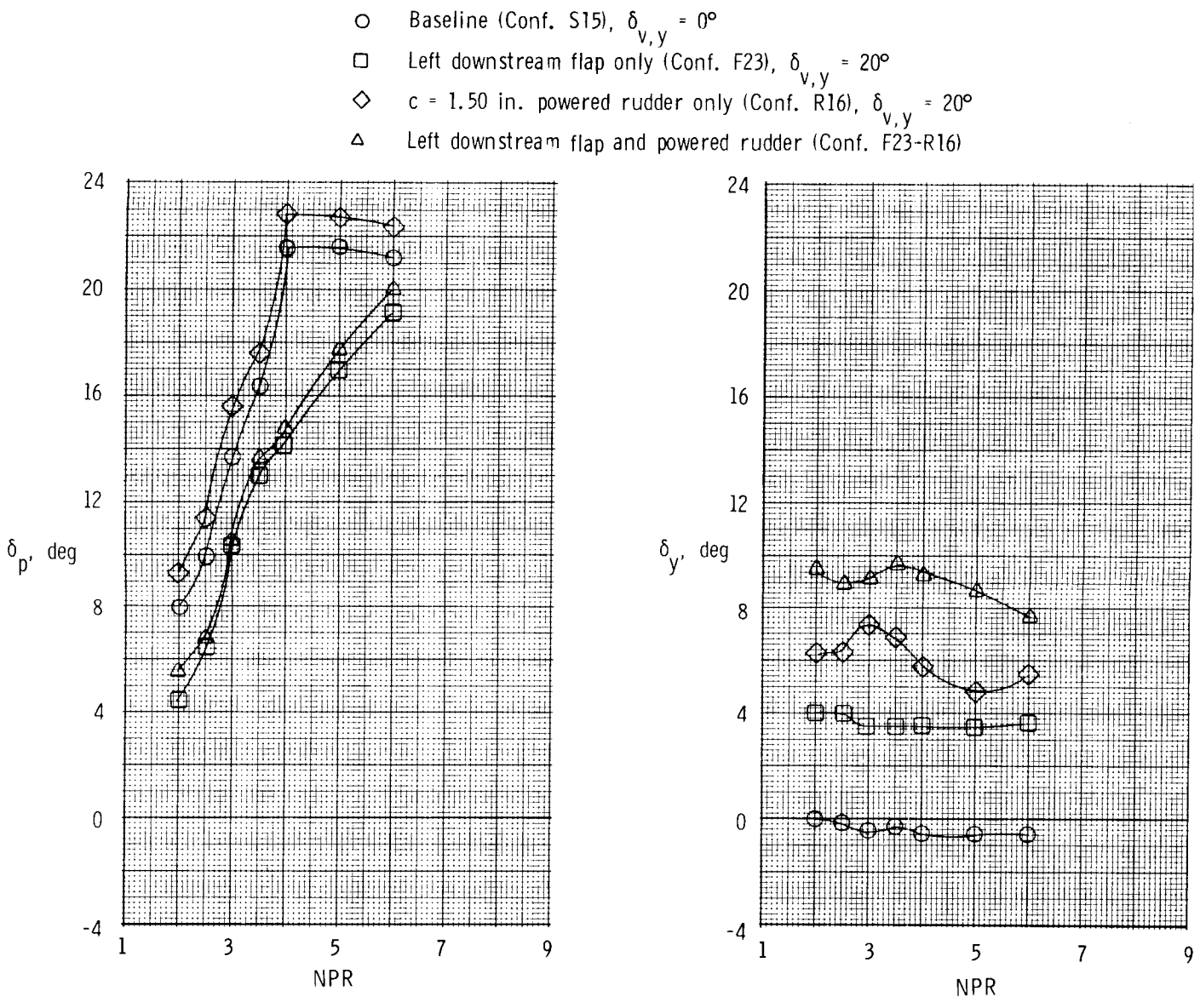

(a) Left downstream flap and powered rudder.

Figure 37. Effect of simultaneous pitch and yaw thrust vectoring on resultant thrust vector angles of 2-D C-D nozzle with combination yaw vectoring concepts installed. A/B power nozzle, $\delta_{v,p} = 20.28°$.

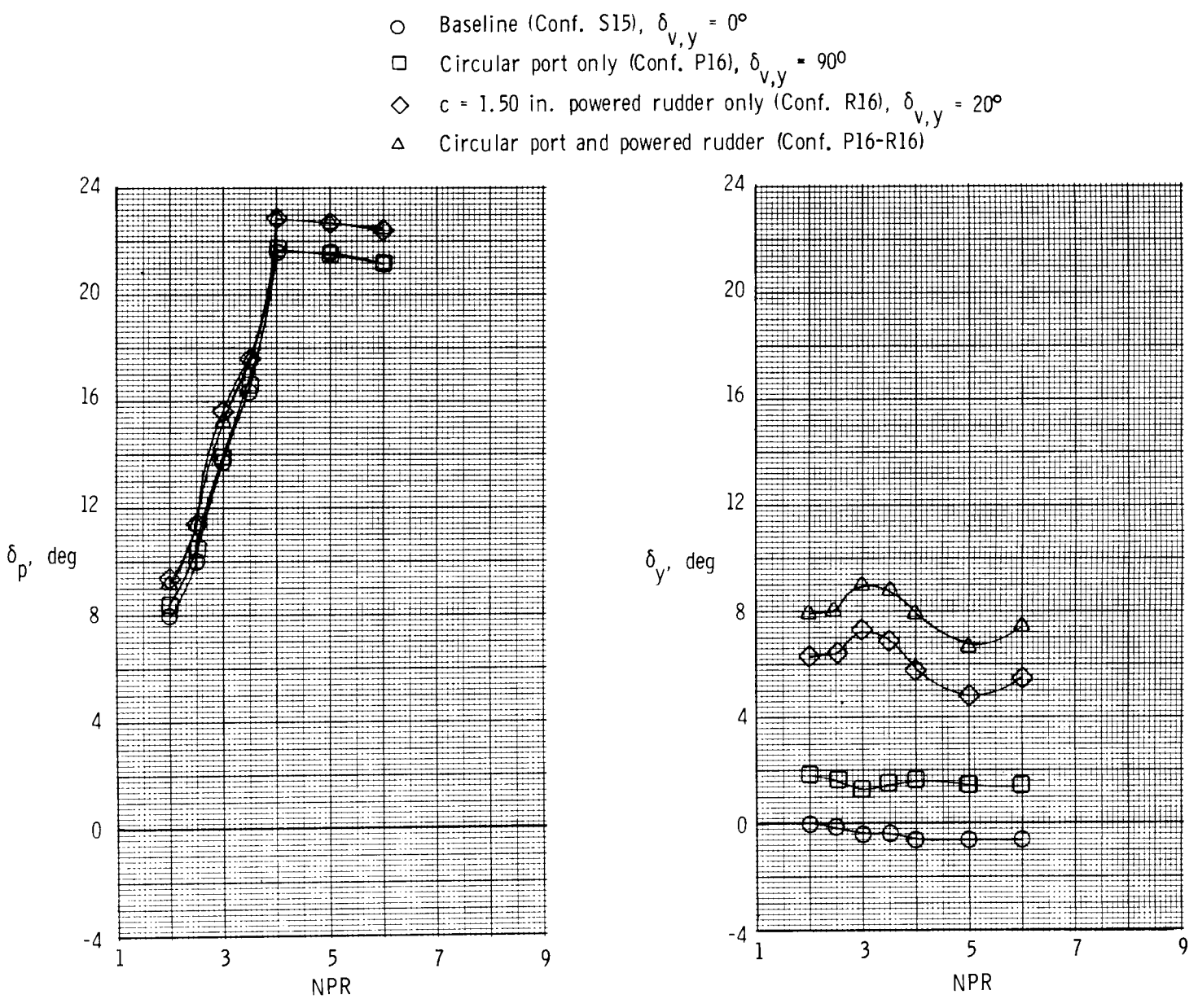

(b) Circular port and powered rudder.

Figure 37. Concluded.

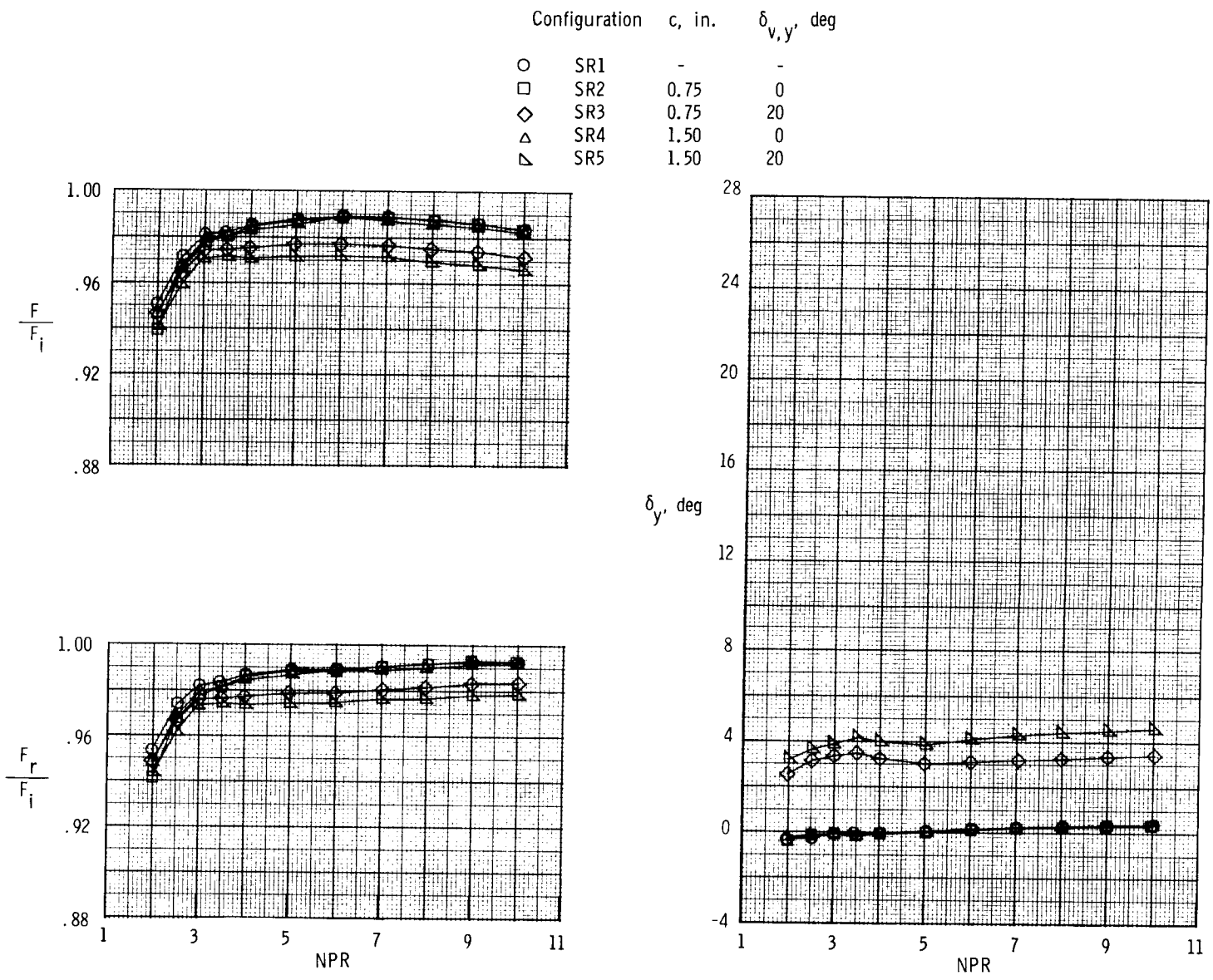

(a) $(A_e/A_t)_i = 1.10$; $(A_e/A_t)_e = 1.41$; $\delta_{v,p} = 0°$.

Figure 38. Effect of yaw vectoring on nozzle thrust ratio, resultant thrust ratio, and resultant yaw vector angle for SERN configurations with post-exit flaps yaw vectoring concept.

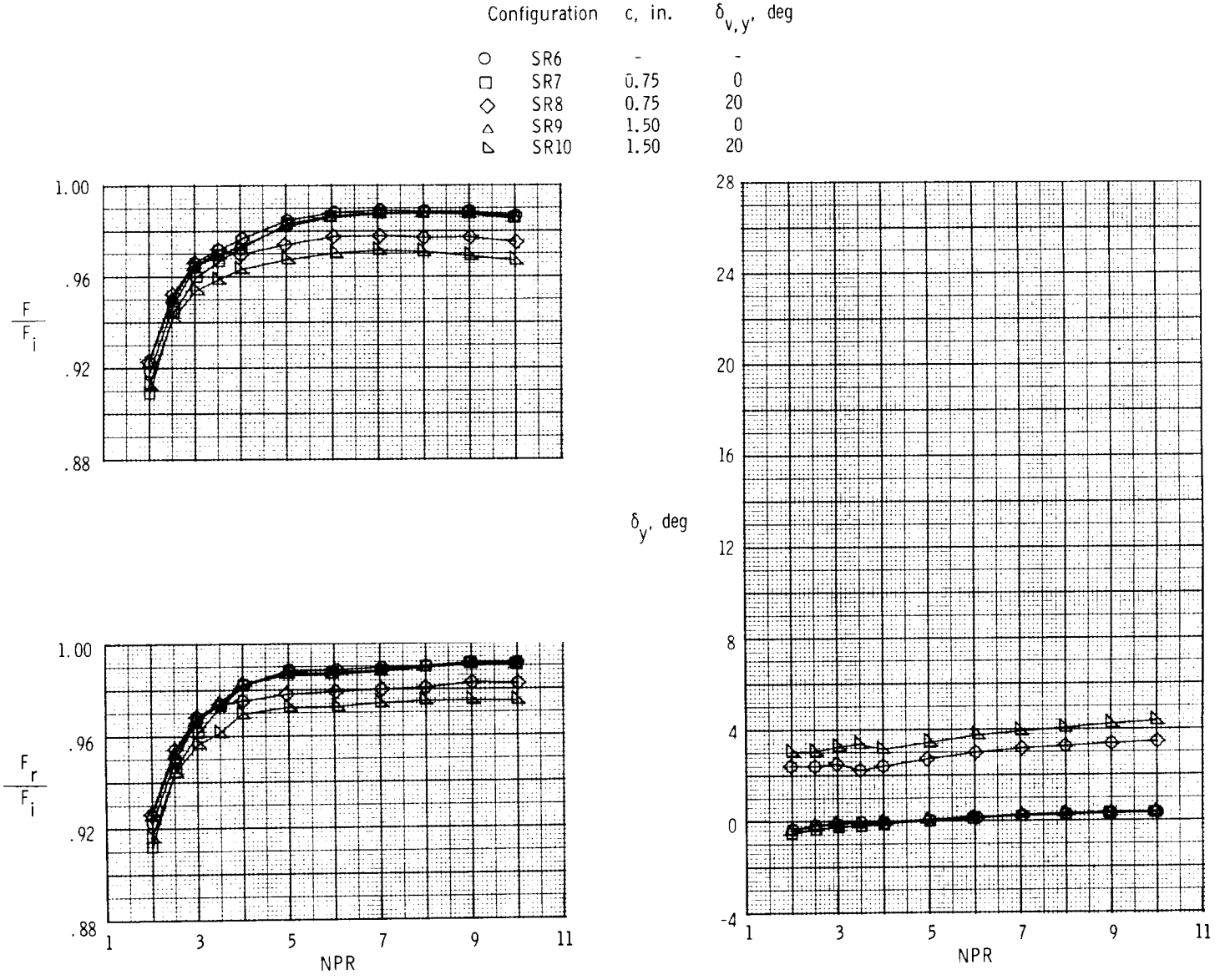

(b) $(A_e/A_t)_i = 1.24$; $(A_e/A_t)_e = 1.50$; $\delta_{v,p} = 0°$.

Figure 38. Continued.

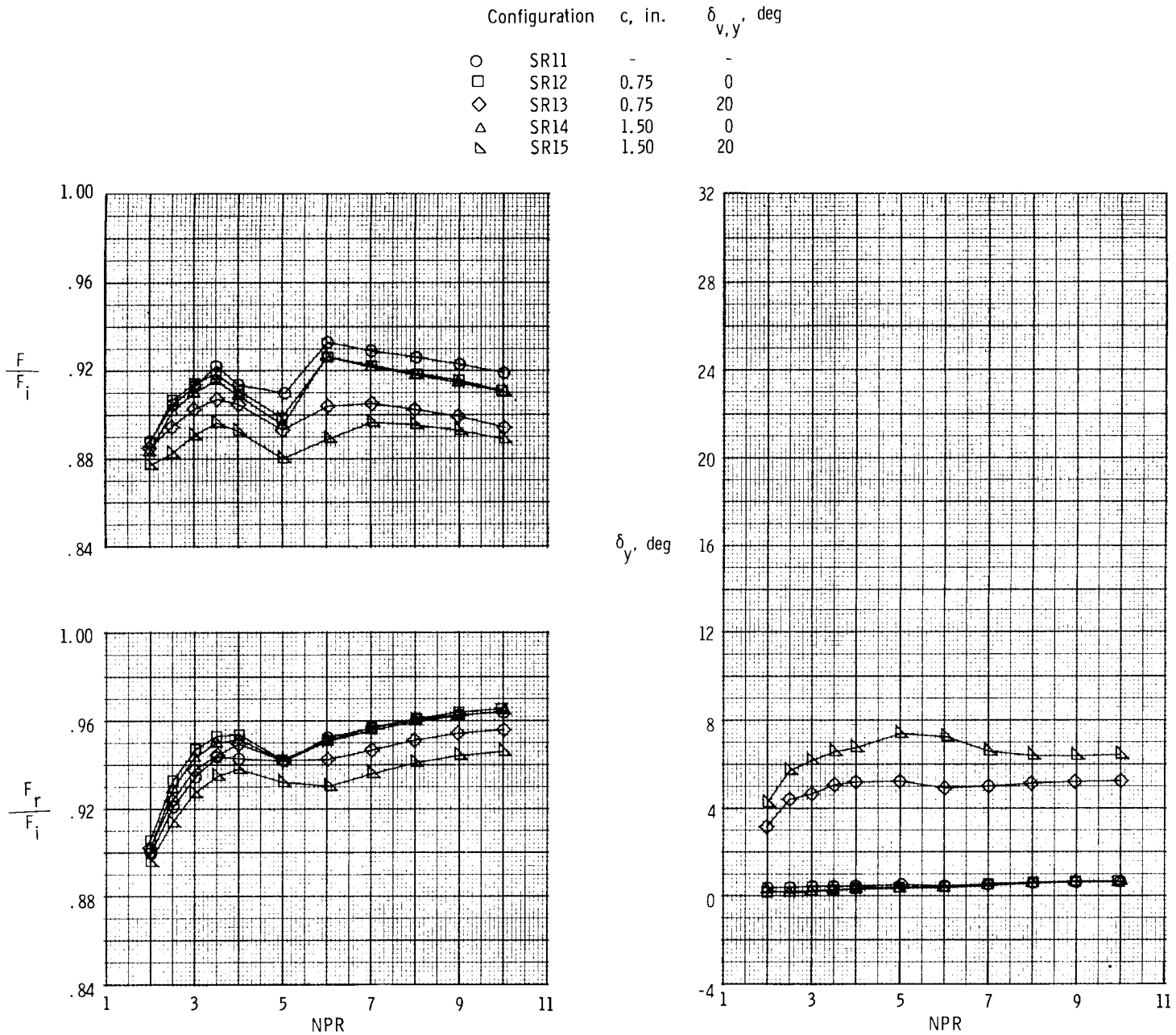

(c) Upper flap pitch vectoring; $\delta_{v,p} = 20°$.

Figure 38. Continued.

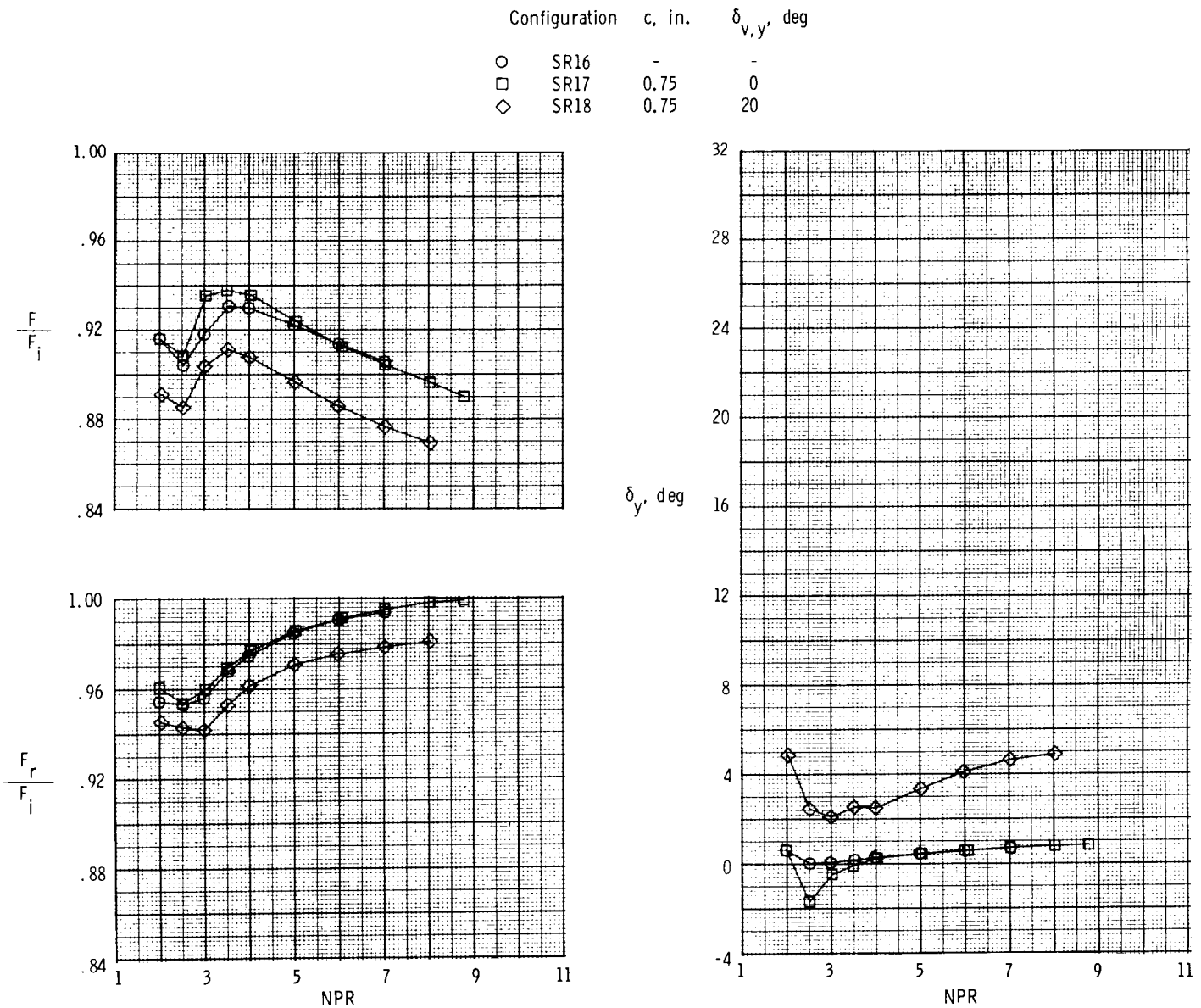

(d) Upper and lower flap pitch vectoring; $\delta_{v,p} = 20°$.

Figure 38. Concluded.

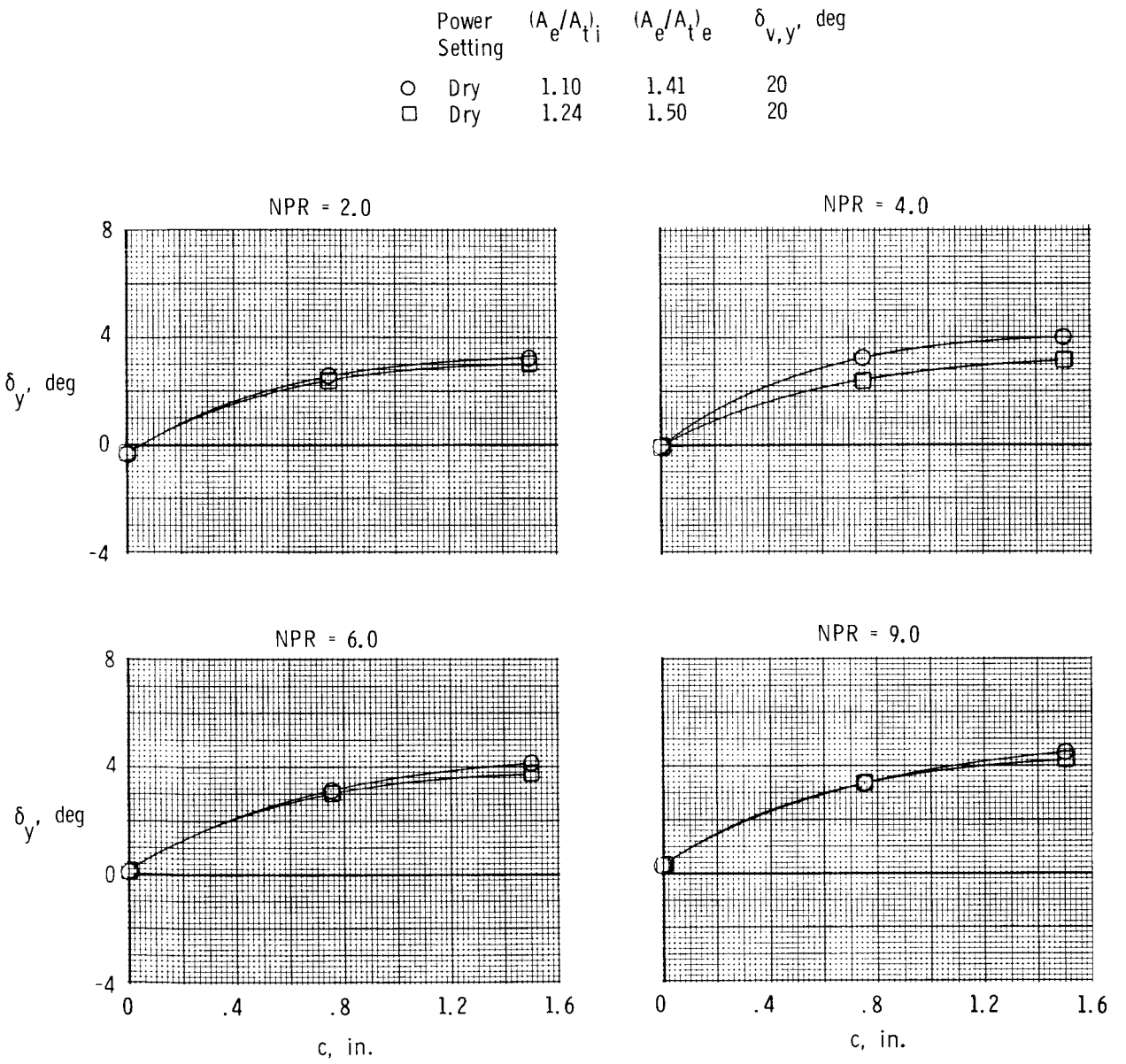

Figure 39. Effect of flap chord length and nozzle expansion ratio on resultant yaw vector angle for dry power SERN with post-exit flaps yaw vectoring concept installed. $\delta_{v,p} = 0°$. Data are cross plotted; symbols are for line identification only.

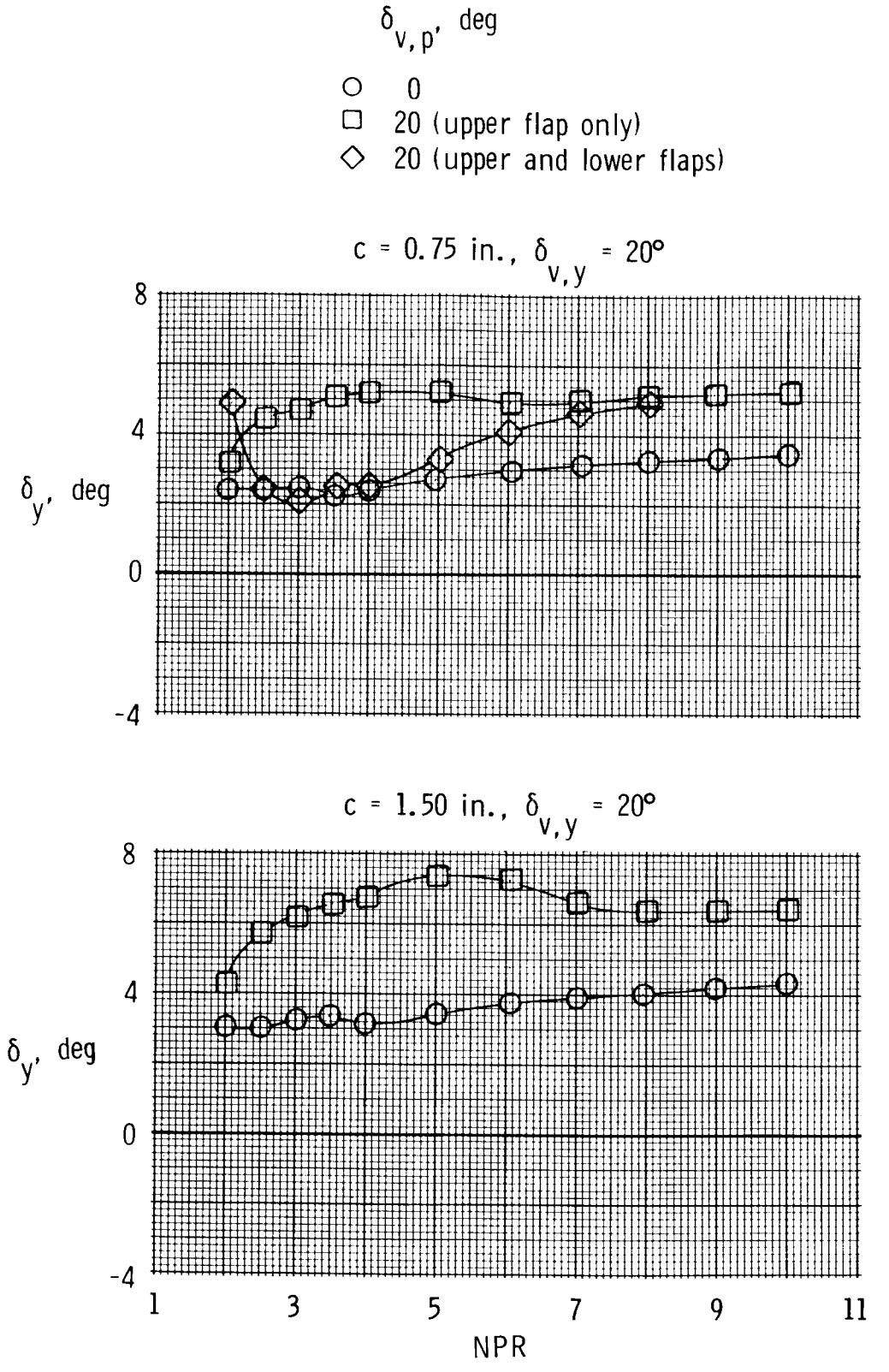

(a) Resultant yaw vector angle.

Figure 40. Effect of simultaneous pitch and yaw thrust vectoring on resultant vector angles of dry power SERN with post-exit flaps yaw vectoring concept installed. Baseline $(A_e/A_t)_i = 1.24$ and $(A_e/A_t)_e = 1.50$.

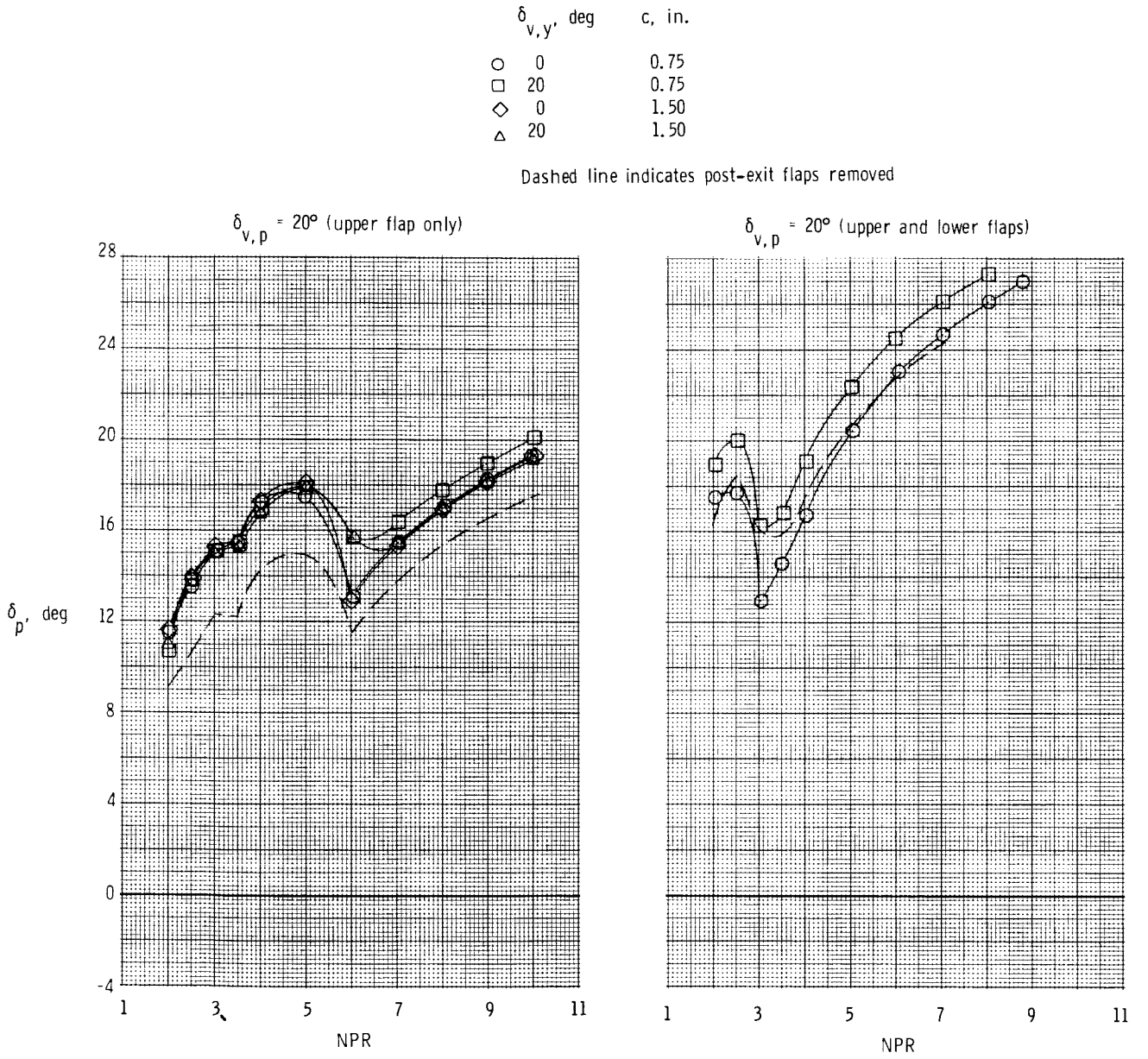

(b) Resultant pitch vector angle.

Figure 40. Concluded.

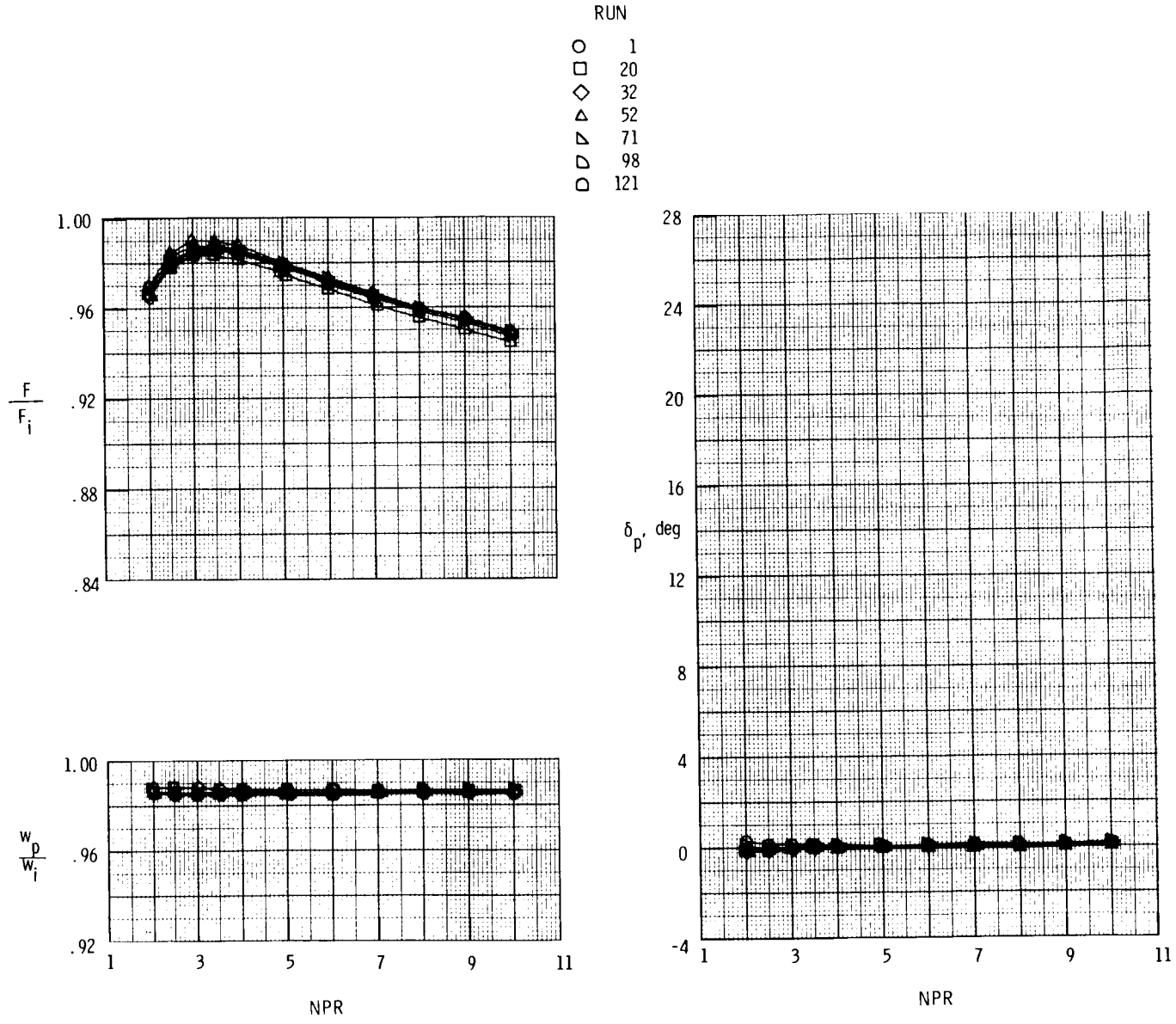

Figure 41. Variation of nozzle thrust ratio, discharge coefficient, and resultant pitch vector angle with nozzle pressure ratio for dry power 2-D C-D nozzle, $A_e/A_t = 1.08$ and $\delta_{v,p} = 0°$. Configuration S1.

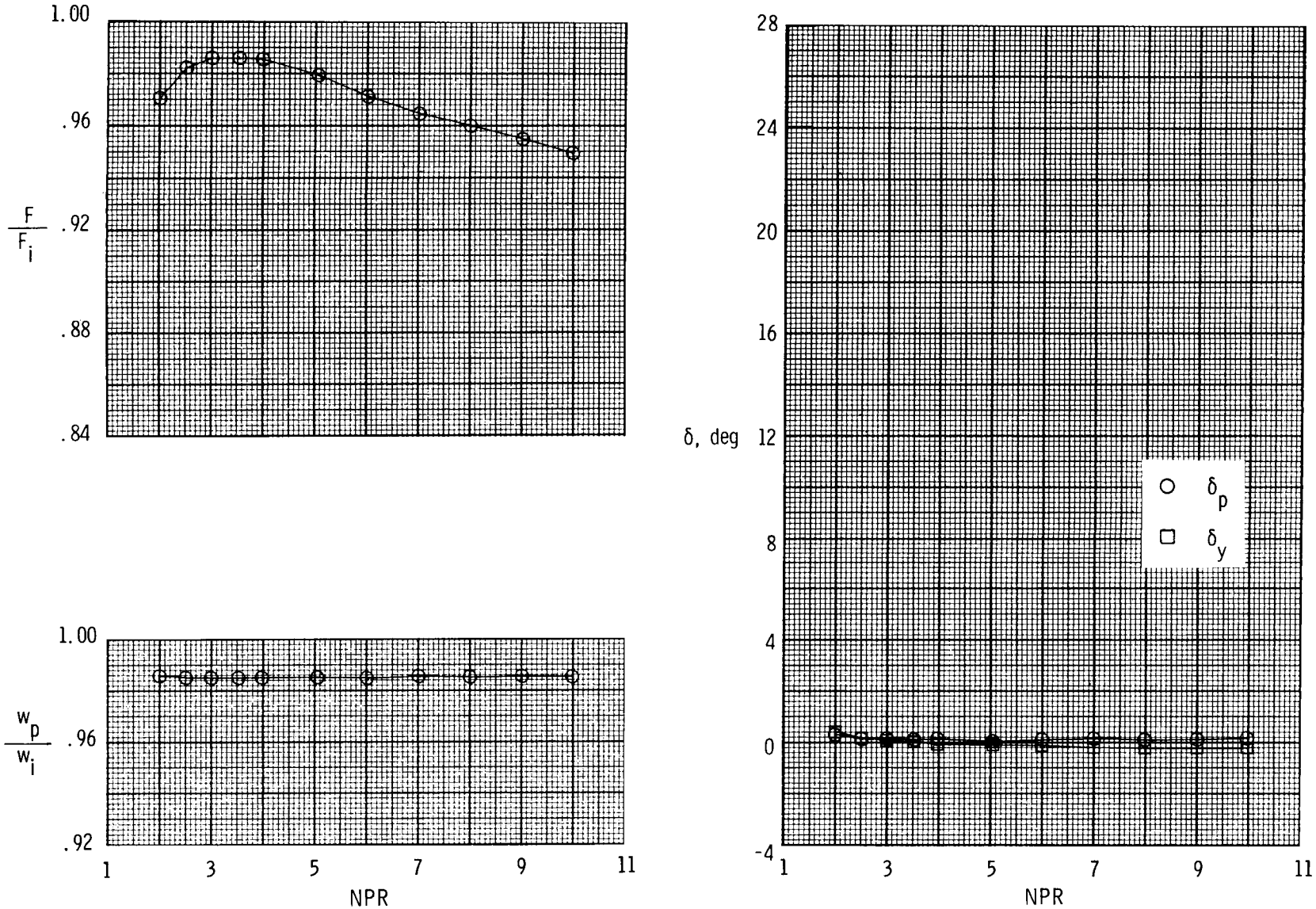

(a) Configuration S1; $(x_s - x_t)/l_s = 1.00$.

Figure 42. Variation of nozzle thrust ratio, discharge coefficient, and resultant thrust vector angles with nozzle pressure ratio for dry power 2-D C-D nozzle, baseline $A_e/A_t = 1.08$ and $\delta_{v,p} = 0°$, with translating sidewall yaw vectoring concept. Dashed line indicates resultant thrust ratio F_r/F_i.

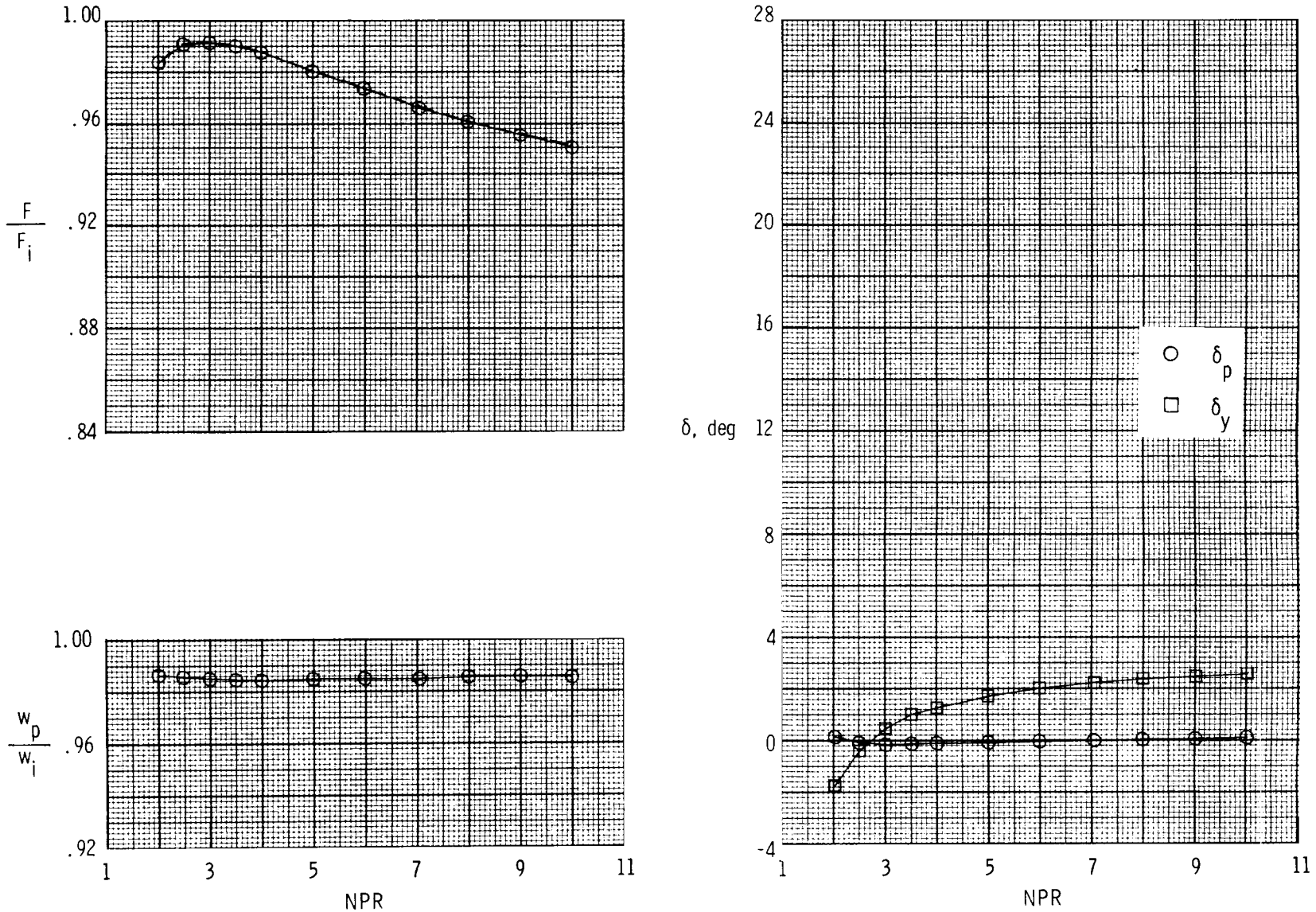

(b) Configuration S2; $(x_s - x_t)/l_s = 0.63$.

Figure 42. Continued.

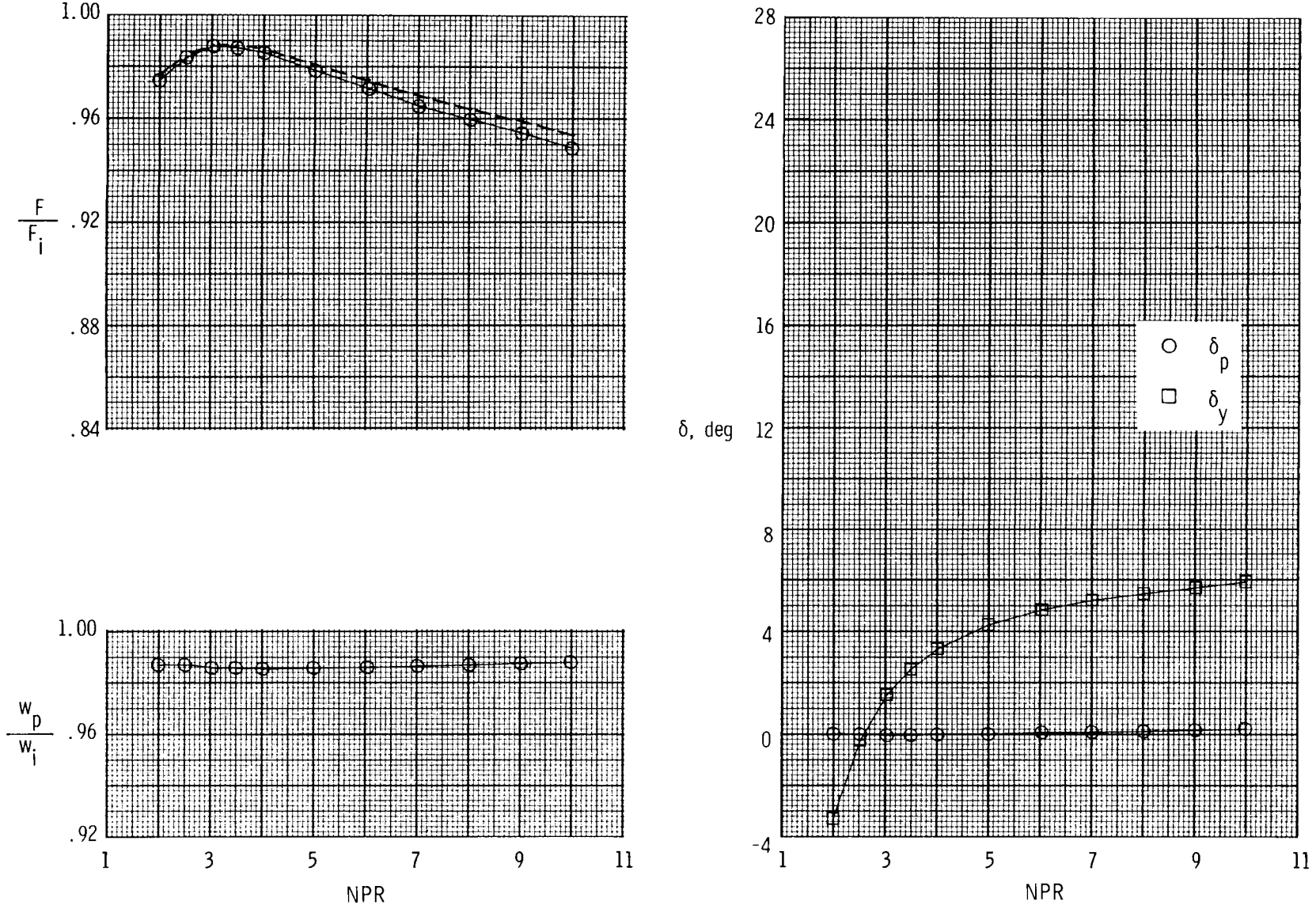

(c) Configuration S3; $(x_s - x_t)/l_s = 0.25$.

Figure 42. Continued.

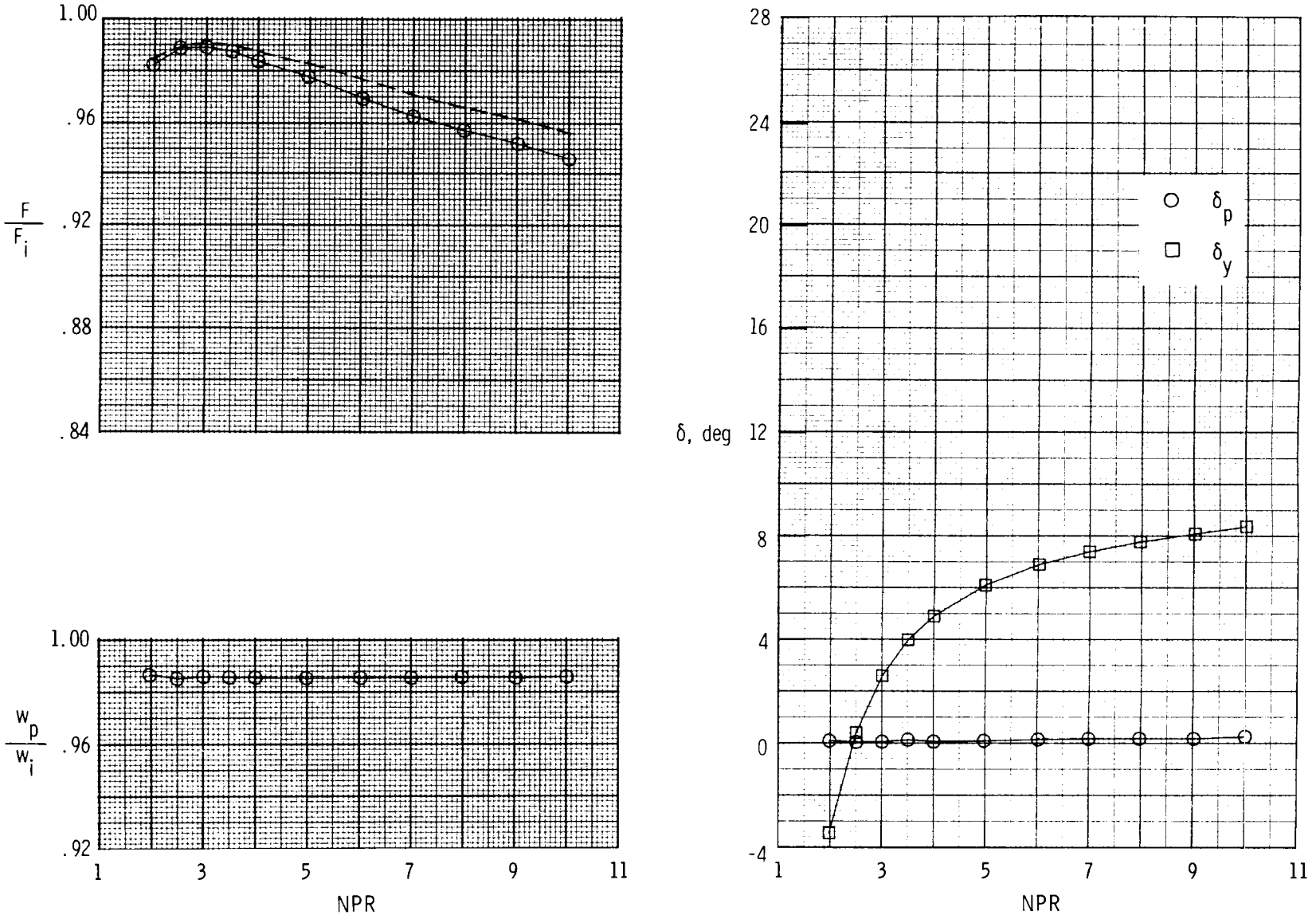

(d) Configuration S4; $(x_s - x_t)/l_s = 0$.

Figure 42. Continued.

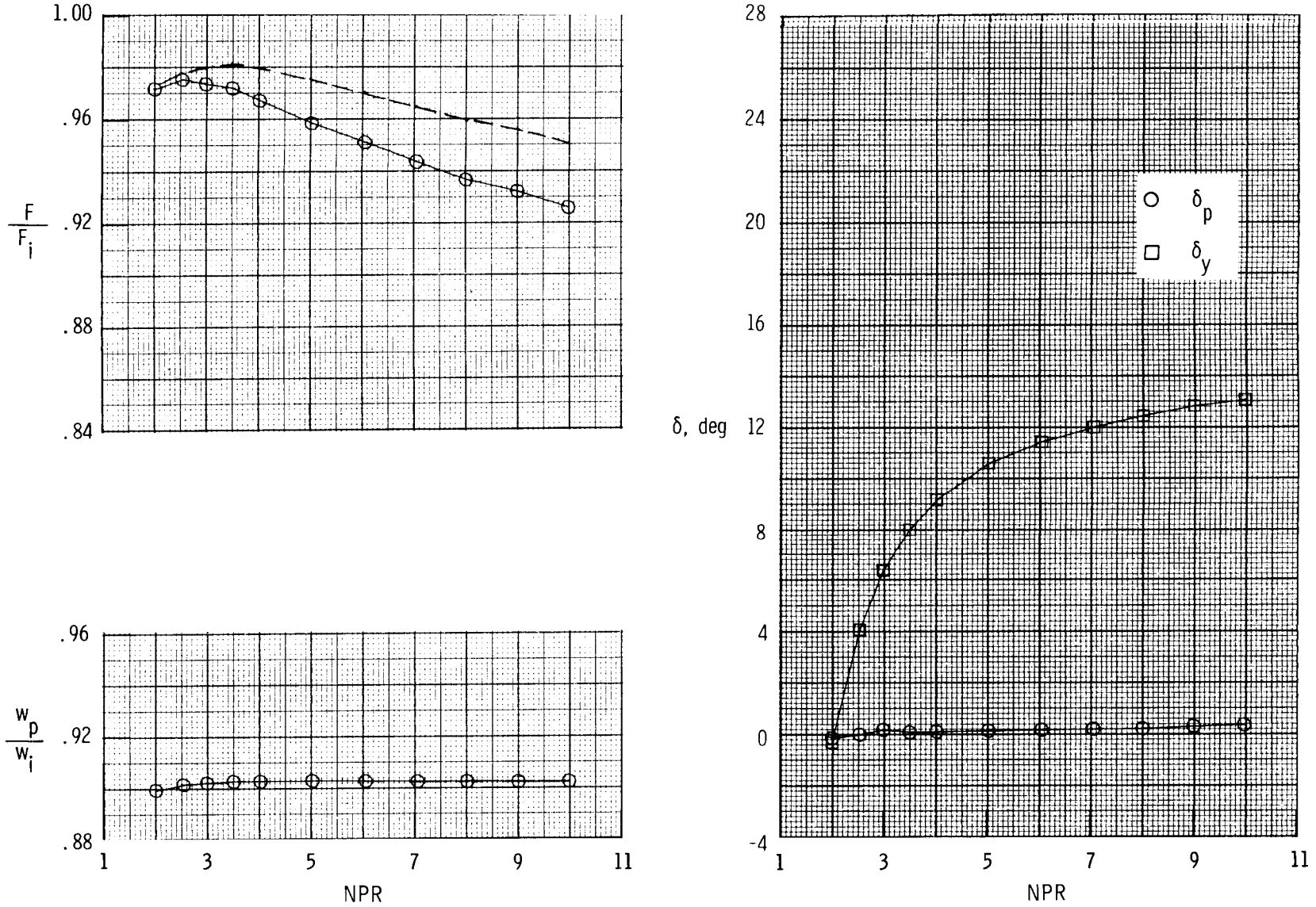

(e) Configuration S5; $(x_s - x_t)/l_s = -0.25$.

Figure 42. Concluded.

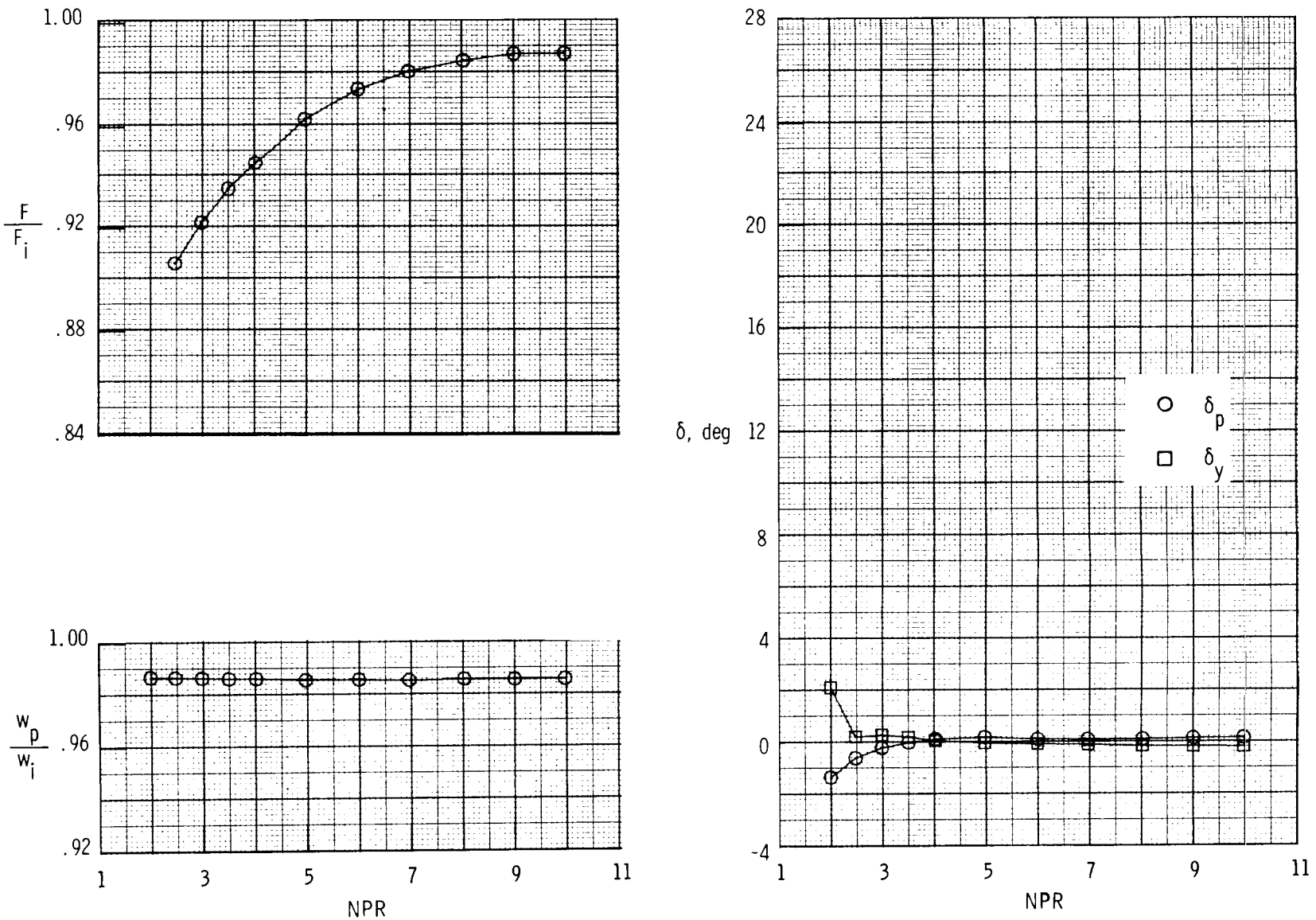

(a) Configuration S6; $(x_s - x_t)/l_s = 1.00$.

Figure 43. Variation of nozzle thrust ratio, discharge coefficient, and resultant thrust vector angles with nozzle pressure ratio for dry power 2-D C-D nozzle, baseline $A_e/A_t = 1.78$ and $\delta_{v,p} = 0°$, with translating sidewall yaw vectoring concept. Dashed line indicates resultant thrust ratio F_r/F_i.

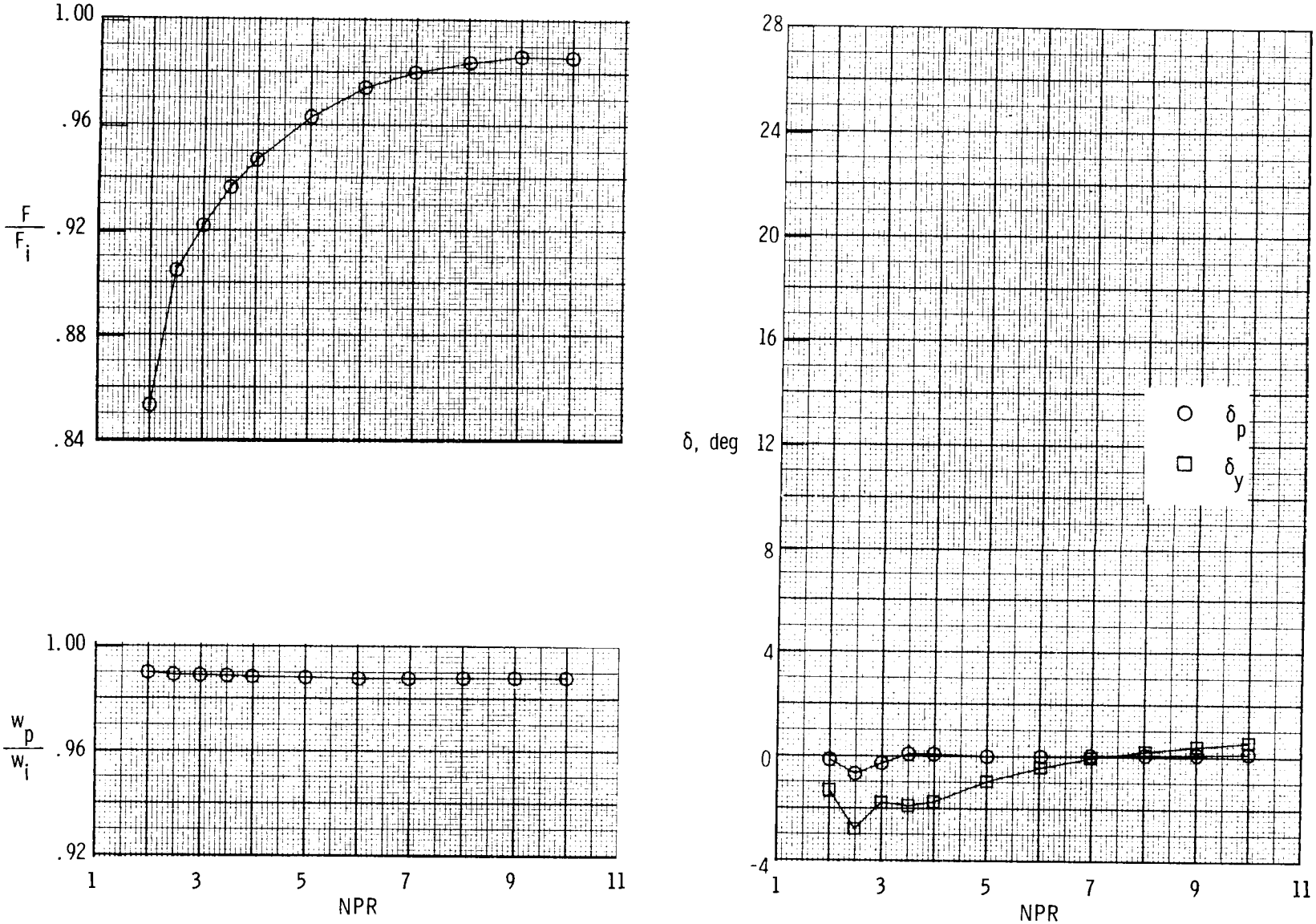

(b) Configuration S7; $(x_s - x_t)/l_s = 0.63$.

Figure 43. Continued.

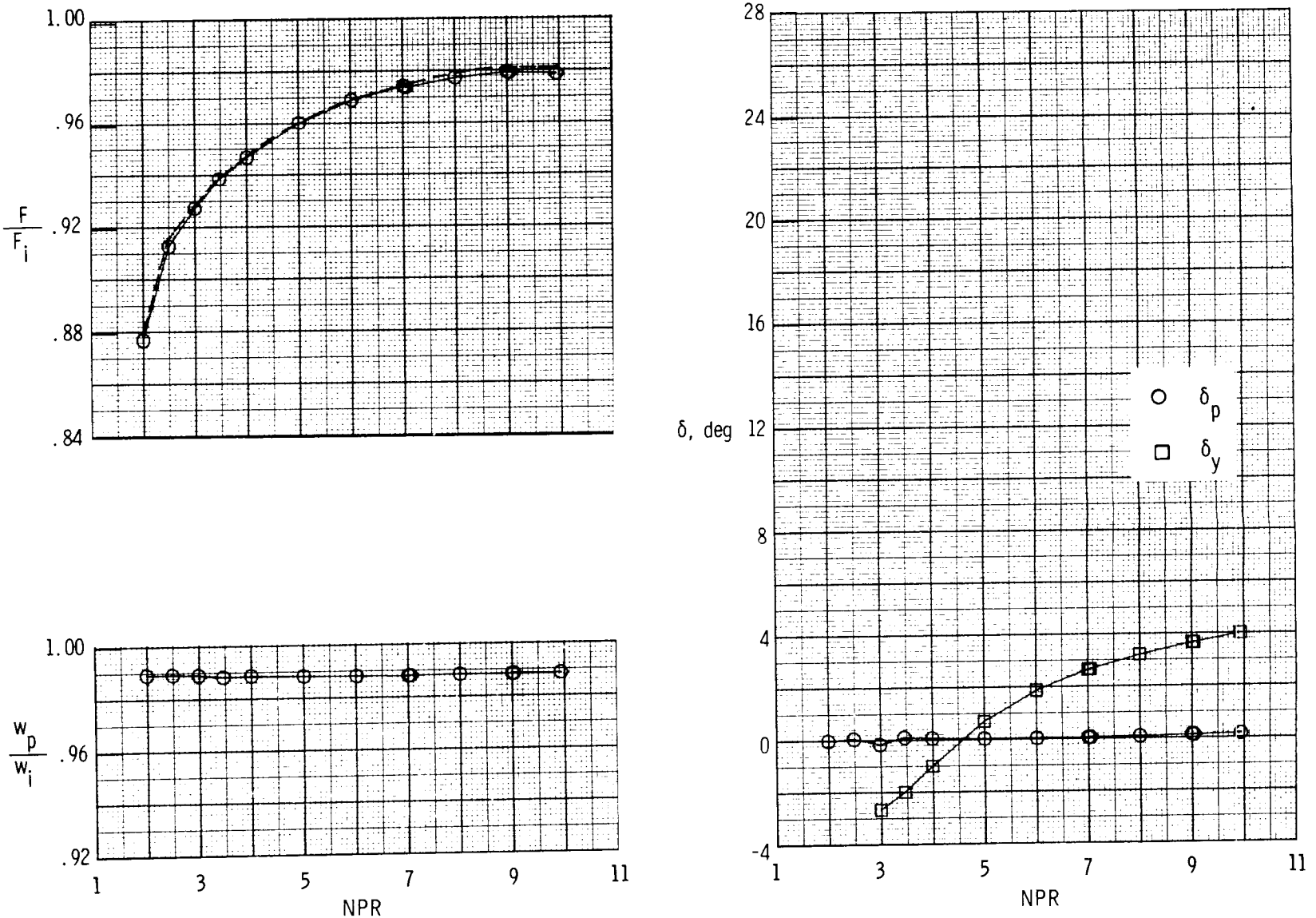

(c) Configuration S8; $(x_s - x_t)/l_s = 0$.

Figure 43. Concluded.

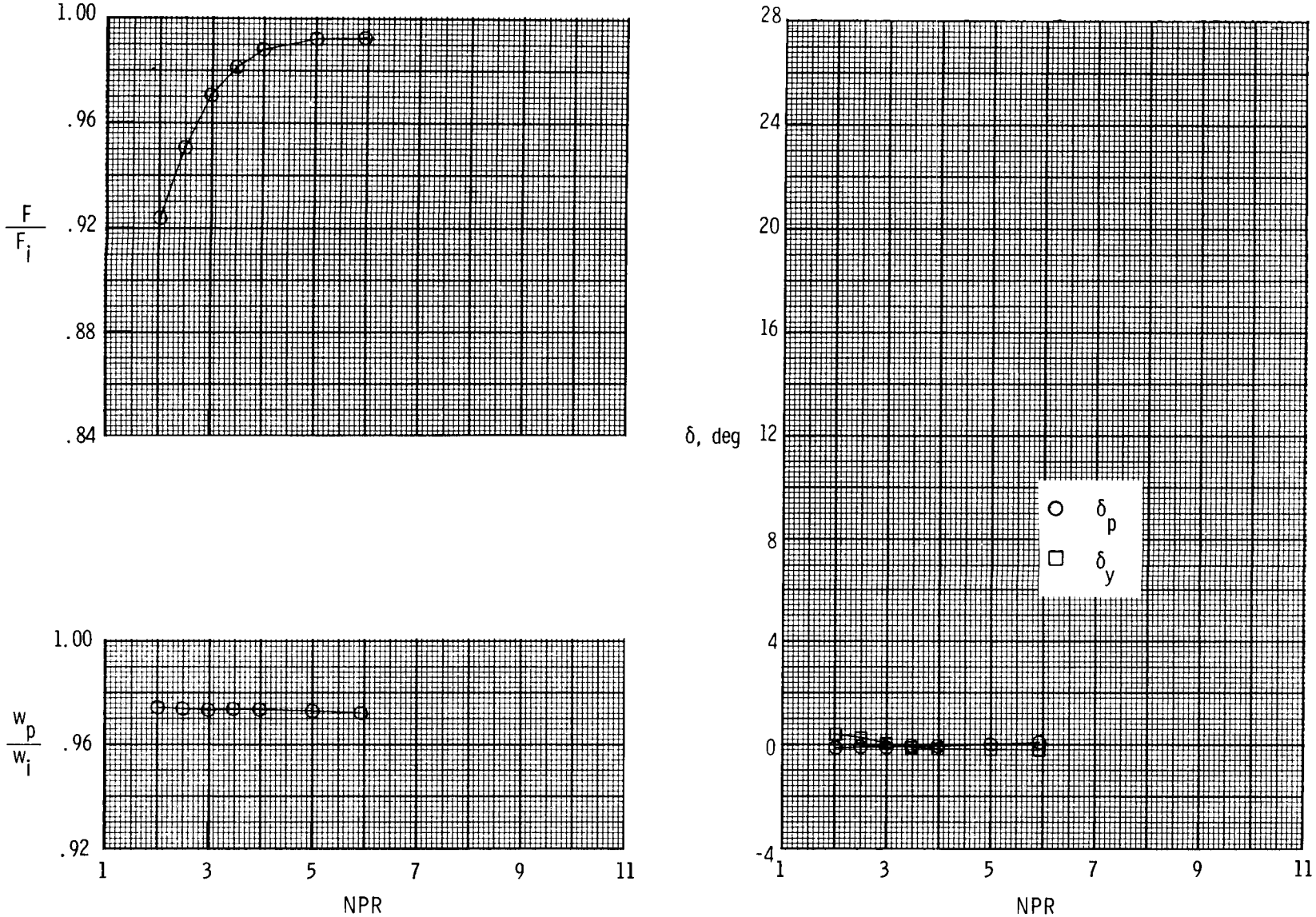

(a) Configuration S9; $(x_s - x_t)/l_s = 1.00$.

Figure 44. Variation of nozzle thrust ratio, discharge coefficient, and resultant thrust vector angles with nozzle pressure ratio for A/B power 2-D C-D nozzle, baseline $A_e/A_t = 1.29$ and $\delta_{v,p} = 0°$, with translating sidewall yaw vectoring concept. Dashed line indicates resultant thrust ratio F_r/F_i.

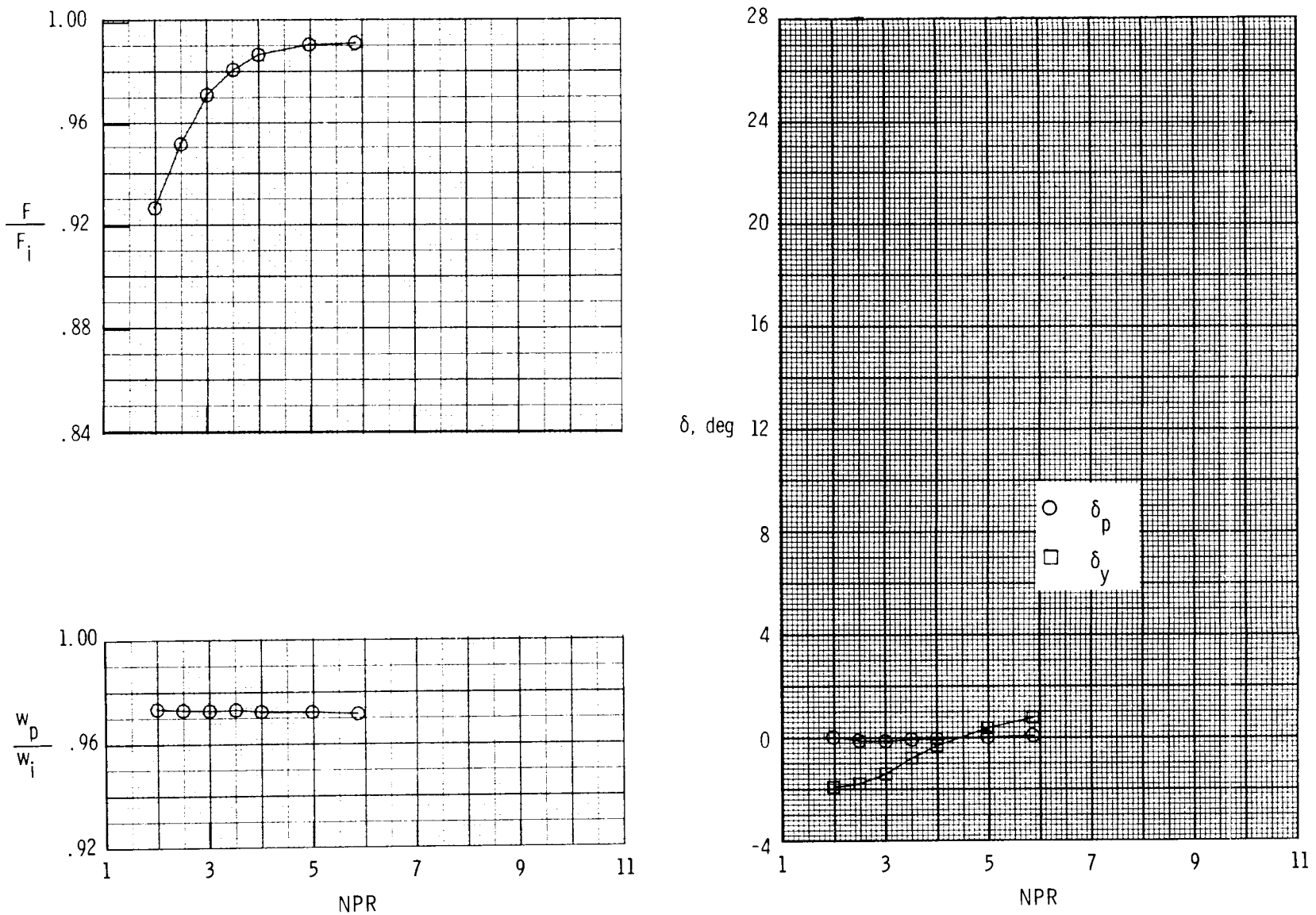

(b) Configuration S10; $(x_s - x_t)/l_s = 0.61$.

Figure 44. Continued.

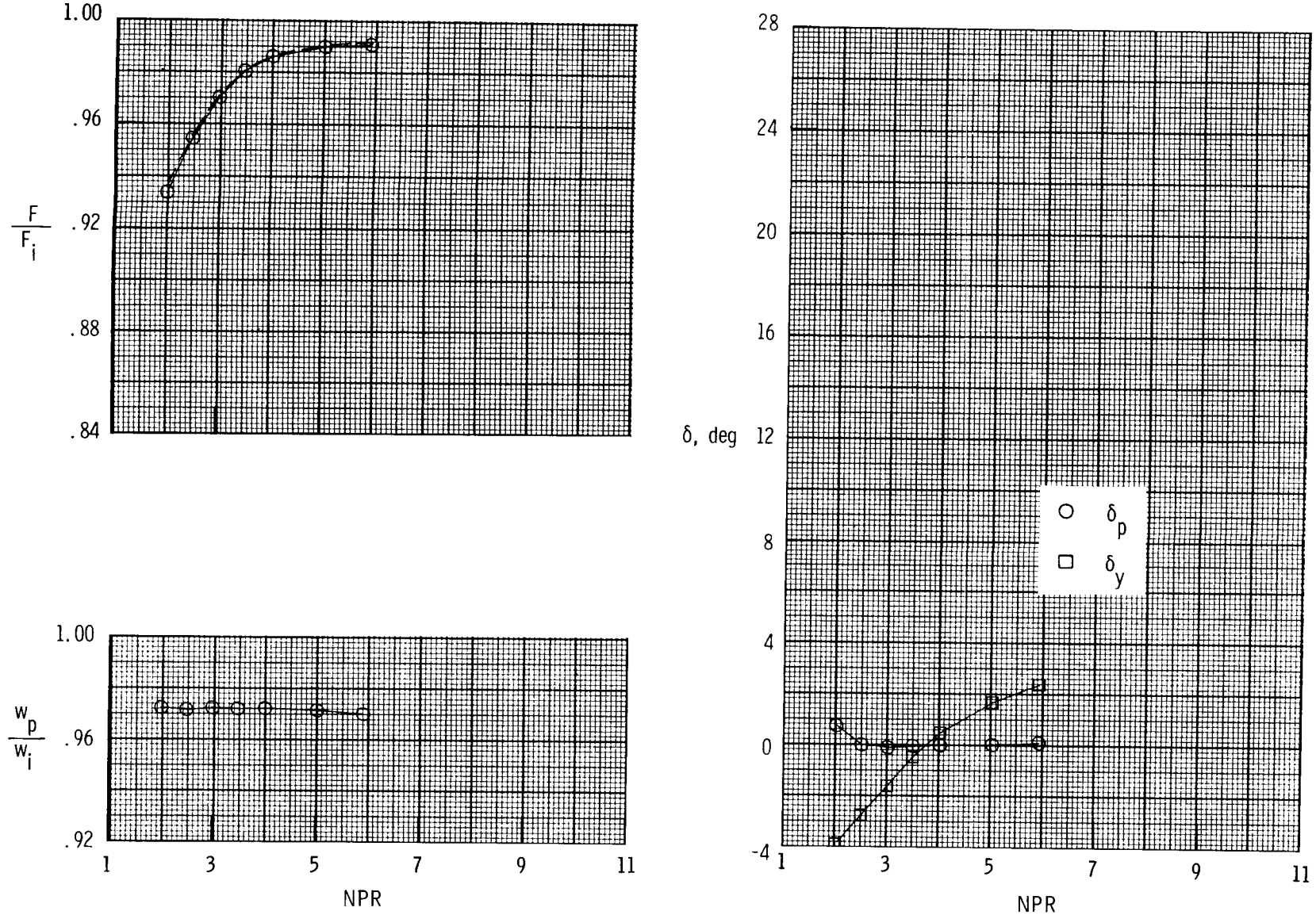

(c) Configuration S11; $(x_s - x_t)/l_s = 0.23$.

Figure 44. Continued.

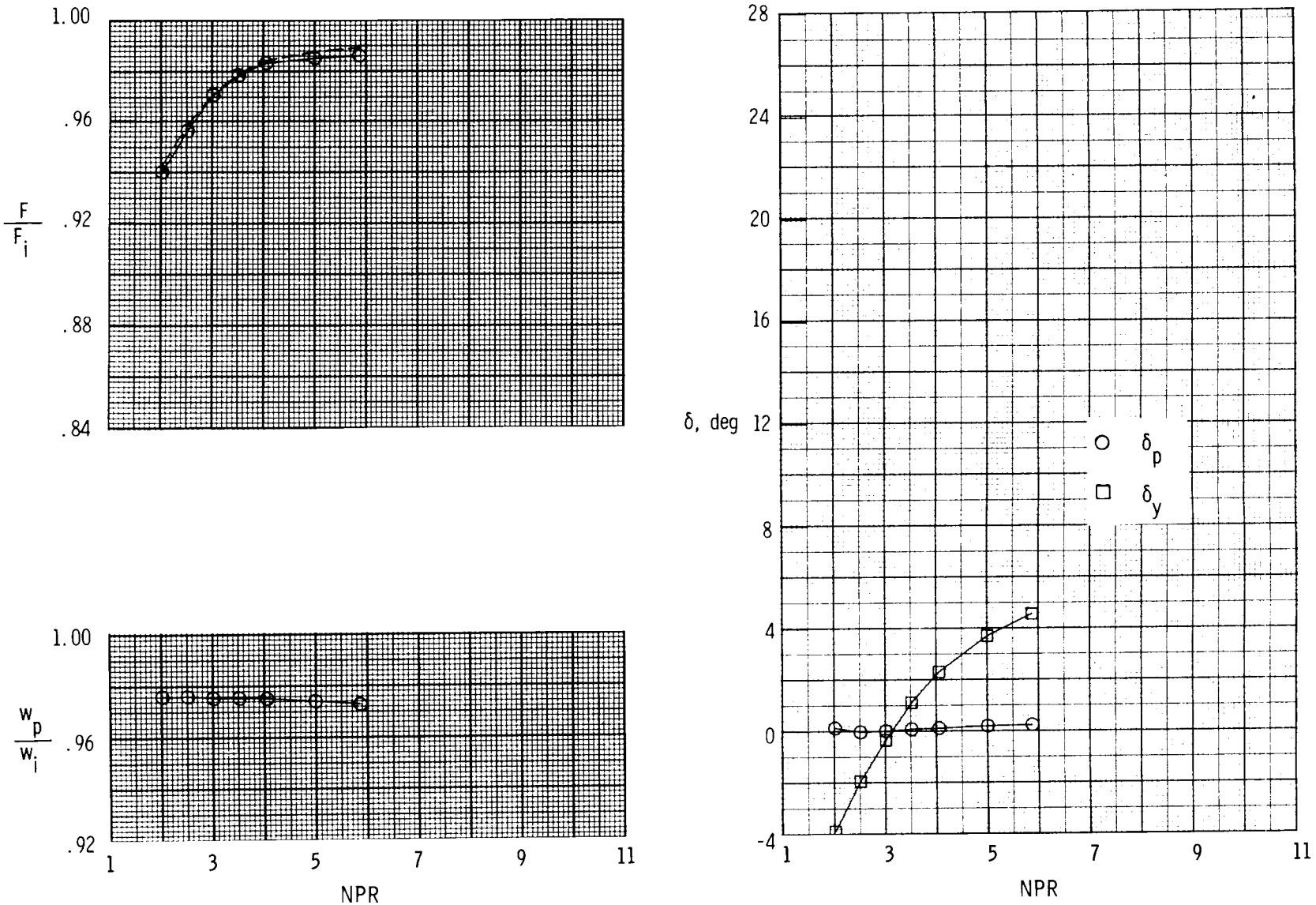

(d) Configuration S12; $(x_s - x_t)/l_s = -0.03$.

Figure 44. Continued.

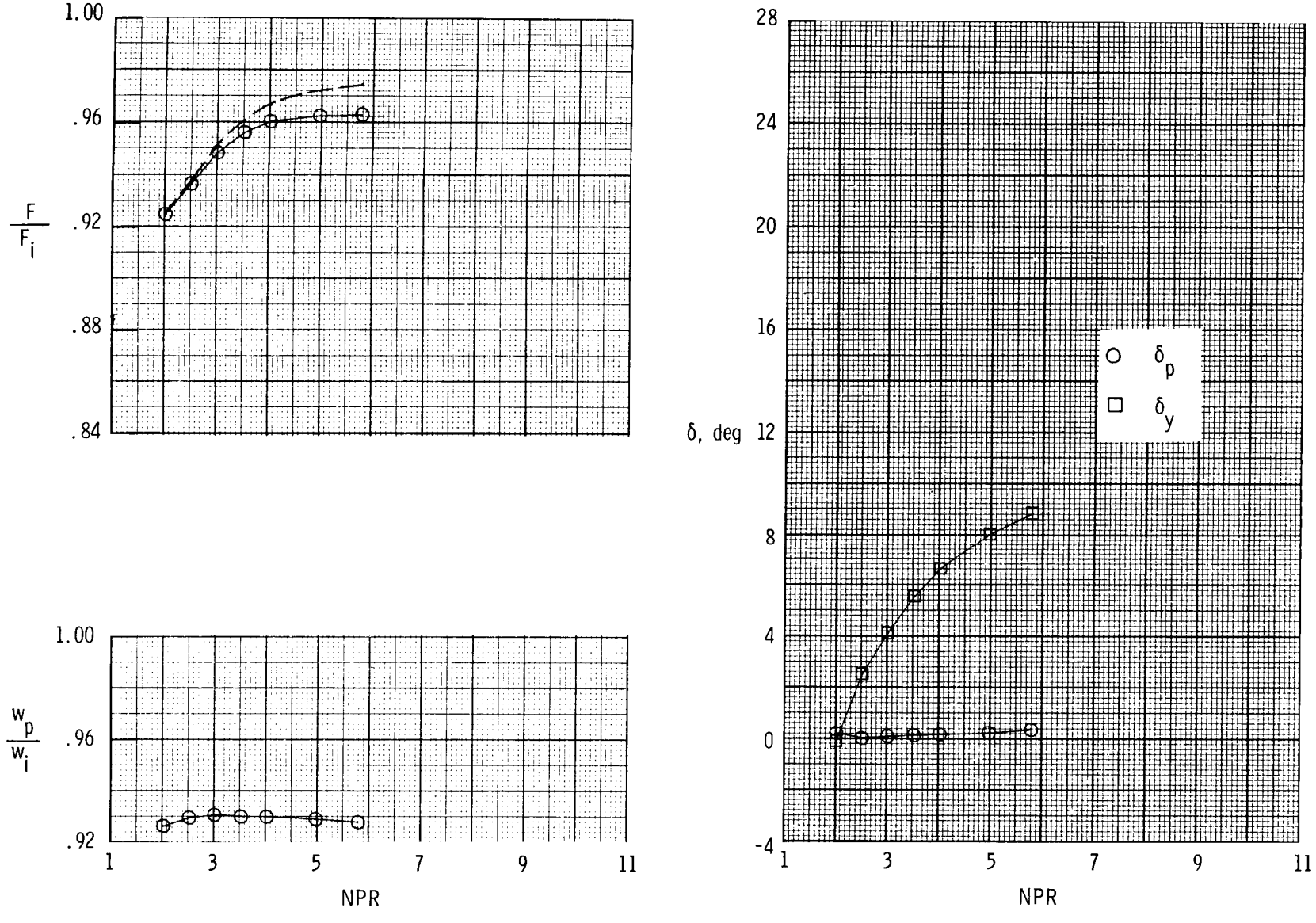

(e) Configuration S13; $(x_s - x_t)/l_s = -0.30$.

Figure 44. Concluded.

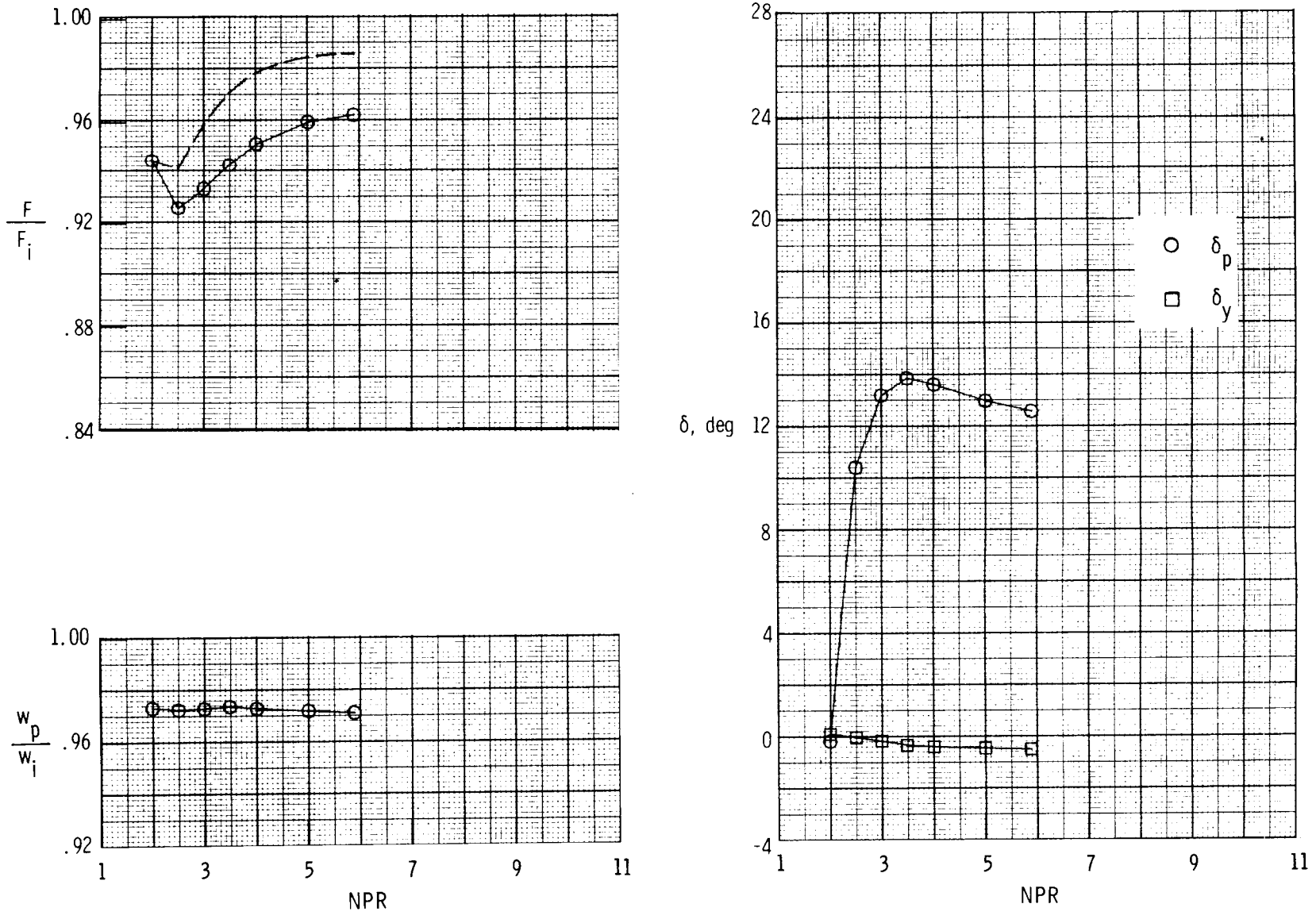

Figure 45. Variation of nozzle thrust ratio, discharge coefficient, and resultant thrust vector angles with nozzle pressure ratio for A/B power 2-D C-D nozzle, baseline $A_e/A_t = 1.35$ and $\delta_{v,p} = 9.79°$. Dashed line indicates resultant thrust ratio F_r/F_i.

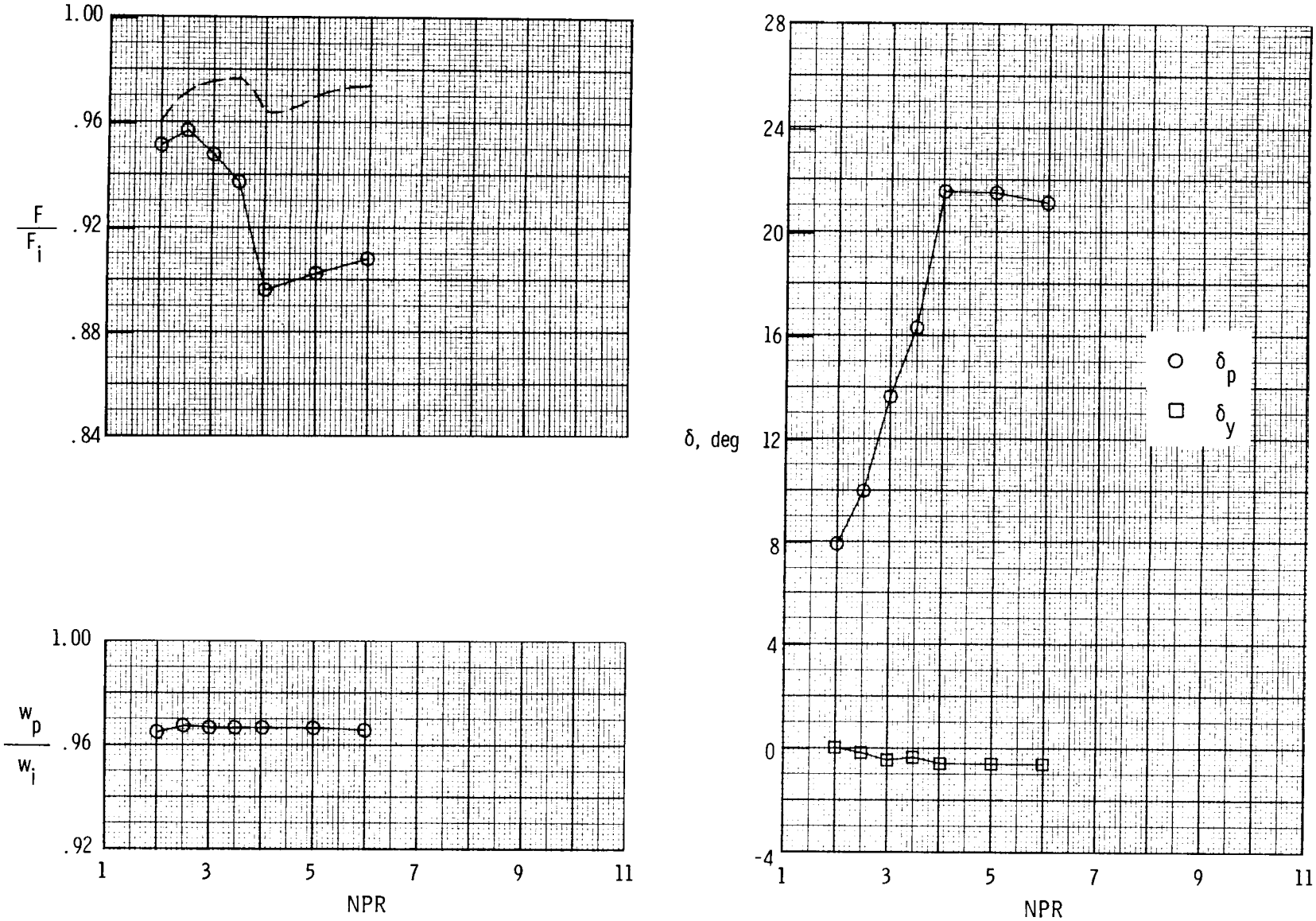

(a) Configuration S15; $(x_s - x_t)/l_s = 1.00$.

Figure 46. Variation of nozzle thrust ratio, discharge coefficient, and resultant thrust vector angles with nozzle pressure ratio for A/B power 2-D C-D nozzle, baseline $A_e/A_t = 1.51$ and $\delta_{v,p} = 20.28°$, with translating sidewall yaw vectoring concept. Dashed line indicates resultant thrust ratio F_r/F_i.

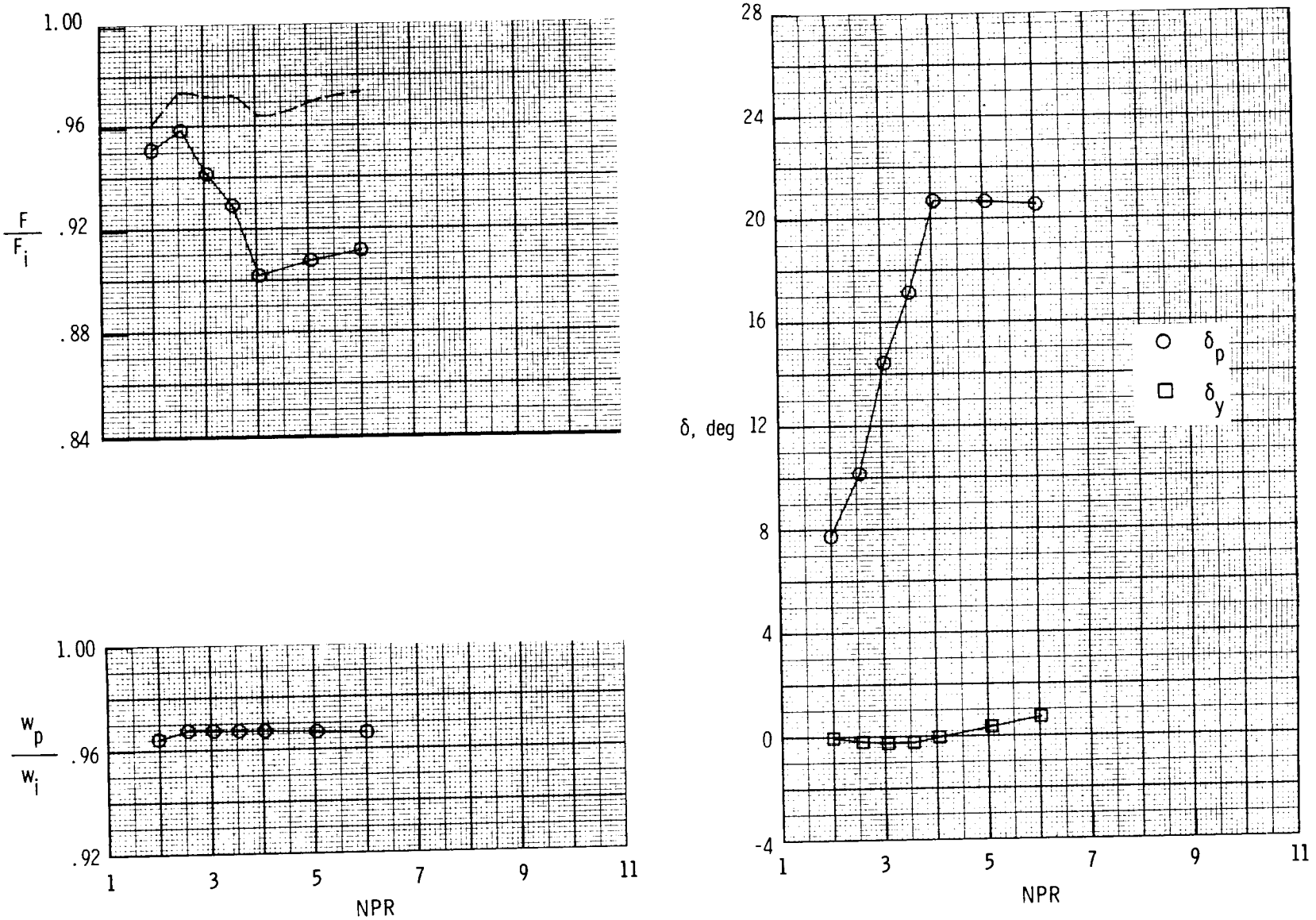

(b) Configuration S16; $(x_s - x_t)/l_s = 0.61$.

Figure 46. Continued.

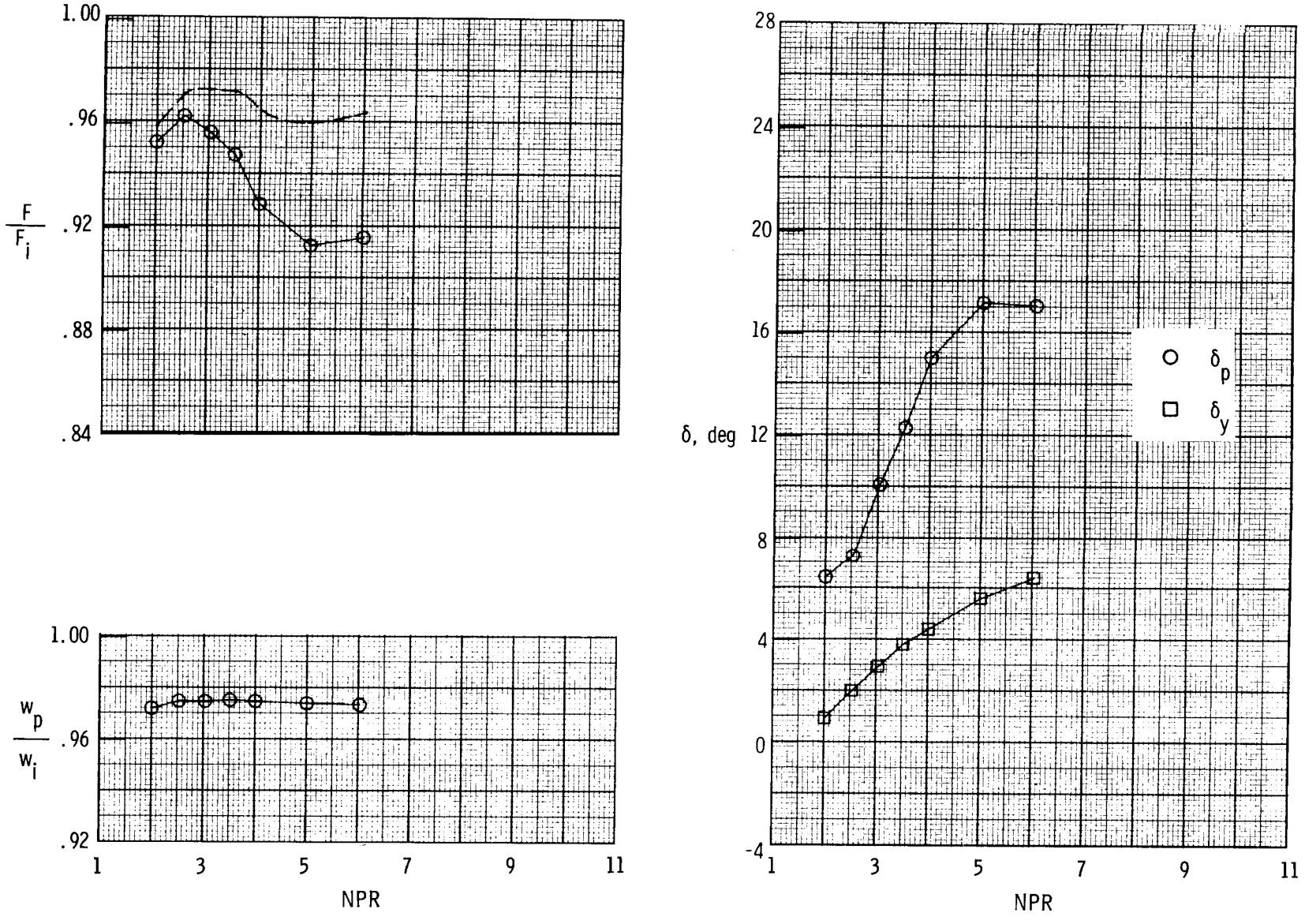

(c) Configuration S17; $(x_s - x_t)/l_s = -0.03$.

Figure 46. Concluded.

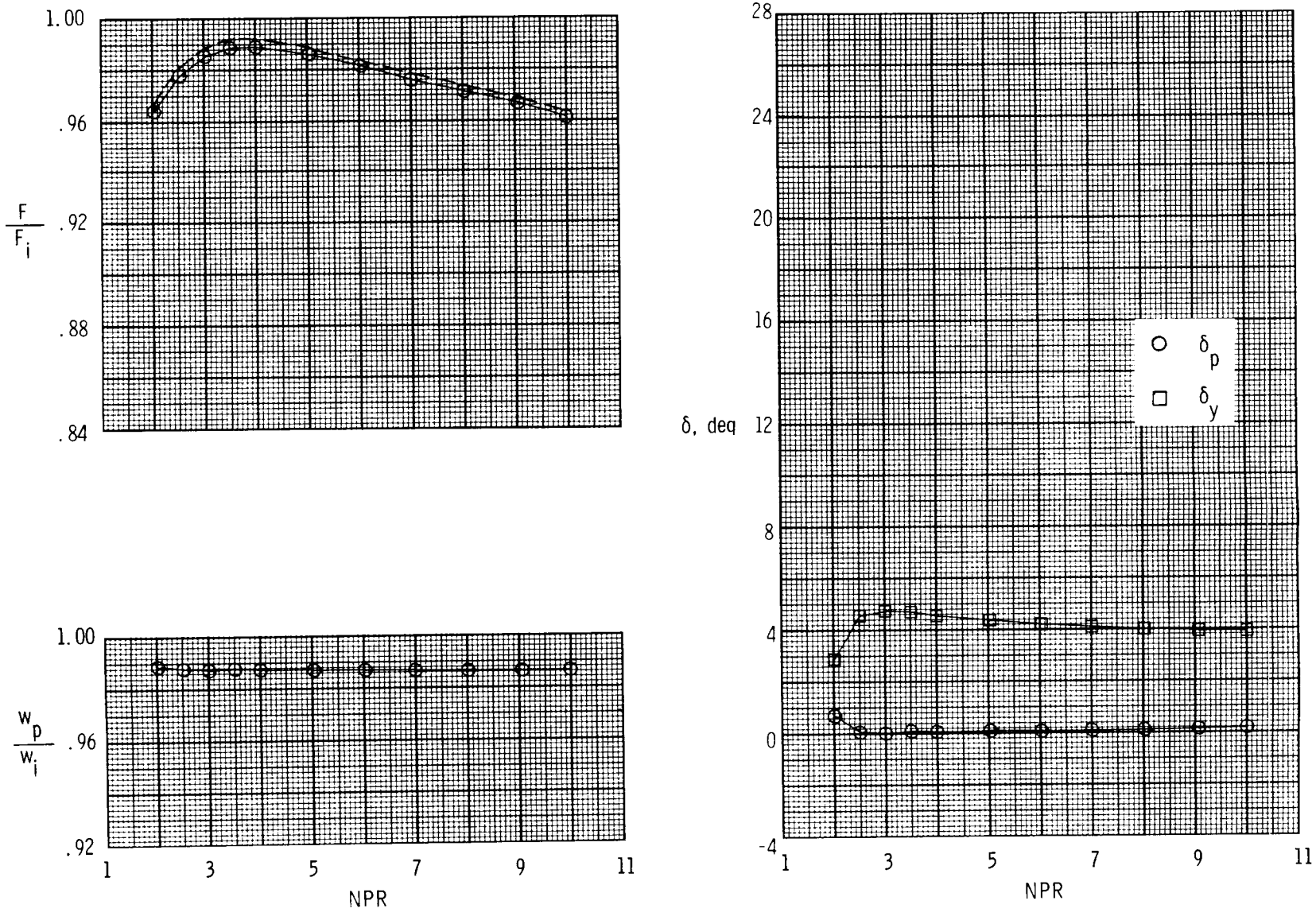

(a) Configuration F1; $x_h = 2.28$ in.; left $\delta_{v,y} = 10°$; right $\delta_{v,y} = 0°$.

Figure 47. Variation of nozzle thrust ratio, discharge coefficient, and resultant thrust vector angles with nozzle pressure ratio for dry power 2-D C-D nozzle, baseline $A_e/A_t = 1.08$ and $\delta_{v,p} = 0°$, with downstream flaps yaw vectoring concept. Dashed line indicates resultant thrust ratio F_r/F_i.

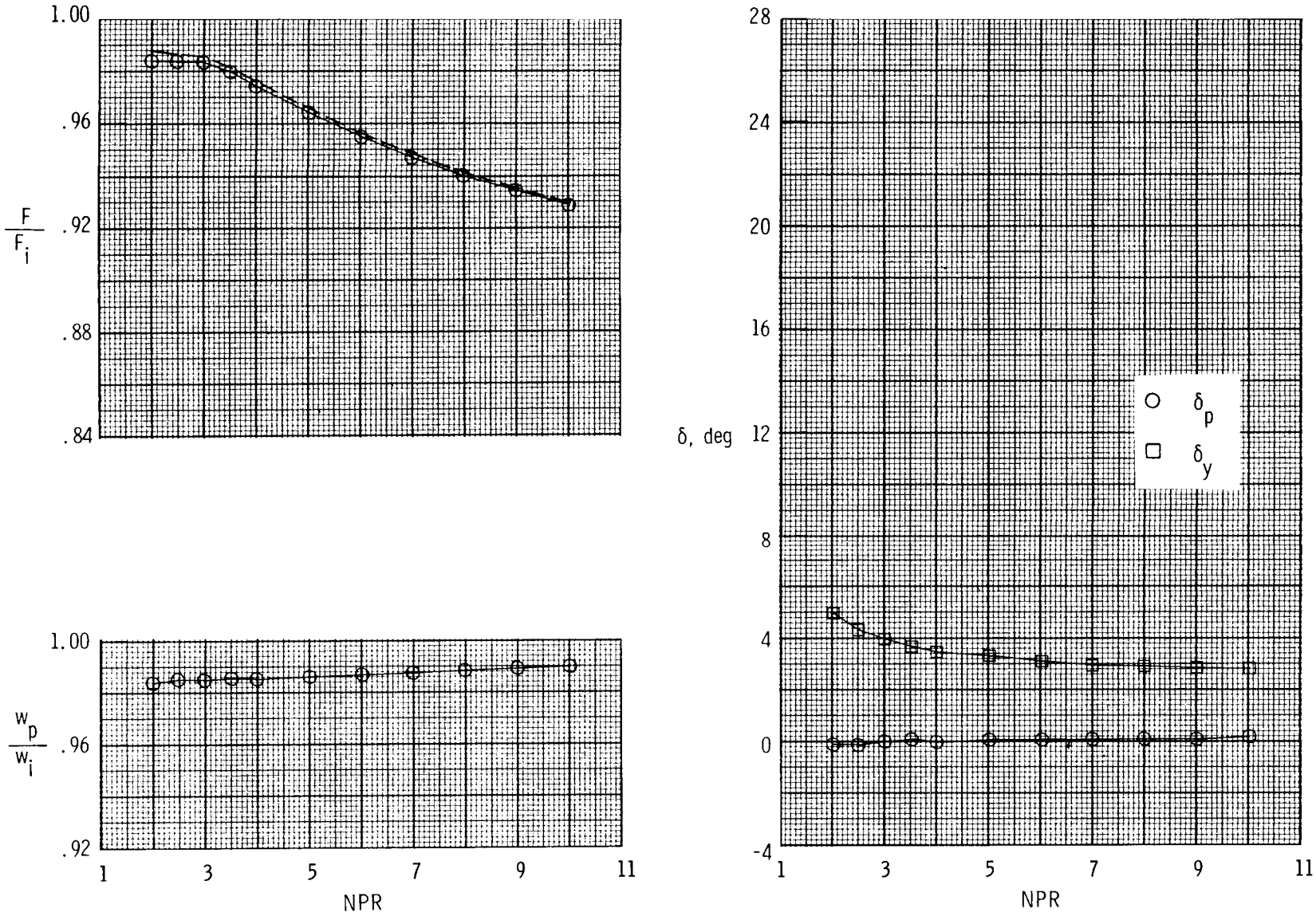

(b) Configuration F2; $x_h = 2.28$ in.; left $\delta_{v,y} = 0°$; right $\delta_{v,y} = 10°$.

Figure 47. Continued.

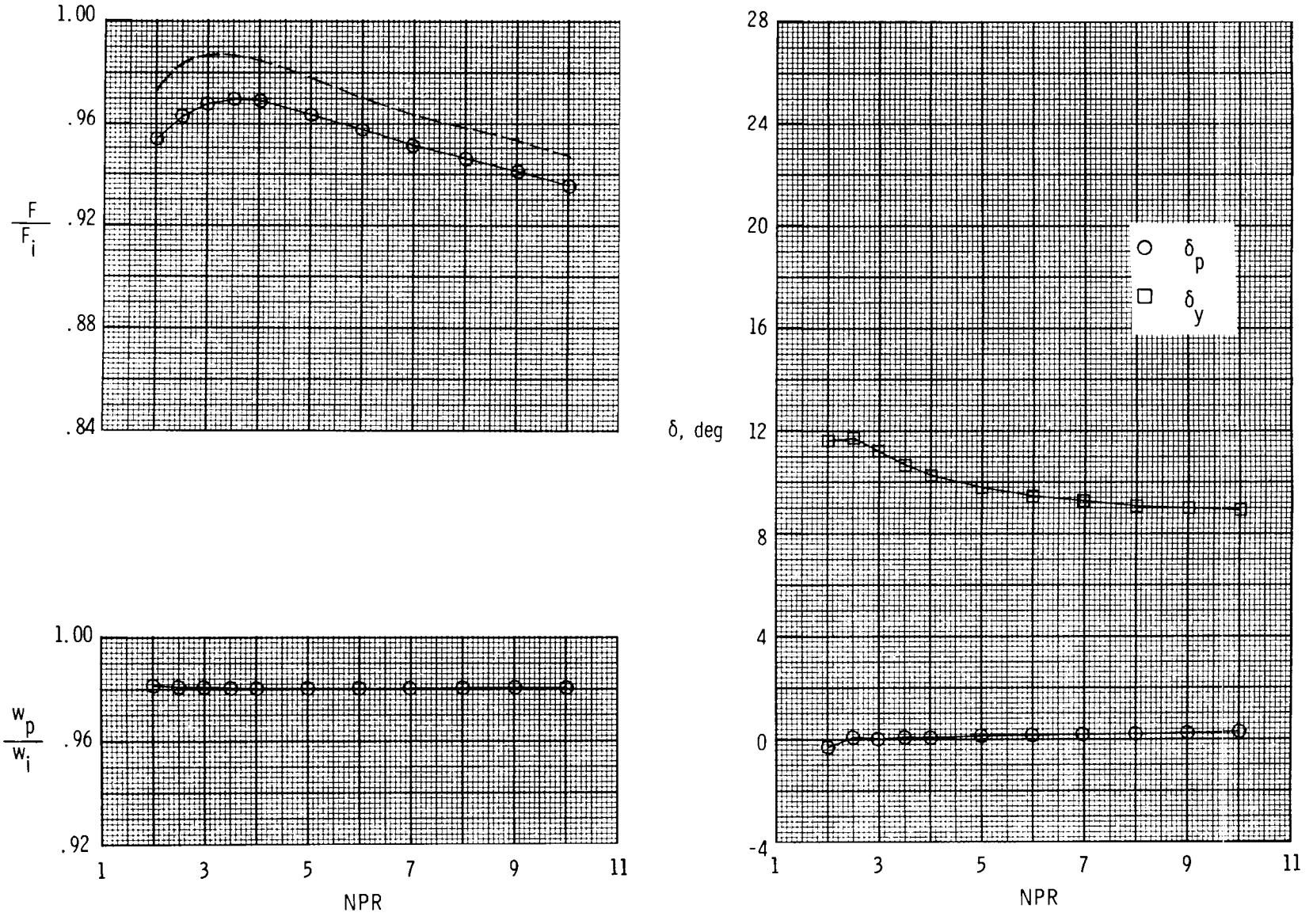

(c) Configuration F3; $x_h = 2.28$ in.; left $\delta_{v,y} = 10°$; right $\delta_{v,y} = 10°$.

Figure 47. Continued.

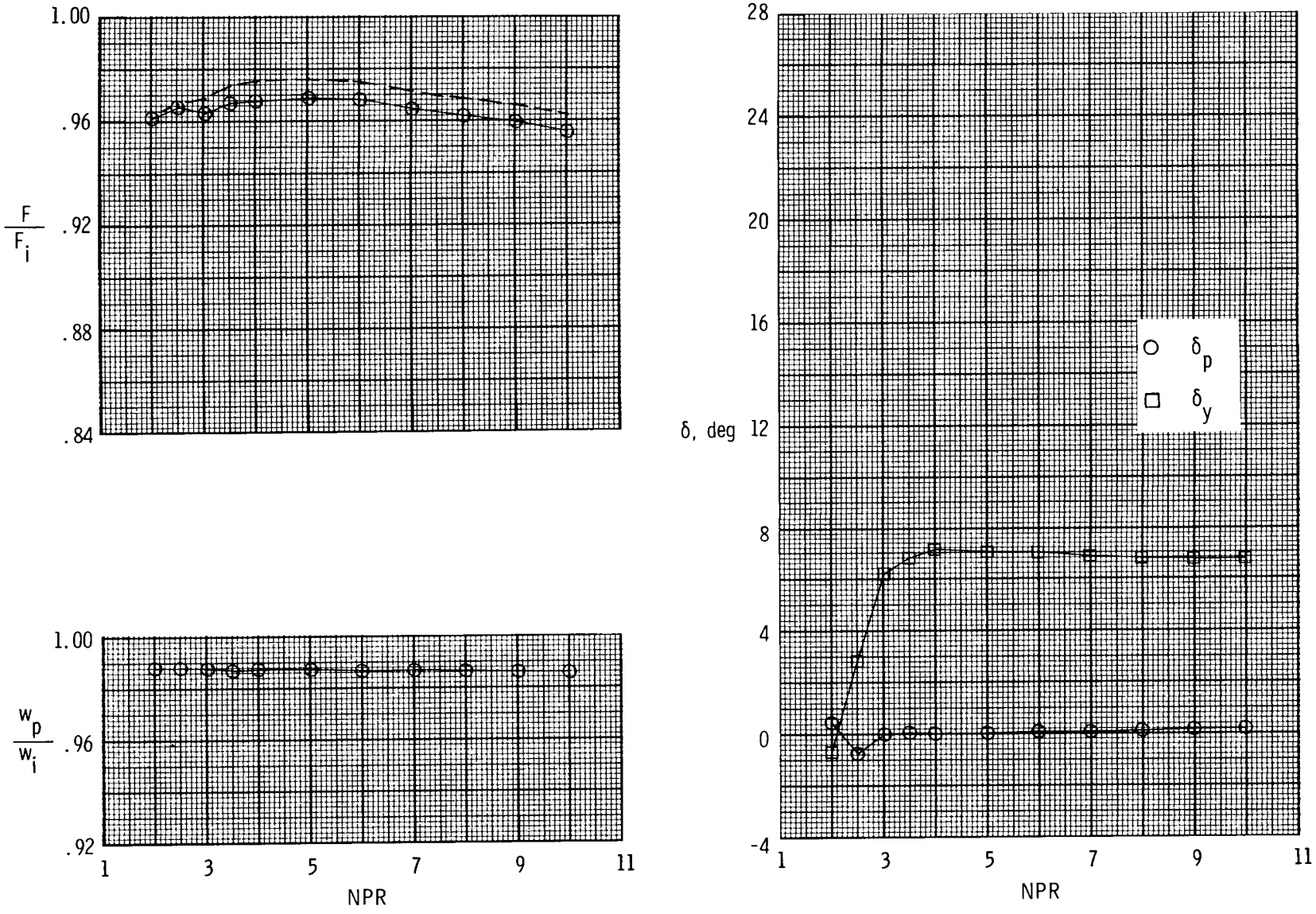

(d) Configuration F4; $x_h = 2.28$ in.; left $\delta_{v,y} = 20°$; right $\delta_{v,y} = 0°$.

Figure 47. Continued.

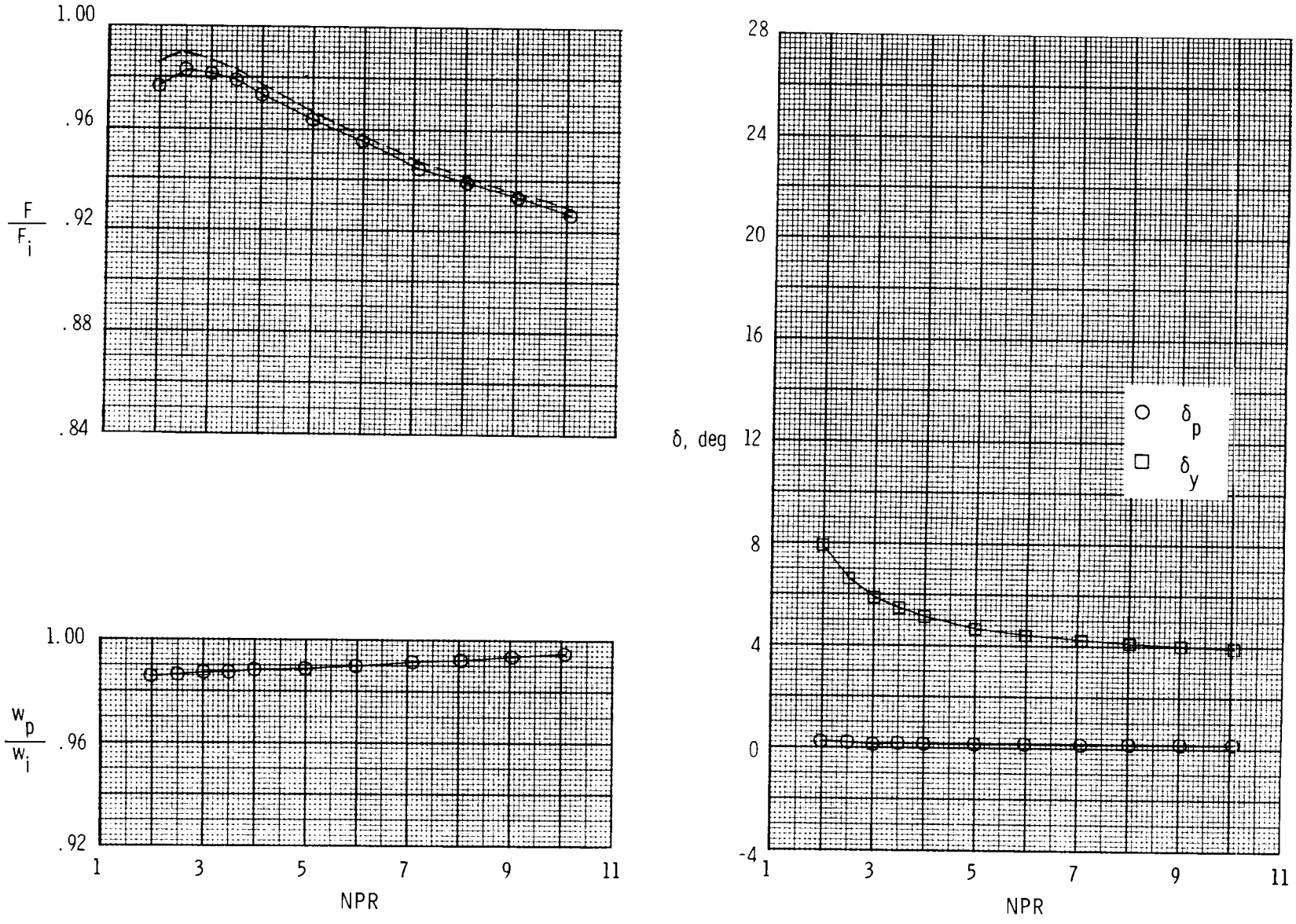

(e) Configuration F5; $x_h = 2.28$ in.; left $\delta_{v,y} = 0°$; right $\delta_{v,y} = 20°$.

Figure 47. Continued.

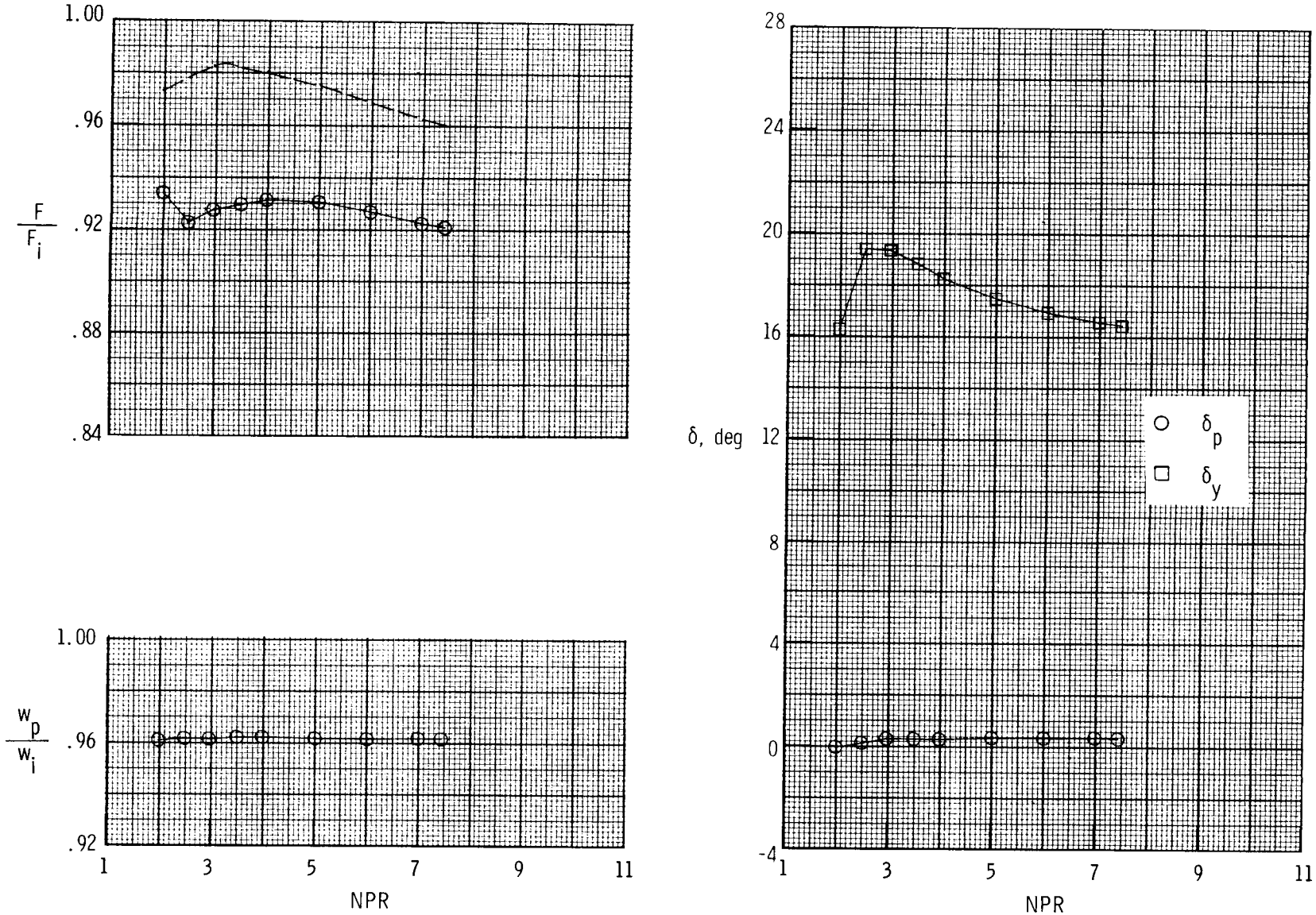

(f) Configuration F6; $x_h = 2.28$ in.; left $\delta_{v,y} = 20°$; right $\delta_{v,y} = 20°$.

Figure 47. Continued.

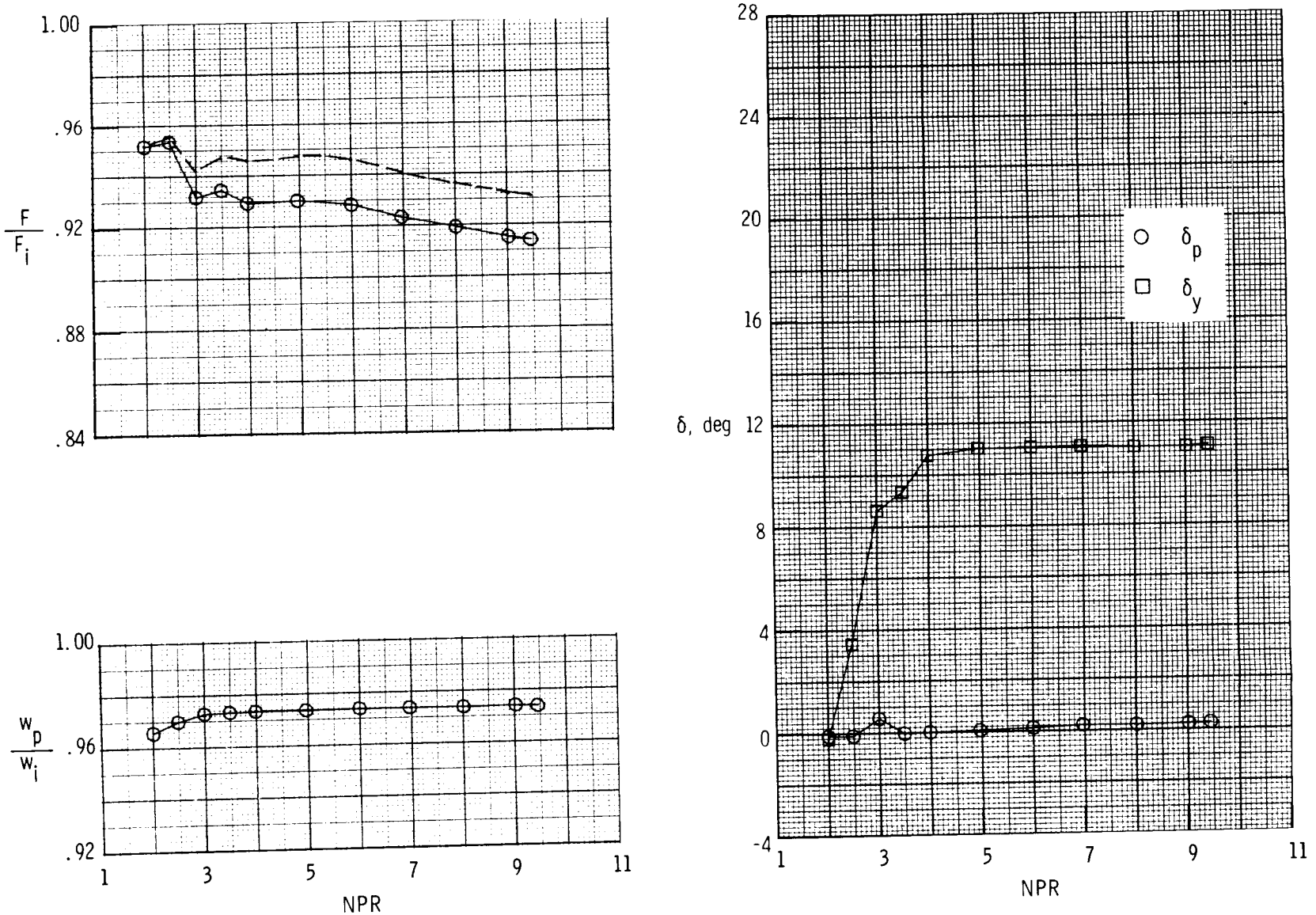

(g) Configuration F7; $x_h = 3.42$; left $\delta_{v,y} = 20°$; right $\delta_{v,y} = 0°$.

Figure 47. Continued.

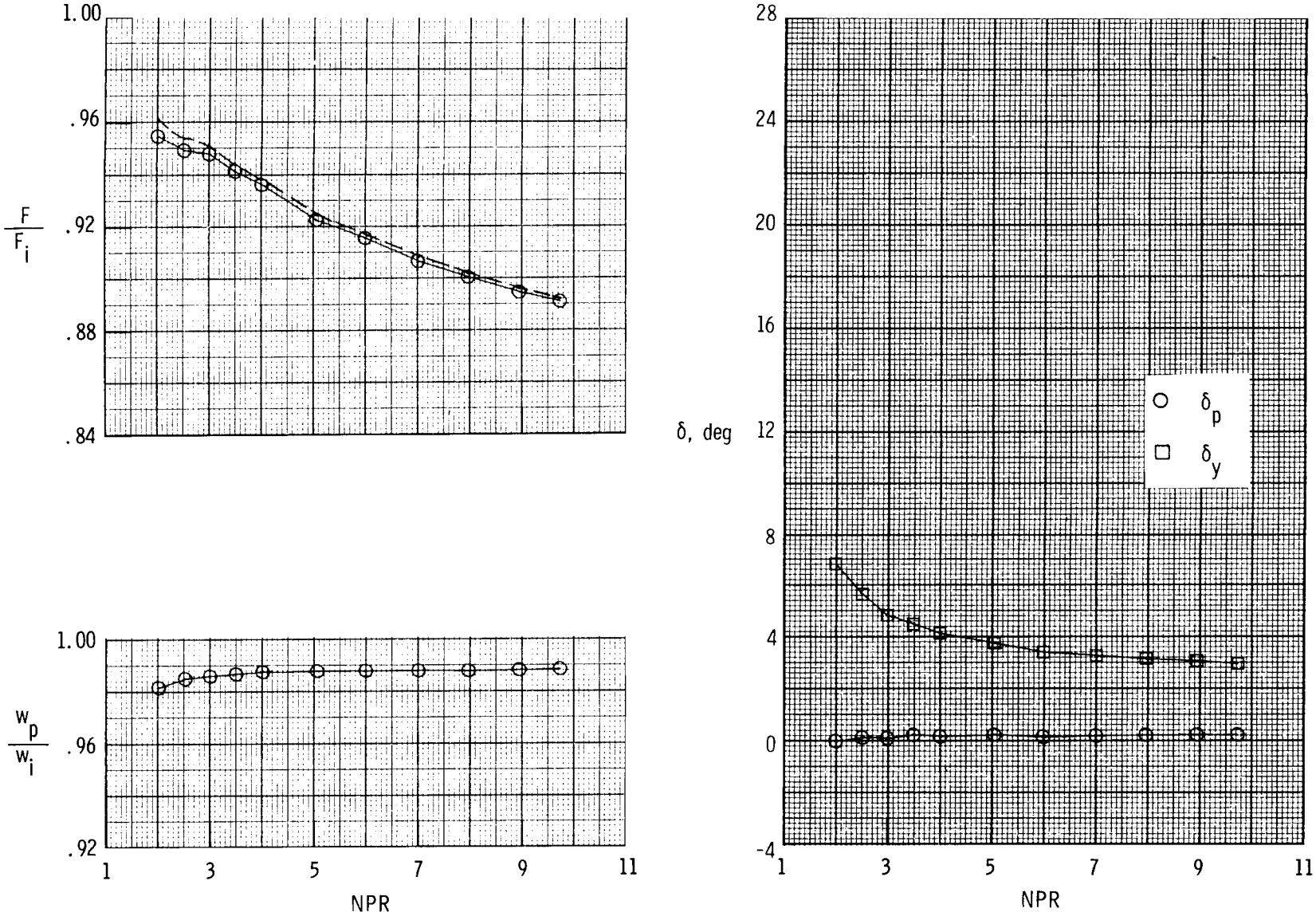

(h) Configuration F8; $x_h = 3.42$ in.; left $\delta_{v,y} = 0°$; right $\delta_{v,y} = 20°$.

Figure 47. Continued.

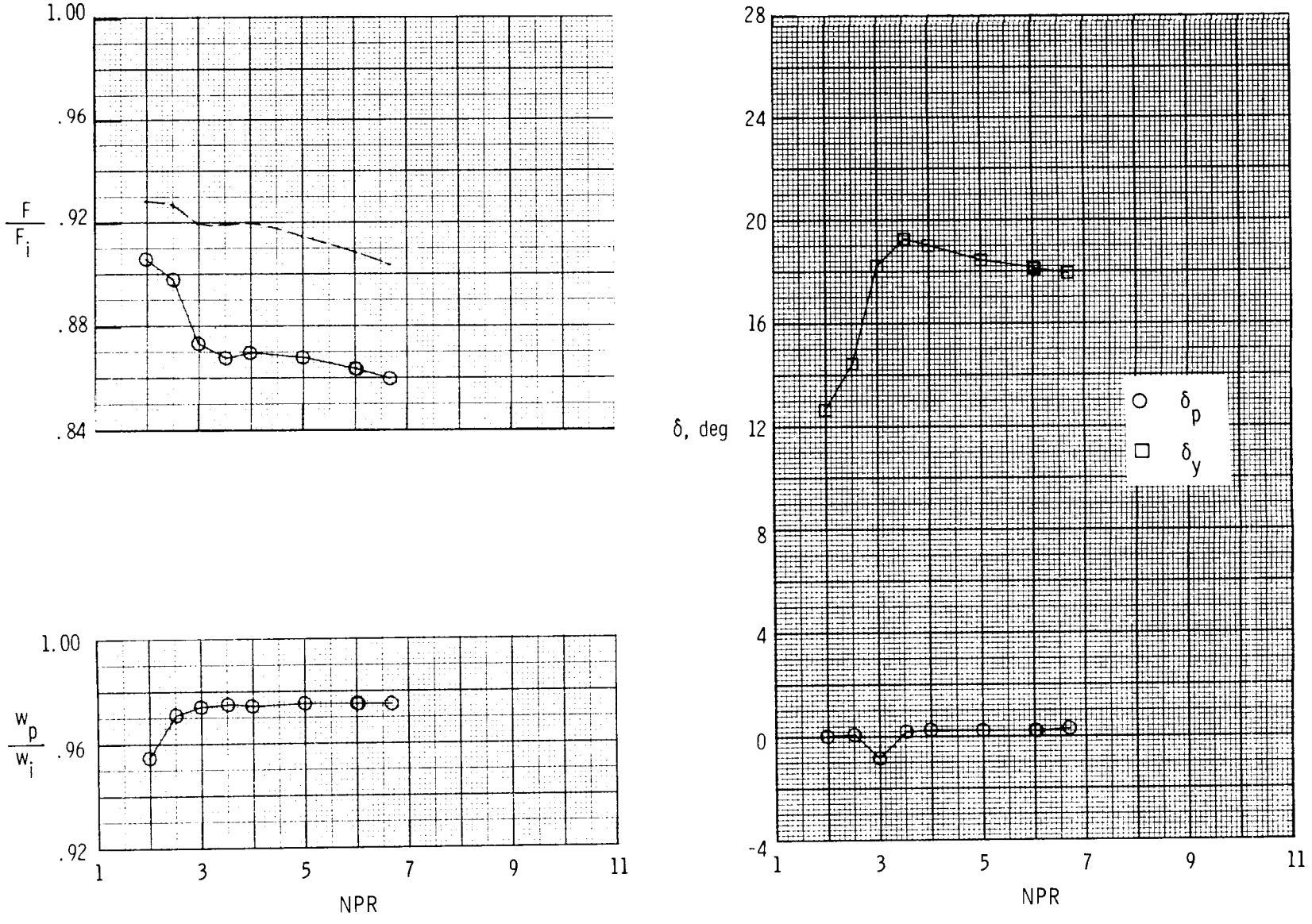

(i) Configuration F9; $x_h = 3.42$ in.; left $\delta_{v,y} = 20°$; right $\delta_{v,y} = 20°$.

Figure 47. Concluded.

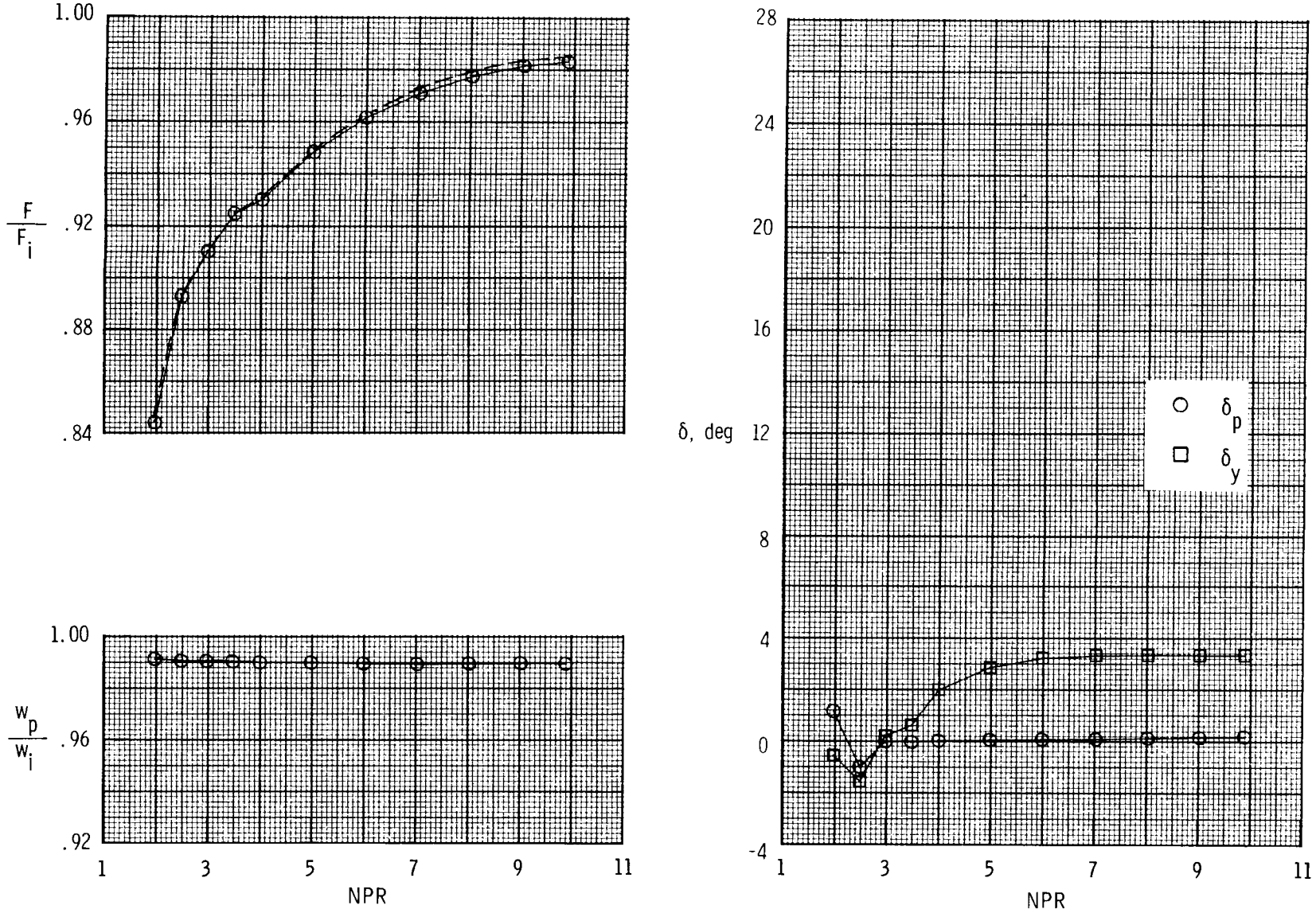

(a) Configuration F10; $x_h = 2.28$ in.; left $\delta_{v,y} = 20°$; right $\delta_{v,y} = 0°$.

Figure 48. Variation of nozzle thrust ratio, discharge coefficient, and resultant thrust vector angles with nozzle pressure ratio for dry power 2-D C-D nozzle, baseline $A_e/A_t = 1.78$ and $\delta_{v,p} = 0°$, with downstream flaps yaw vectoring concept. Dashed line indicates resultant thrust ratio F_r/F_i.

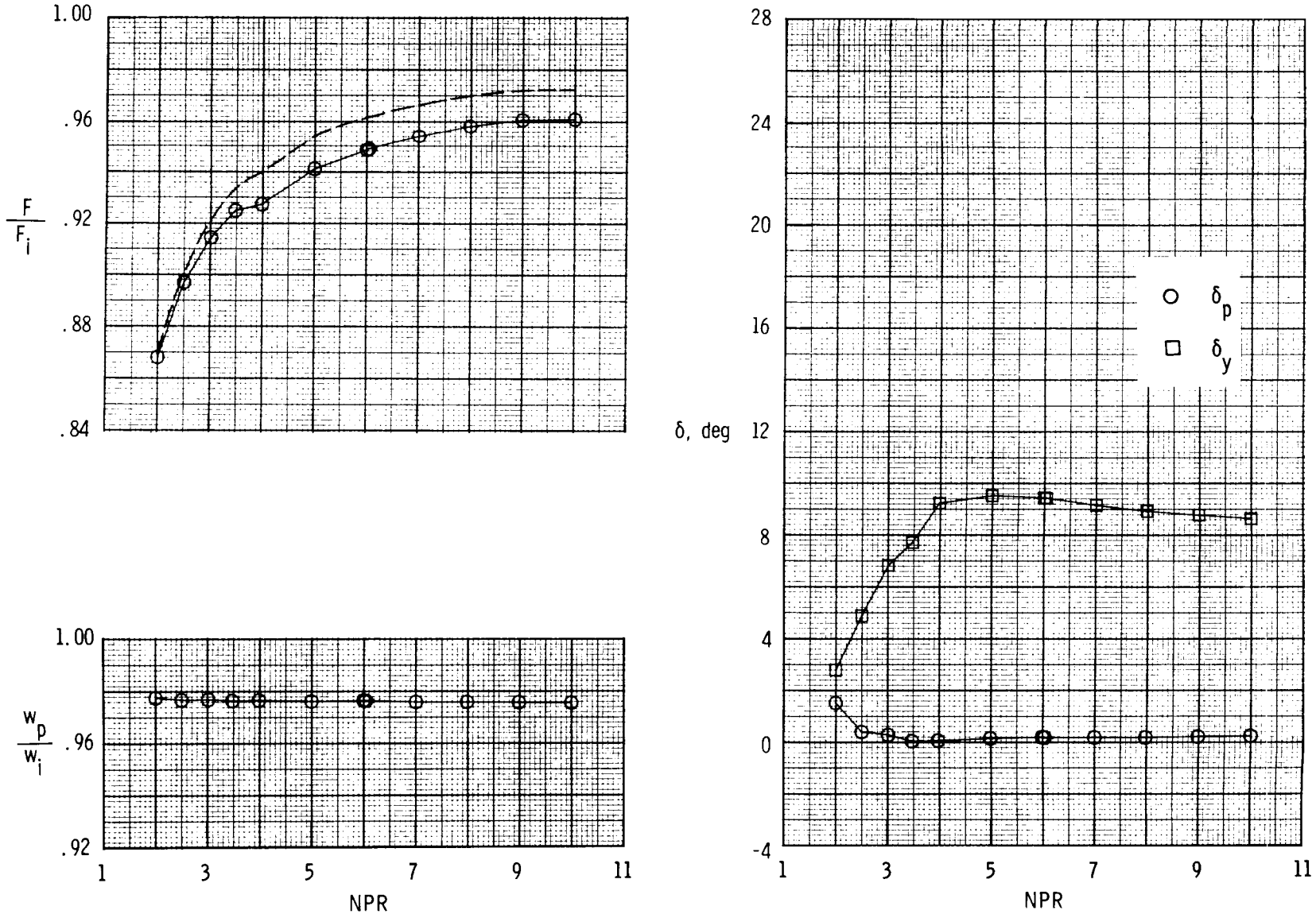

(b) Configuration F11; $x_h = 2.28$ in.; left $\delta_{v,y} = 20°$; right $\delta_{v,y} = 20°$.

Figure 48. Continued.

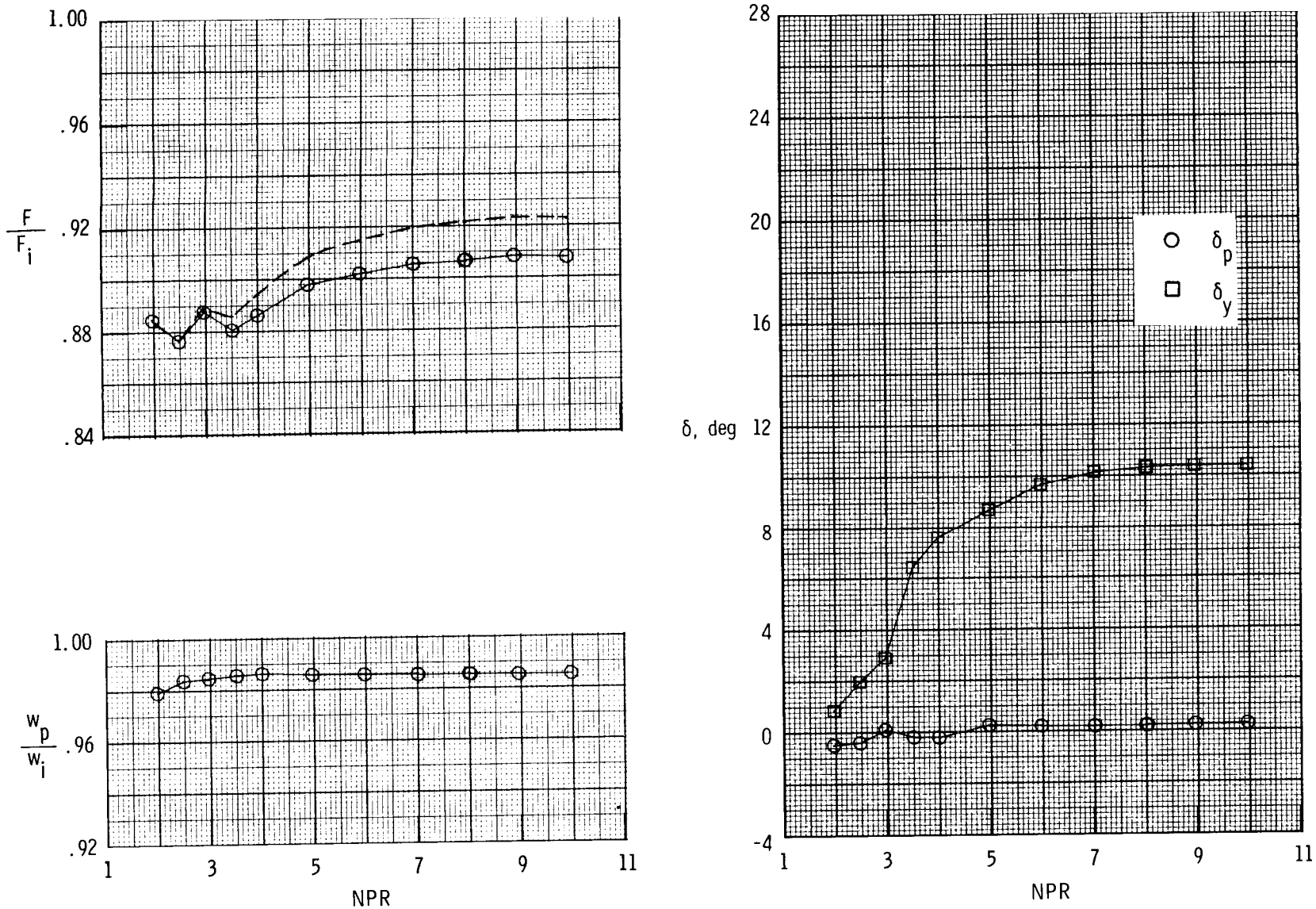

(c) Configuration F12; $x_h = 3.42$ in.; left $\delta_{v,y} = 20°$; right $\delta_{v,y} = 20°$.

Figure 48. Concluded.

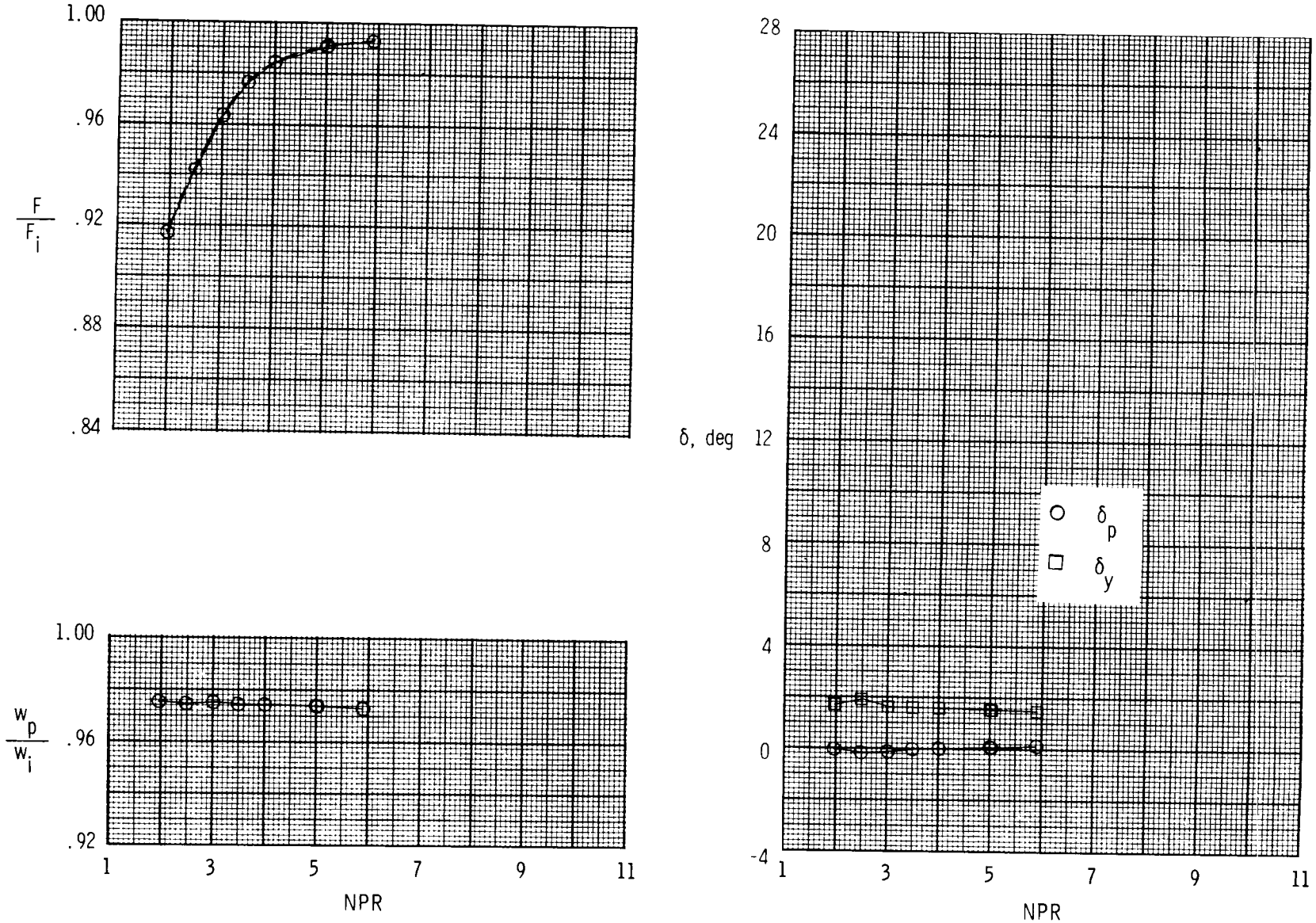

(a) Configuration F13; $x_h = 2.28$ in.; left $\delta_{v,y} = 10°$; right $\delta_{v,y} = 0°$.

Figure 49. Variation of nozzle thrust ratio, discharge coefficient, and resultant thrust vector angles with nozzle pressure ratio for A/B power 2-D C-D nozzle, baseline $A_e/A_t = 1.29$ and $\delta_{v,p} = 0°$, with downstream flaps yaw vectoring concept. Dashed line indicates resultant thrust ratio F_r/F_i.

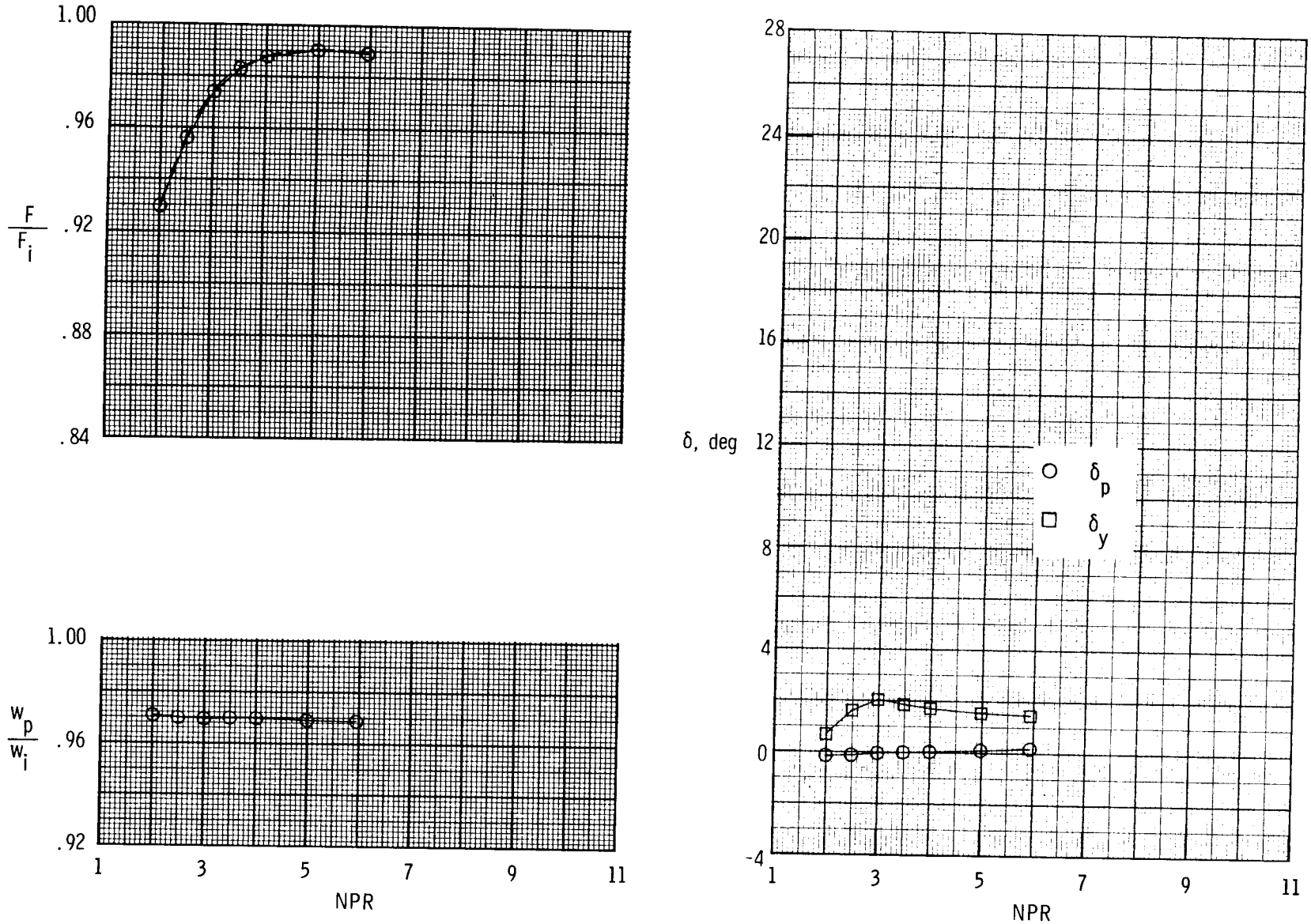

(b) Configuration F14; $x_h = 2.28$ in.; left $\delta_{v,y} = 0°$; right $\delta_{v,y} = 10°$.

Figure 49. Continued.

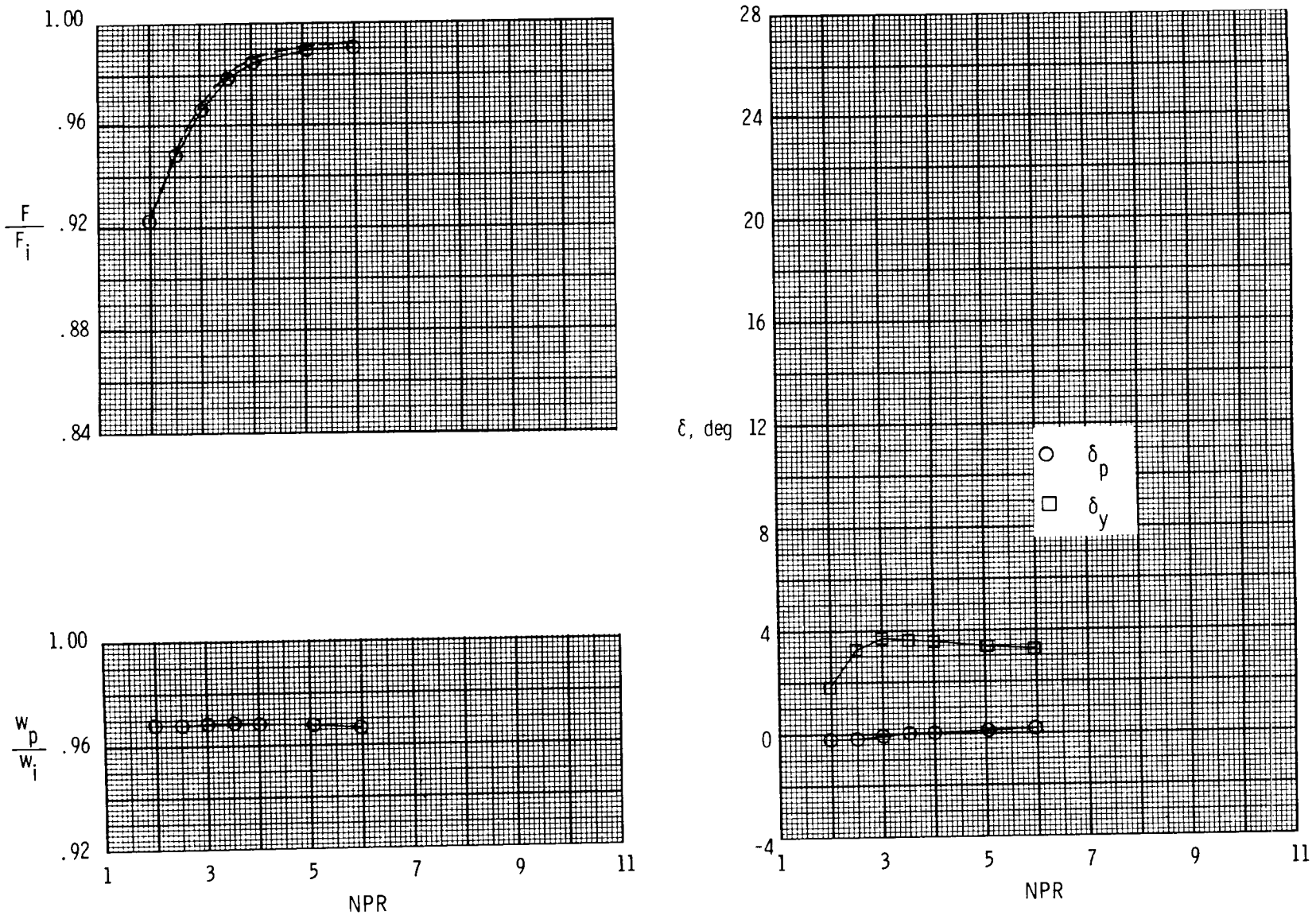

(c) Configuration F15; $x_h = 2.28$ in.; left $\delta_{v,y} = 10°$; right $\delta_{v,y} = 10°$.

Figure 49. Continued.

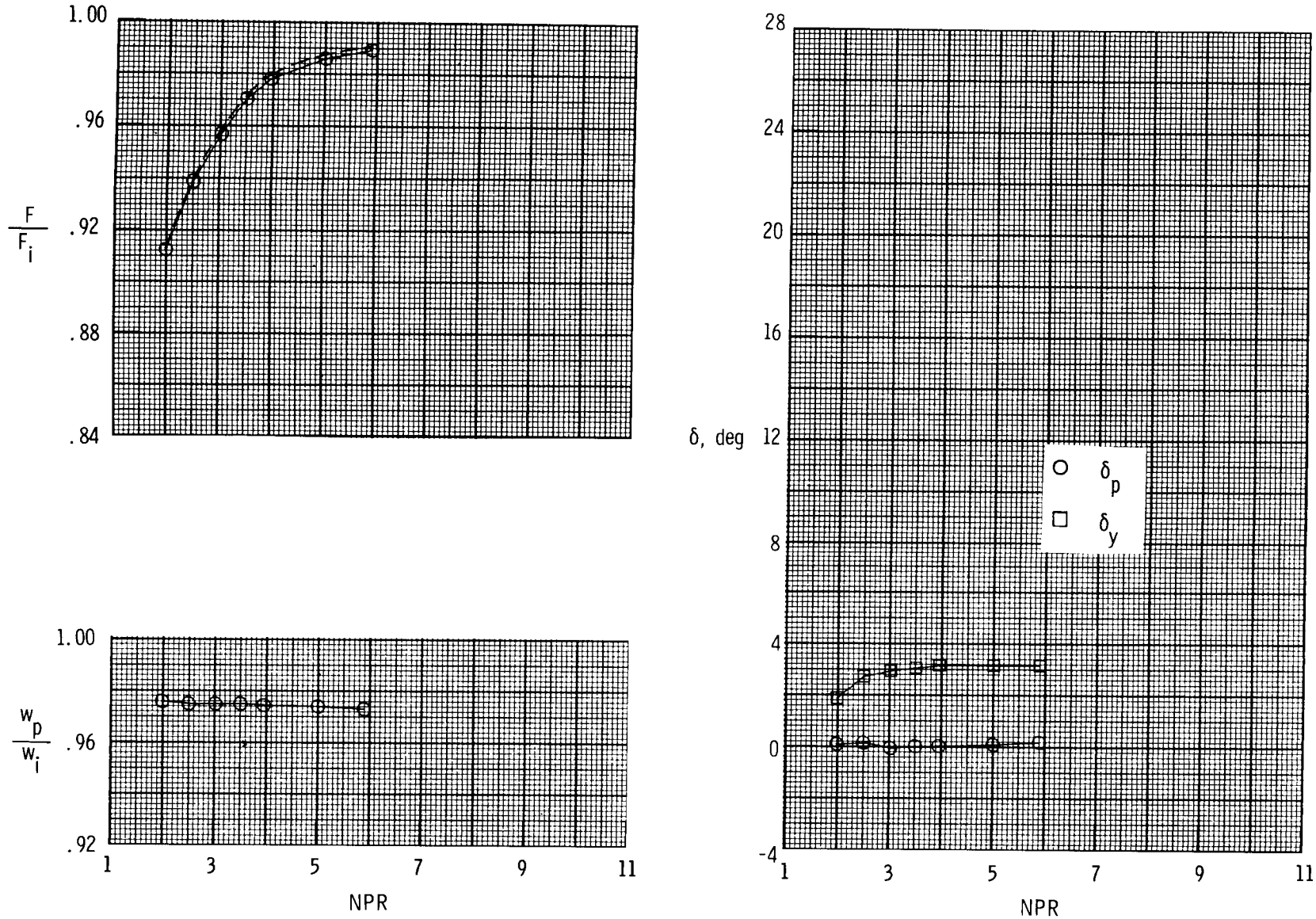

(d) Configuration F16; $x_h = 2.28$ in.; left $\delta_{v,y} = 20°$; right $\delta_{v,y} = 0°$.

Figure 49. Continued.

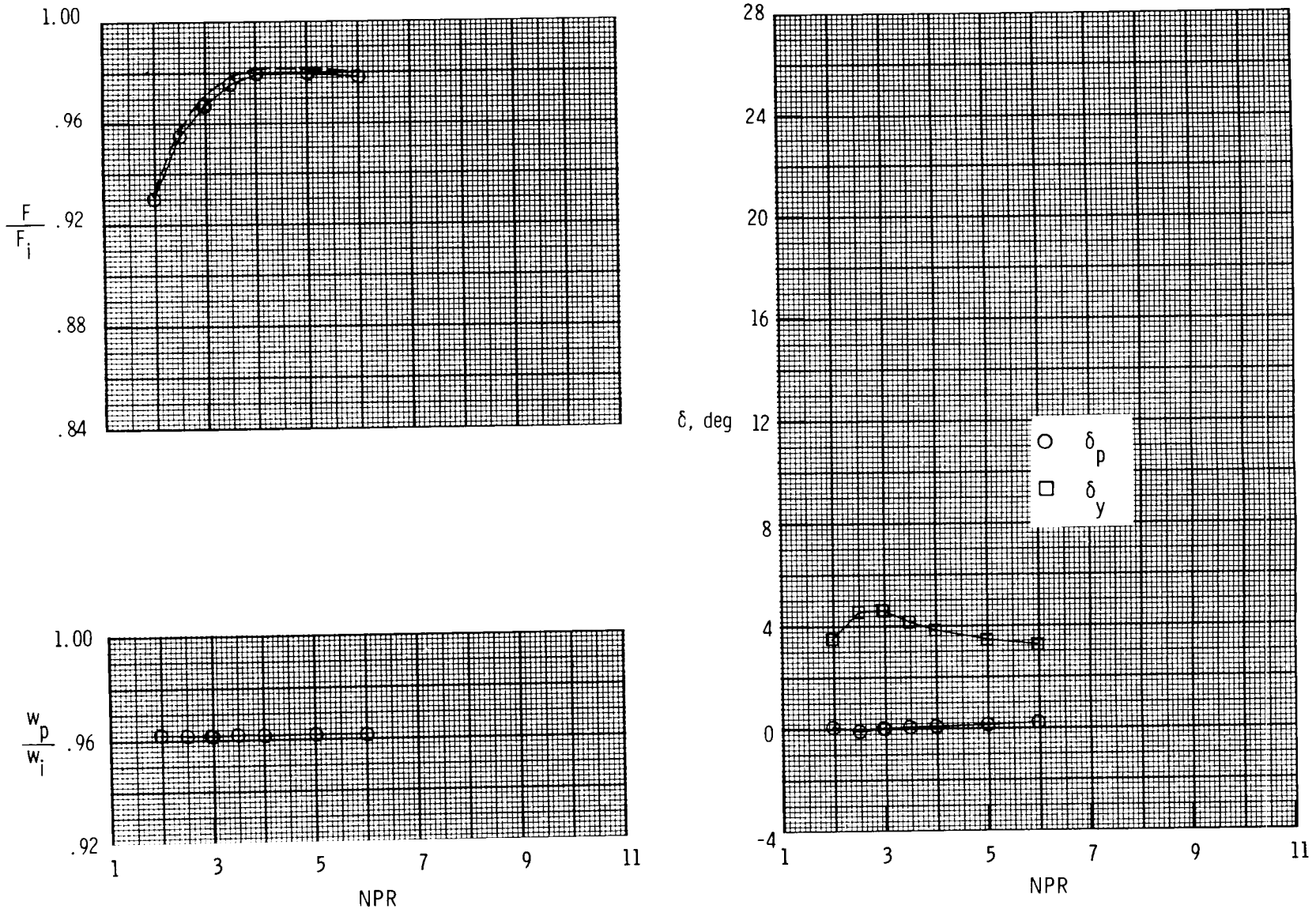

(e) Configuration F17; $x_h = 2.28$ in.; left $\delta_{v,y} = 0°$; right $\delta_{v,y} = 20°$.

Figure 49. Continued.

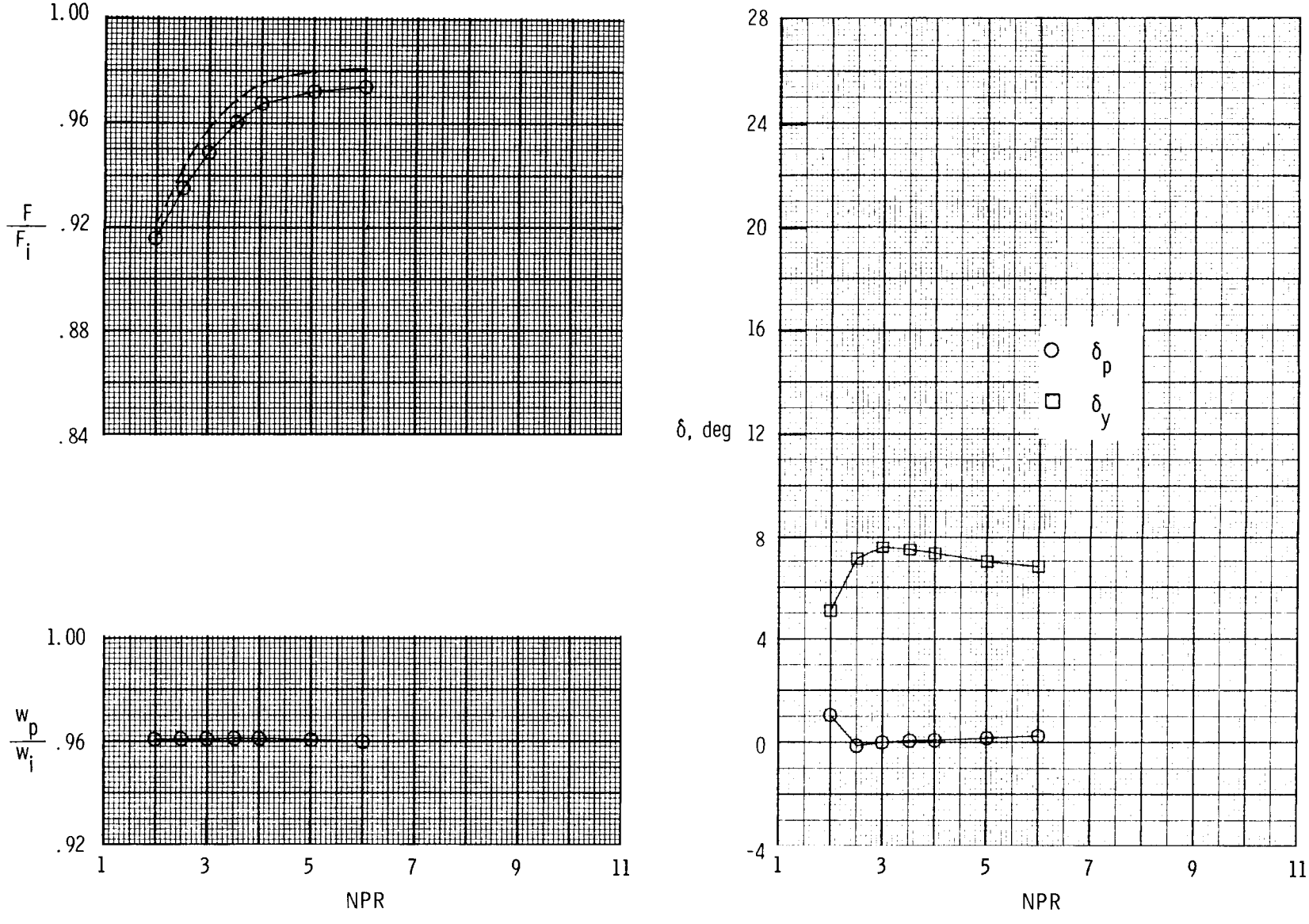

(f) Configuration F18; $x_h = 2.28$ in.; left $\delta_{v,y} = 20°$; right $\delta_{v,y} = 20°$.

Figure 49. Continued.

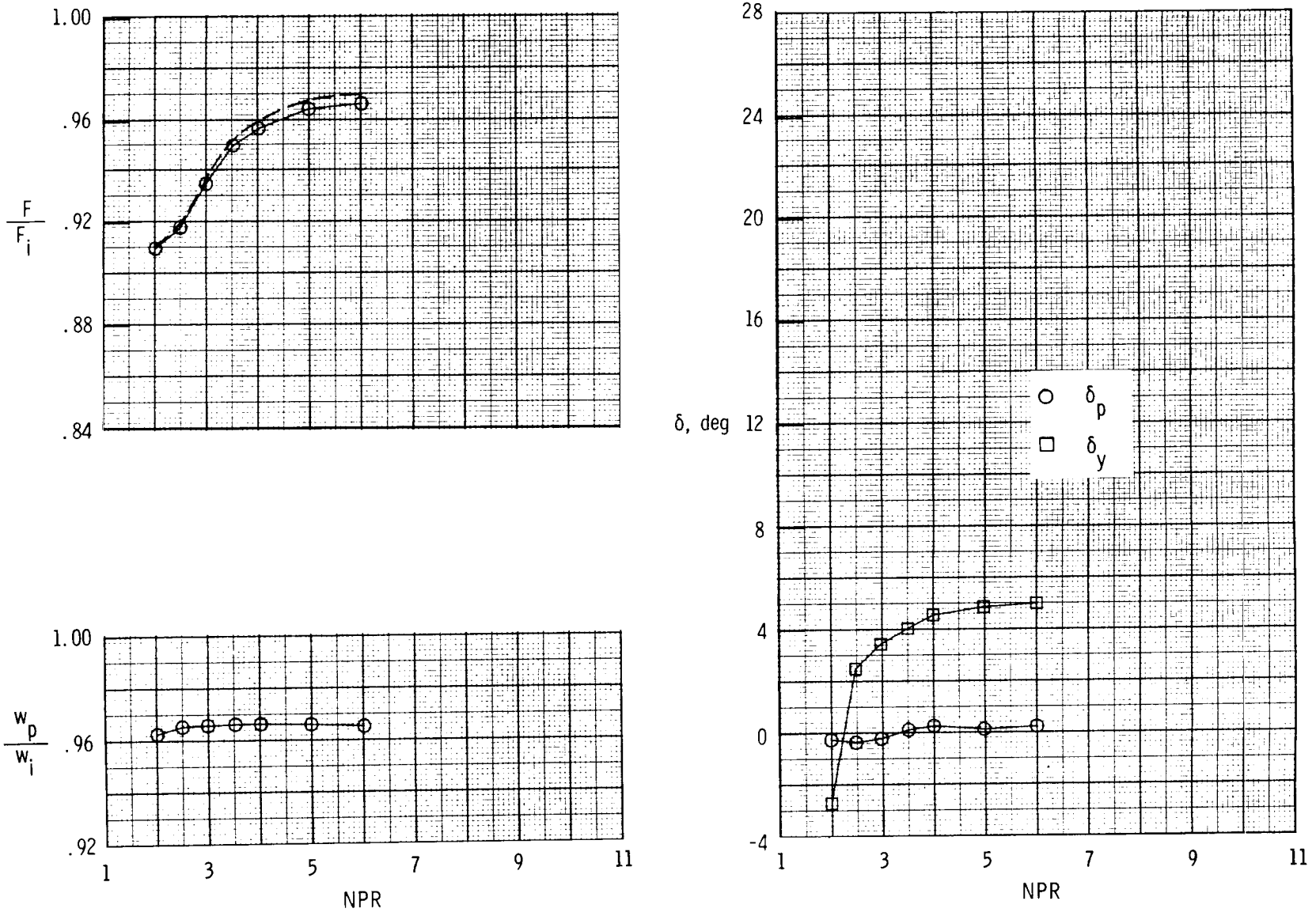

(g) Configuration F19; $x_h = 3.42$ in.; left $\delta_{v,y} = 20°$; right $\delta_{v,y} = 0°$.

Figure 49. Continued.

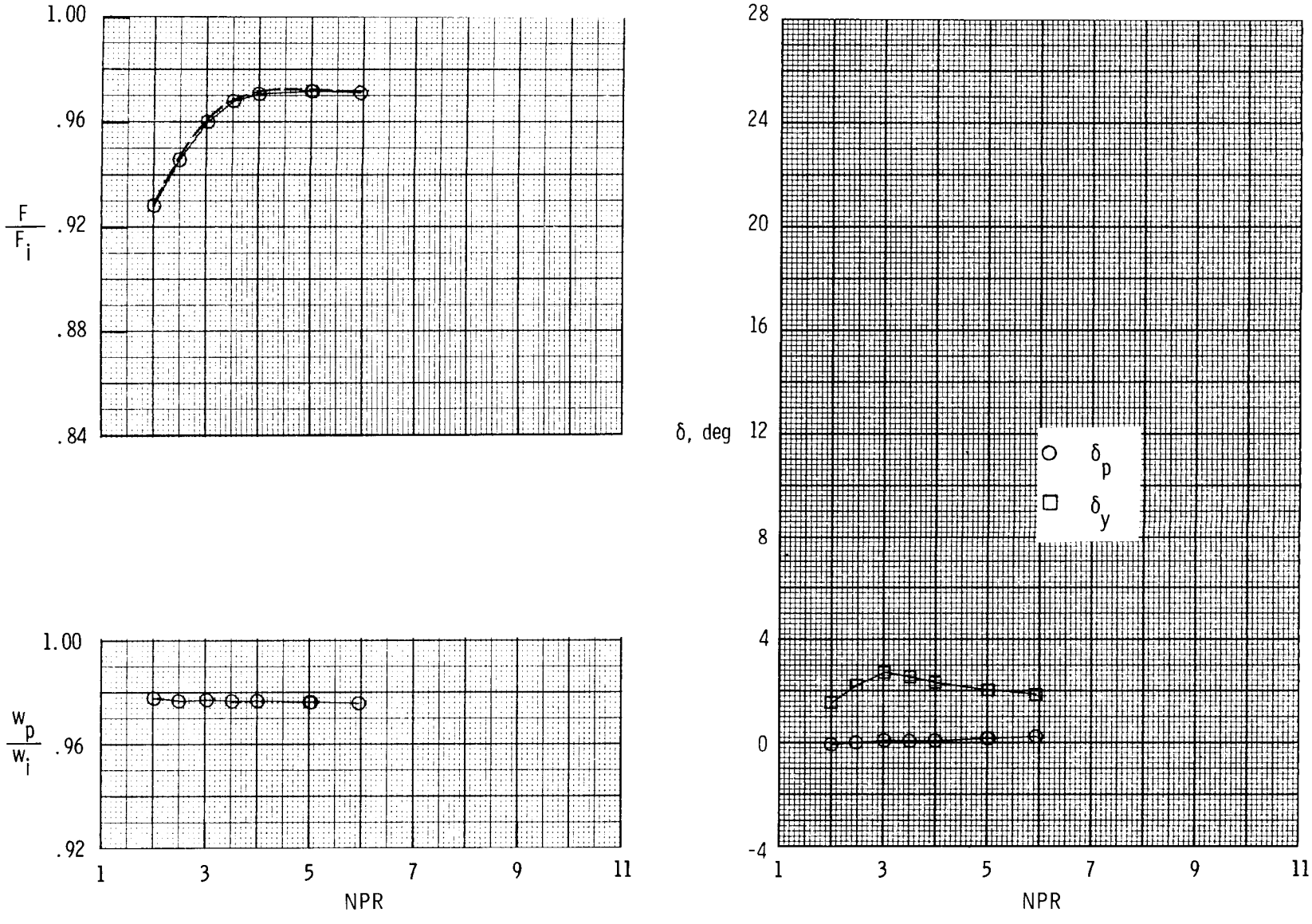

(h) Configuration F20; $x_h = 3.42$ in.; left $\delta_{v,y} = 0°$; right $\delta_{v,y} = 20°$.

Figure 49. Continued.

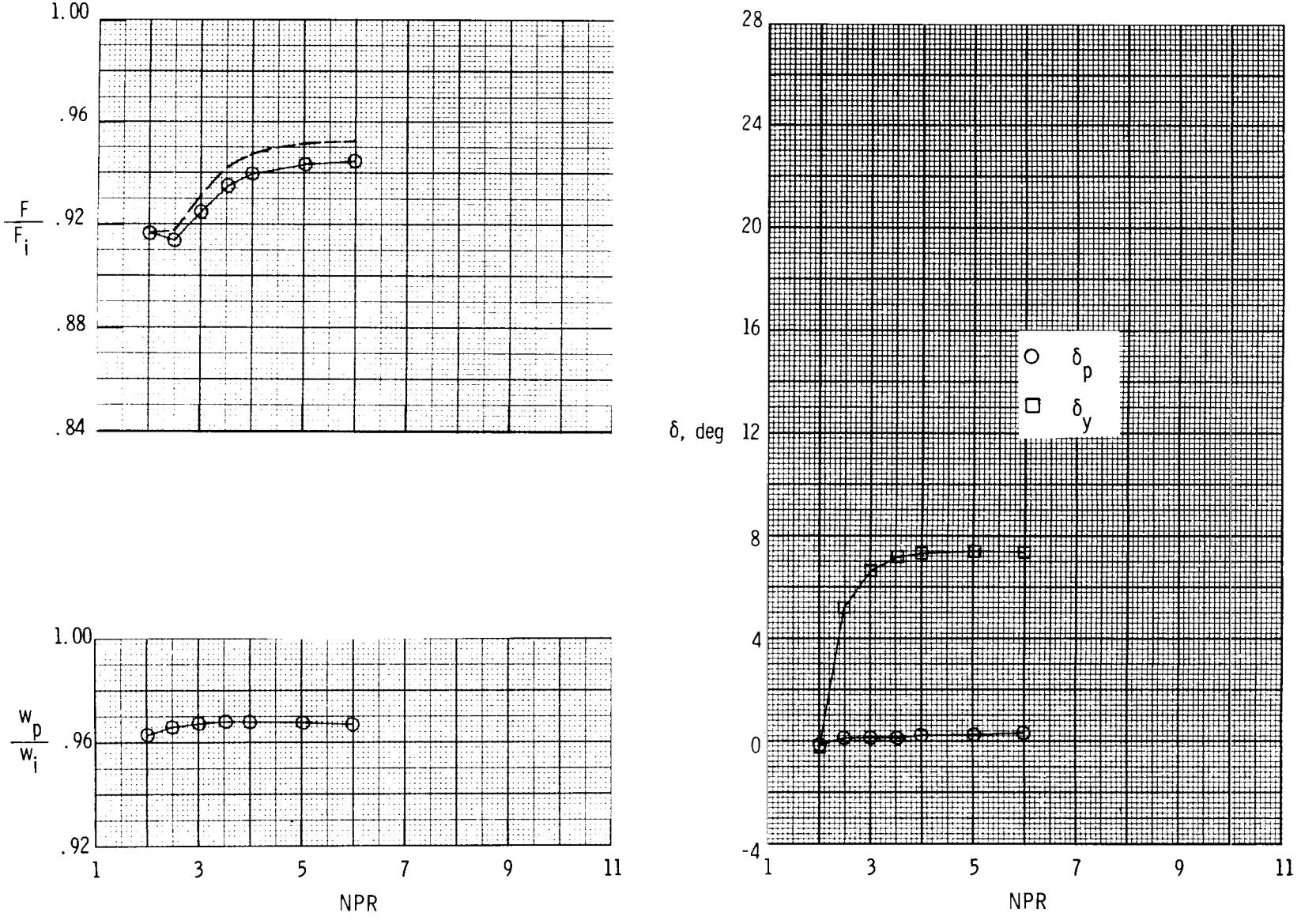

(i) Configuration F21; $x_h = 3.42$ in.; left $\delta_{v,y} = 20°$; right $\delta_{v,y} = 20°$.

Figure 49. Concluded.

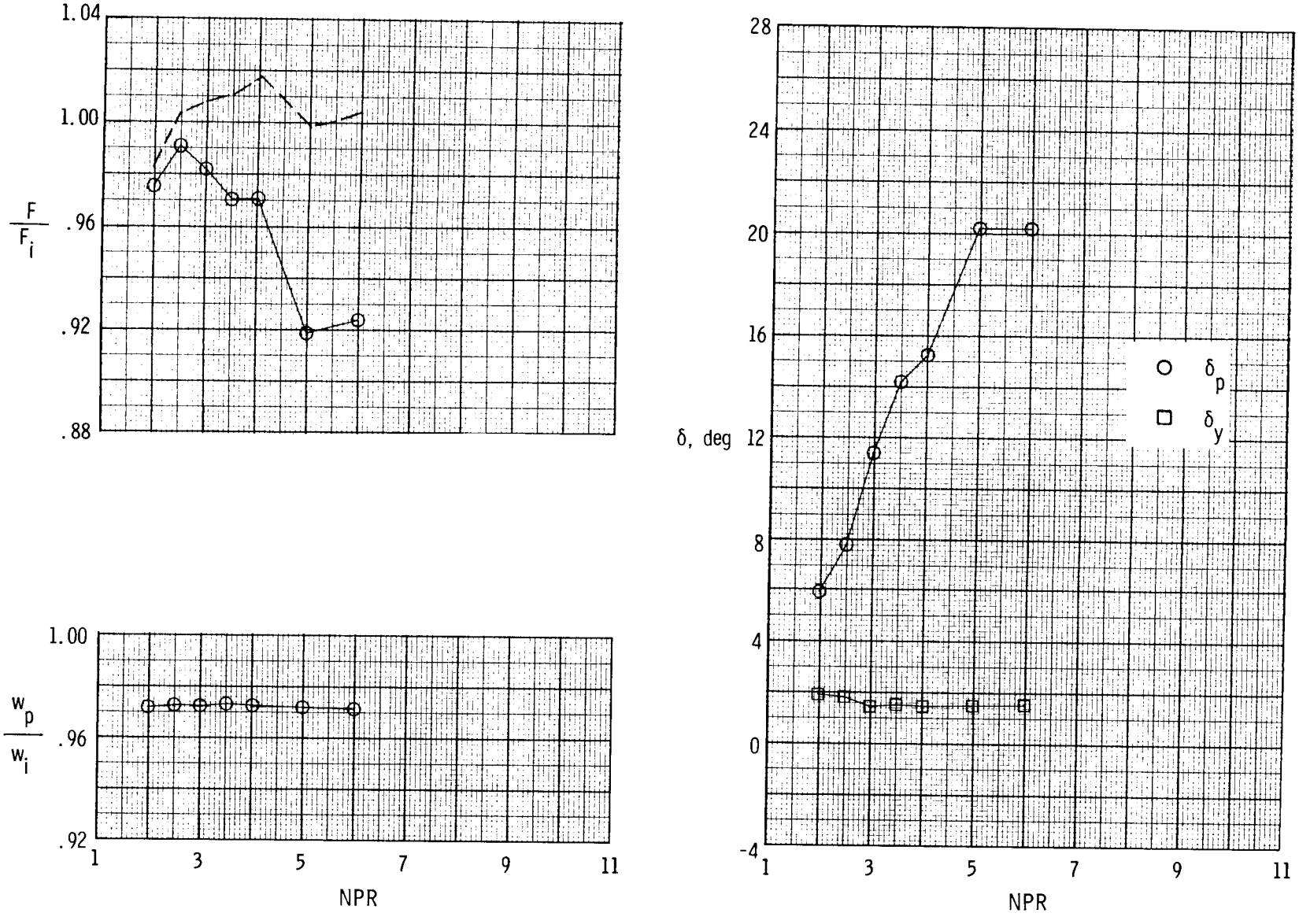

(a) Configuration F22; $x_h = 2.28$ in.; left $\delta_{v,y} = 10°$; right $\delta_{v,y} = 0°$.

Figure 50. Variation of nozzle thrust ratio, discharge coefficient, and resultant thrust vector angles with nozzle pressure ratio for A/B power 2-D C-D nozzle, baseline $A_e/A_t = 1.51$ and $\delta_{v,p} = 20.28°$, with downstream flaps yaw vectoring concept. Dashed line indicates resultant thrust ratio F_r/F_i.

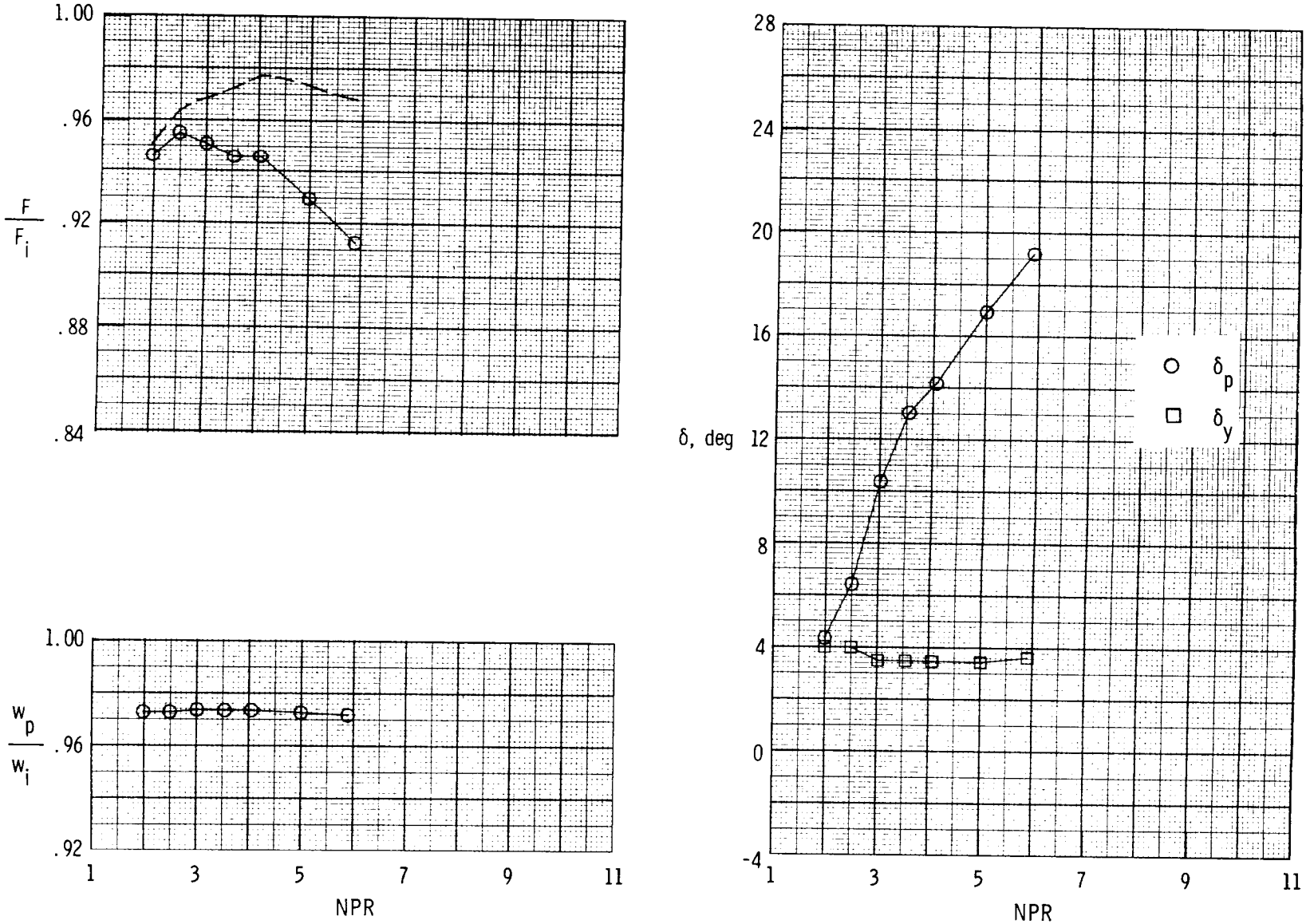

(b) Configuration F23; $x_h = 2.28$ in.; left $\delta_{v,y} = 20°$; right $\delta_{v,y} = 0°$.

Figure 50. Concluded.

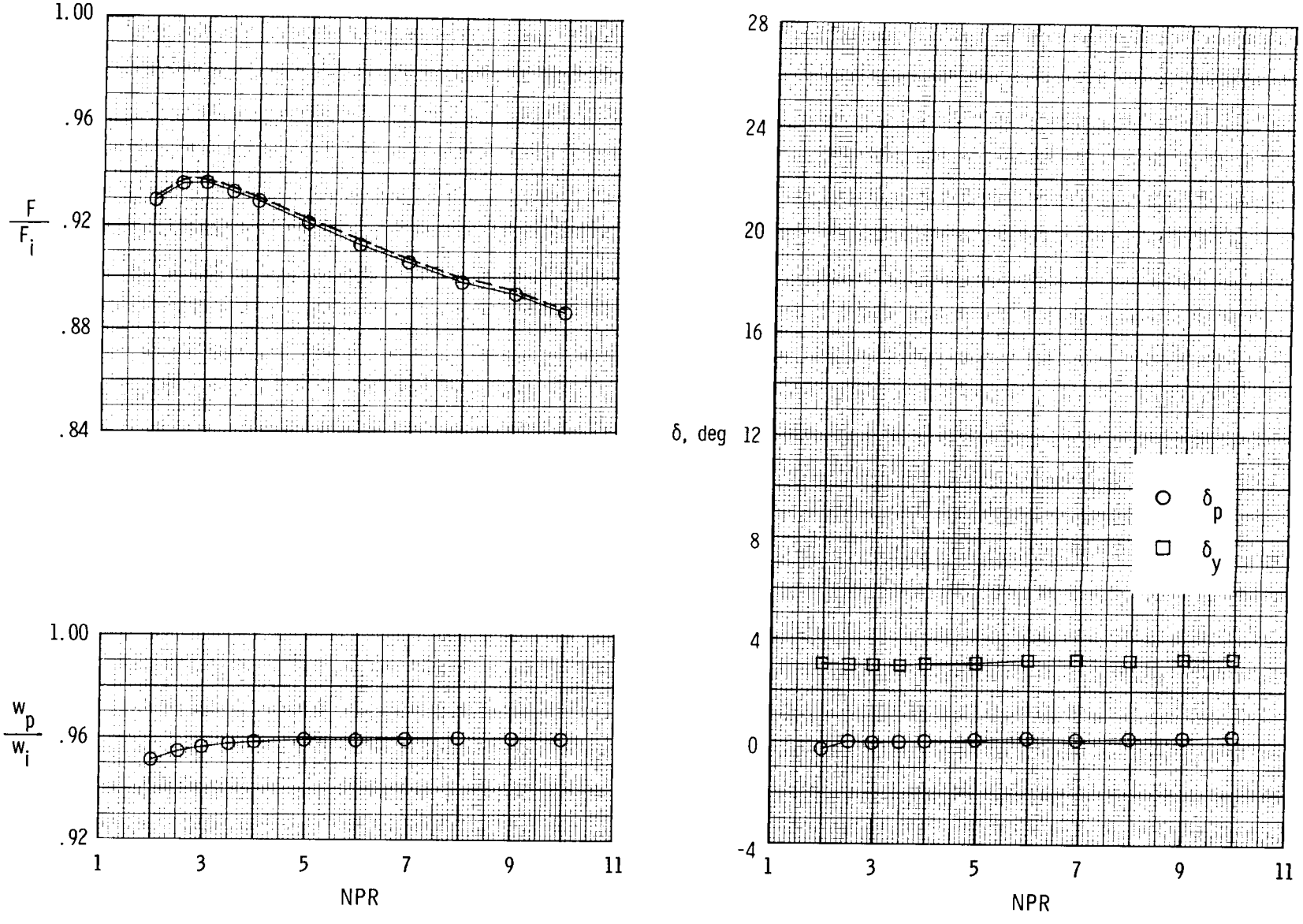

(a) Configuration P1; circular port; $\delta_{v,y} = 90°$.

Figure 51. Variation of nozzle thrust ratio, discharge coefficient, and resultant thrust vector angles with nozzle pressure ratio for dry power 2-D C-D nozzle, baseline $A_e/A_t = 1.08$ and $\delta_{v,p} = 0°$, with upstream port/flap yaw vectoring concept. Dashed line indicates resultant thrust ratio F_r/F_i.

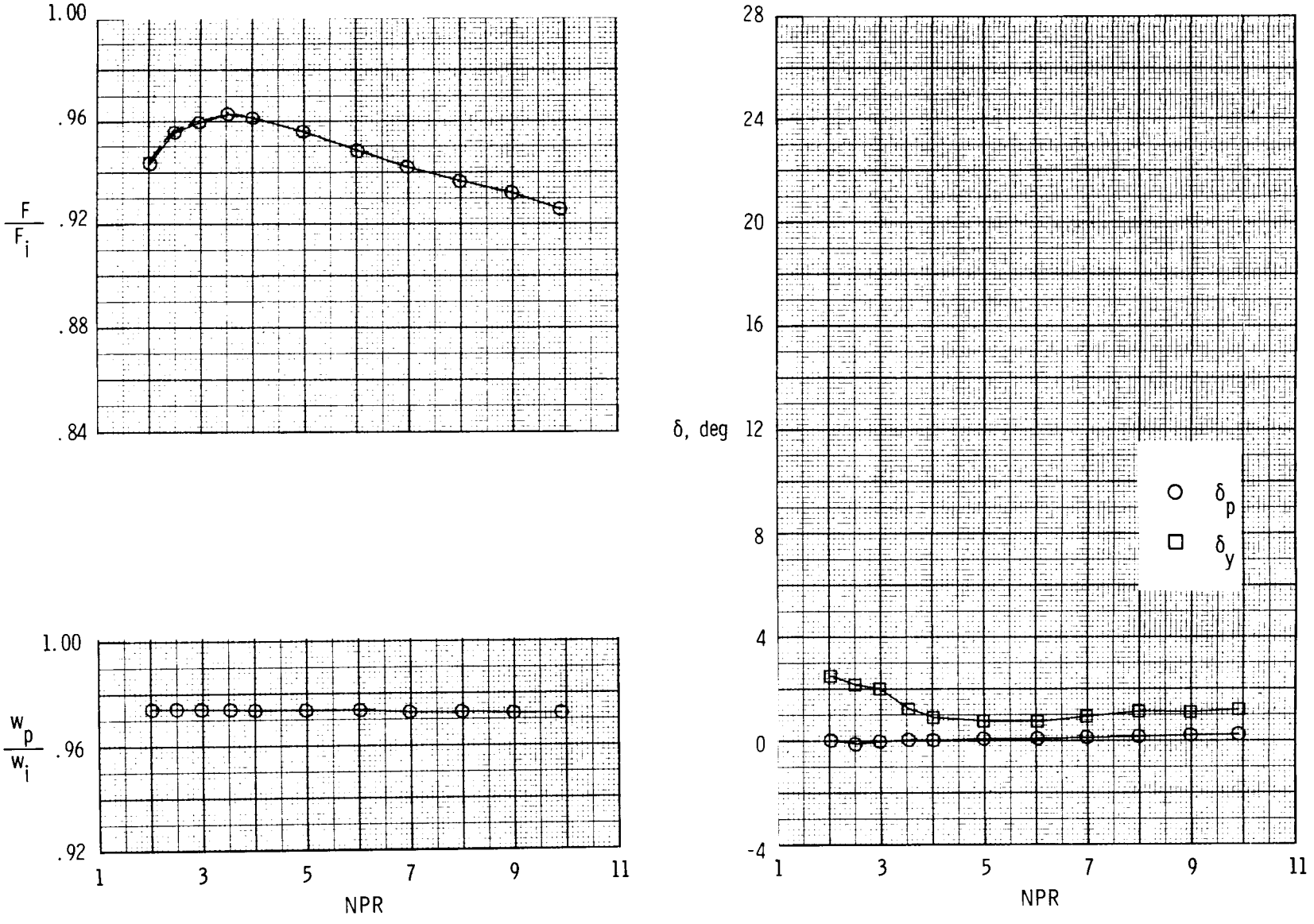

(b) Configuration P2; $x_h = 0.70$ in.; $\delta_{v,y} = 40°$.

Figure 51. Continued.

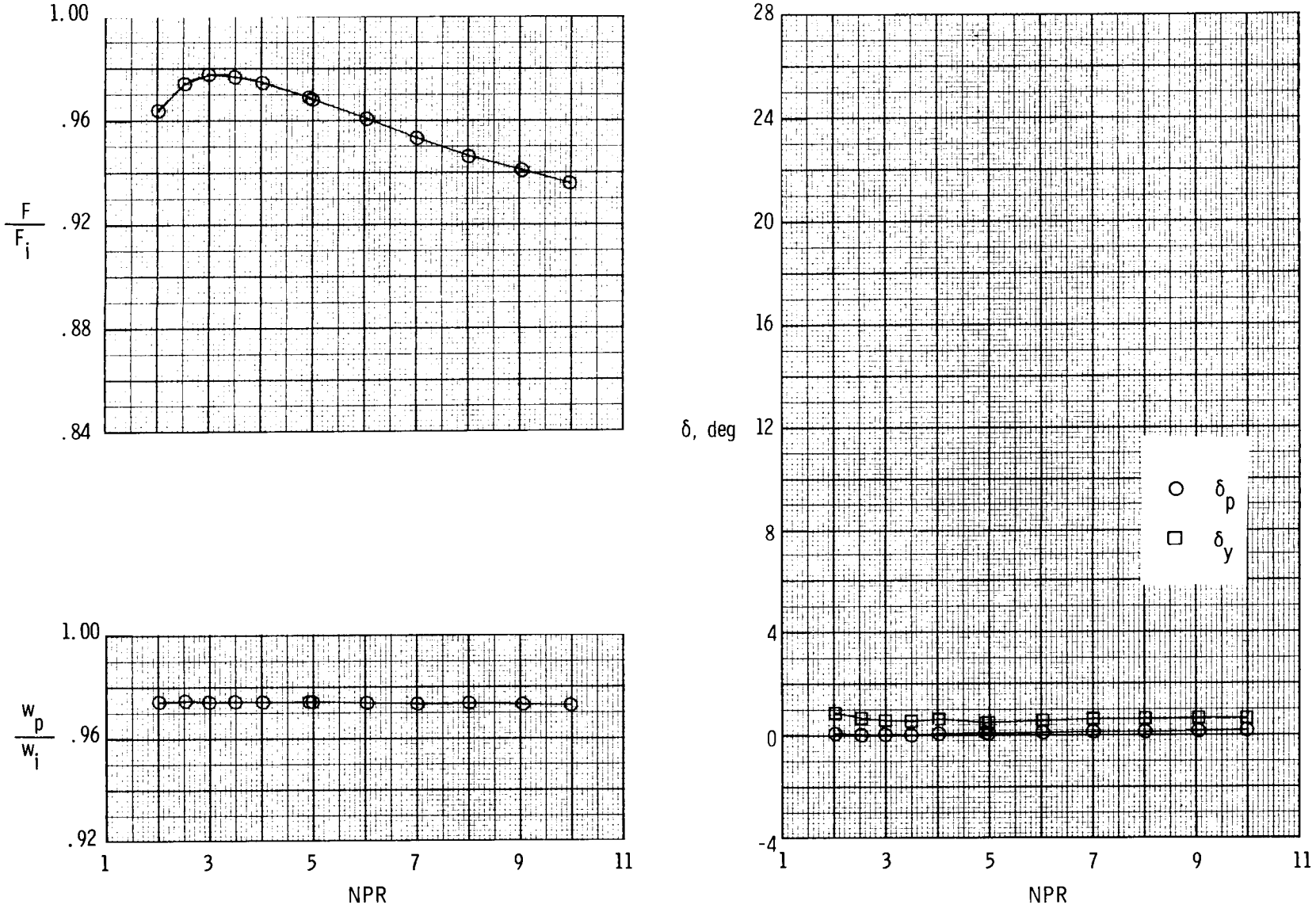

(c) Configuration P3; $x_h = 1.38$ in.; $\delta_{v,y} = 20°$.

Figure 51. Continued.

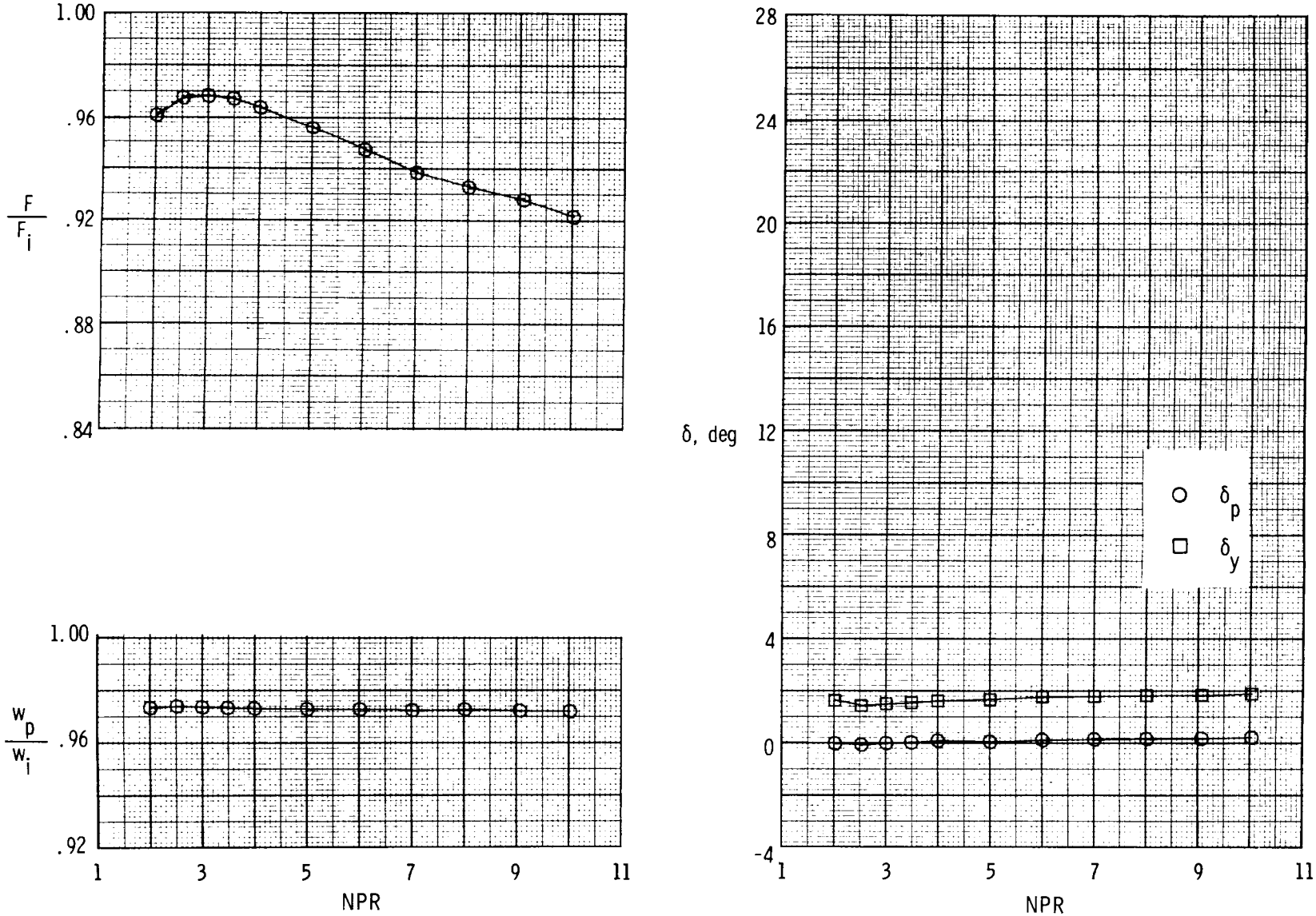

(d) Configuration P4; $x_h = 1.38$ in.; $\delta_{v,y} = 40°$.

Figure 51. Continued.

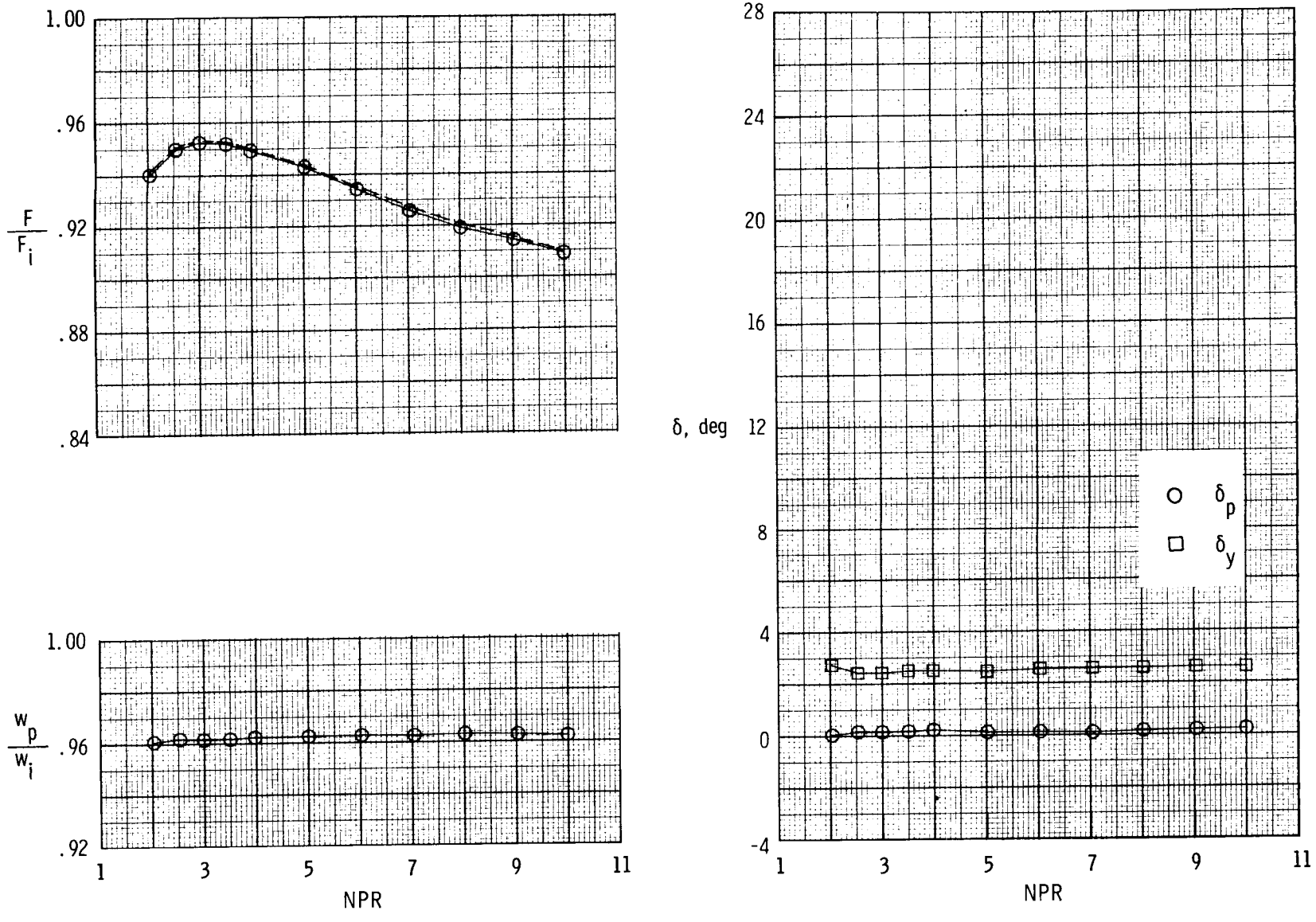

(e) Configuration P5; $x_h = 1.98$ in.; $\delta_{v,y} = 40°$.

Figure 51. Concluded.

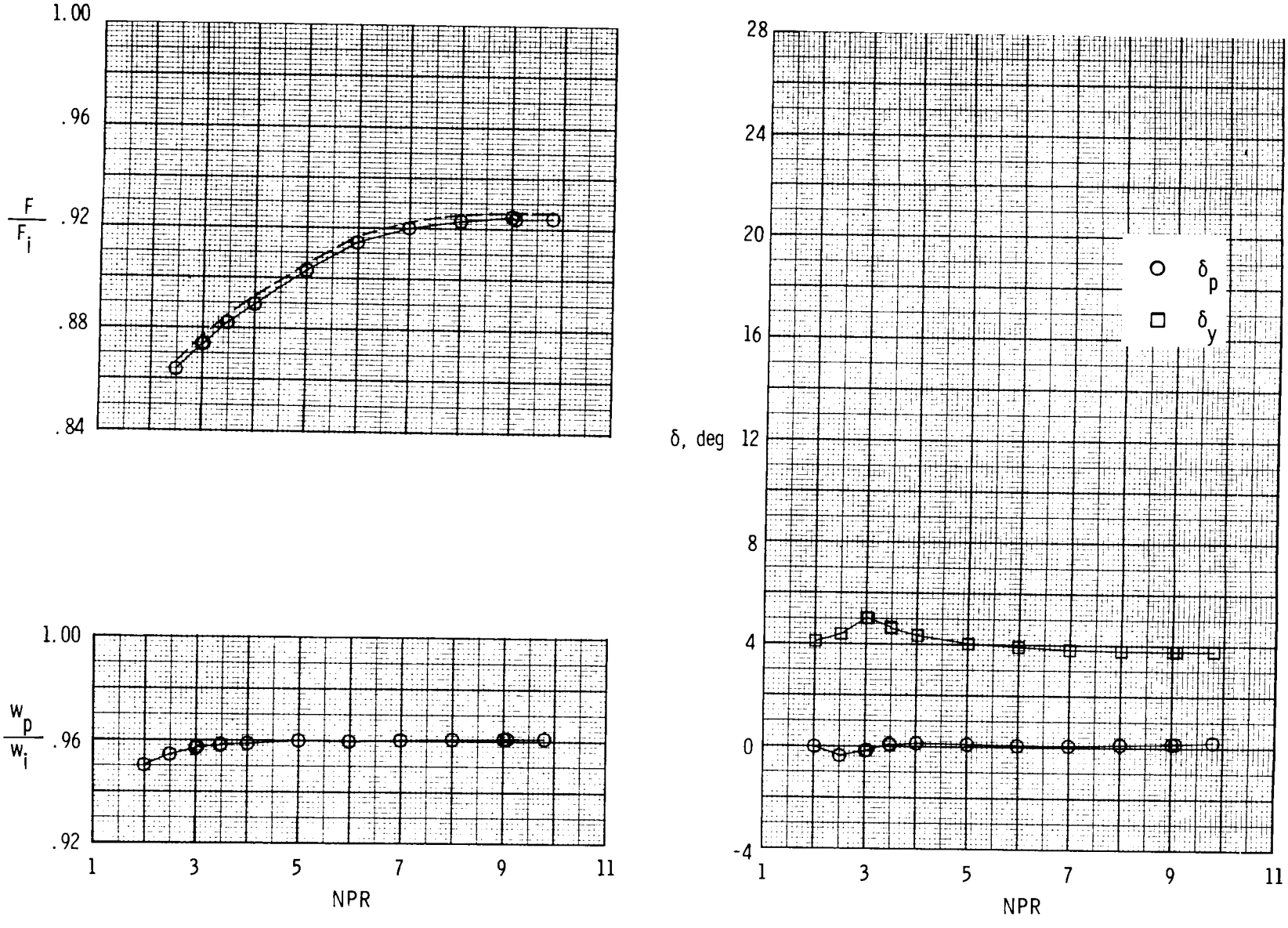

(a) Configuration P6; circular port; $\delta_{v,y} = 90°$.

Figure 52. Variation of nozzle thrust ratio, discharge coefficient, and resultant thrust vector angles with nozzle pressure ratio for dry power 2-D C-D nozzle, baseline $A_e/A_t = 1.78$ and $\delta_{v,p} = 0°$, with upstream port/flap yaw vectoring concept. Dashed line indicates resultant thrust ratio F_r/F_i.

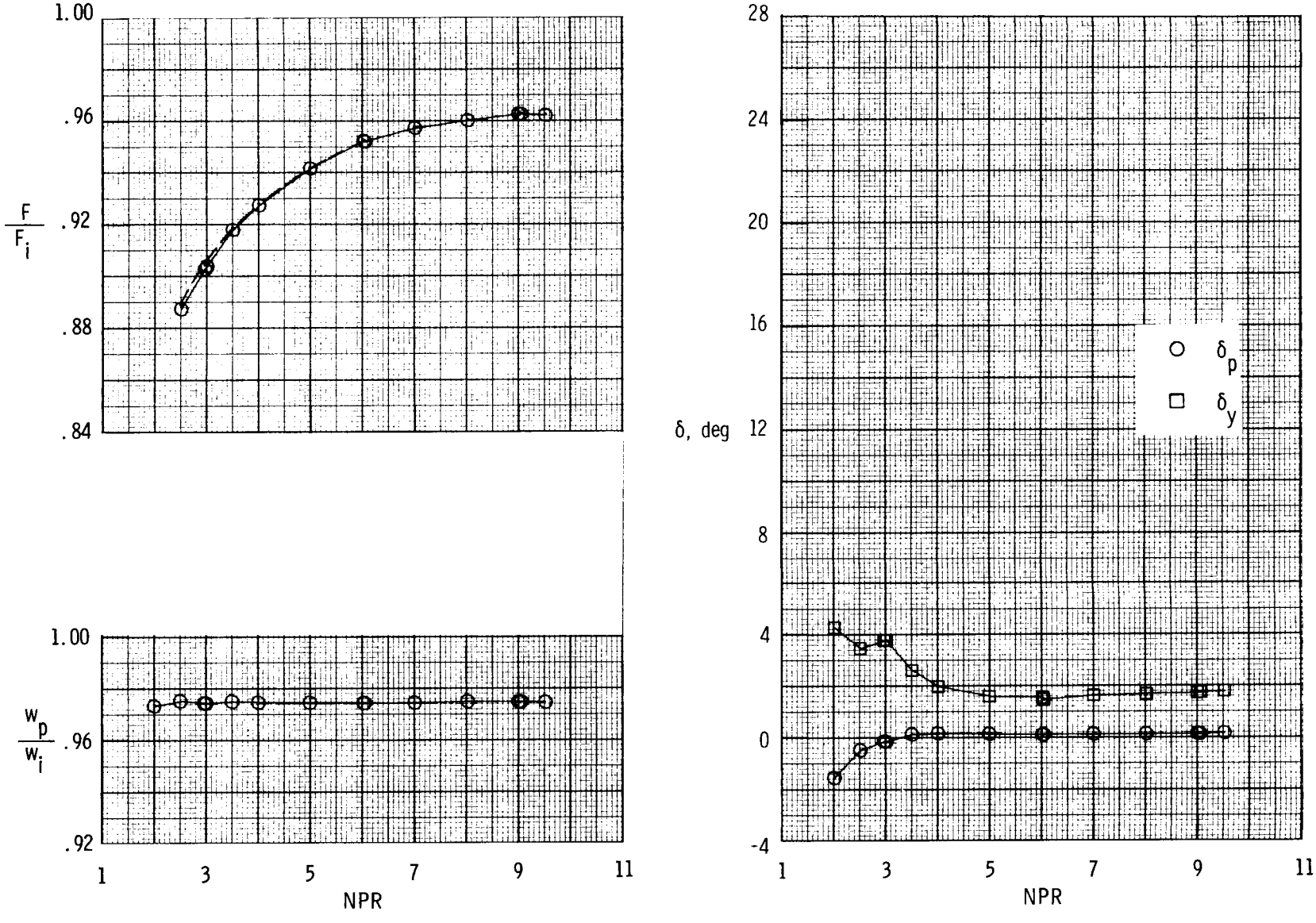

(b) Configuration P7; $x_h = 0.70$ in.; $\delta_{v,y} = 40°$

Figure 52. Continued.

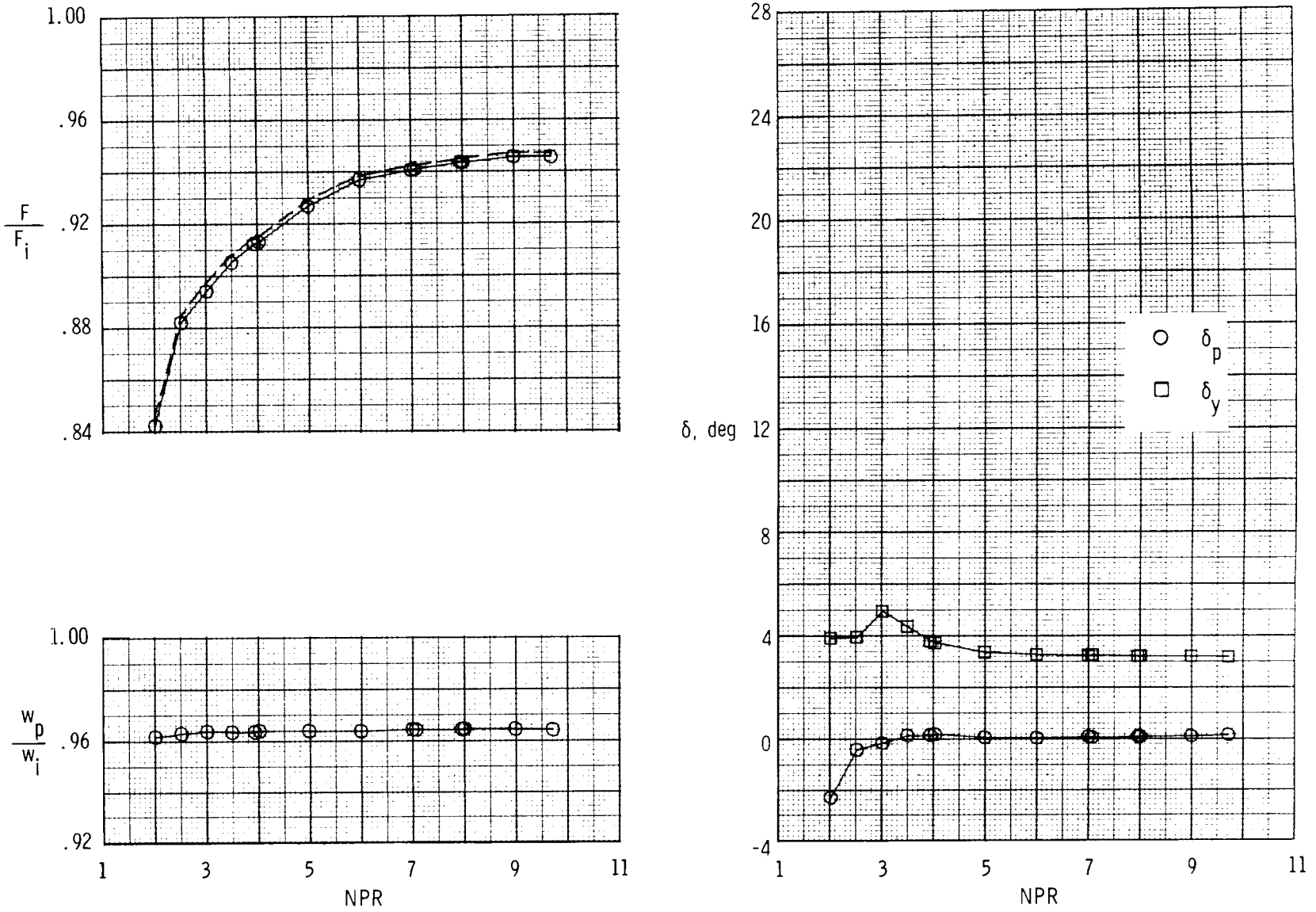

(c) Configuration P8; $x_h = 1.98$ in.; $\delta_{v,y} = 40°$.

Figure 52. Concluded.

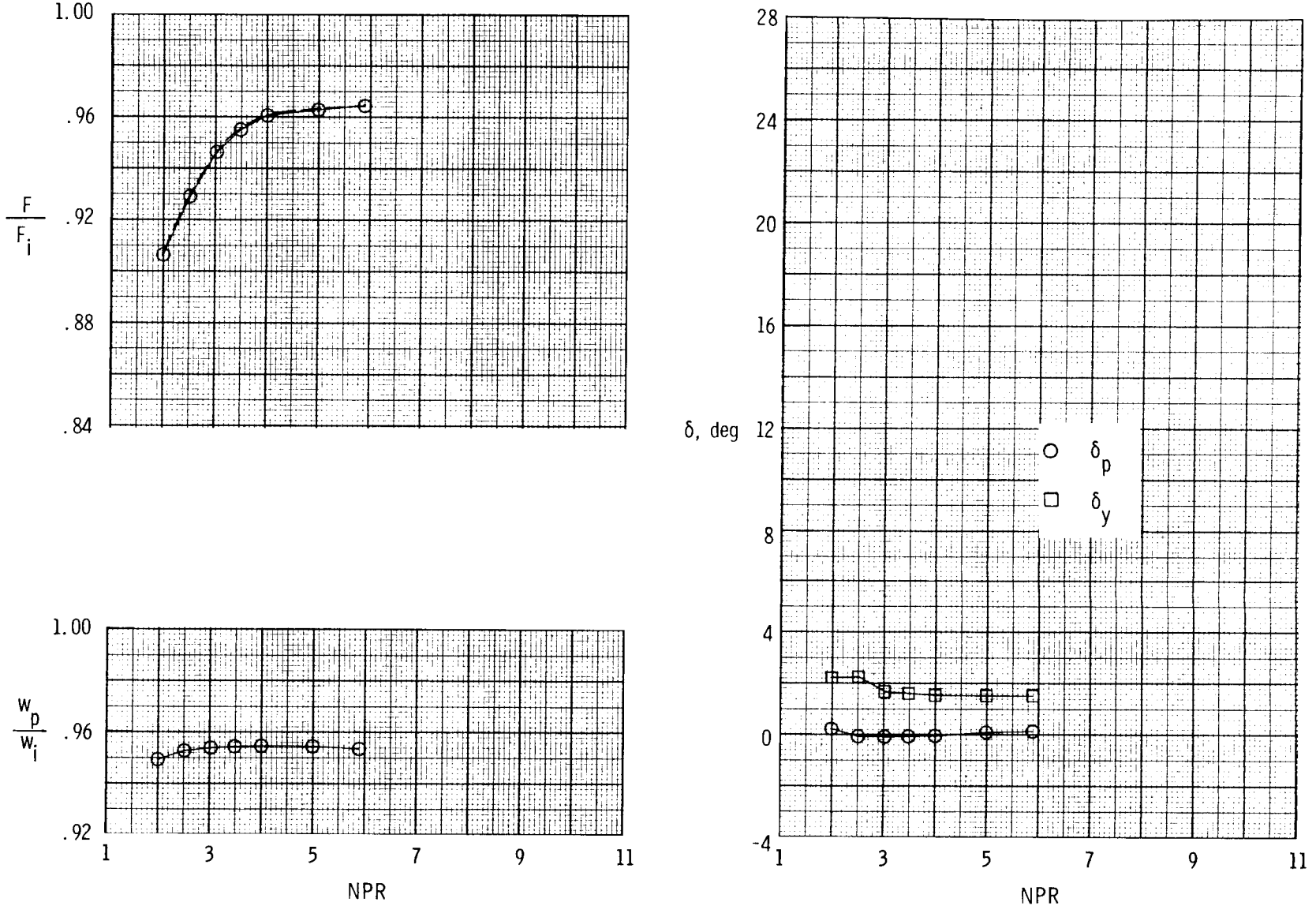

(a) Configuration P9; circular port; $\delta_{v,y} = 90°$.

Figure 53. Variation of nozzle thrust ratio, discharge coefficient, and resultant thrust vector angles with nozzle pressure ratio for A/B power 2-D C-D nozzle, baseline $A_e/A_t = 1.29$ and $\delta_{v,p} = 0°$, with upstream port/flap yaw vectoring concept. Dashed line indicates resultant thrust ratio F_r/F_i.

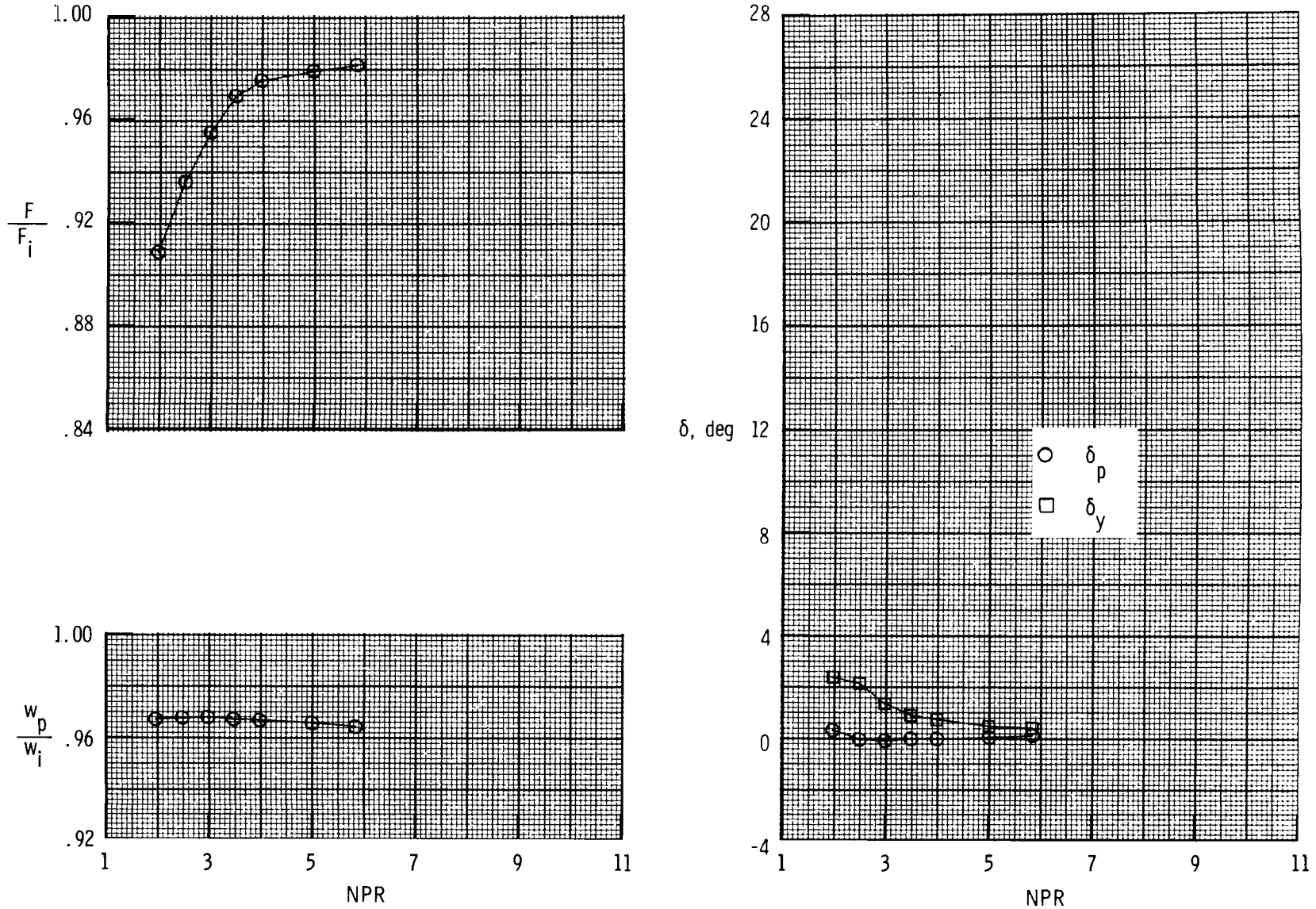

(b) Configuration P10; $x_h = 0.70$ in.; $\delta_{v,y} = 40°$.

Figure 53. Continued.

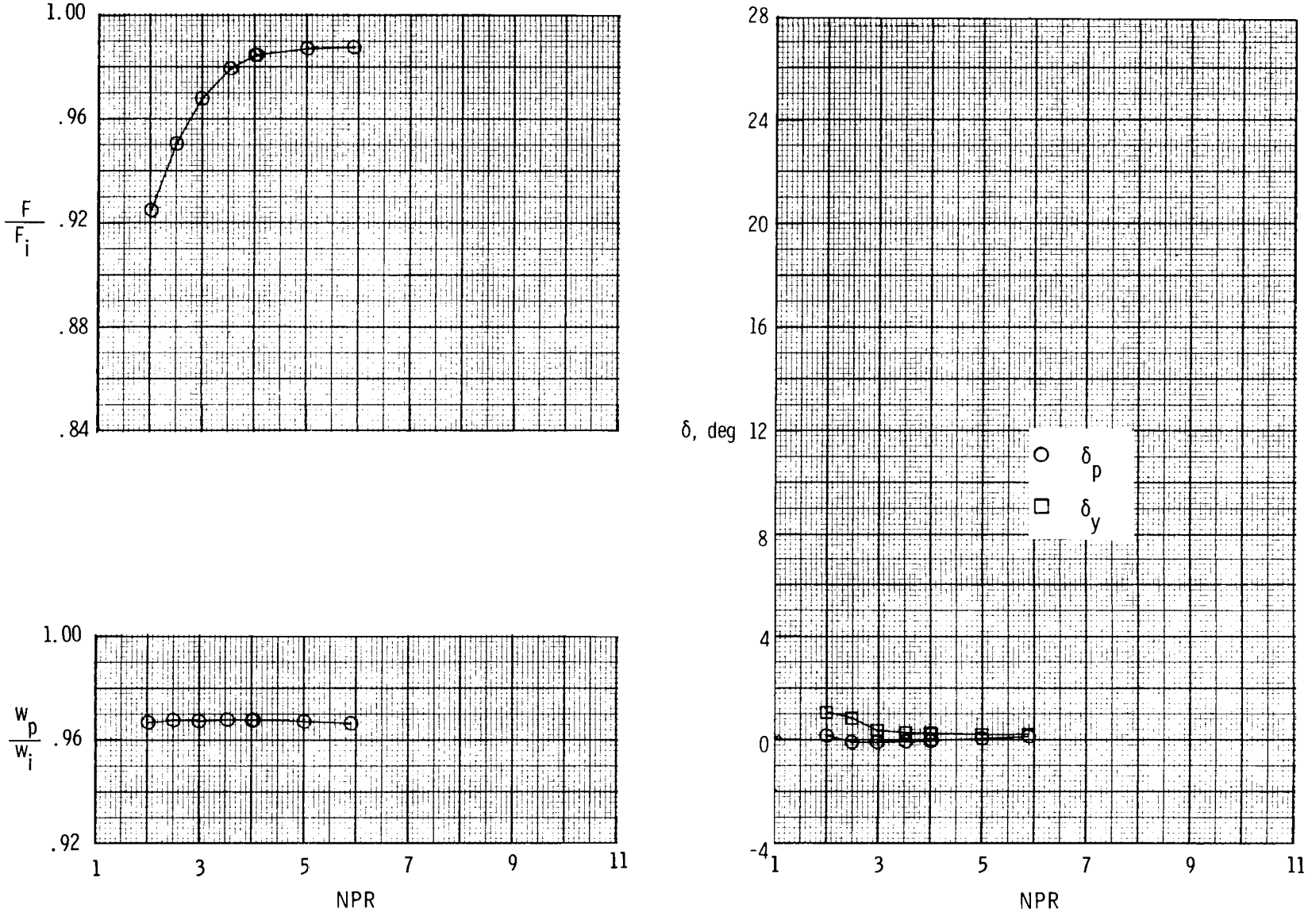

(c) Configuration P11; $x_h = 1.38$ in.; $\delta_{v,y} = 20°$.

Figure 53. Continued.

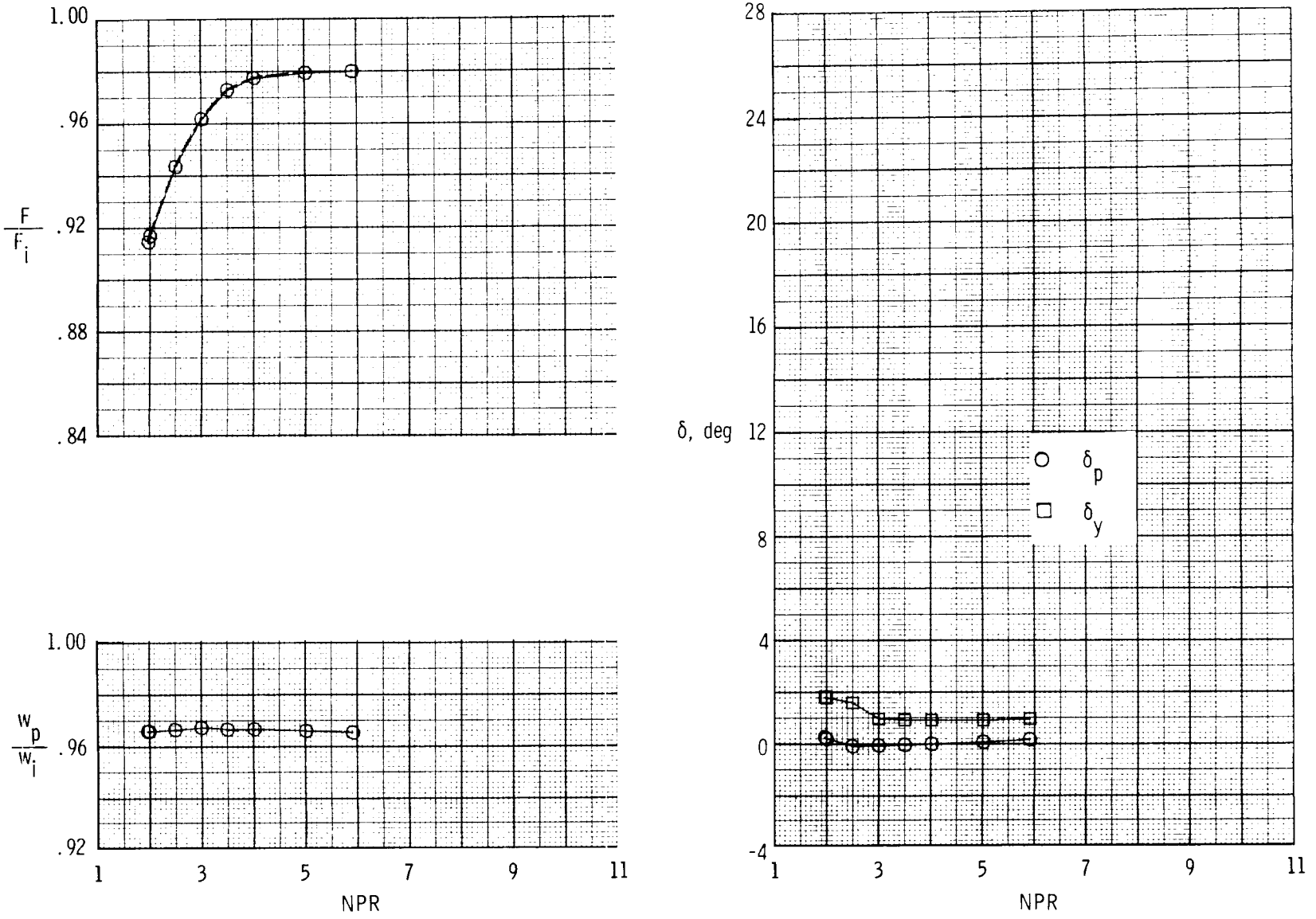

(d) Configuration P12; $x_h = 1.38$ in.; $\delta_{v,y} = 40°$.

Figure 53. Continued.

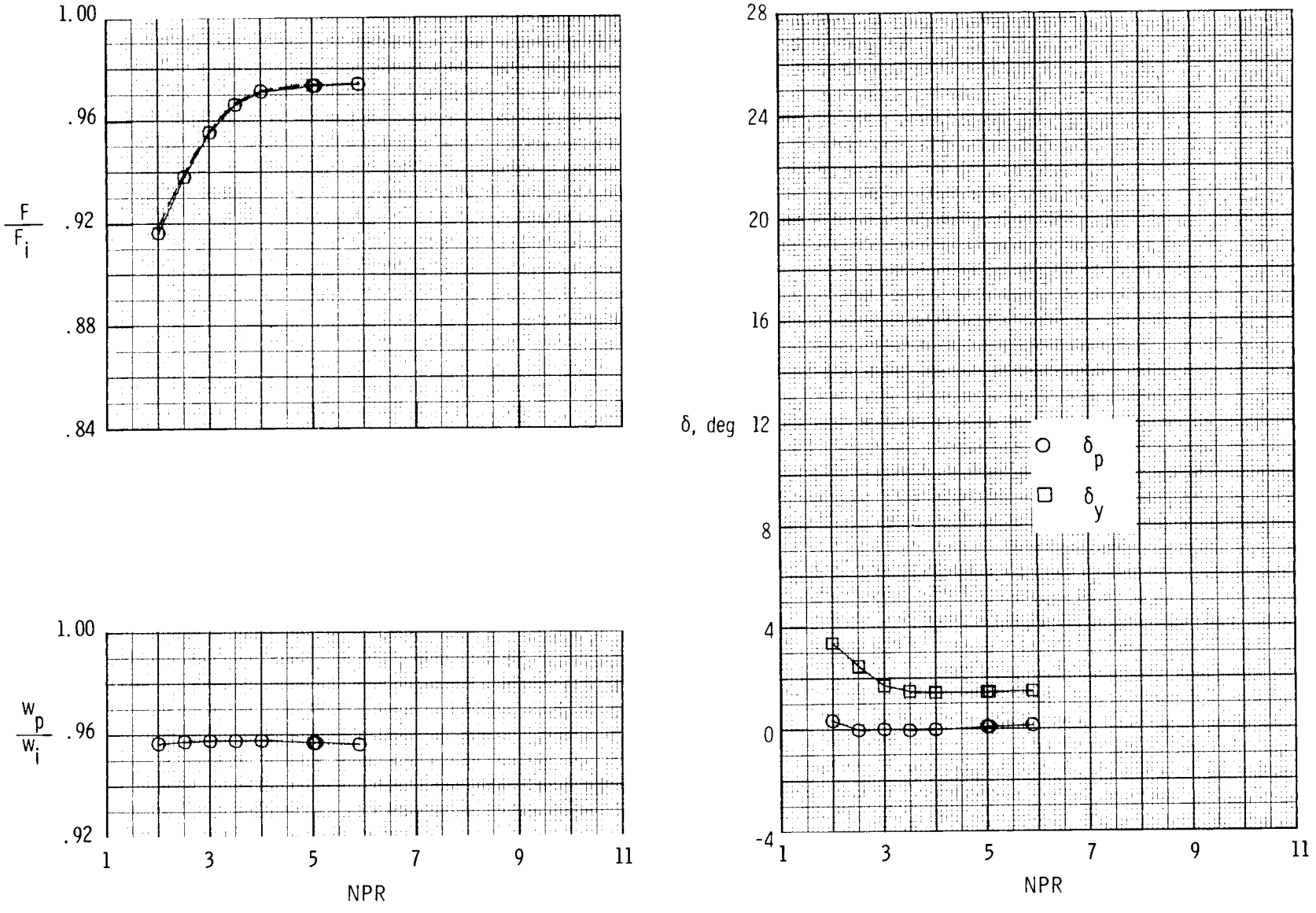

(e) Configuration P13; $x_h = 1.98$ in.; $\delta_{v,y} = 40°$.

Figure 53. Concluded.

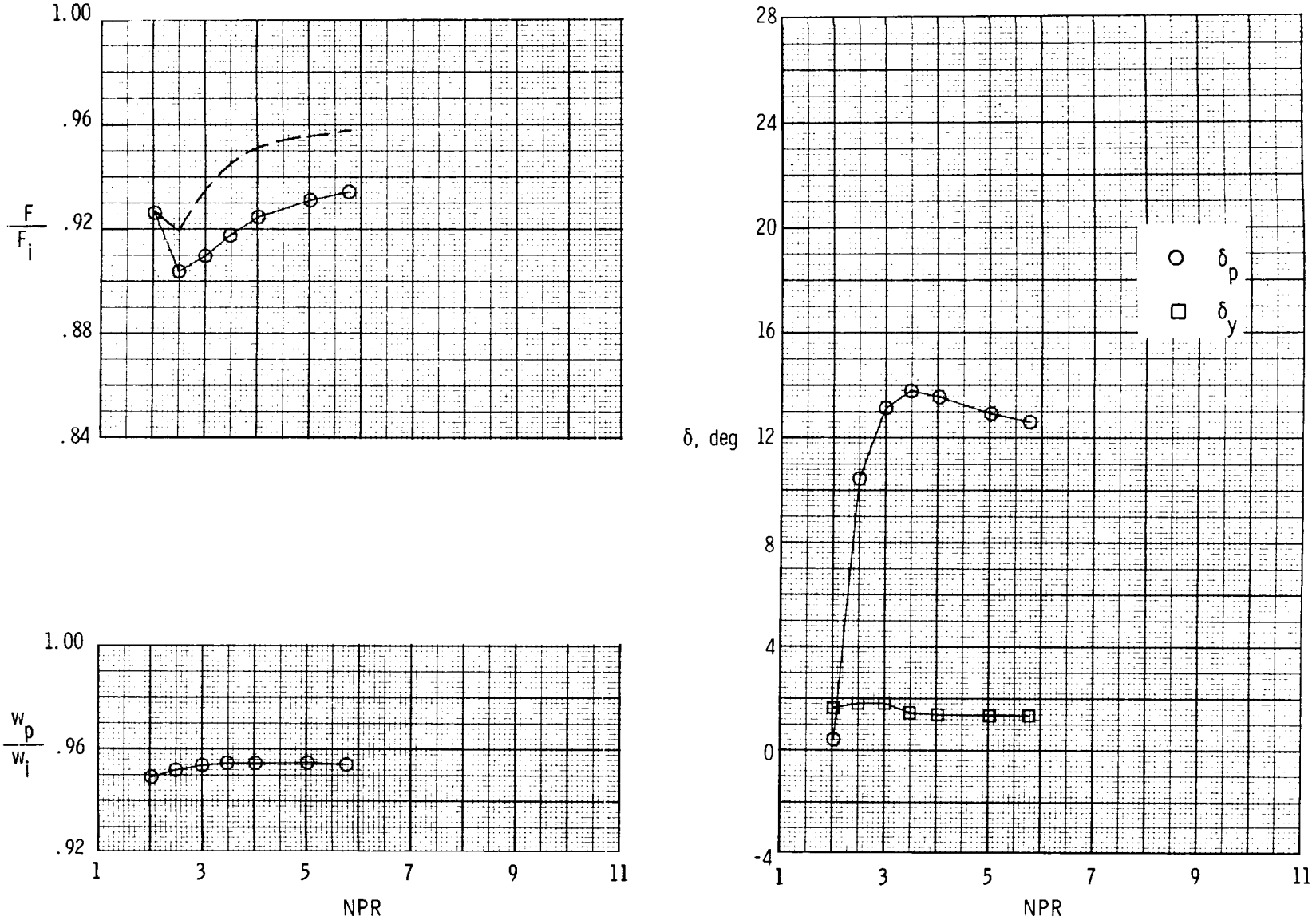

(a) Configuration P14; circular port; $\delta_{v,y} = 90°$.

Figure 54. Variation of nozzle thrust ratio, discharge coefficient, and resultant thrust vector angles with nozzle pressure ratio for A/B power 2-D C-D nozzle baseline $A_e/A_t = 1.35$ and $\delta_{v,p} = 9.79°$, with upstream port/flap yaw vectoring concept. Dashed line indicates resultant thrust ratio F_r/F_i.

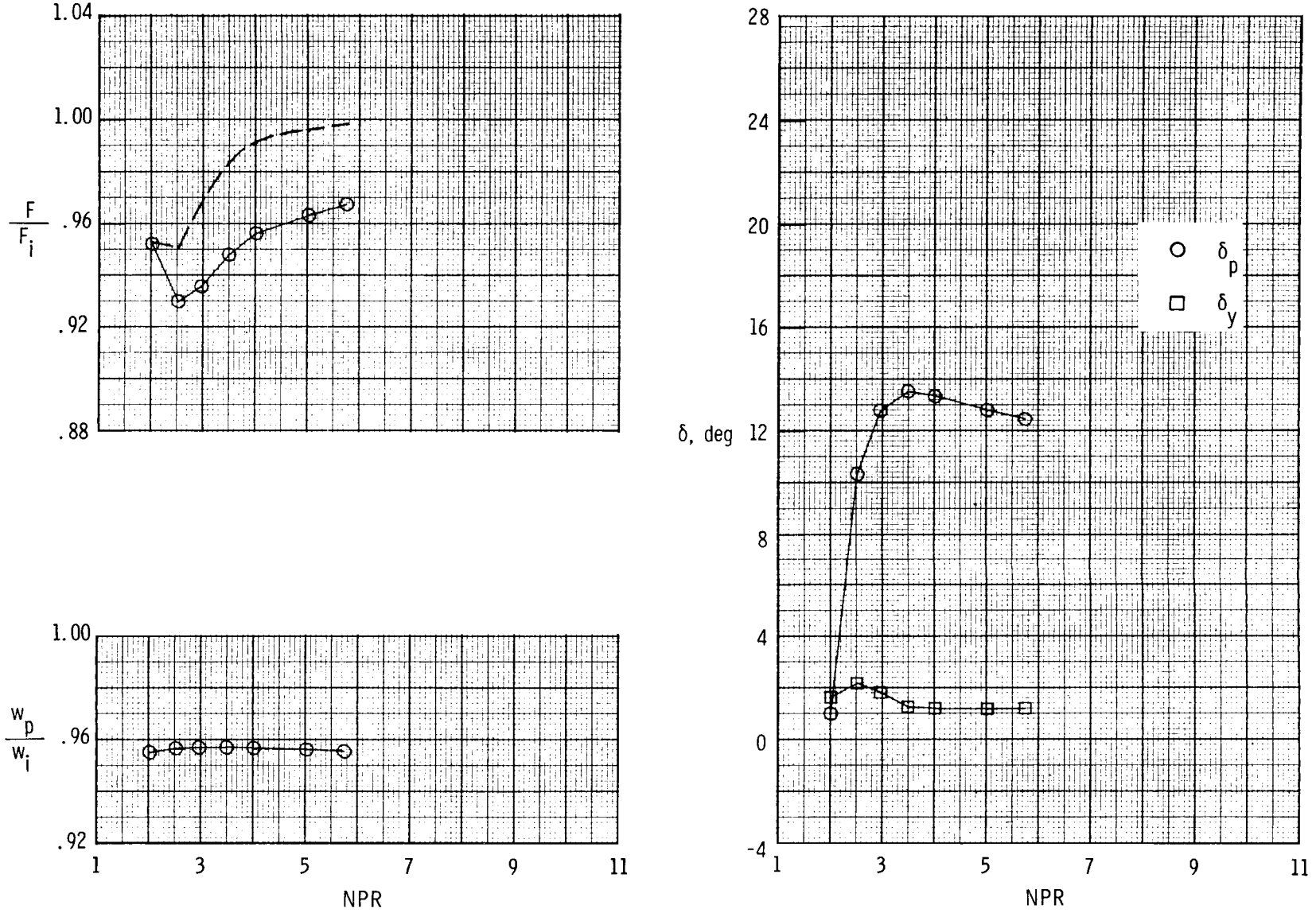

(b) Configuration P15; $x_h = 1.38$ in.; $\delta_{v,y} = 40°$.

Figure 54. Concluded.

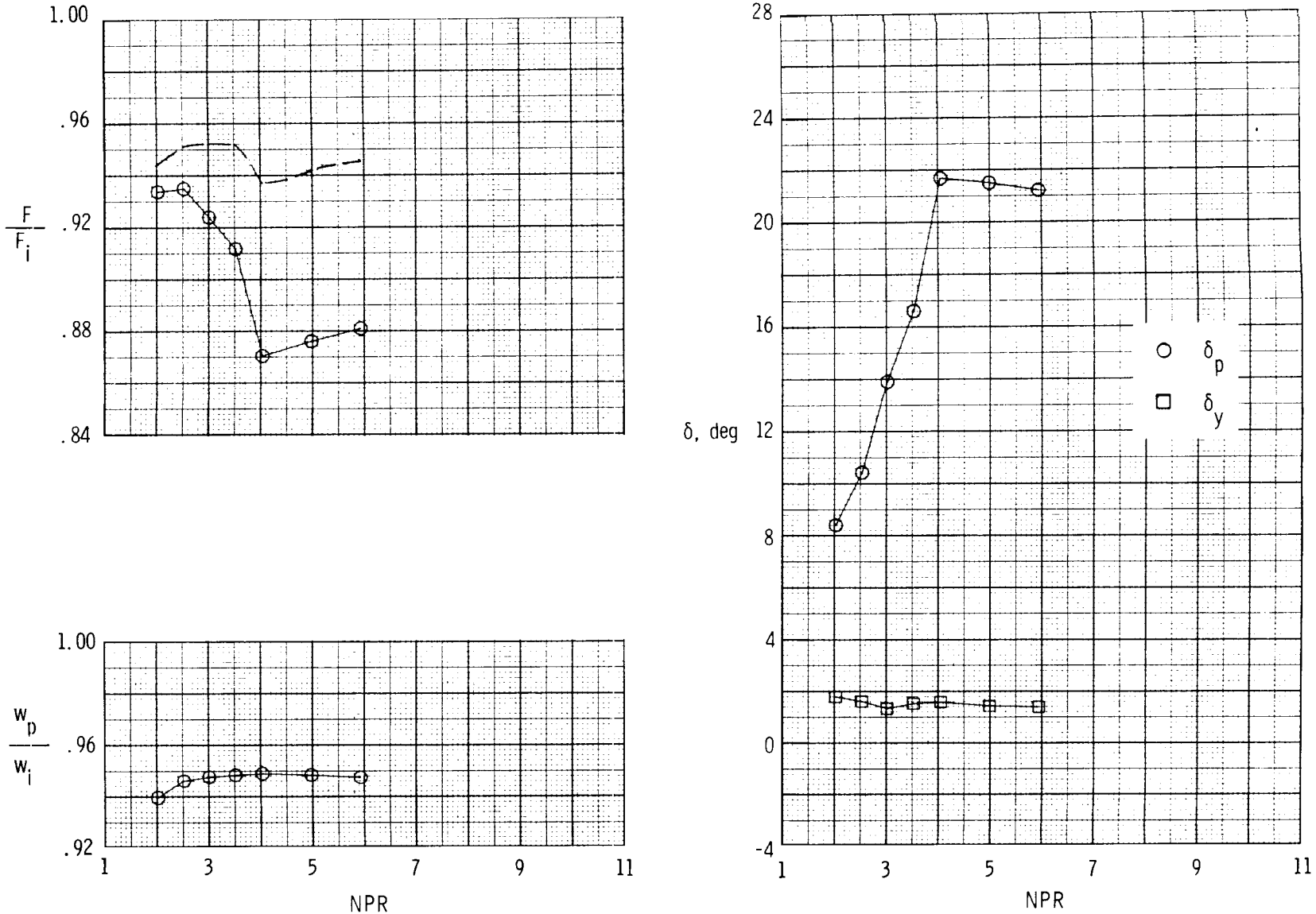

(a) Configuration P16; circular port; $\delta_{v,y} = 90°$.

Figure 55. Variation of nozzle thrust ratio, discharge coefficient, and resultant thrust vector angles with nozzle pressure ratio for A/B power 2-D C-D nozzle, baseline $A_e/A_t = 1.51$ and $\delta_{v,p} = 20.28°$, with upstream port/flap yaw vectoring concept. Dashed line indicates resultant thrust ratio F_r/F_i.

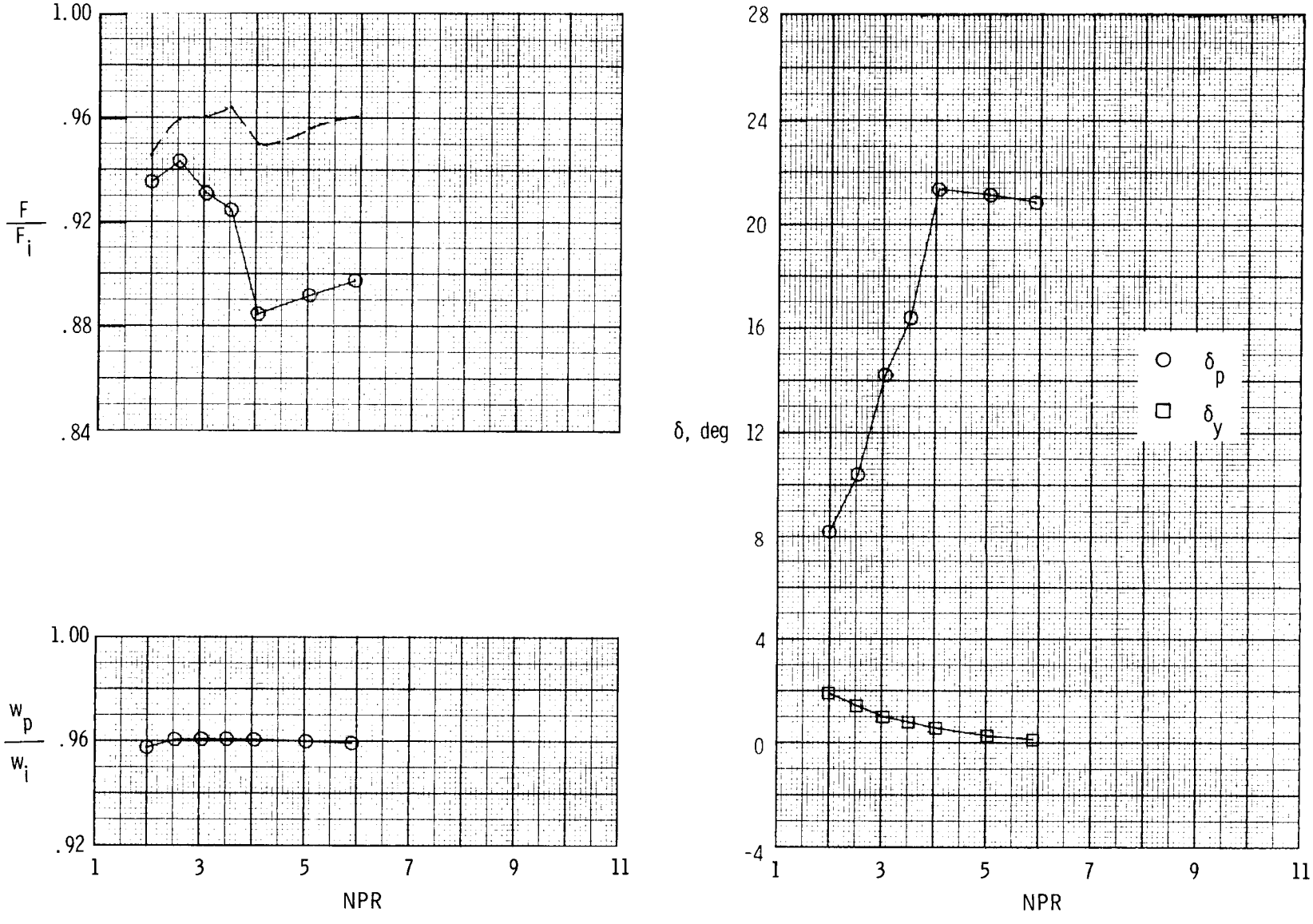

(b) Configuration P17; $x_h = 0.70$ in.; $\delta_{v,y} = 40°$.

Figure 55. Continued.

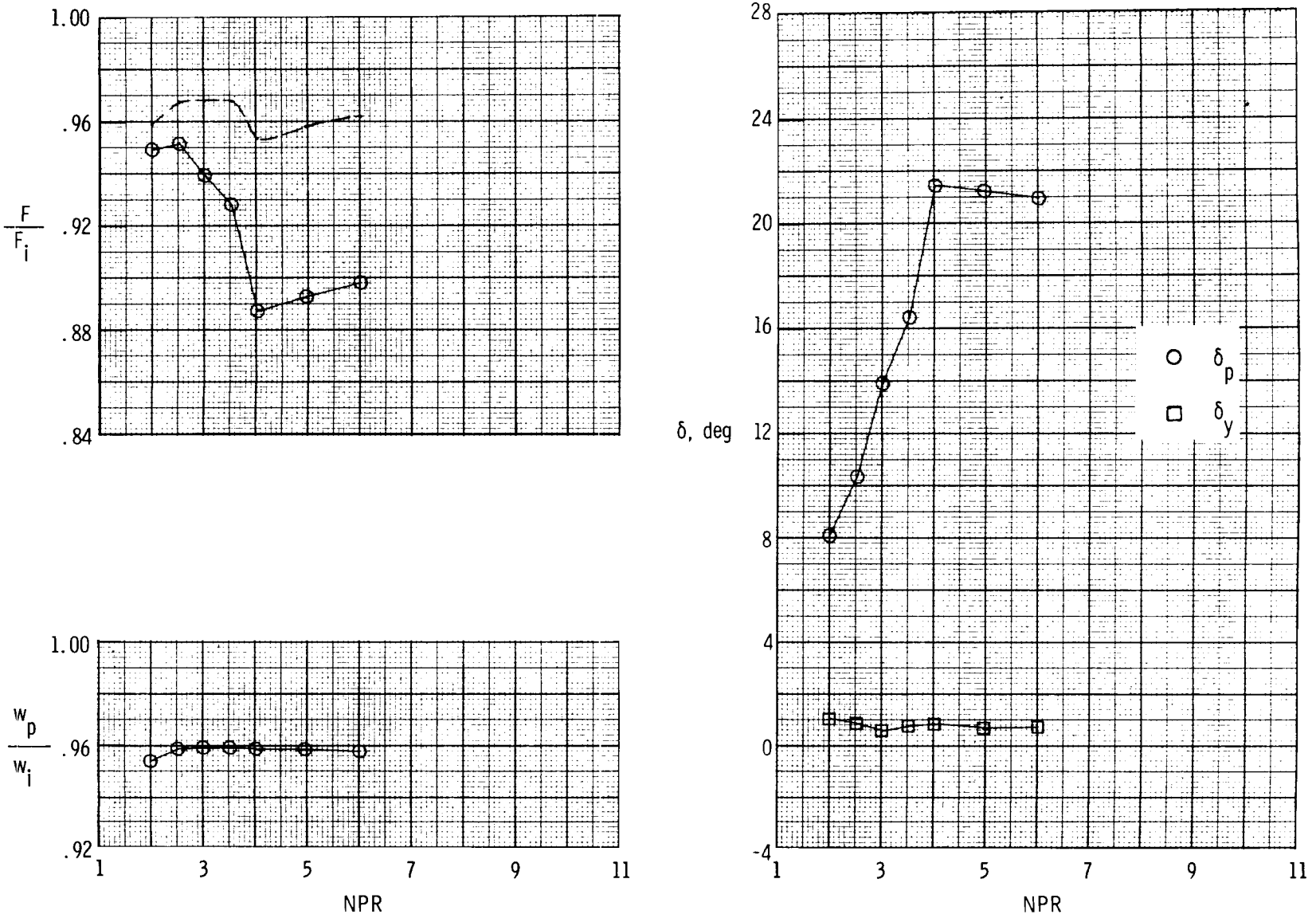

(c) Configuration P18; $x_h = 1.38$ in.; $\delta_{v,y} = 40°$.

Figure 55. Continued.

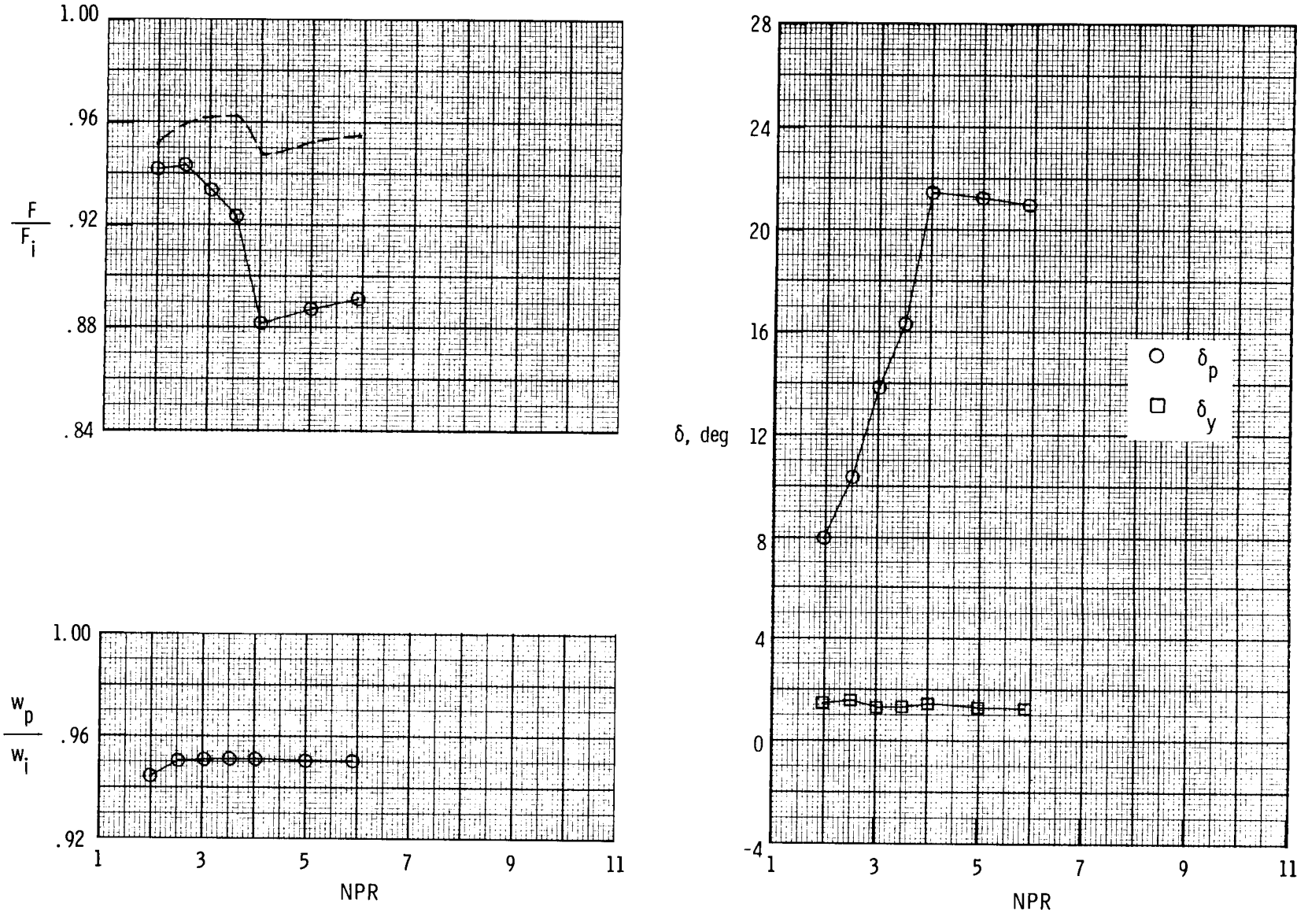

(d) Configuration P19; $x_h = 1.98$ in.; $\delta_{v,y} = 40°$.

Figure 55. Concluded.

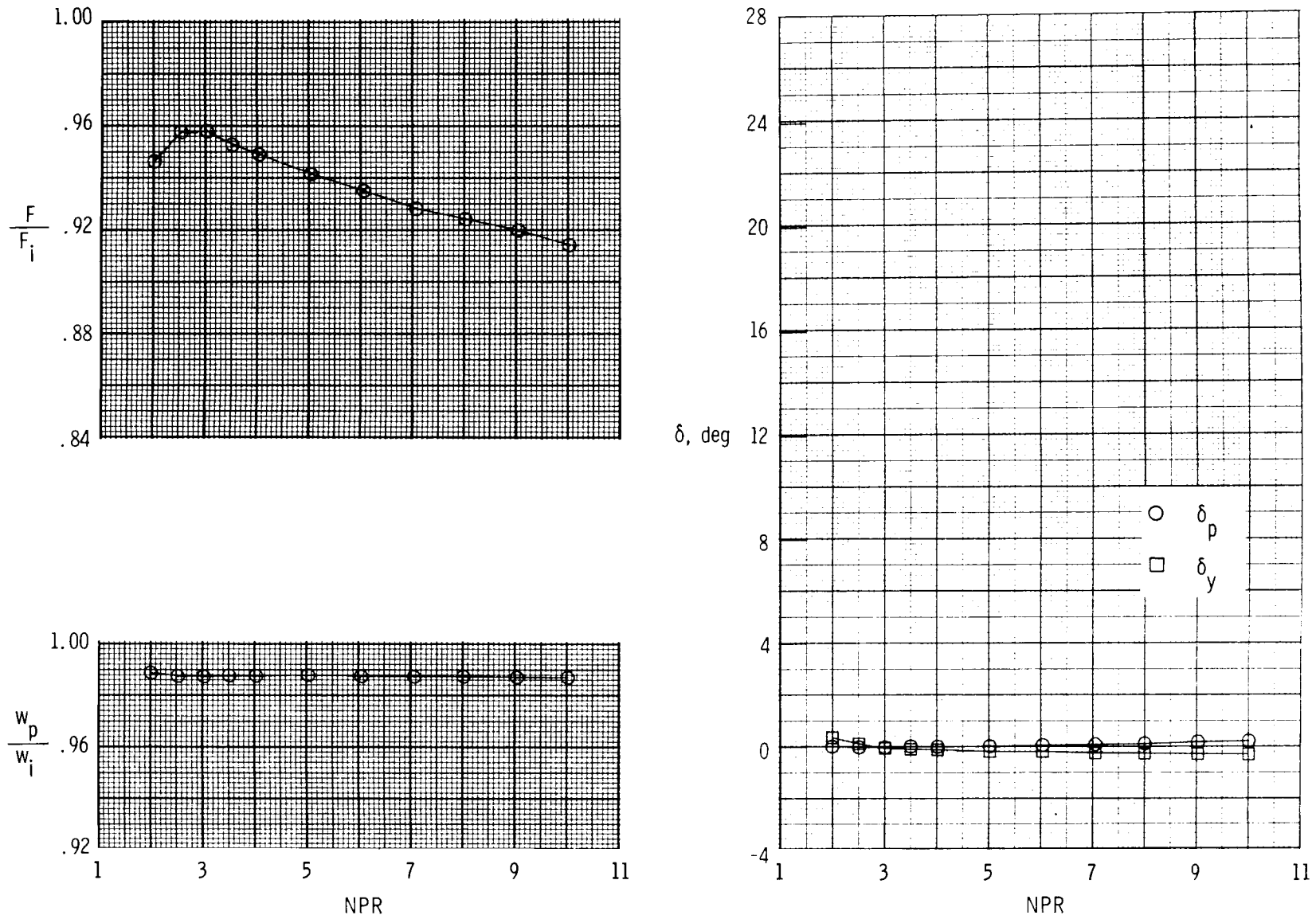

(a) Configuration R1; $c = 0.75$ in.; $\delta_{v,y} = 0°$.

Figure 56. Variation of nozzle thrust ratio, discharge coefficient, and resultant thrust vector angles with nozzle pressure ratio for dry power 2-D C-D nozzle, baseline $A_e/A_t = 1.08$ and $\delta_{v,p} = 0°$, with powered rudder yaw vectoring concept. Dashed line indicates resultant thrust ratio F_r/F_i.

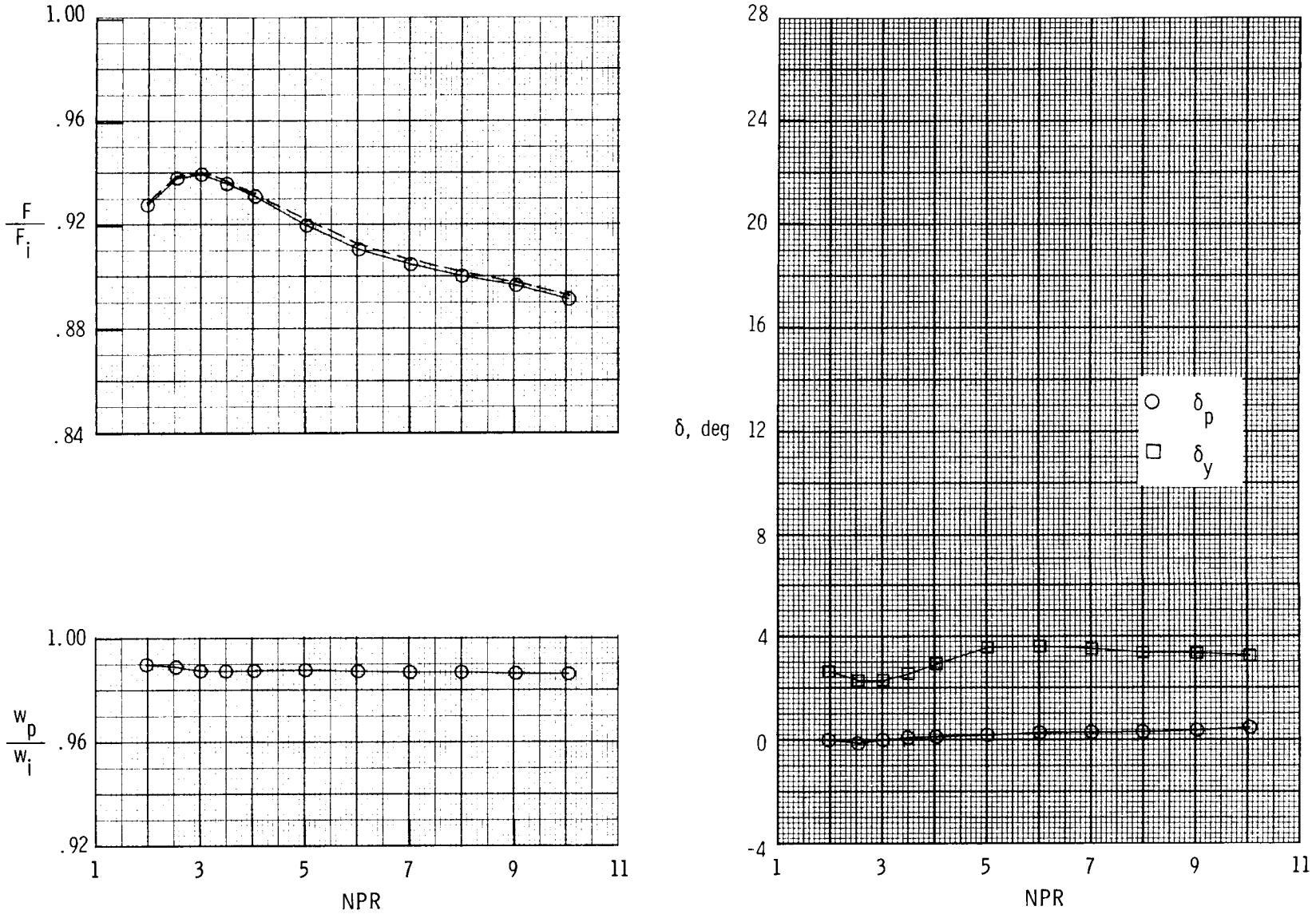

(b) Configuration R2; $c = 0.75$ in.; $\delta_{v,y} = 20°$.

Figure 56. Continued.

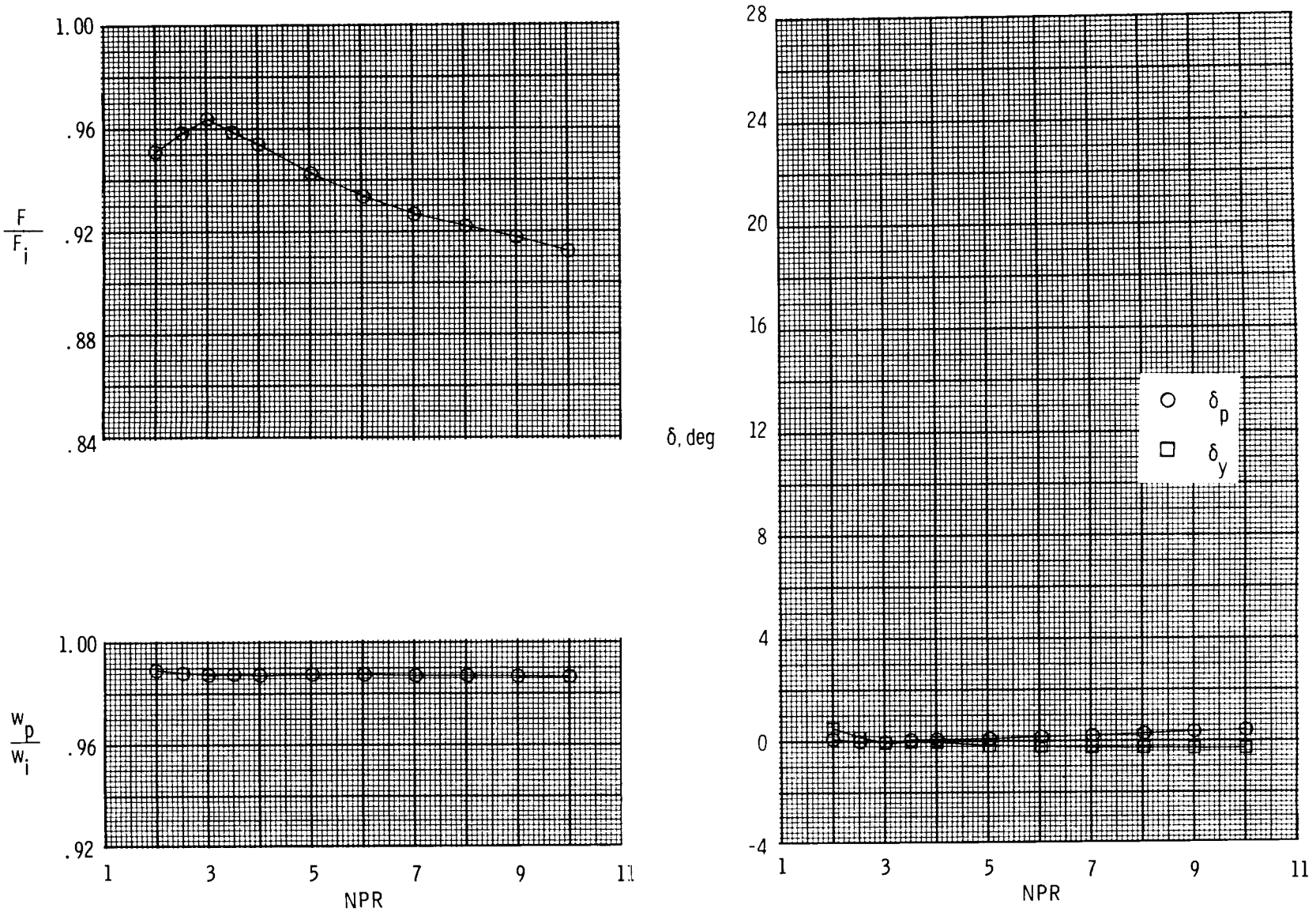

(c) Configuration R3; $c = 1.50$ in.; $\delta_{v,y} = 0°$.

Figure 56. Continued.

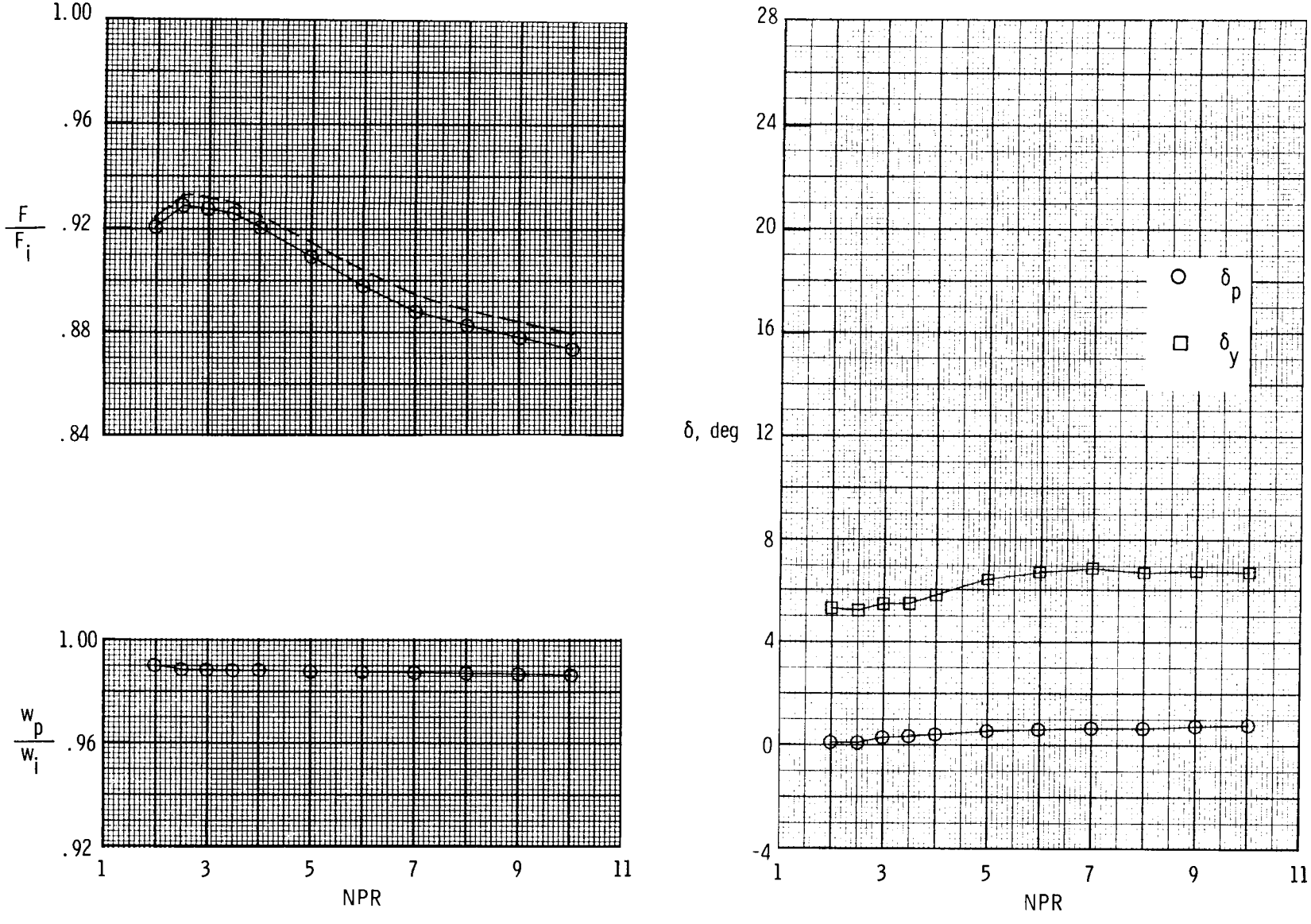

(d) Configuration R4; $c = 1.50$ in.; $\delta_{v,y} = 20°$.

Figure 56. Concluded.

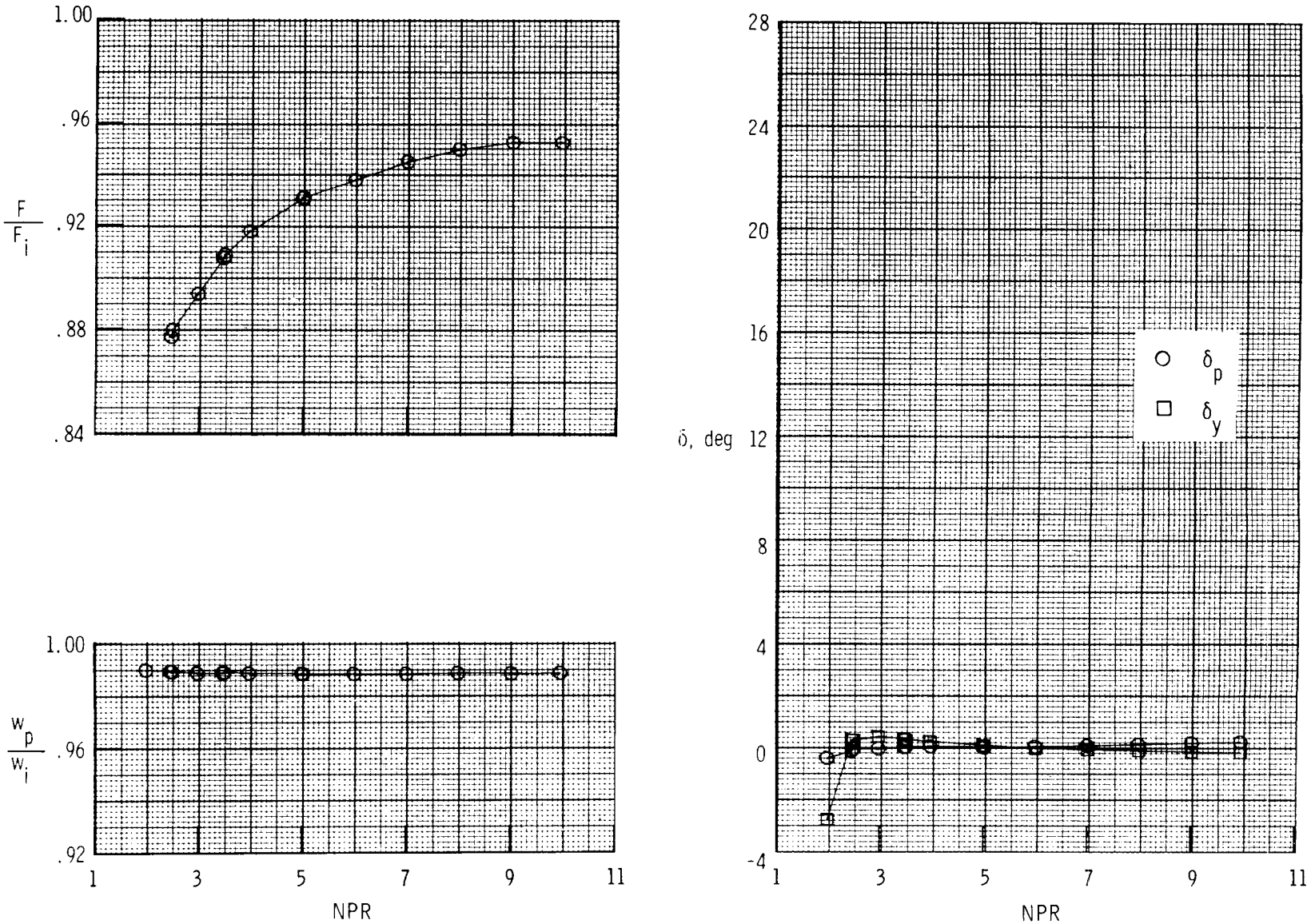

(a) Configuration R5; $c = 0.75$ in.; $\delta_{v,y} = 0°$.

Figure 57. Variation of nozzle thrust ratio, discharge coefficient, and resultant thrust vector angles with nozzle pressure ratio for dry power 2-D C-D nozzle, baseline $A_e/A_t = 1.78$ and $\delta_{v,p} = 0°$, with powered rudder yaw vectoring concept. Dashed line indicates resultant thrust ratio F_r/F_i.

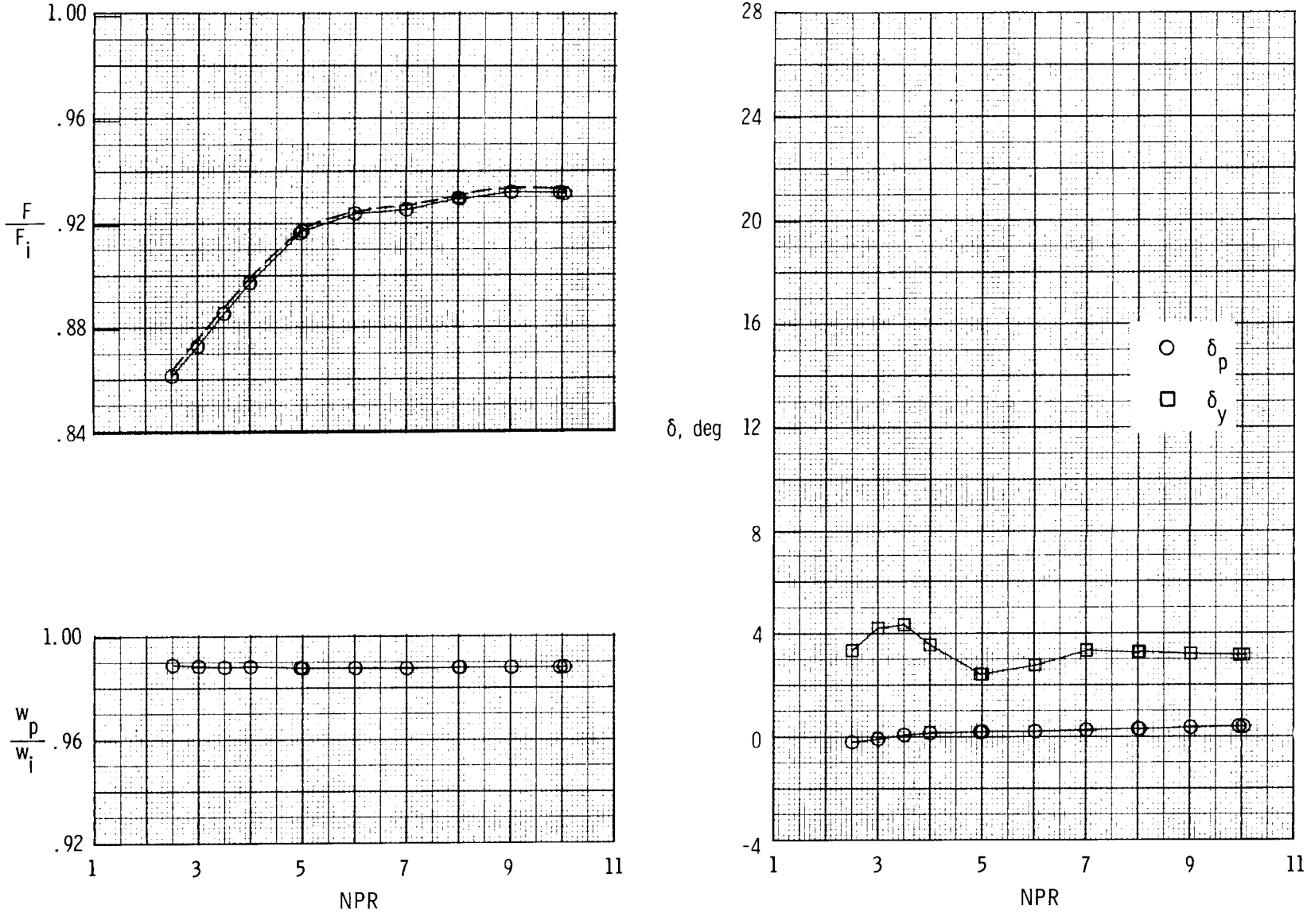

(b) Configuration R6; $c = 0.75$ in.; $\delta_{v,y} = 20°$.

Figure 57. Continued.

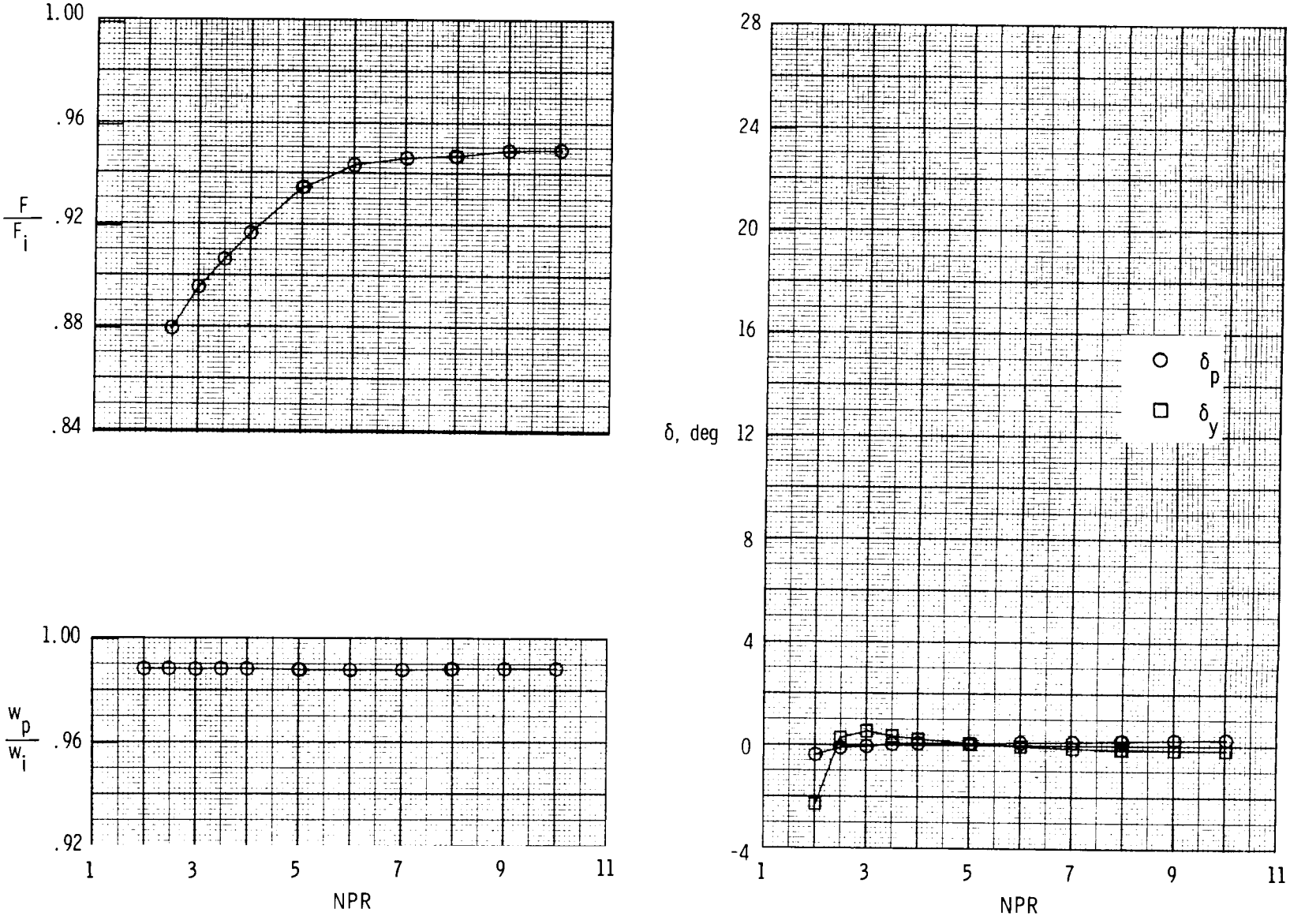

(c) Configuration R7; $c = 1.50$ in.; $\delta_{v,y} = 0°$.

Figure 57. Continued.

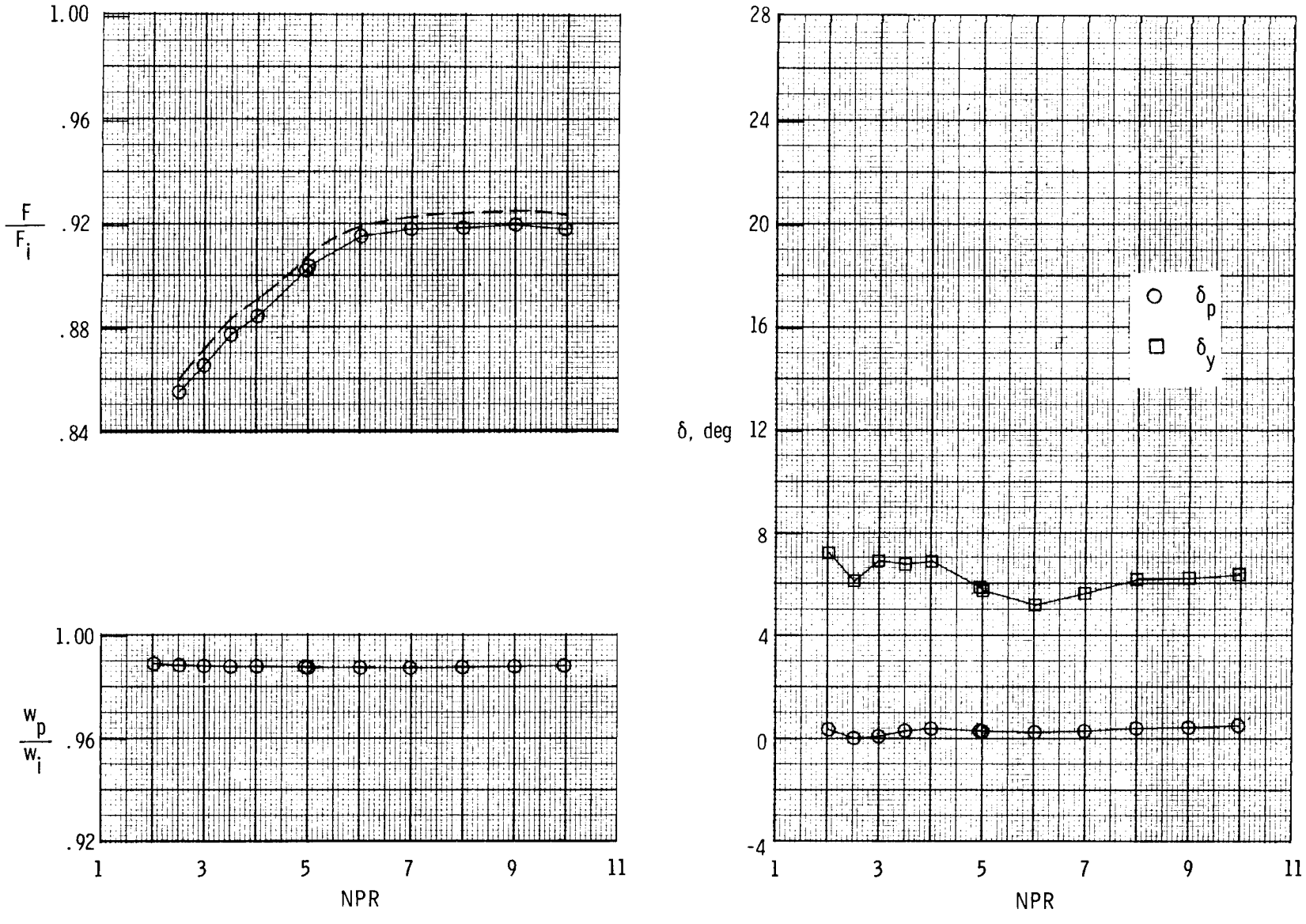

(d) Configuration R8; $c = 1.50$ in.; $\delta_{v,y} = 20°$.

Figure 57. Concluded.

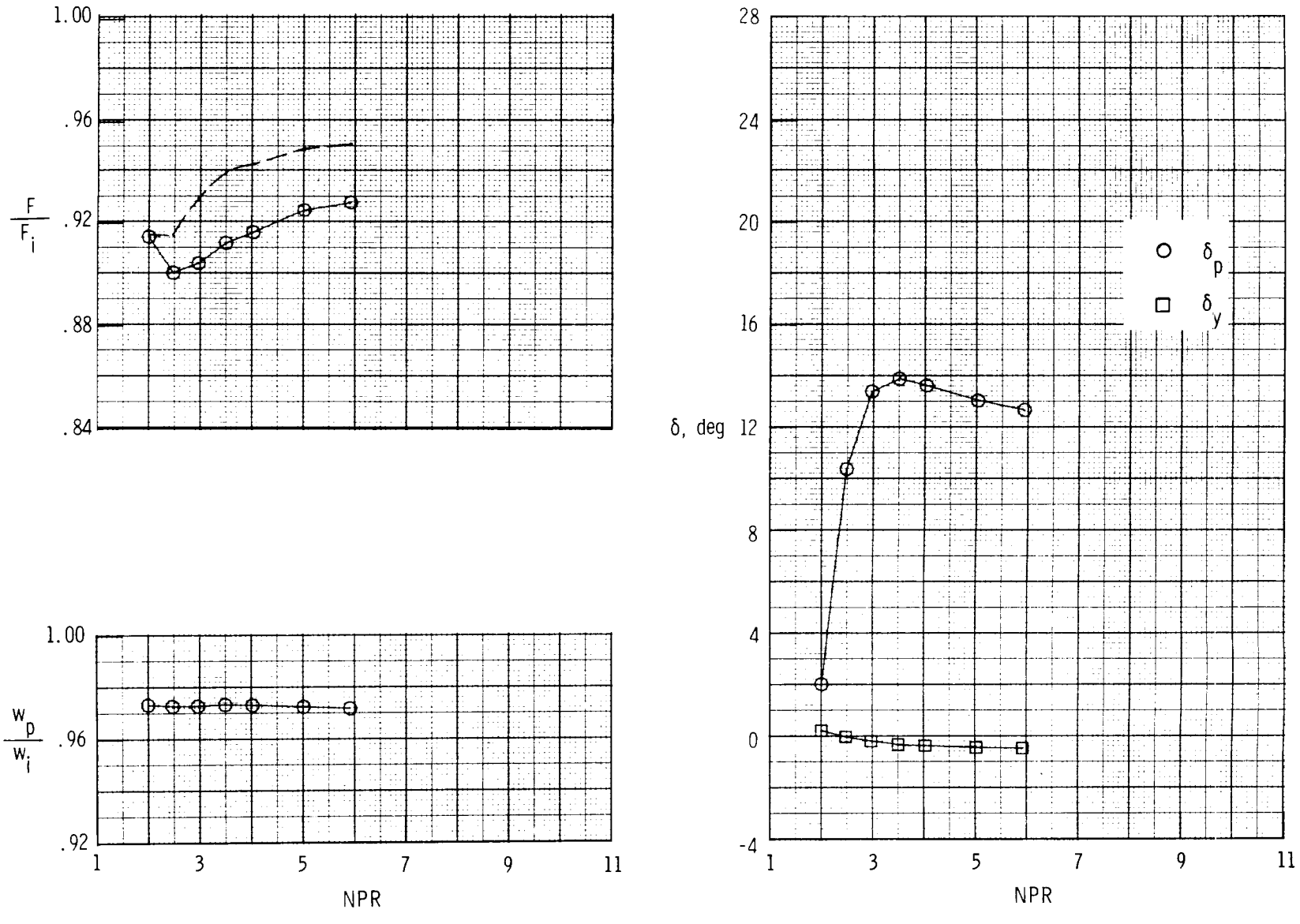

(a) Configuration R9; $c = 0.75$ in.; $\delta_{v,y} = 0°$.

Figure 58. Variation of nozzle thrust ratio, discharge coefficient, and resultant thrust vector angles with nozzle pressure ratio for A/B power 2-D C-D nozzle, baseline $A_e/A_t = 1.35$ and $\delta_{v,p} = 9.79°$, with powered rudder yaw vectoring concept. Dashed line indicates resultant thrust ratio F_r/F_i.

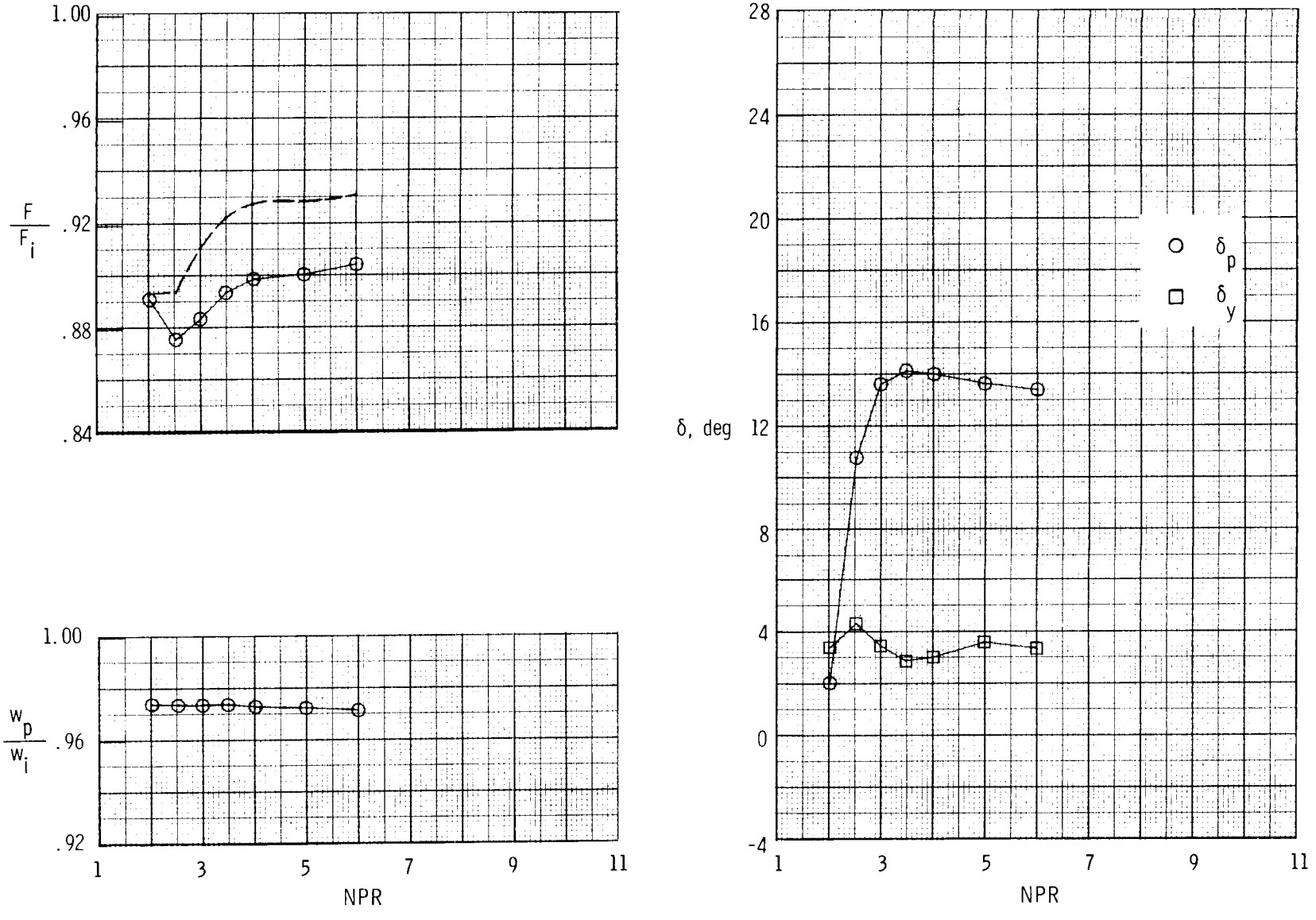

(b) Configuration R10; $c = 0.75$ in.; $\delta_{v,y} = 20°$.

Figure 58. Continued.

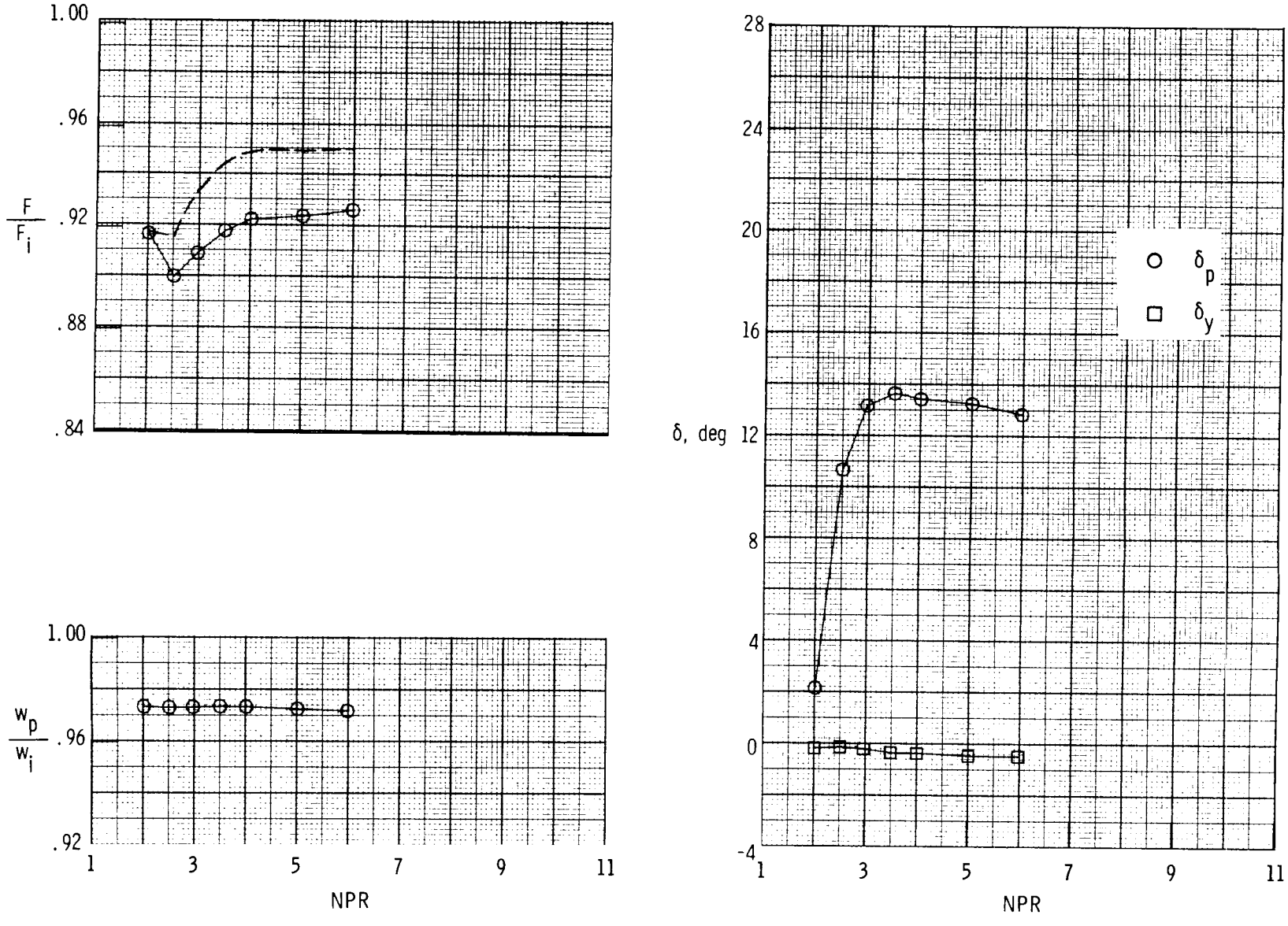

(c) Configuration R11; $c = 1.50$ in.; $\delta_{v,y} = 0°$.

Figure 58. Continued.

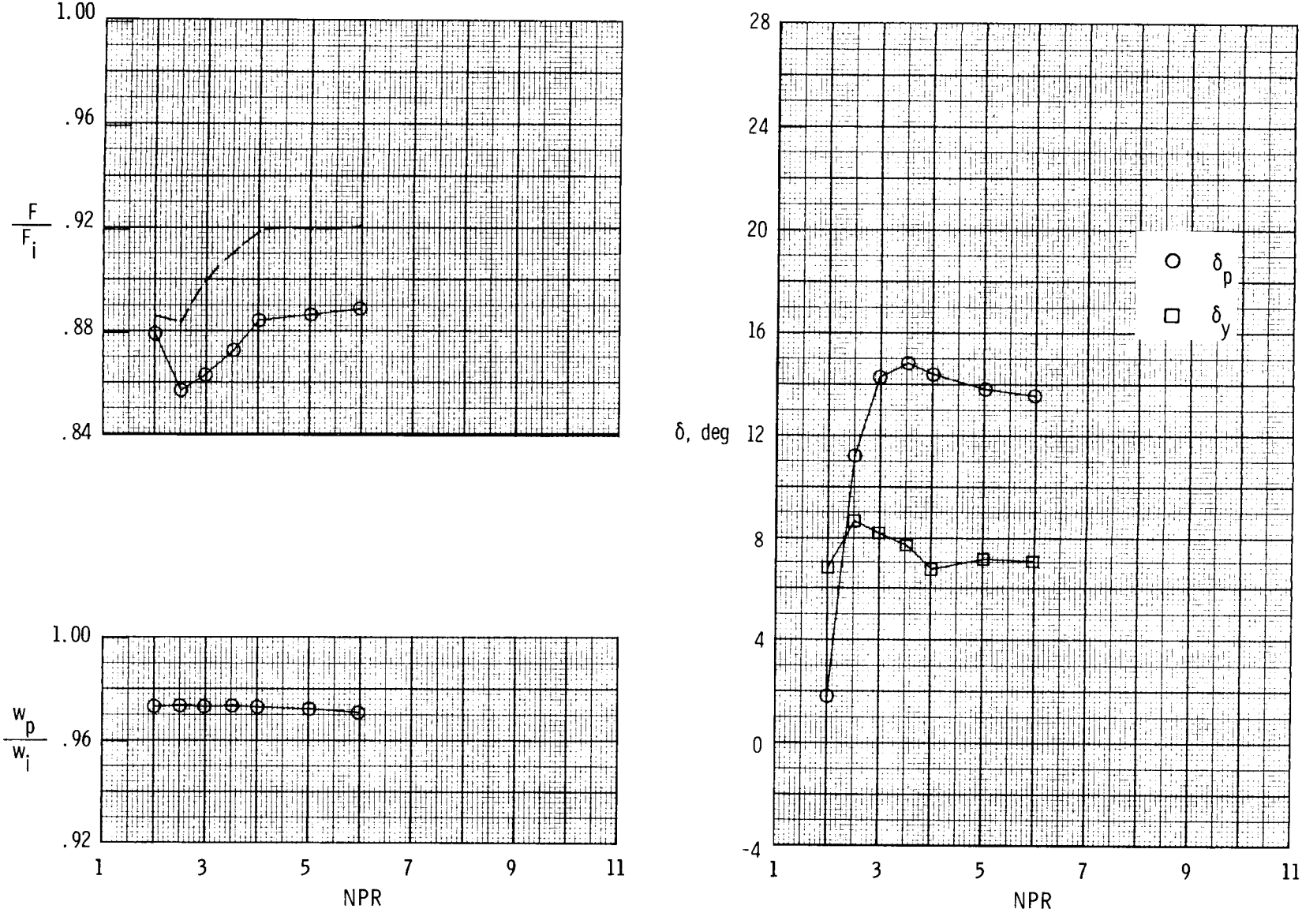

(d) Configuration R12; $c = 1.50$ in.; $\delta_{v,y} = 20°$.

Figure 58. Concluded.

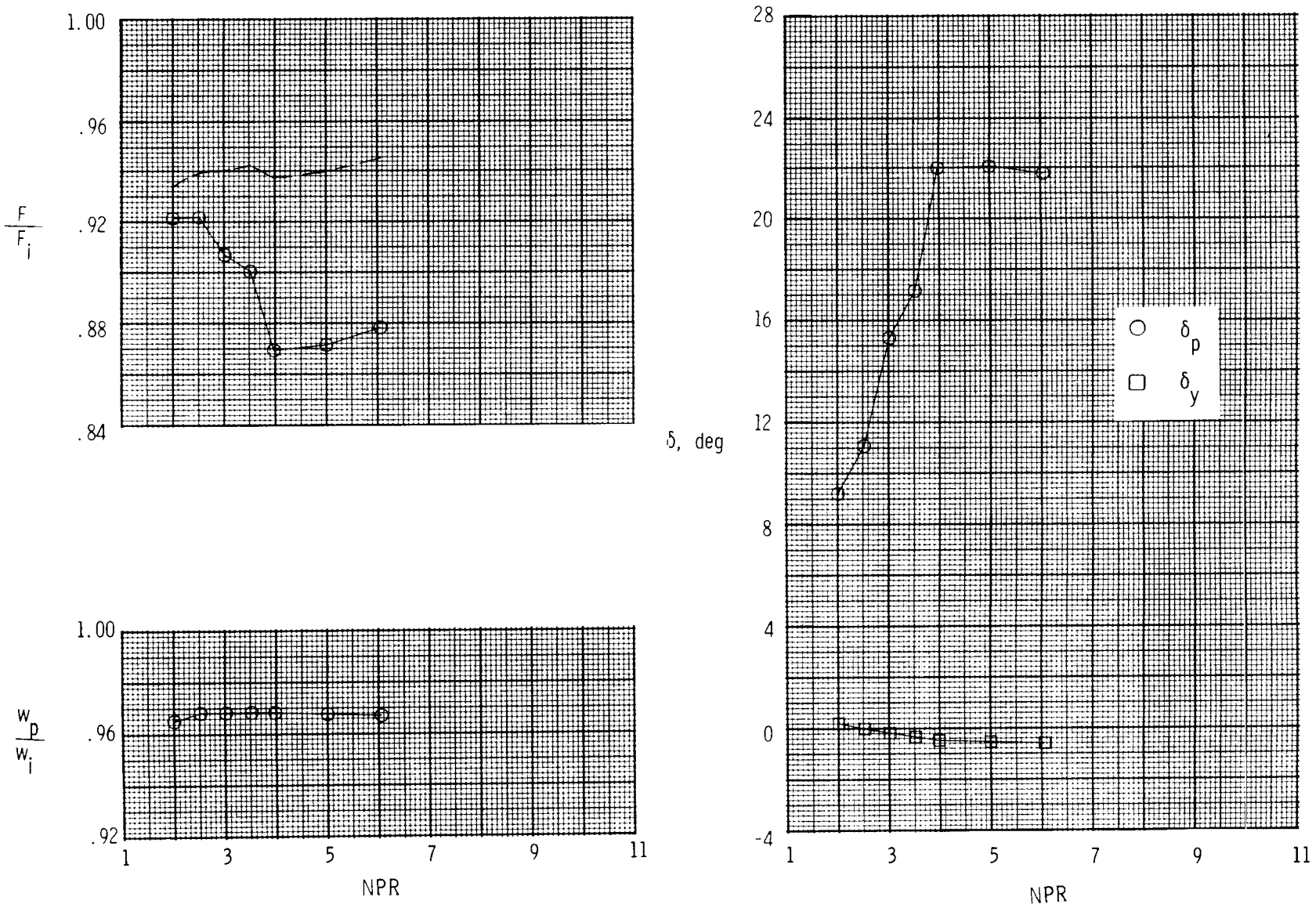

(a) Configuration R13; $c = 0.75$ in.; $\delta_{v,y} = 0°$.

Figure 59. Variation of nozzle thrust ratio, discharge coefficient, and resultant thrust vector angles with nozzle pressure ratio for A/B power 2-D C-D nozzle, baseline $A_e/A_t = 1.51$ and $\delta_{v,p} = 20.28°$, with powered rudder yaw vectoring concept. Dashed line indicates resultant thrust ratio F_r/F_i.

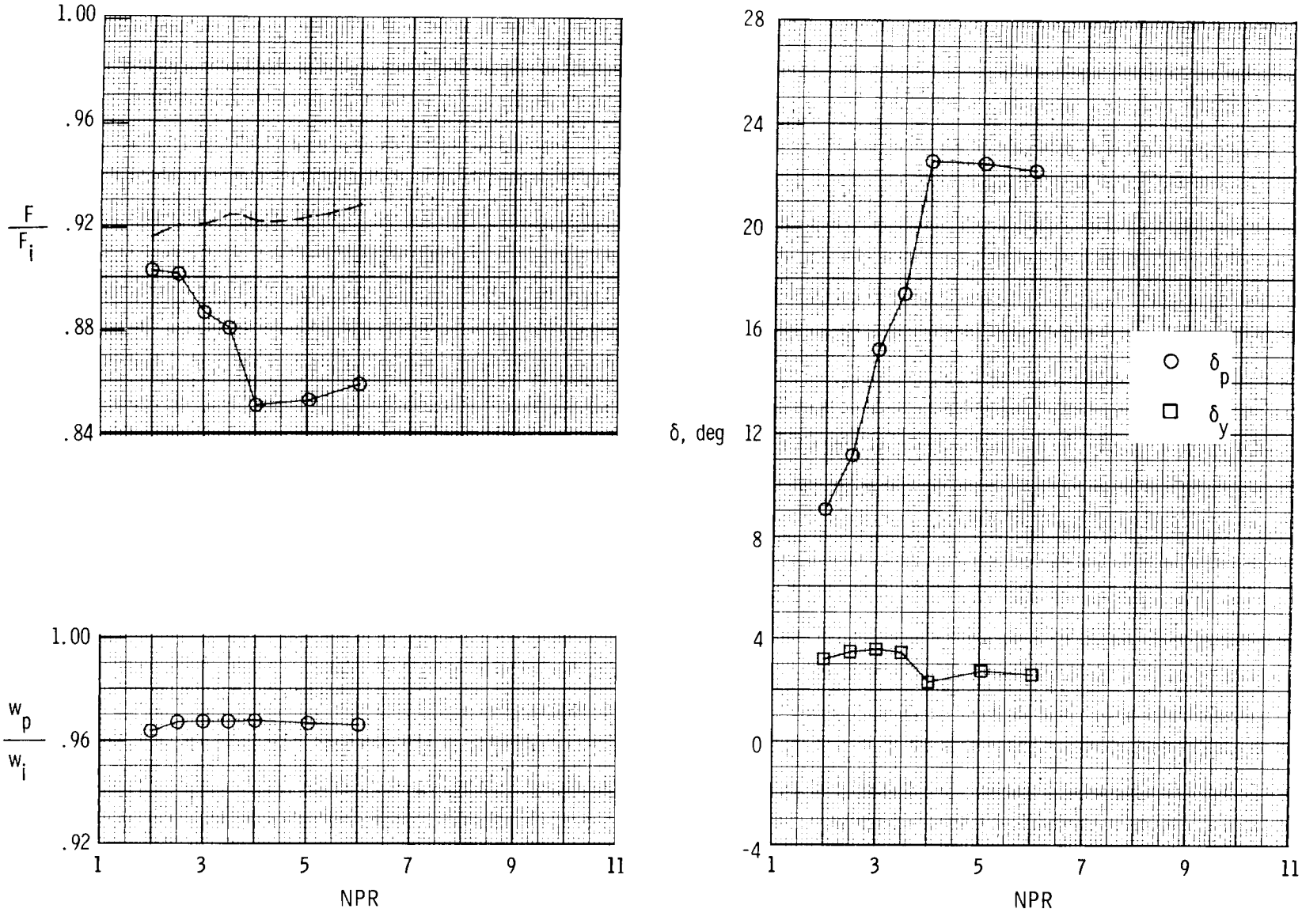

(b) Configuration R14; $c = 0.75$ in.; $\delta_{v,y} = 20°$.

Figure 59. Continued.

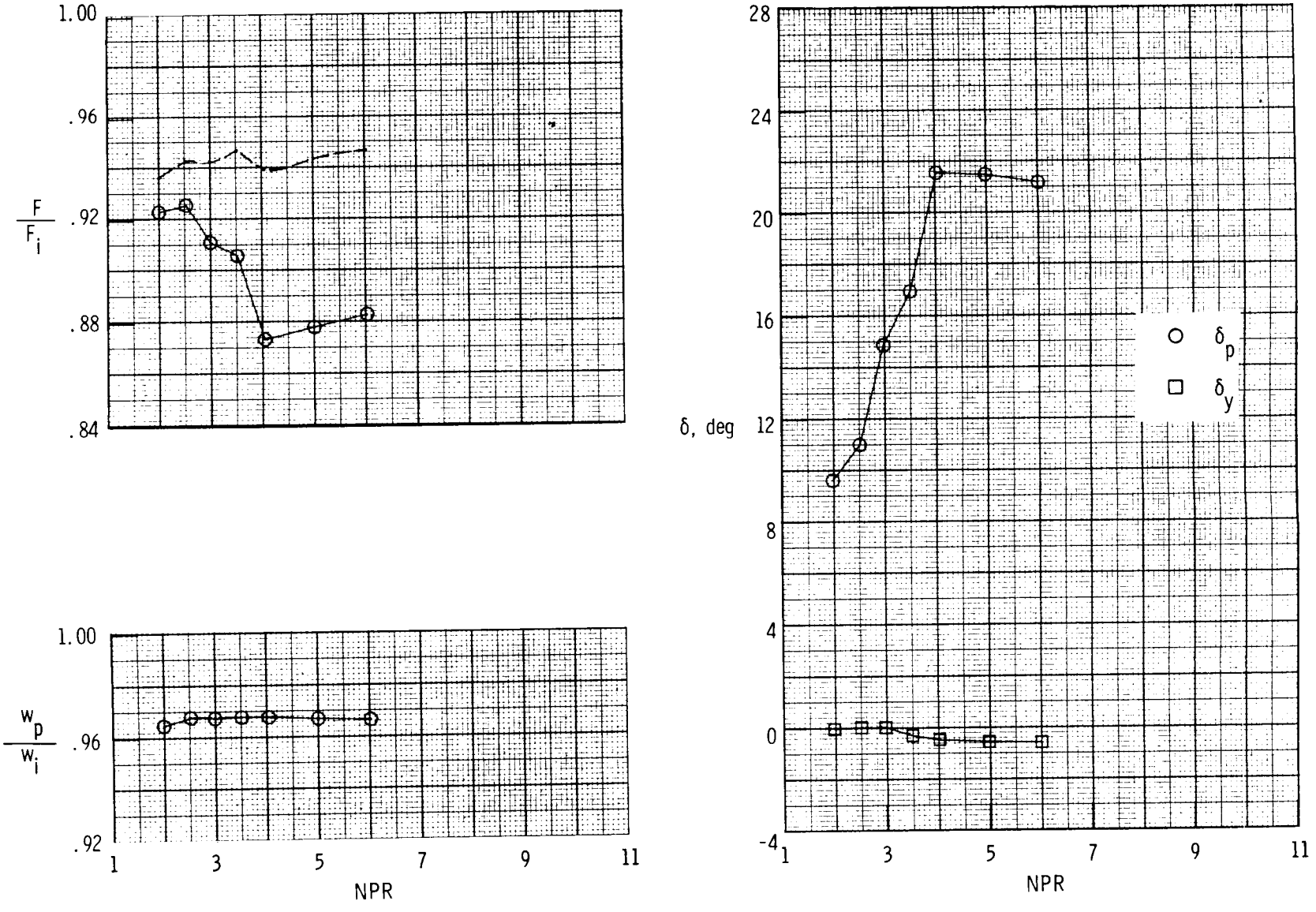

(c) Configuration R15; $c = 1.50$ in.; $\delta_{v,y} = 0°$.

Figure 59. Continued.

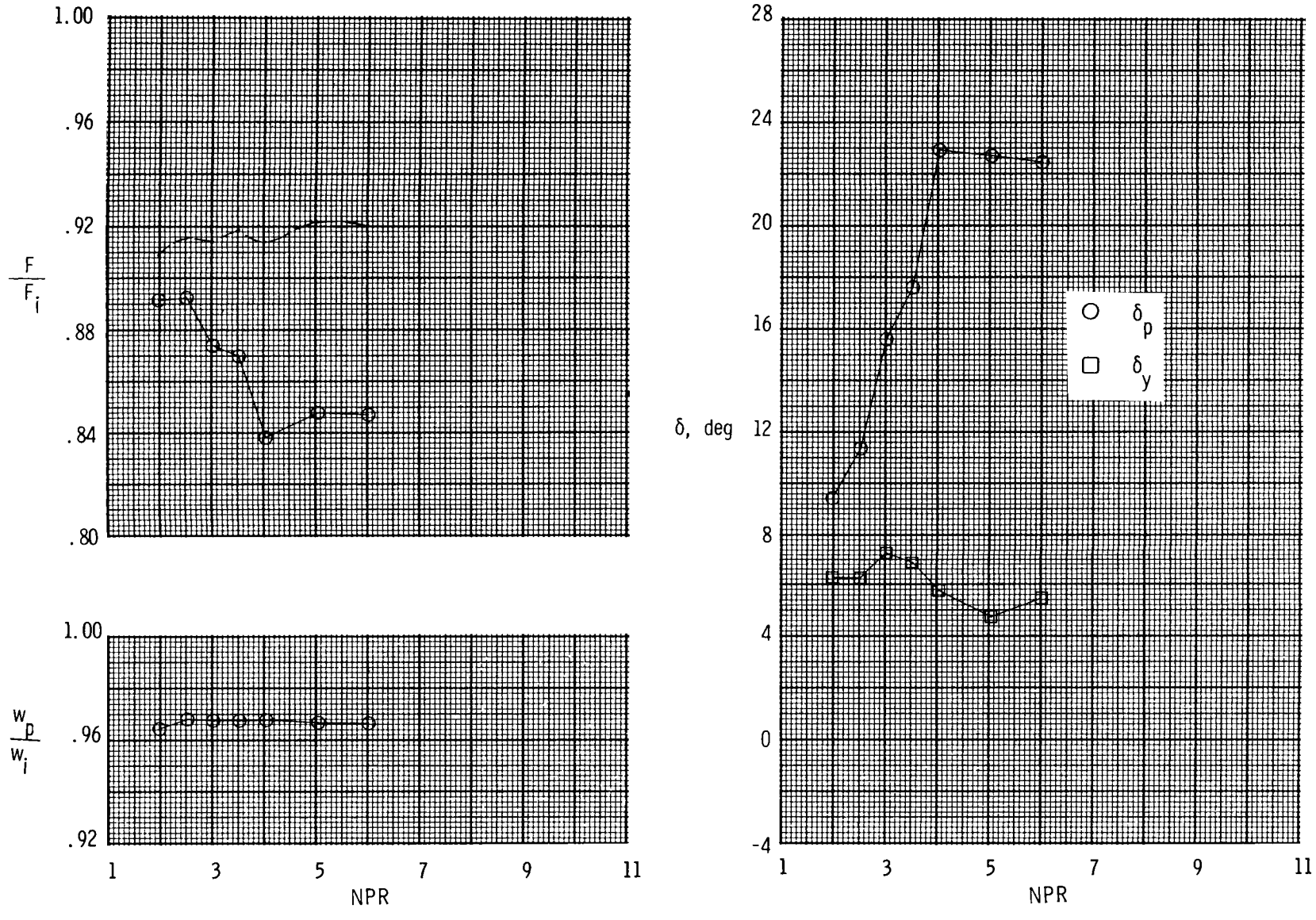

(d) Configuration R16; $c = 1.50$ in.; $\delta_{v,y} = 20°$.

Figure 59. Concluded.

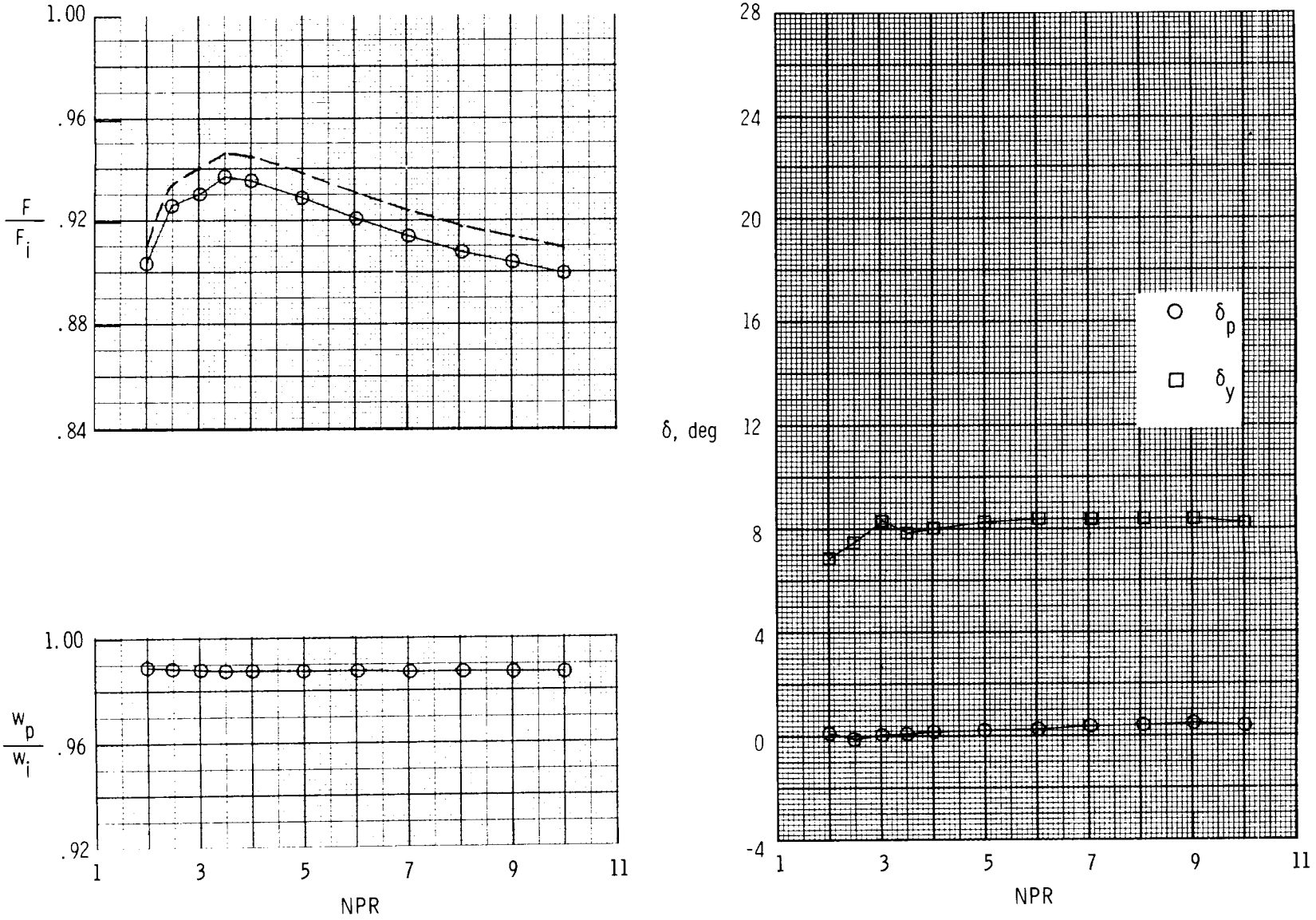

(a) Configuration F1-R4; $x_h = 2.28$ in.; $c = 1.50$ in.; left $\delta_{v,y} = 10°$; right $\delta_{v,y} = 0°$; rudder $\delta_{v,y} = 20°$.

Figure 60. Variation of nozzle thrust ratio, discharge coefficient, and resultant thrust vector angles with nozzle pressure ratio for dry power 2-D C-D nozzle, baseline $A_e/A_t = 1.08$ and $\delta_{v,p} = 0°$, with combination of downstream flap and powered rudder yaw vectoring concepts. Dashed line indicates resultant thrust ratio F_r/F_i.

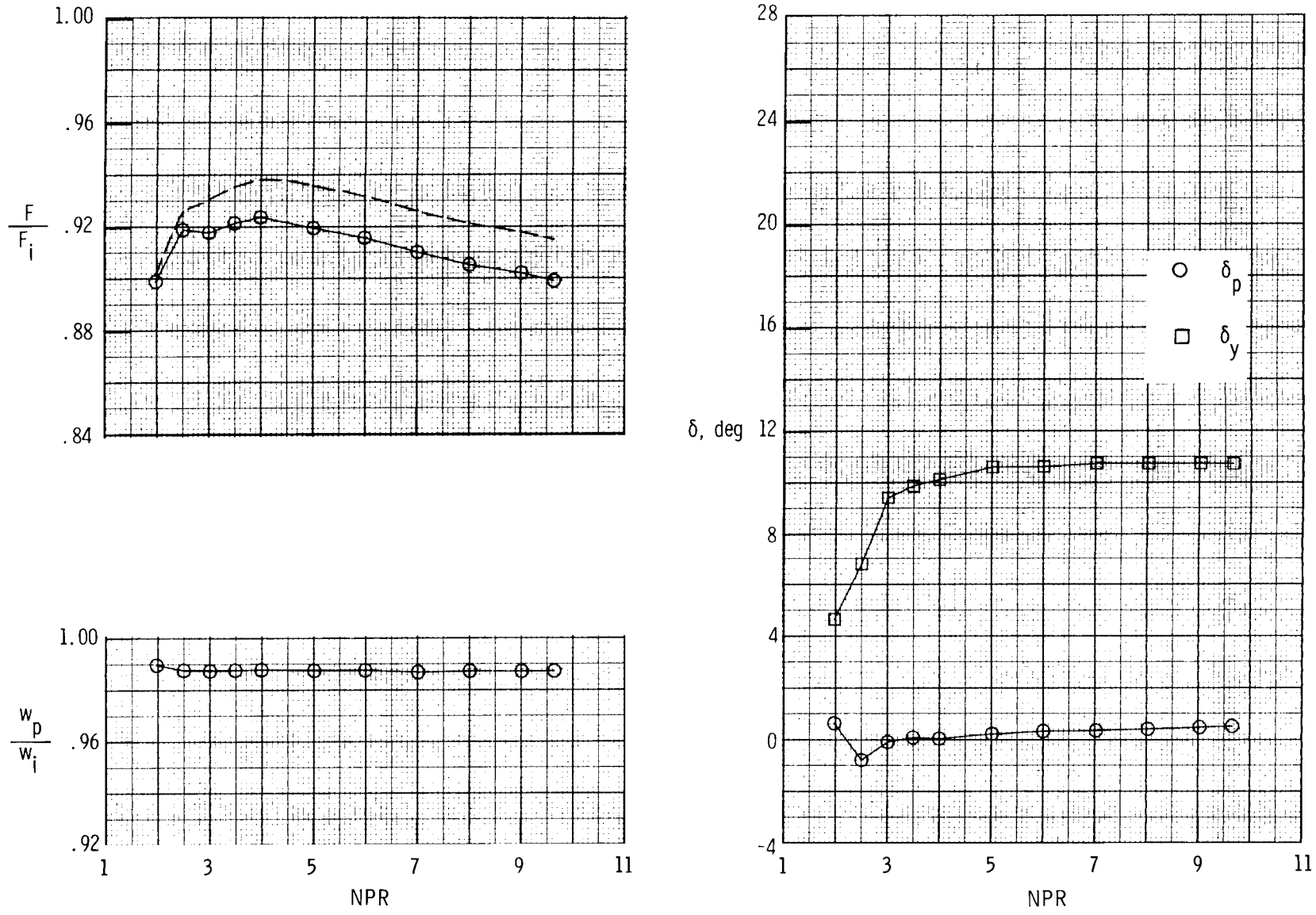

(b) Configuration F4-R4; $x_h = 2.28$ in.; $c = 1.50$ in.; left $\delta_{v,y} = 20°$; right $\delta_{v,y} = 0°$; rudder $\delta_{v,y} = 20°$.

Figure 60. Continued.

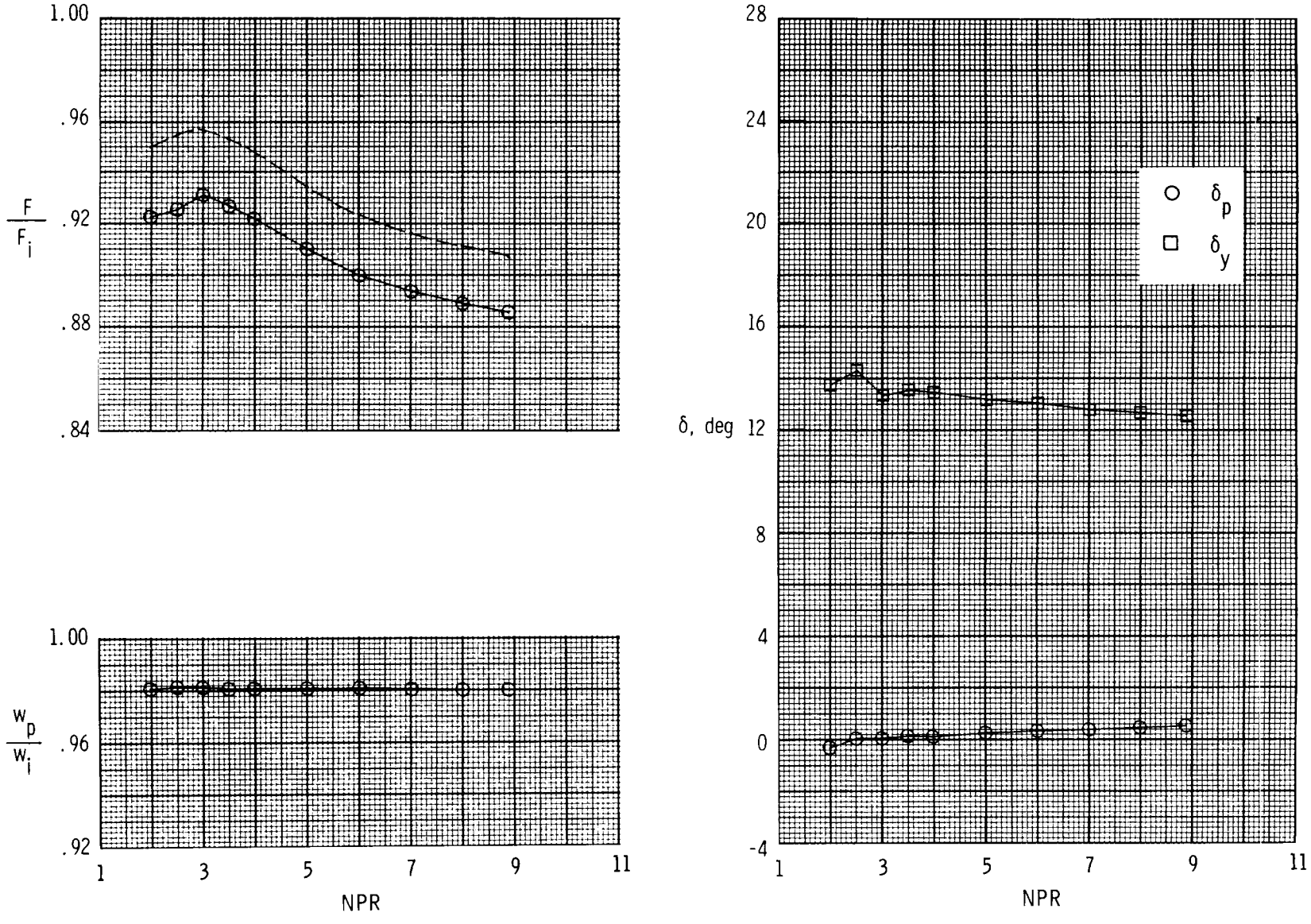

(c) Configuration F3-R4; $x_h = 2.28$ in.; $c = 1.50$ in.; left $\delta_{v,y} = 10°$; right $\delta_{v,y} = 10°$; rudder $\delta_{v,y} = 20°$.

Figure 60. Continued.

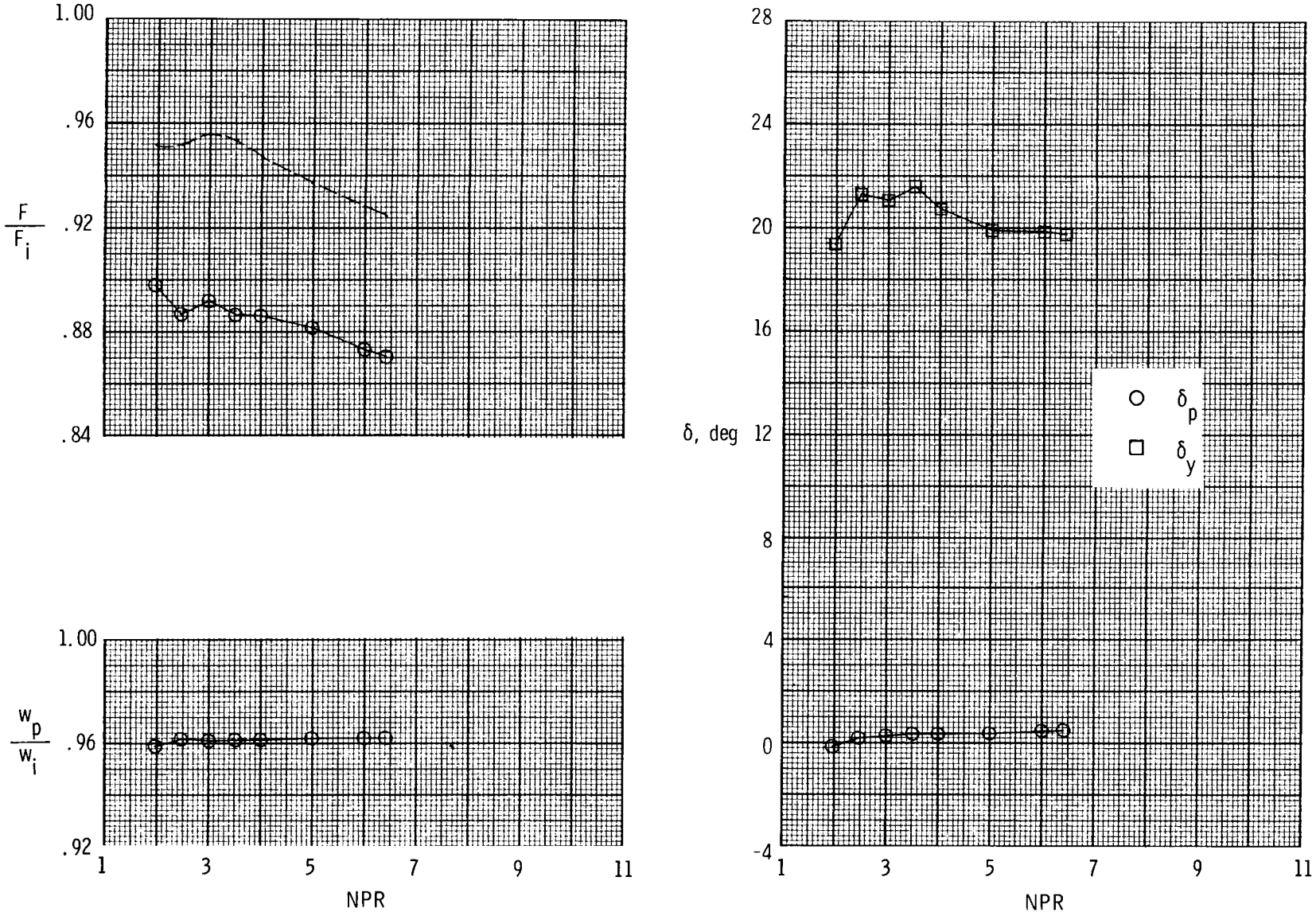

(d) Configuration F6-R4; $x_h = 2.28$ in.; $c = 1.50$ in.; left $\delta_{v,y} = 20°$; right $\delta_{v,y} = 20°$; rudder $\delta_{v,y} = 20°$.

Figure 60. Continued.

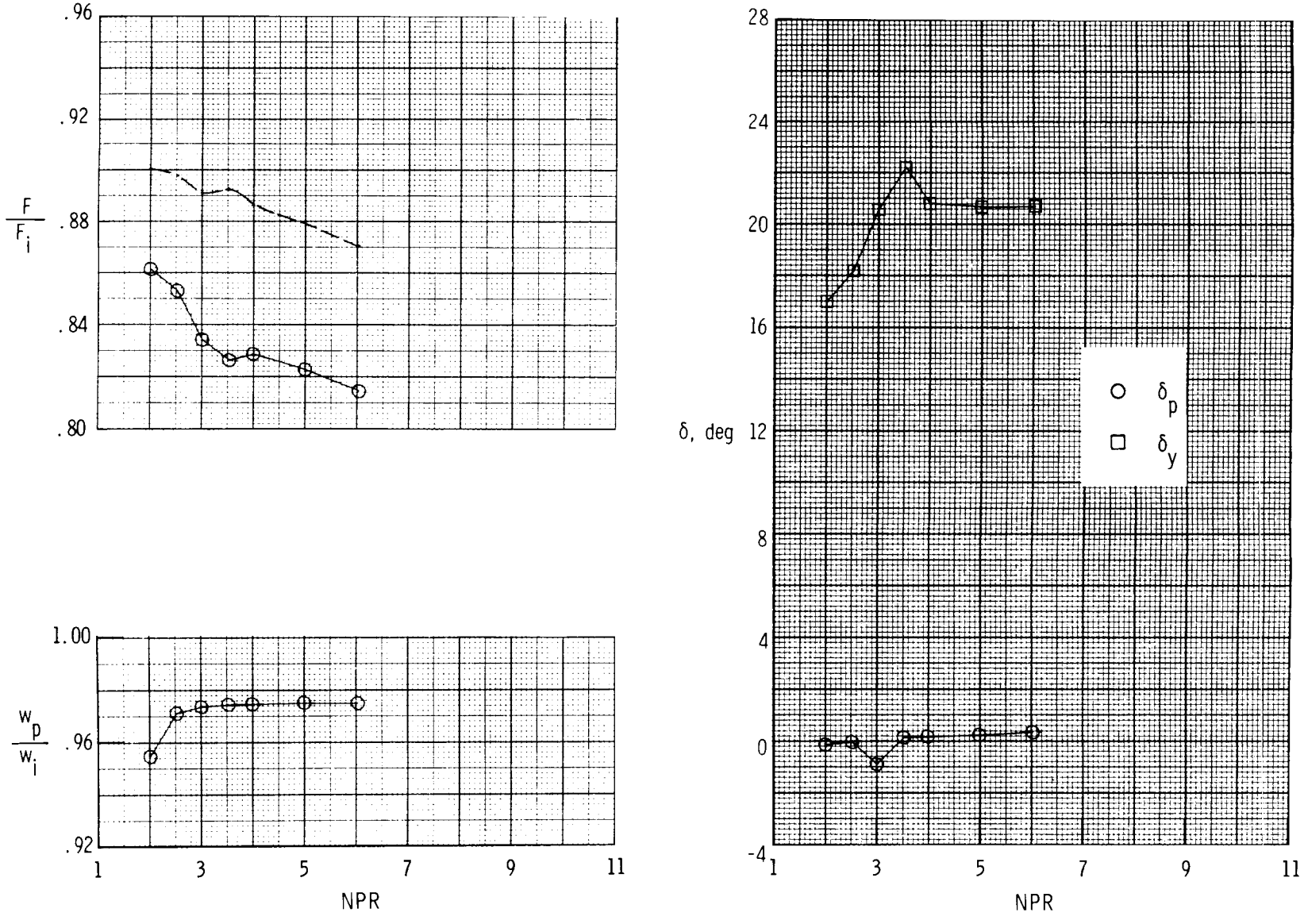

(e) Configuration F9-R4; $x_h = 3.42$ in.; $c = 1.50$ in.; left $\delta_{v,y} = 20°$; right $\delta_{v,y} = 20°$; rudder $\delta_{v,y} = 20°$.

Figure 60. Concluded.

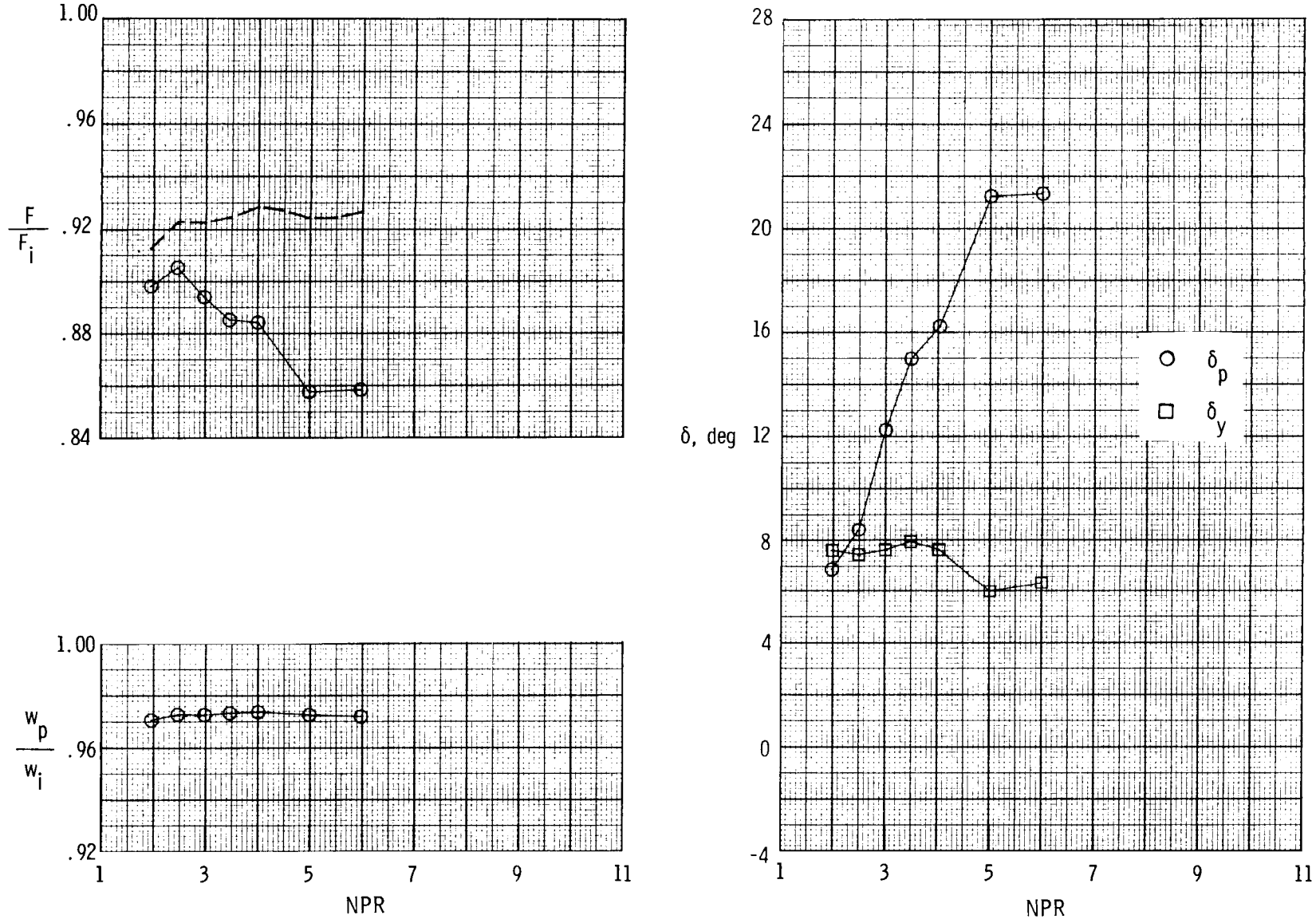

(a) Configuration F22-R16; $x_h = 2.28$ in.; $c = 1.50$ in.; left $\delta_{v,y} = 10°$; right $\delta_{v,y} = 0°$; rudder $\delta_{v,y} = 20°$.

Figure 61. Variation of nozzle thrust ratio, discharge coefficient, and resultant thrust vector angles with nozzle pressure ratio for A/B power 2-D C-D nozzle, baseline $A_e/A_t = 1.51$ and $\delta_{v,p} = 20.28°$, with combination of downstream flap and powered yaw vectoring concepts.

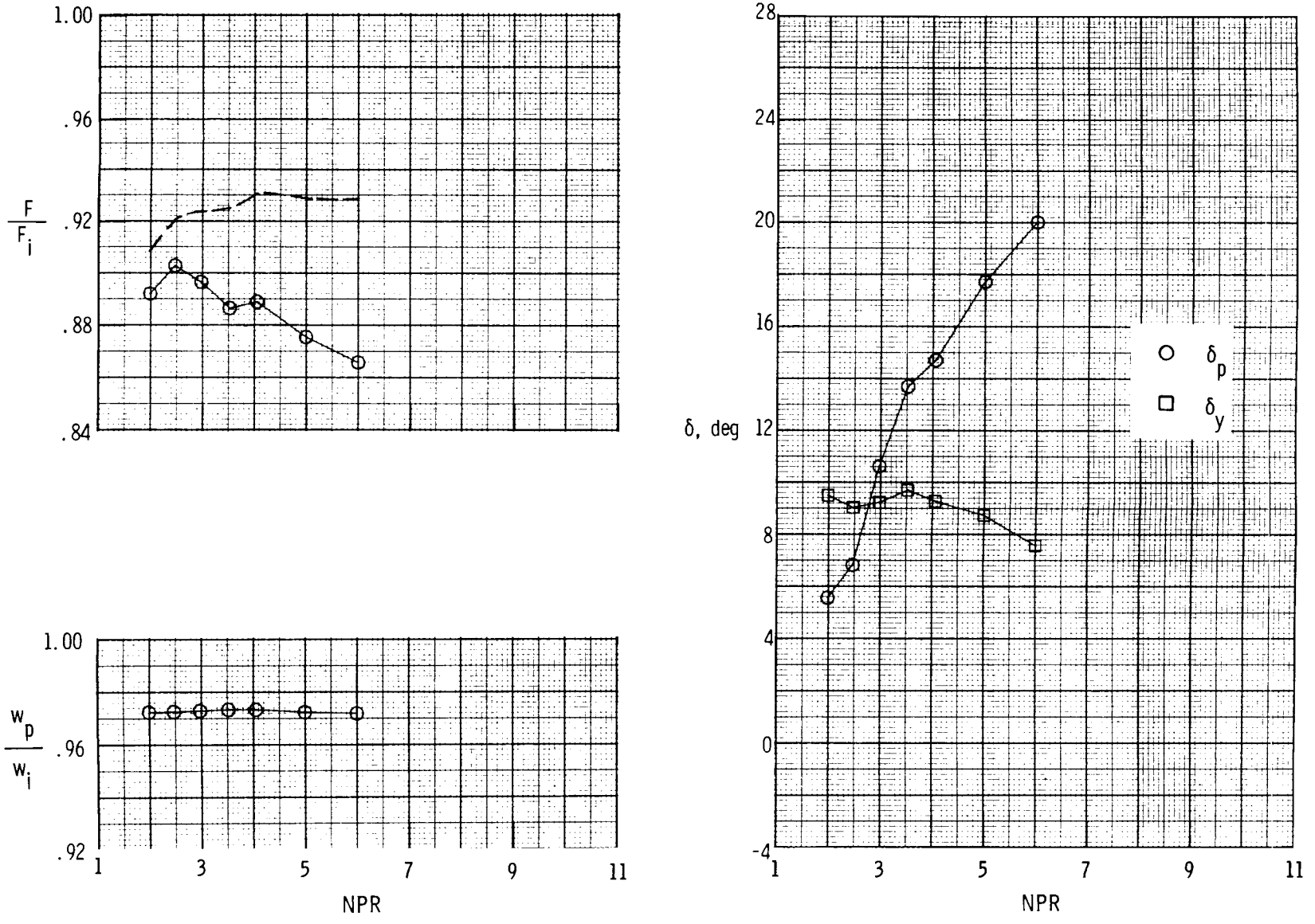

(b) Configuration F23-R16; $x_h = 2.28$ in.; $c = 1.50$ in.; left $\delta_{v,y} = 20°$; right $\delta_{v,y} = 0°$; rudder $\delta_{v,y} = 20°$.

Figure 61. Concluded.

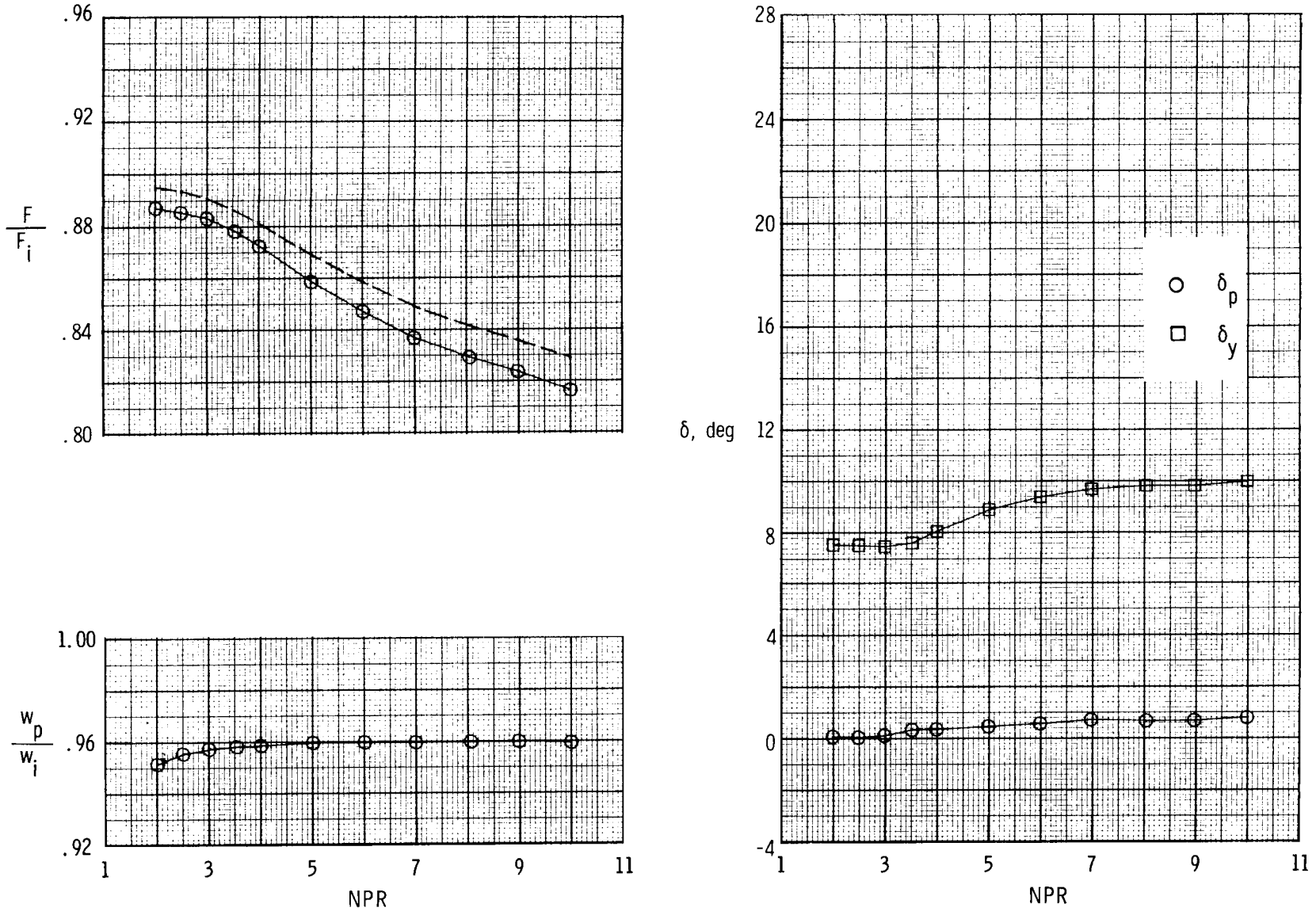

(a) Configuration P1-R4; $c = 1.50$ in.; $A_p = 0.44$ in^2; port/flap $\delta_{v,y} = 90°$; rudder $\delta_{v,y} = 20°$.

Figure 62. Variation of nozzle thrust ratio, discharge coefficient, and resultant thrust vector angles with nozzle pressure ratio for dry power 2-D C-D nozzle, baseline $A_e/A_t = 1.08$ and $\delta_{v,p} = 0°$, with combination of upstream port/flap and powered rudder yaw vectoring concepts.

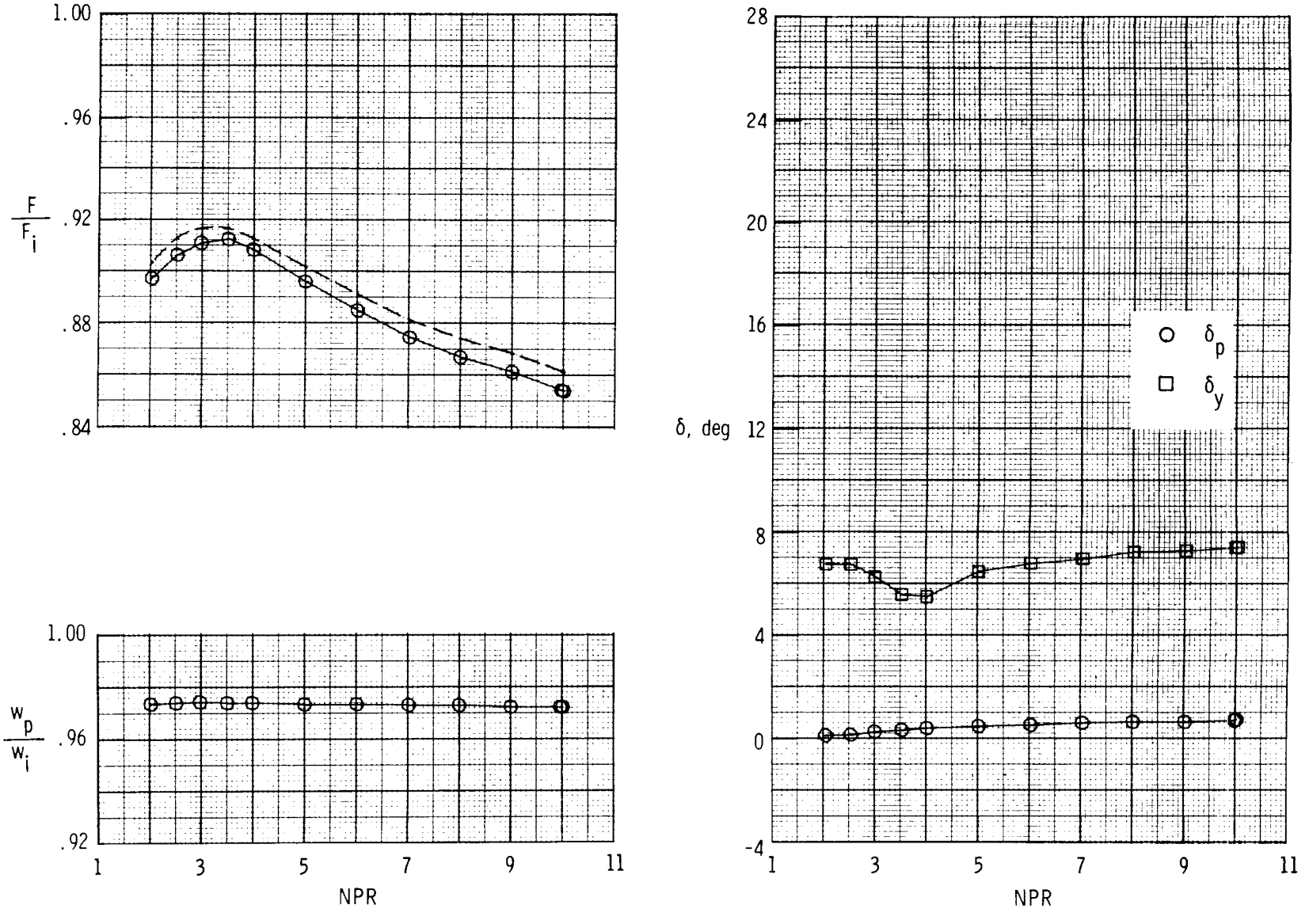

(b) Configuration P2-R4; $c = 1.50$ in.; $A_p = 0.33$ in^2; $x_h = 0.70$ in.; port/flap $\delta_{v,y} = 40°$; rudder $\delta_{v,y} = 20°$.

Figure 62. Concluded.

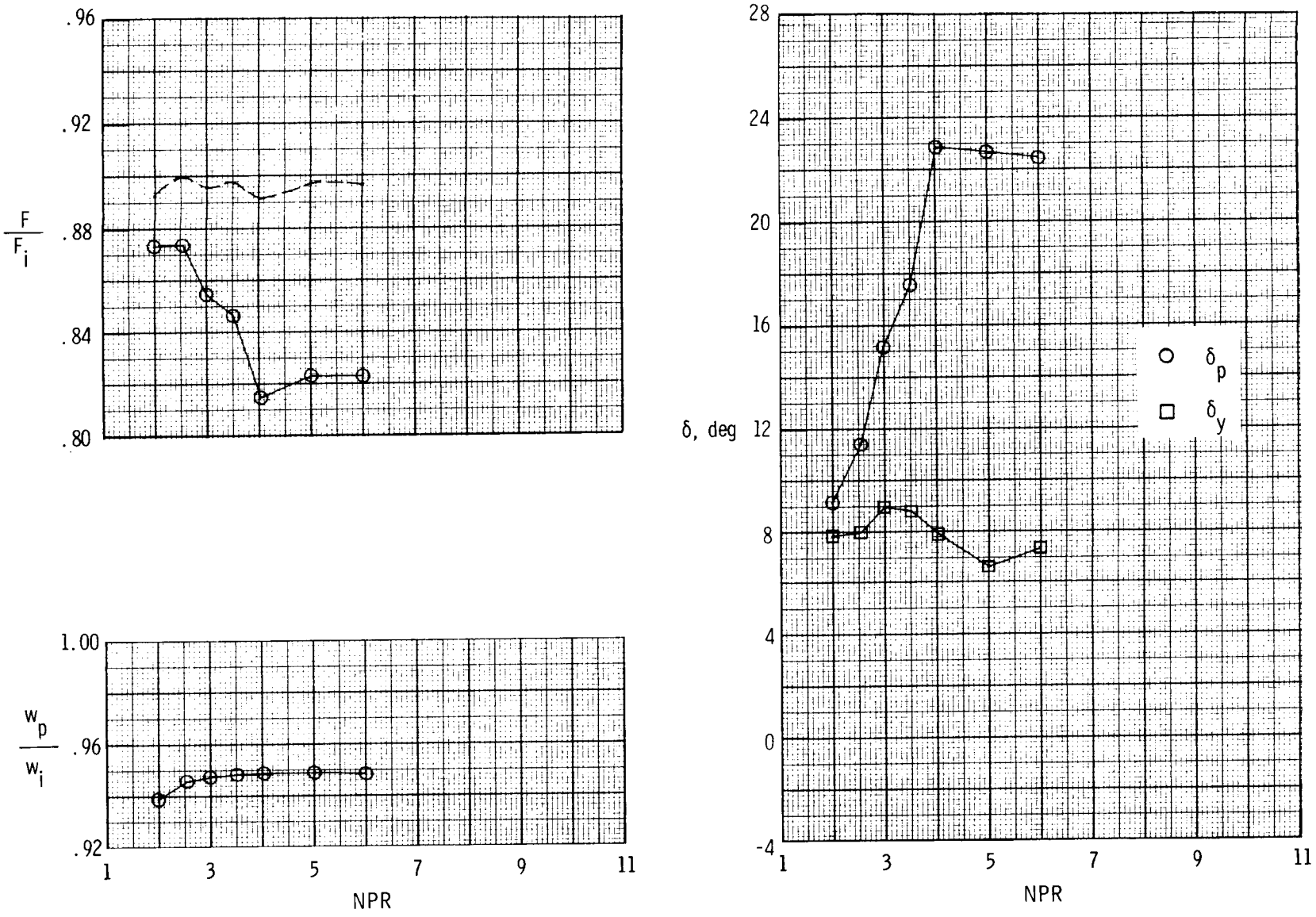

(a) Configuration P16-R16; $c = 1.50$ in.; $A_p = 0.44$ in^2; port/flap $\delta_{v,y} = 90°$; rudder $\delta_{v,y} = 20°$.

Figure 63. Variation of nozzle thrust ratio, discharge coefficient, and resultant thrust vector angles with nozzle pressure ratio for A/B power 2-D C-D nozzle, $\delta_{v,p} = 20.28°$, with combination of upstream port/flap and powered rudder yaw vectoring concepts.

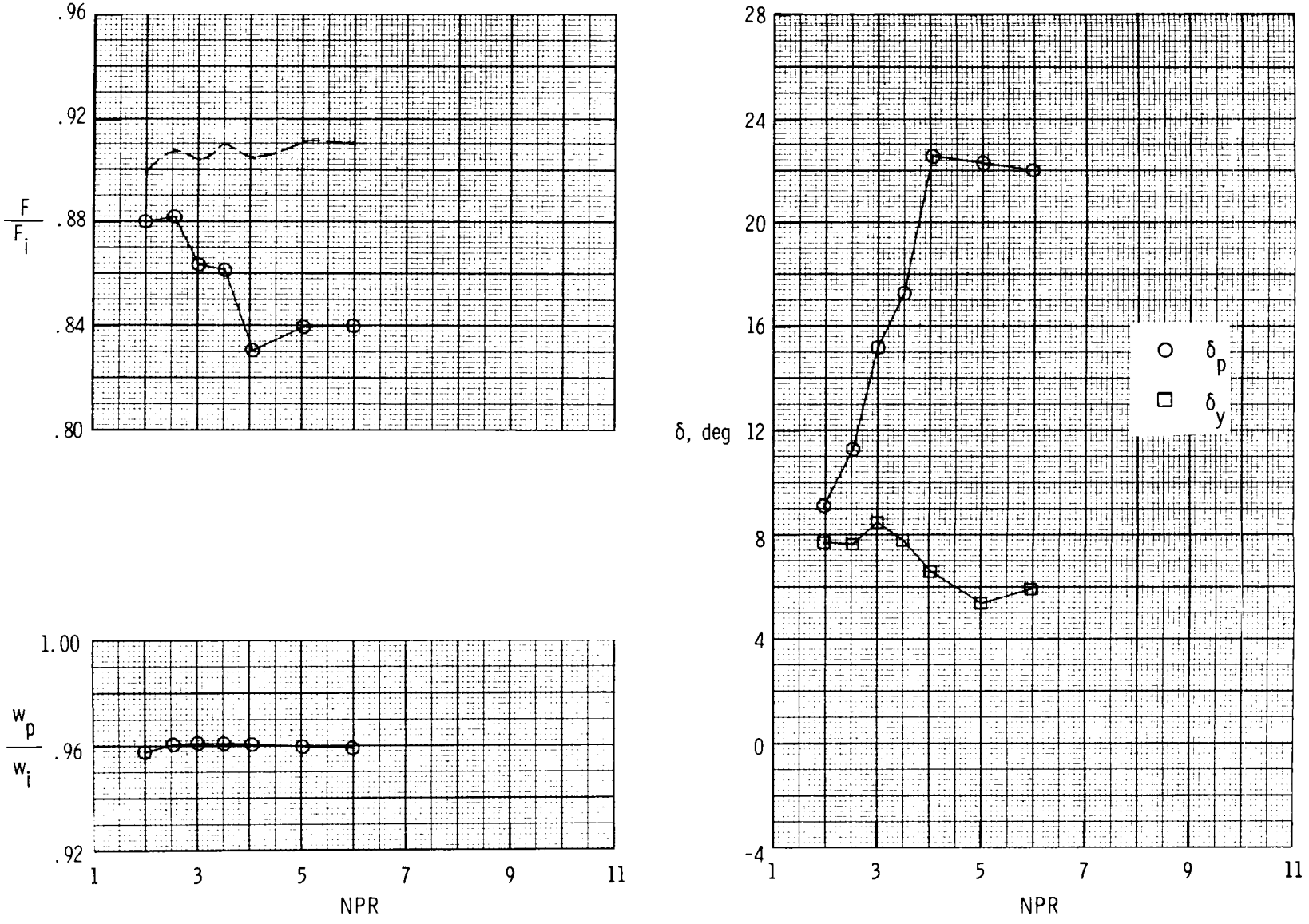

(b) Configuration P17-R16; $c = 1.50$ in.; $A_p = 0.33$ in^2; $x_h = 0.70$ in.; port/flap $\delta_{v,y} = 40°$; rudder $\delta_{v,y} = 20°$.

Figure 63. Concluded.

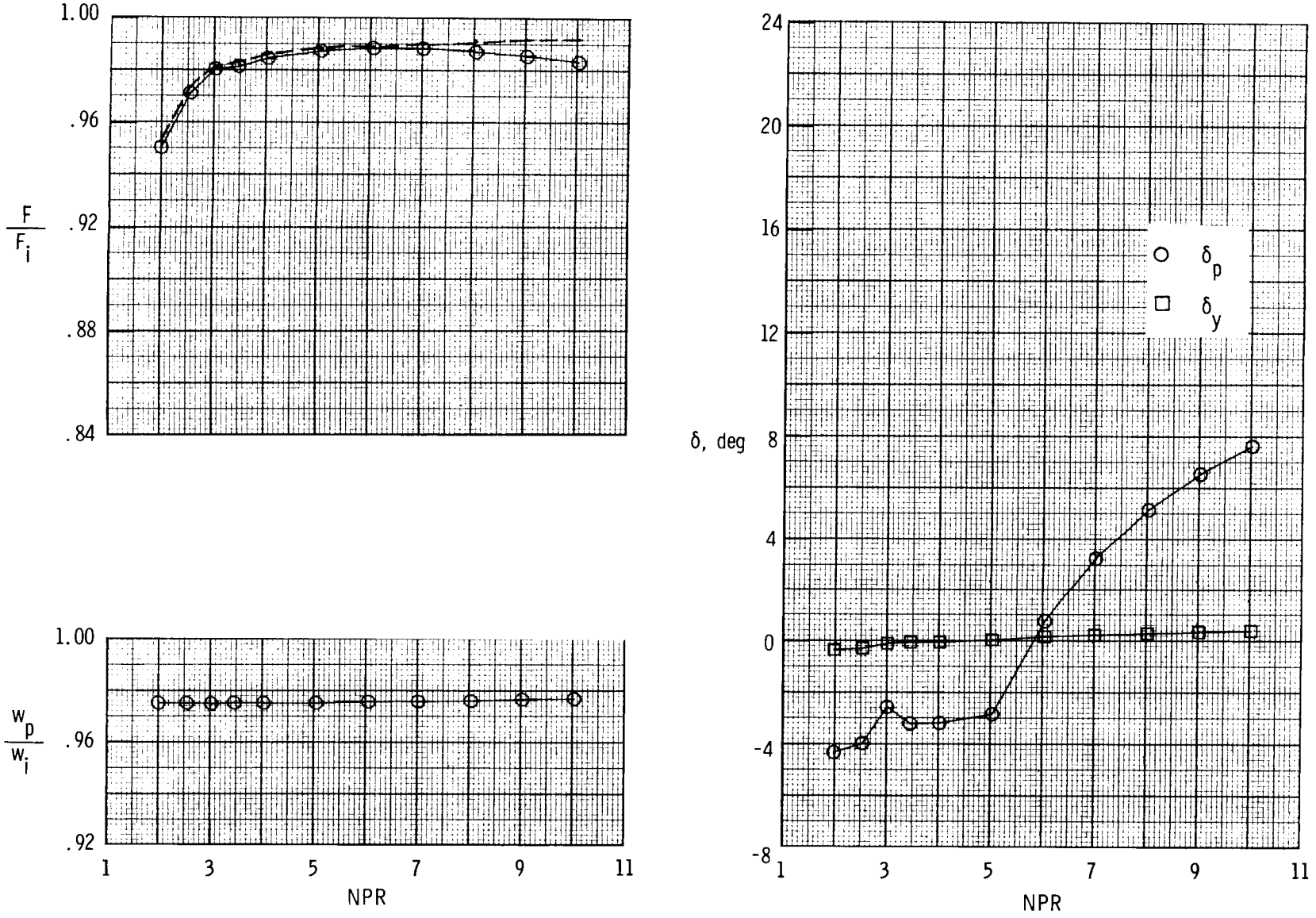

(a) Configuration SR1; yaw vector flaps off.

Figure 64. Variation of nozzle thrust ratio, discharge coefficient, and resultant thrust vector angles with nozzle pressure ratio for dry power SERN, $(A_e/A_t)_i = 1.10$, $(A_e/A_t)_e = 1.41$, and $\delta_{v,p} = 0°$, with post-exit flaps yaw vectoring concept. Dashed line indicates resultant thrust ratio F_r/F_i.

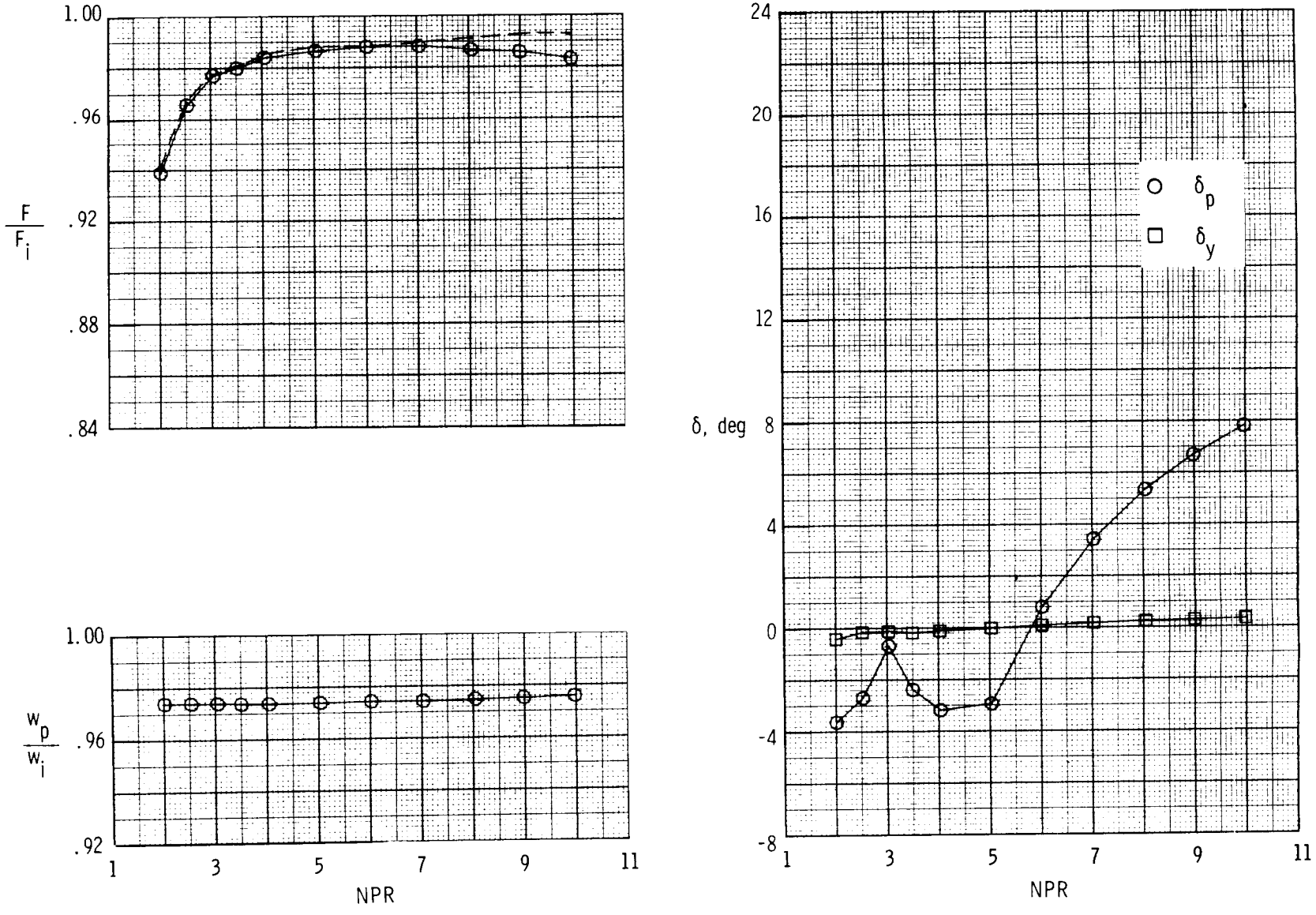

(b) Configuration SR2; $c = 0.75$ in.; $\delta_{v,y} = 0°$.

Figure 64. Continued.

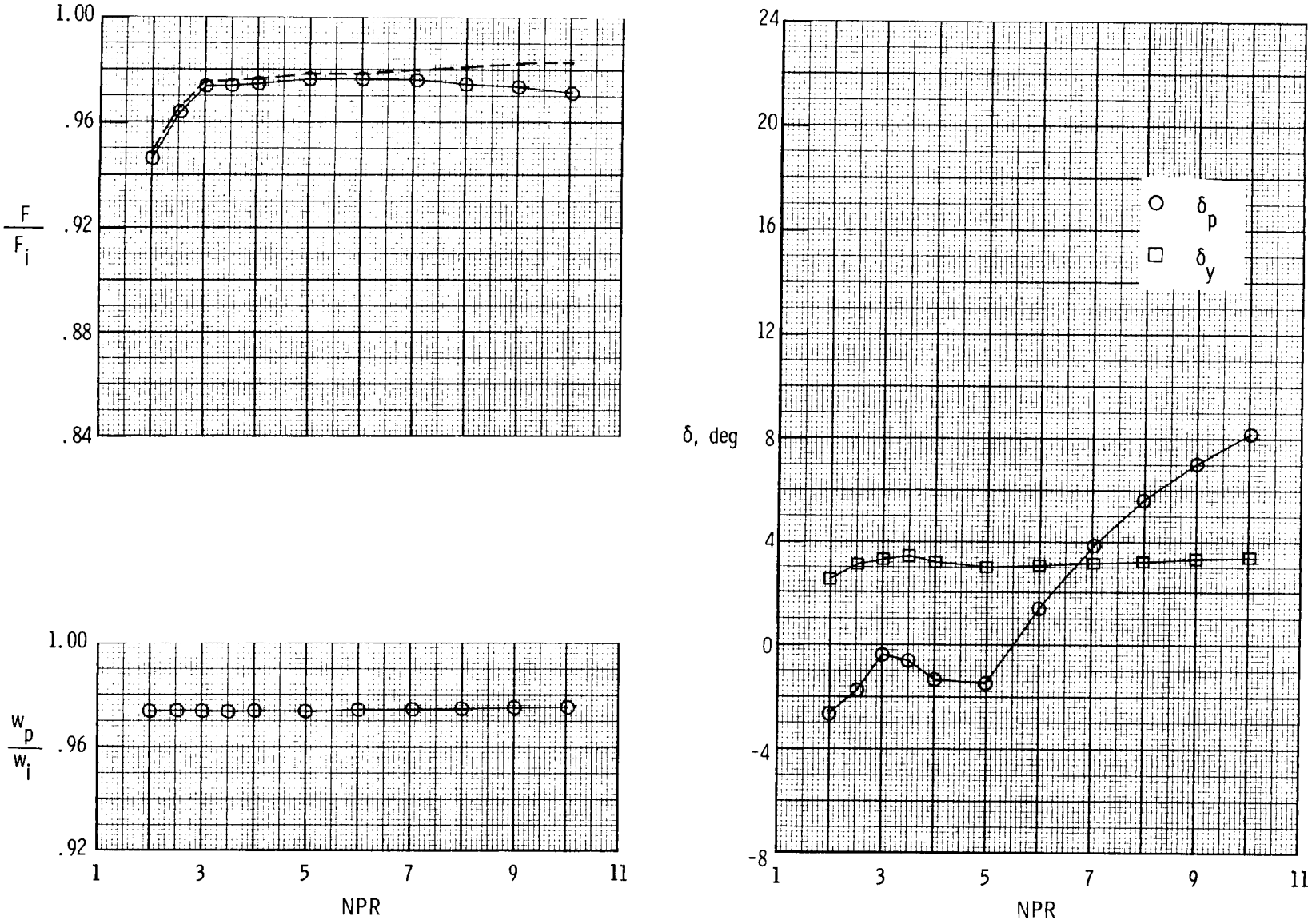

(c) Configuration SR3; $c = 0.75$ in.; $\delta_{v,y} = 20°$.

Figure 64. Continued.

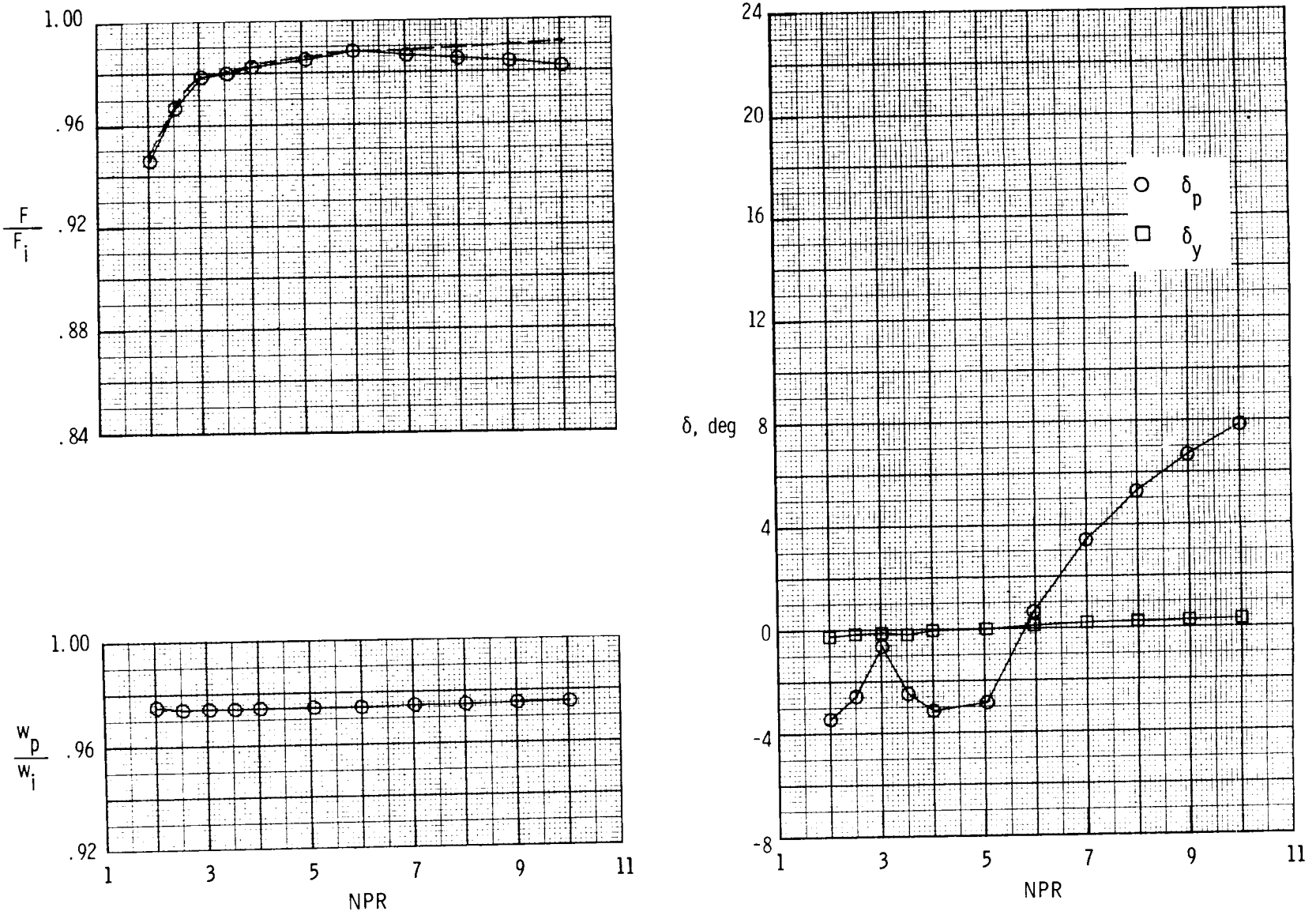

(d) Configuration SR4; $c = 1.50$ in.; $\delta_{v,y} = 0°$.

Figure 64. Continued.

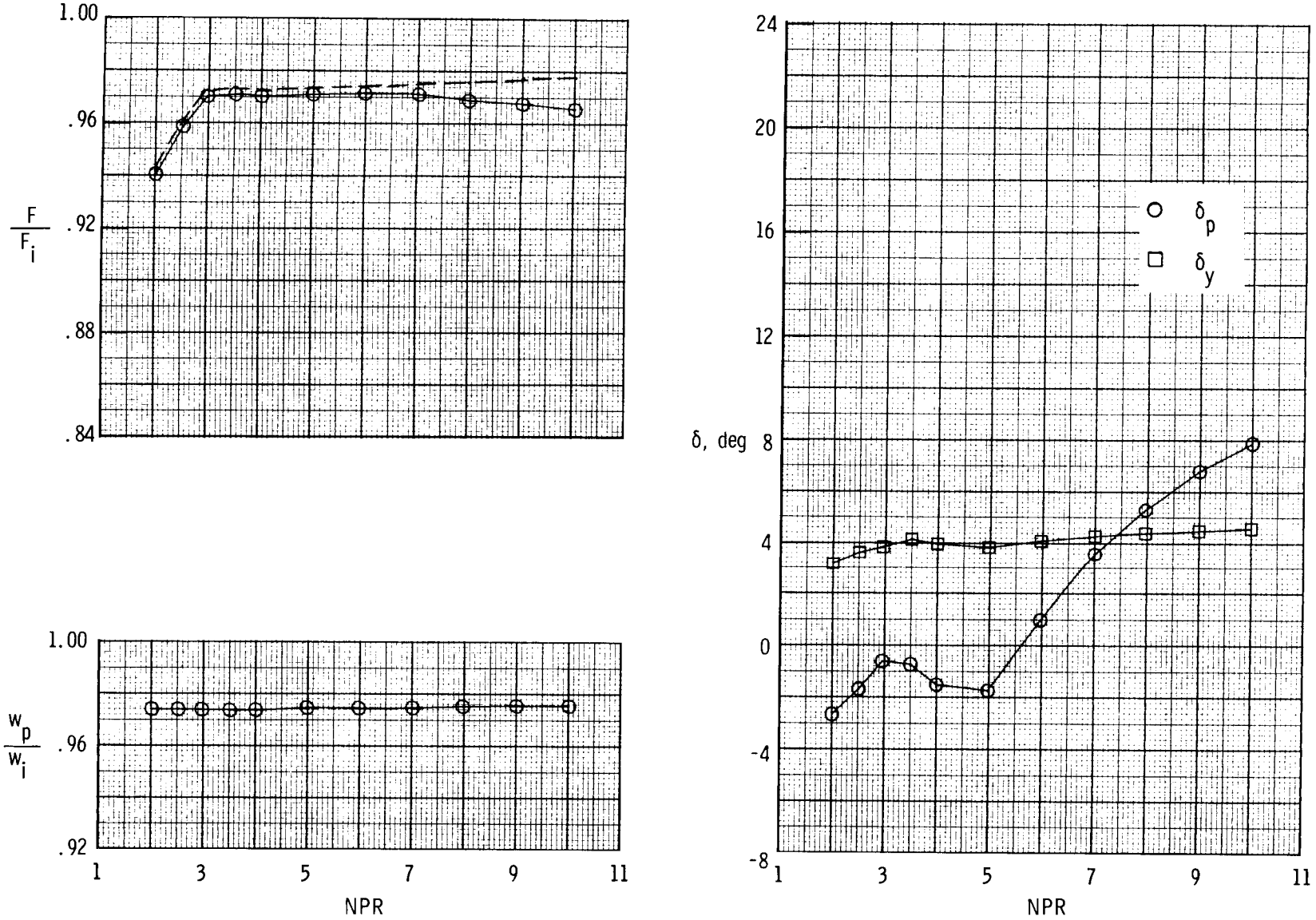

(e) Configuration SR5; $c = 1.50$ in.; $\delta_{v,y} = 20°$.

Figure 64. Concluded.

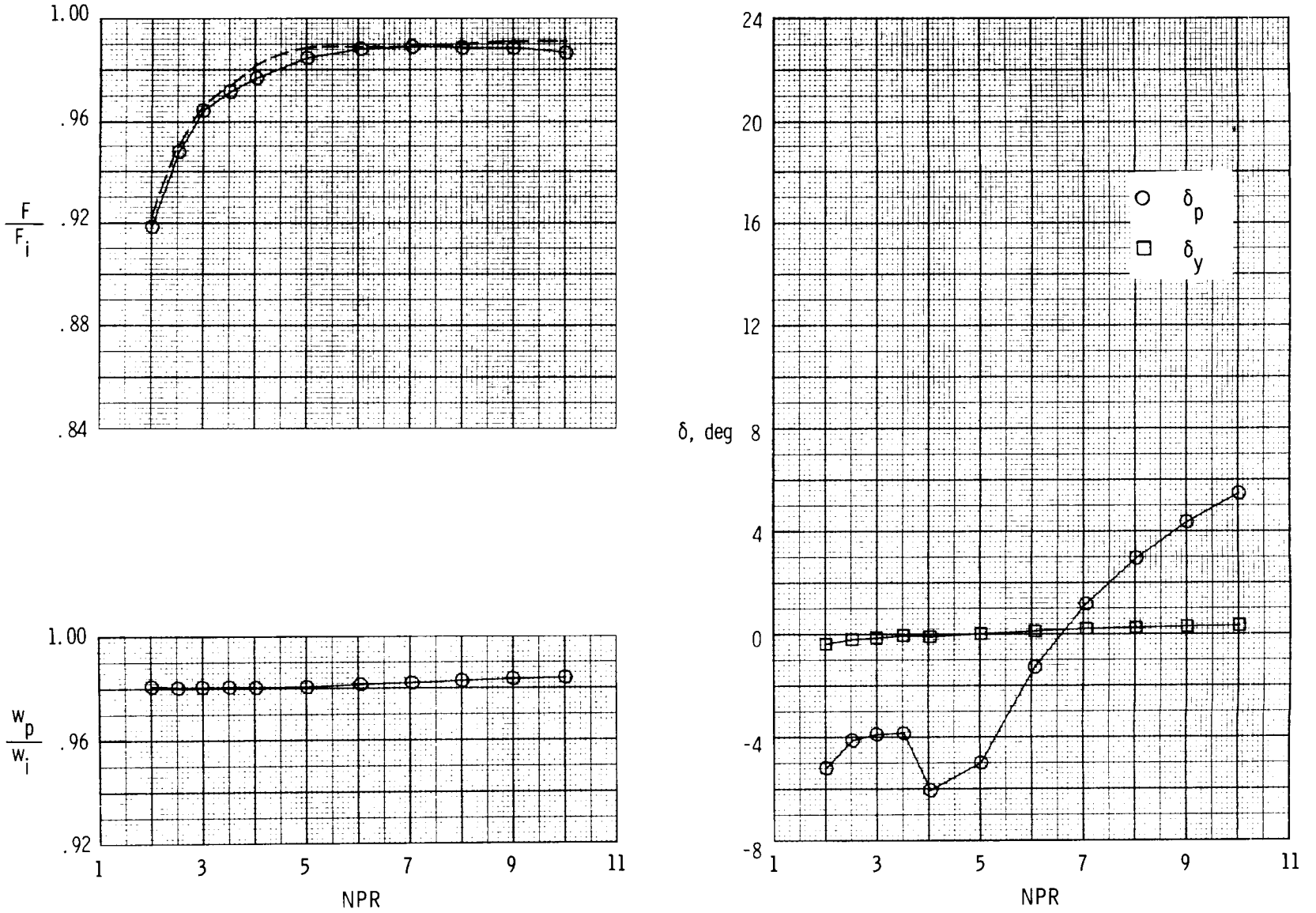

(a) Configuration SR6; yaw vector flaps off.

Figure 65. Variation of nozzle thrust ratio, discharge coefficient, and resultant thrust vector angles with nozzle pressure ratio for dry power SERN, $(A_e/A_t)_i = 1.24, (A_e/A_t)_e = 1.50$ and $\delta_{v,p} = 0°$, with post-exit flaps yaw vectoring concept. Dashed line indicates resultant thrust ratio F_r/F_i.

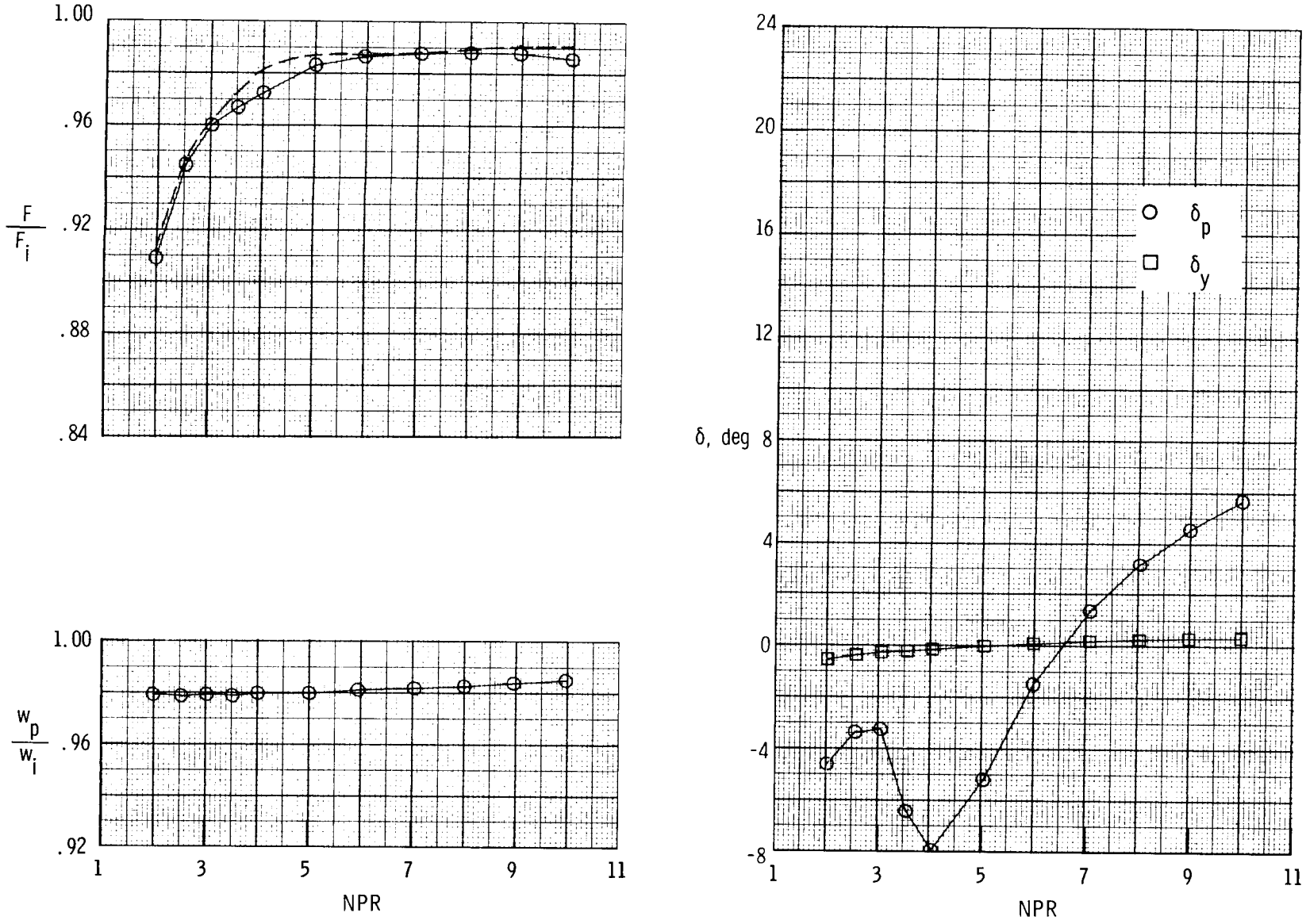

(b) Configuration SR7; $c = 0.75$ in.; $\delta_{v,y} = 0°$.

Figure 65. Continued.

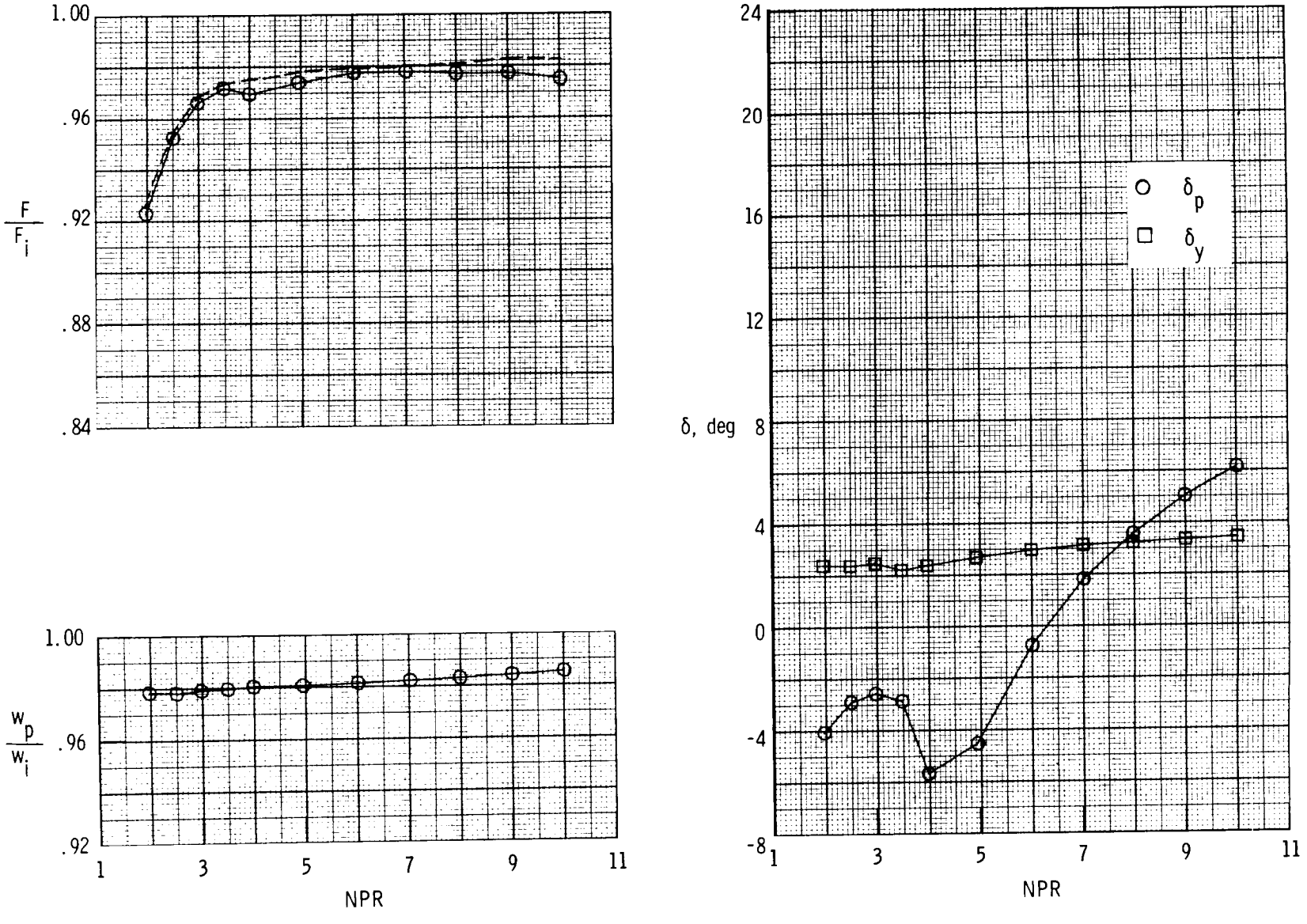

(c) Configuration SR8; $c = 0.75$ in.; $\delta_{v,y} = 20°$.

Figure 65. Continued.

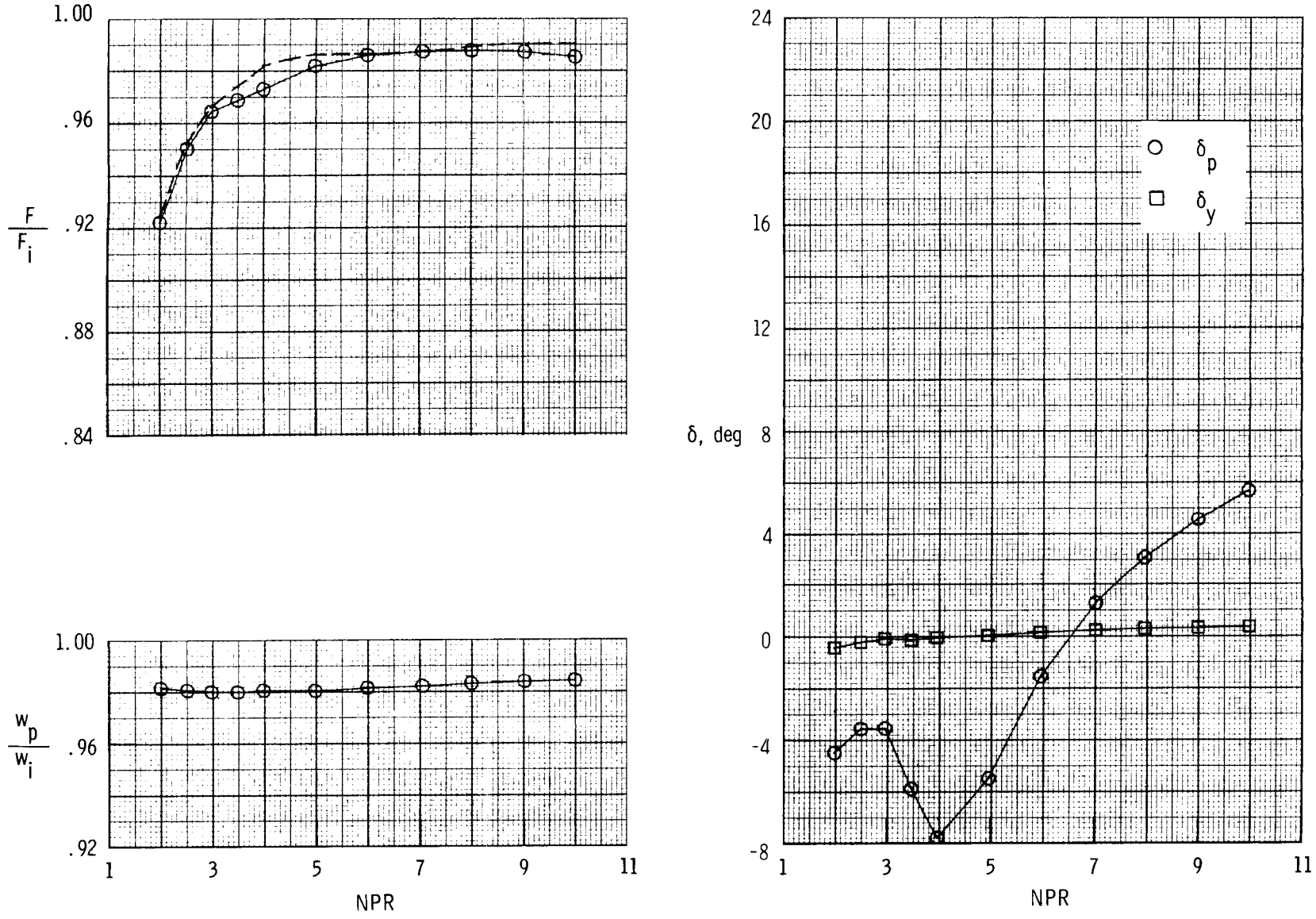

(d) Configuration SR9; $c = 1.50$ in.; $\delta_{v,y} = 0°$.

Figure 65. Continued.

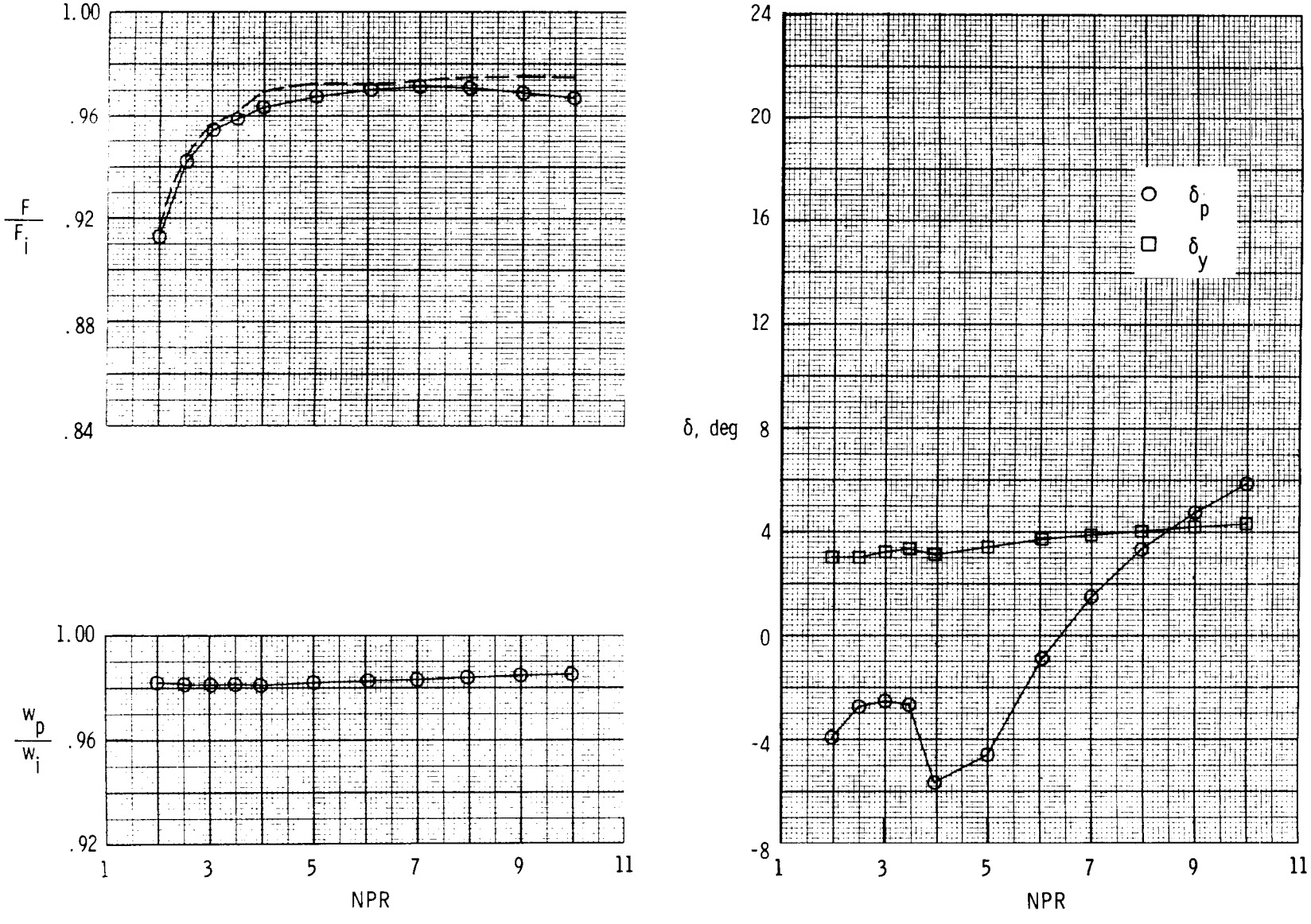

(e) Configuration SR10; $c = 1.50$ in.; $\delta_{v,y} = 20°$.

Figure 65. Concluded.

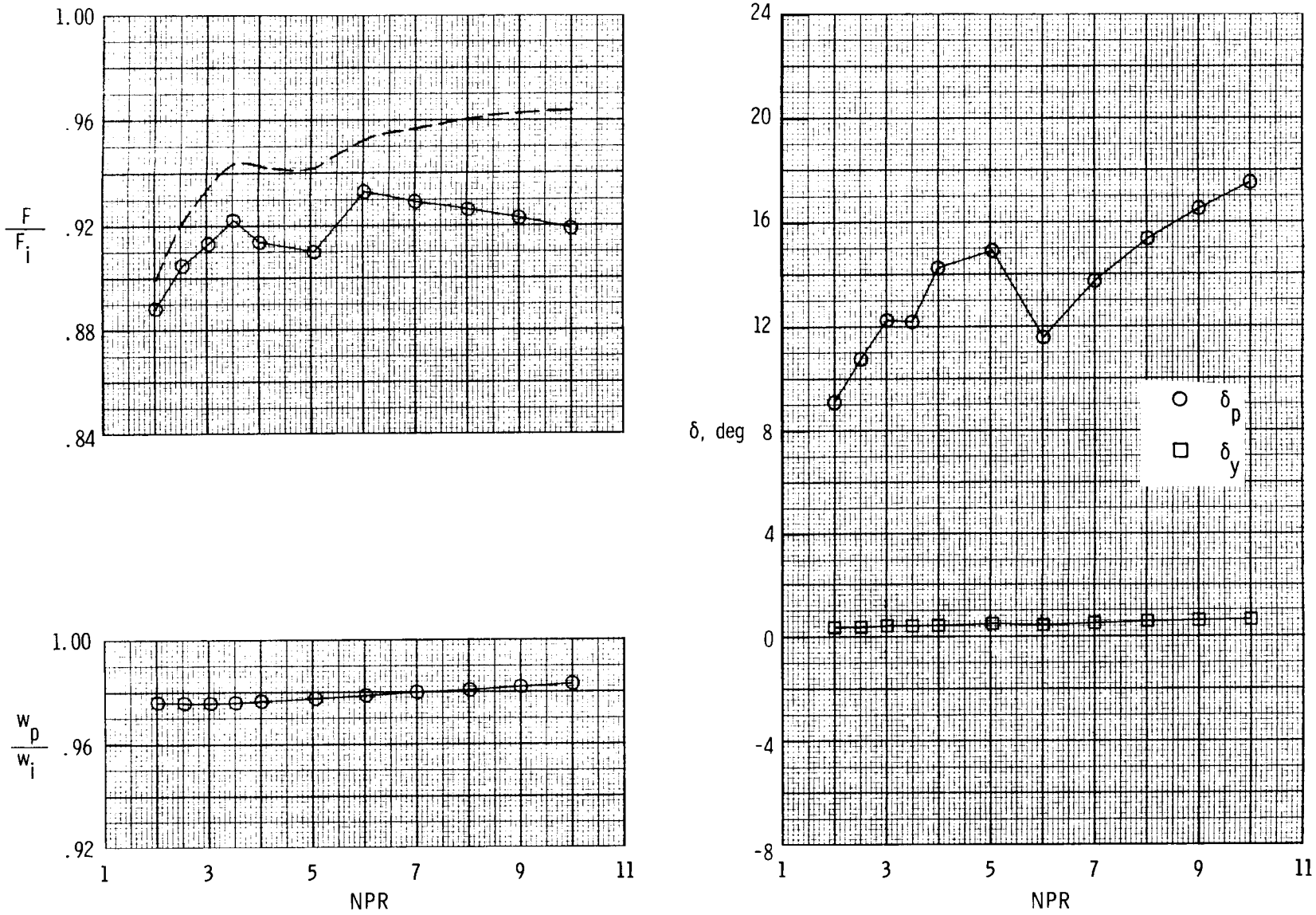

(a) Configuration SR11; yaw vector flaps off.

Figure 66. Variation of nozzle thrust ratios, discharge coefficient, and resultant thrust vector angles with nozzle pressure ratio for dry power SERN, baseline $(A_e/A_t)_i = 1.24$, baseline $(A_e/A_t)_e = 1.50$, and $\delta_{v,p} = 20°$ (upper flap), with post-exit flaps yaw vectoring concept. Dashed line indicates resultant thrust ratio F_r/F_i.

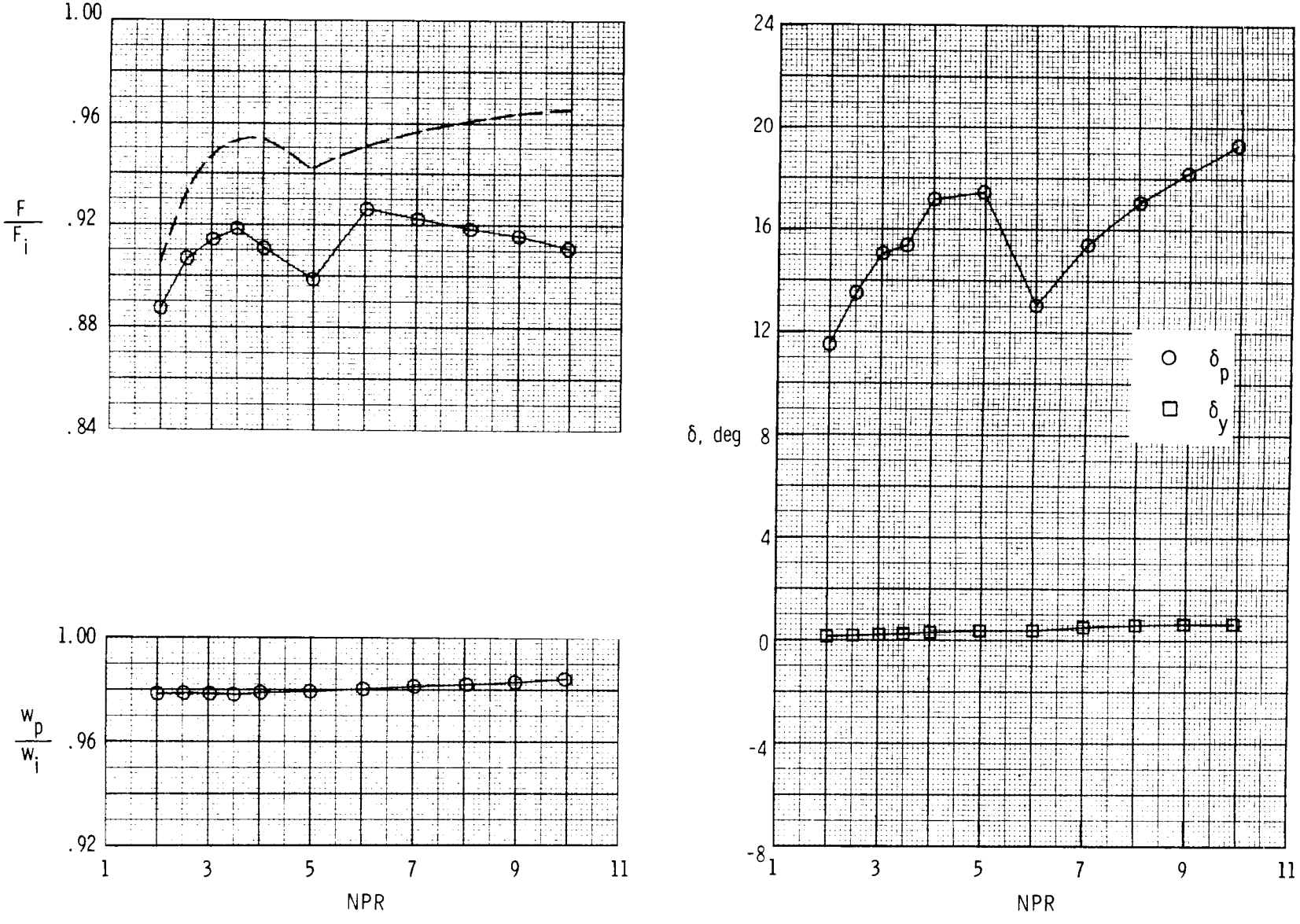

(b) Configuration SR12; $c = 0.75$ in.; $\delta_{v,y} = 0°$.

Figure 66. Continued.

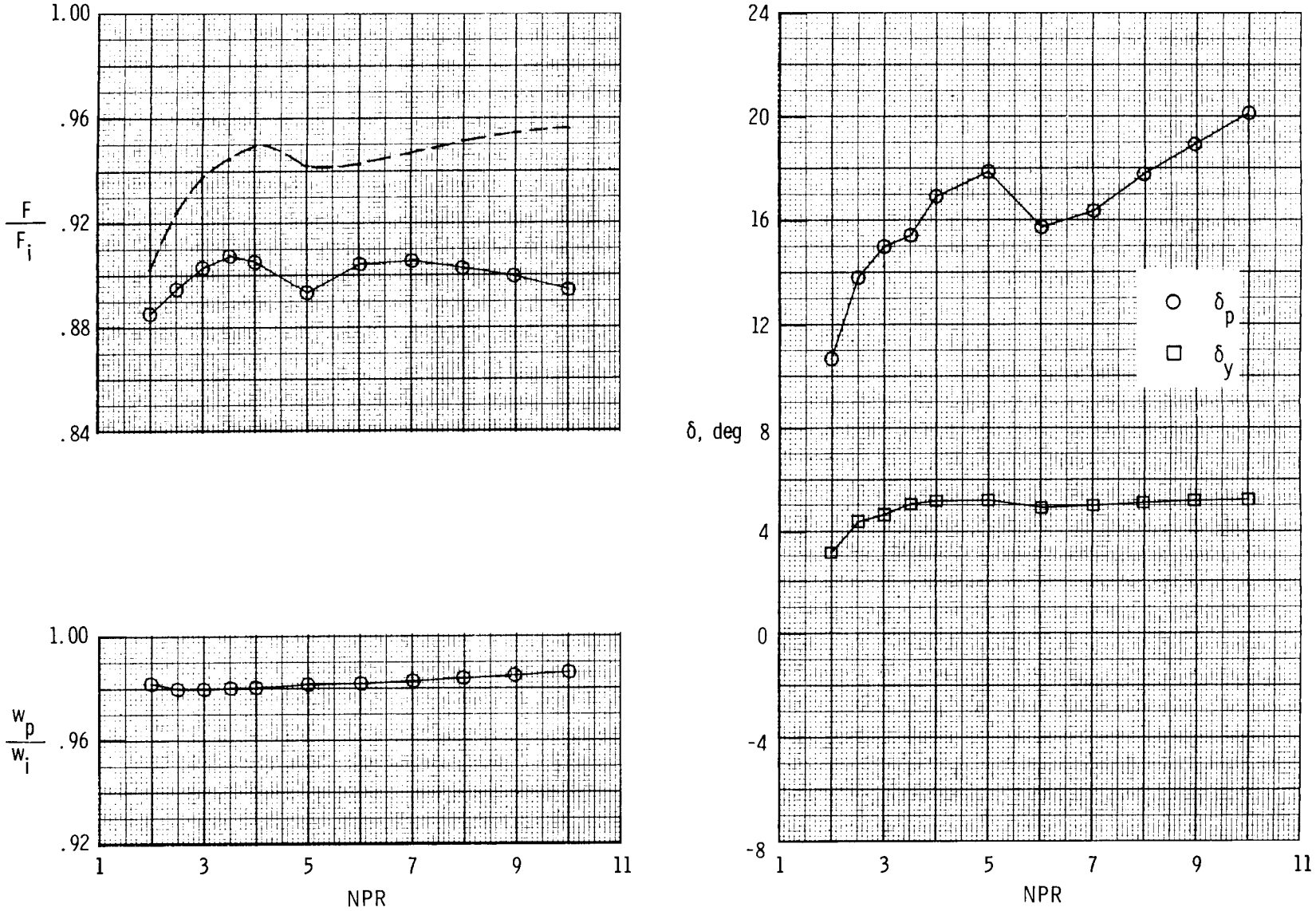

(c) Configuration SR13; $c = 0.75$ in.; $\delta_{v,y} = 20°$.

Figure 66. Continued.

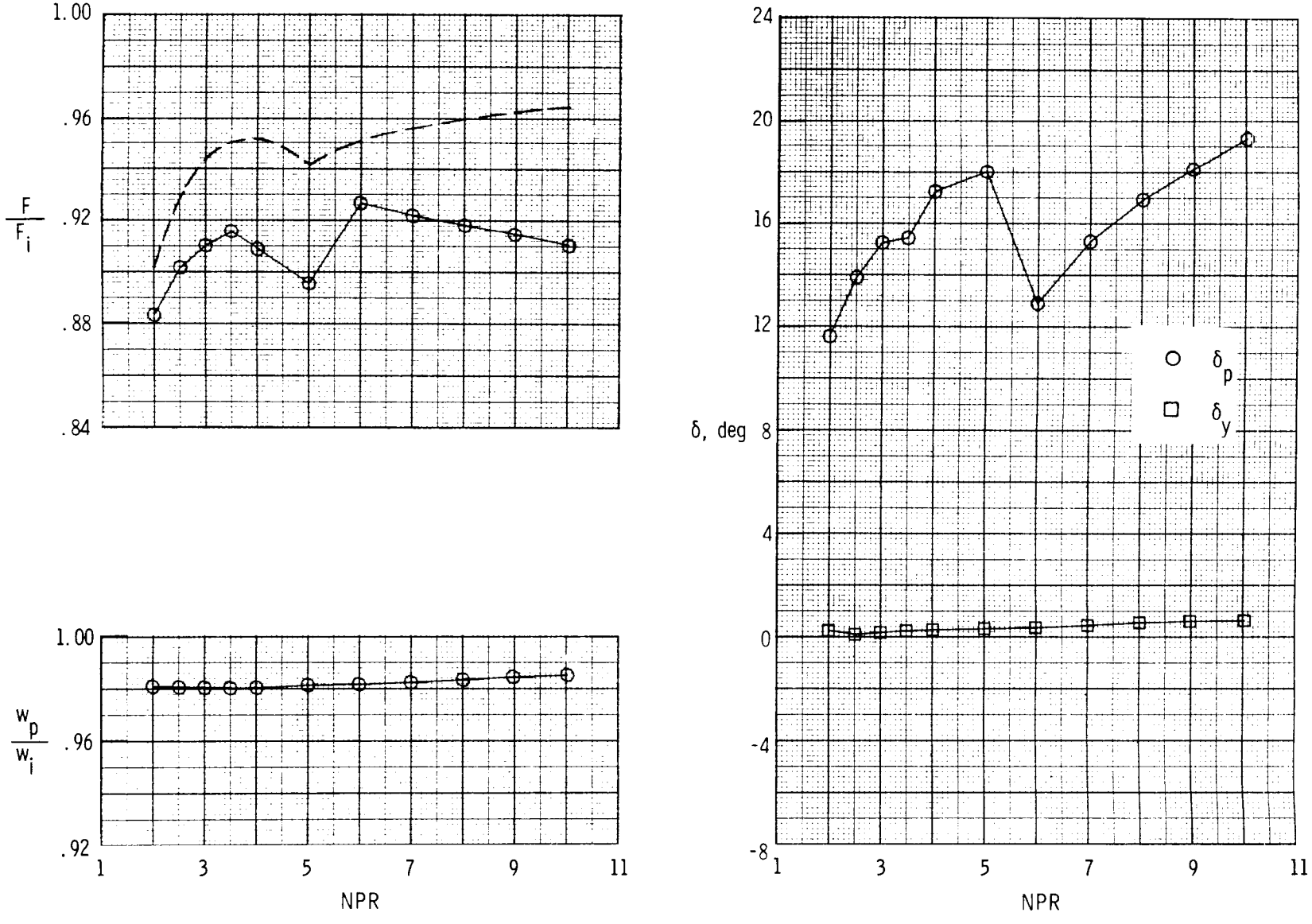

(d) Configuration SR14; $c = 1.50$ in.; $\delta_{v,y} = 0°$.

Figure 66. Continued.

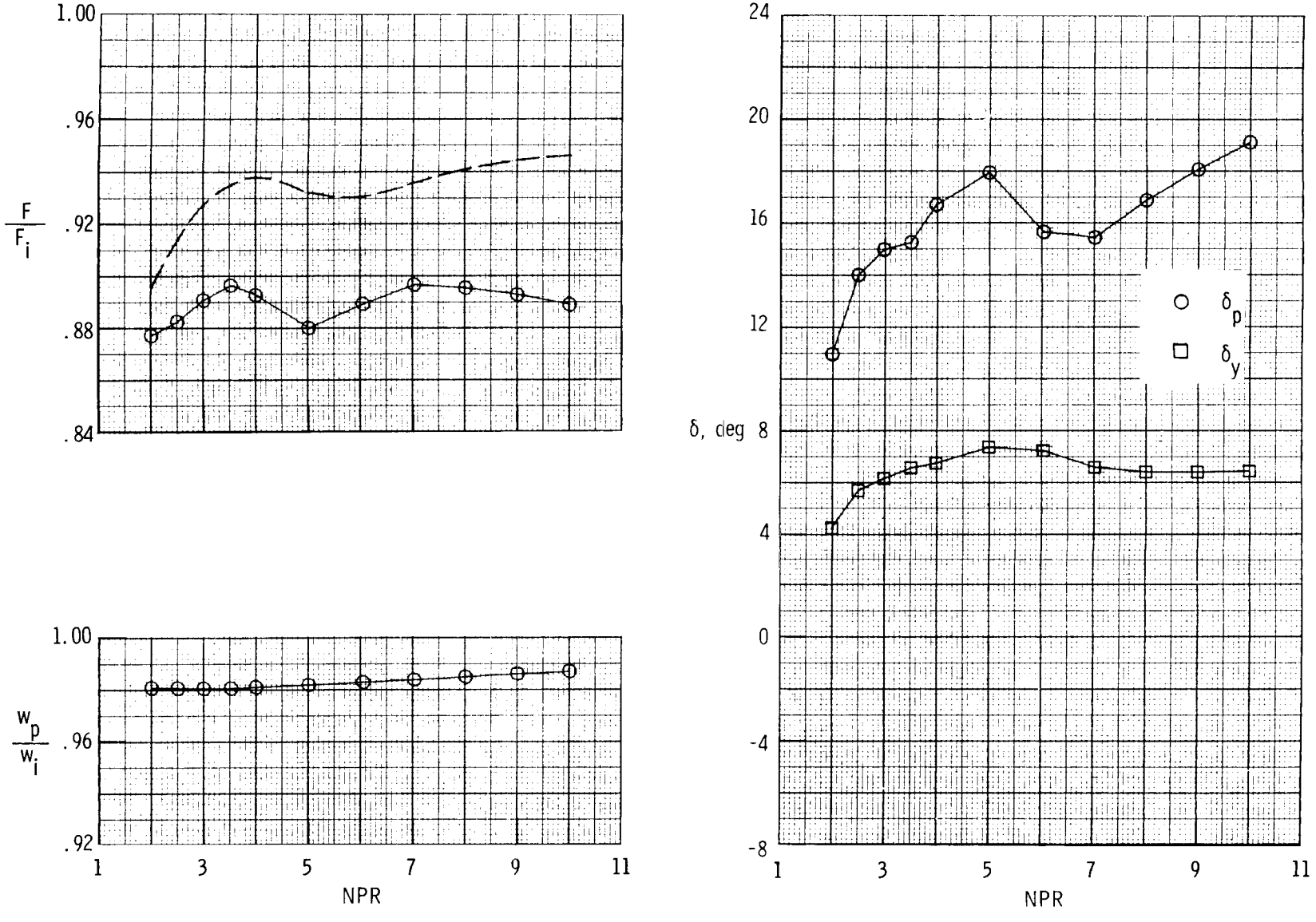

(e) Configuration SR15; $c = 1.50$ in.; $\delta_{v,y} = 20°$.

Figure 66. Concluded.

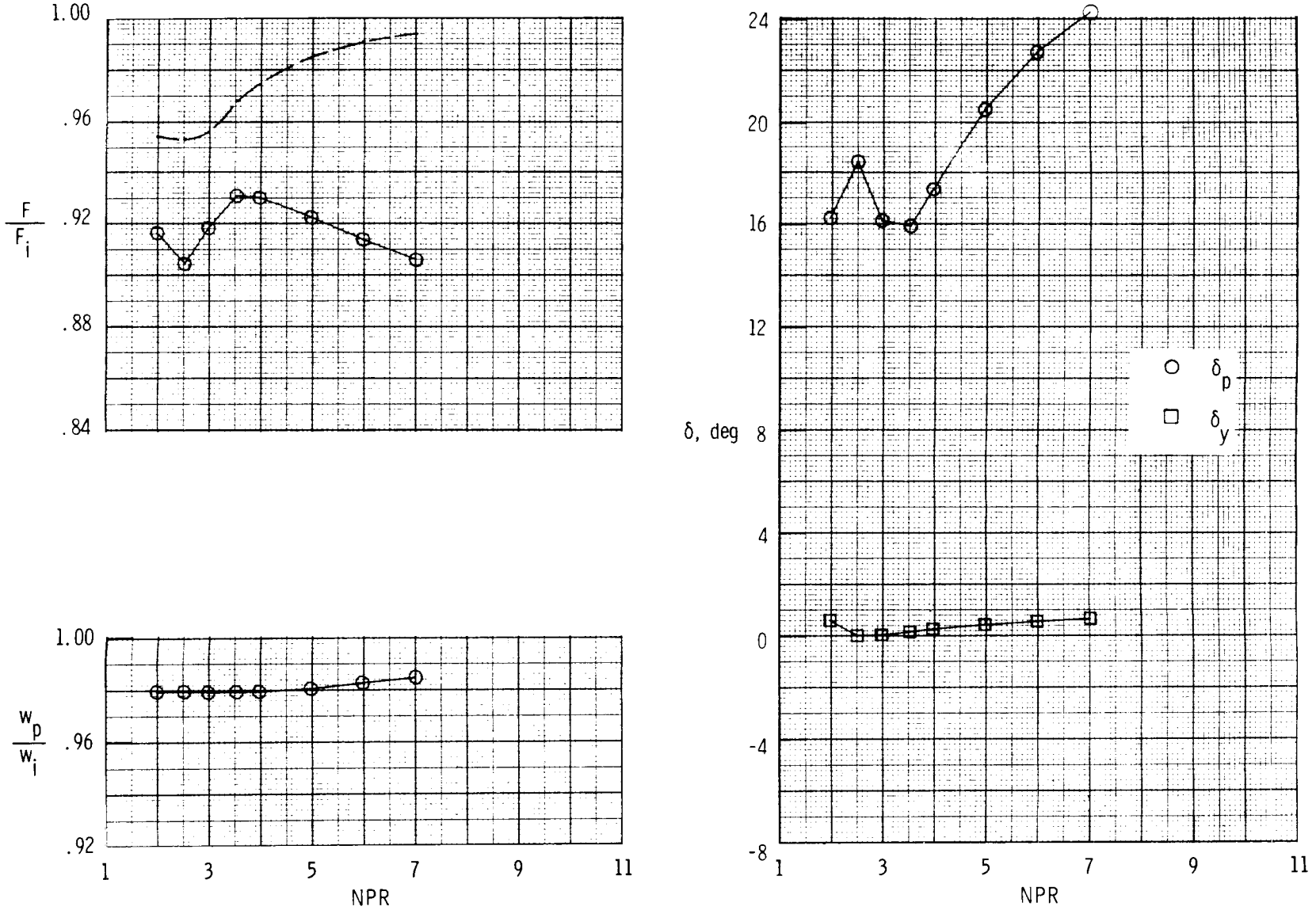

(a) Configuration SR16; yaw vector flaps off.

Figure 67. Variation of nozzle thrust ratio, discharge coefficient, and resultant thrust vector angles with nozzle pressure ratio for dry power SERN, baseline $(A_e/A_t)_i = 1.24$, baseline $(A_e/A_t)_e = 1.50$ and $\delta_{v,p} = 20°$ (upper and lower flaps), with post-exit flaps yaw vectoring concept. Dashed line indicates resultant thrust ratio F_r/F_i.

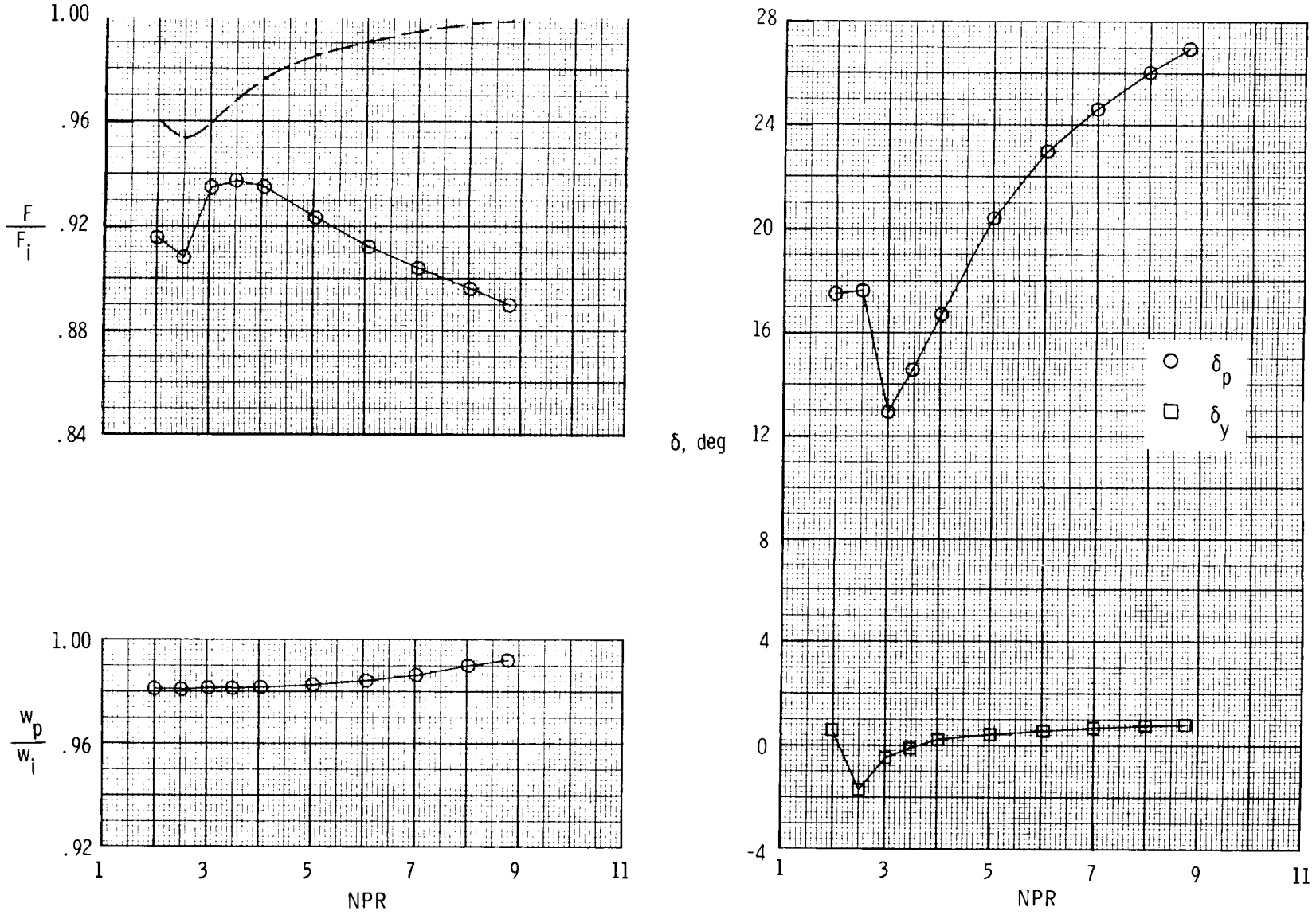

(b) Configuration SR17; $c = 0.75$ in.; $\delta_{v,y} = 0°$.

Figure 67. Continued.

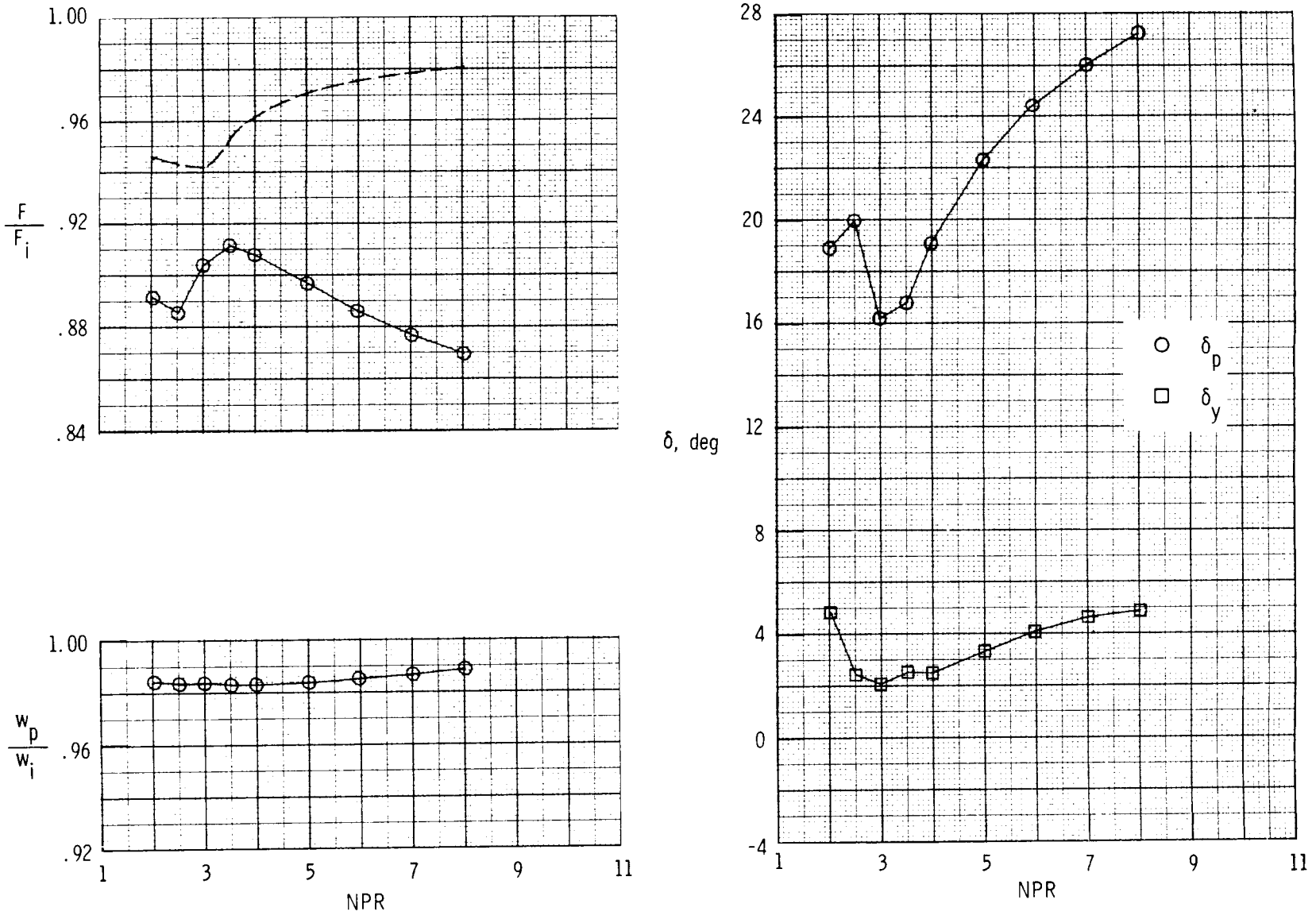

(c) Configuration SR18; $c = 0.75$ in.; $\delta_{v,y} = 20°$.

Figure 67. Concluded.

1. Report No.	2. Government Accession No.	3. Recipient's Catalog No.
NASA TP-2432		

4. Title and Subtitle	5. Report Date
Static Investigation of Several Yaw Vectoring Concepts on Nonaxisymmetric Nozzles	June 1985
	6. Performing Organization Code: 505-40-90-01
7. Author(s): Mary L. Mason and Bobby L. Berrier	8. Performing Organization Report No.: L-15890
9. Performing Organization Name and Address: NASA Langley Research Center, Hampton, VA 23665	10. Work Unit No.
	11. Contract or Grant No.
12. Sponsoring Agency Name and Address: National Aeronautics and Space Administration, Washington, DC 20546	13. Type of Report and Period Covered: Technical Paper
	14. Sponsoring Agency Code

15. Supplementary Notes

16. Abstract

A test has been conducted in the static test facility of the Langley 16-Foot Transonic Tunnel to determine the flow-turning capability and the effects on nozzle internal performance of several yaw vectoring concepts. Nonaxisymmetric convergent-divergent nozzles with throat areas simulating dry and afterburning power settings and single expansion ramp nozzles with a throat area simulating a dry power setting were modified for yaw thrust vectoring. Forward-thrust and pitch-vectored nozzle configurations were tested with each yaw vectoring concept. Four basic yaw vectoring concepts were investigated on the nonaxisymmetric convergent-divergent nozzles: translating sidewall, downstream (of throat) flaps, upstream (of throat) port/flap, and powered rudder. Selected combinations of the rudder with downstream flaps or upstream port/flap were also tested. A single yaw vectoring concept, post-exit flaps, was investigated on the single expansion ramp nozzles. All testing was conducted at static (no external flow) conditions and nozzle pressure ratios varied from 2.0 up to 10.0.

17. Key Words (Suggested by Authors(s))
Nonaxisymmetric nozzles
Yaw thrust vectoring
Internal performance

18. Distribution Statement
Unclassified Unlimited

Subject Category 02

19. Security Classif.(of this report)	20. Security Classif.(of this page)	21. No. of Pages	22. Price
Unclassified	Unclassified	217	A10

For sale by the National Technical Information Service, Springfield, Virginia 22161

NASA-Langley, 1

National Aeronautics and Space Administration

Washington, D.C.
20546

Official Business
Penalty for Private Use, $300

SPECIAL FOURTH CLASS MAIL
BOOK

Postage and Fees Paid
National Aeronautics and
Space Administration
NASA-451

NASA

POSTMASTER: If Undeliverable (Section 158 Postal Manual) Do Not Return